SYNTHESIS AND CHARACTERIZATION OF NOVEL TBAF-PROMOTED DESILYLATION OF FLUOROGENIC 3-CYANO-7-HYDROXY-4-METHYLCOUMARIN DERIVATIVES AS POTENTIAL RAPID FLUORIDE DETECTORS IN POTABLE WATER

BY

EDWIN OTIENO AKUMU

A THESIS SUBMITTED TO THE SCHOOL OF SCIENCE IN PARTIAL FULFILMENT OF THE REQUIREMENTS FOR THE DEGREE OF DOCTOR OF PHILOSOPHY IN ORGANIC CHEMISTRY, UNIVERSITY OF ELDORET, KENYA.

JULY, 2021

DECLARATION

This thesis is my original work and has not been presented for a degree in any other University. No part of this thesis may be reproduced without the prior written permission of the author and/or University of Eldoret.

Signature………………………….Date…………………………………

EDWIN OTIENO AKUMU

SC/PHD/004/15

Declaration by the Supervisors

This thesis has been submitted for examination with our approval as University Supervisors.

Signature………………………….   Date……………………………

DR. STEPHEN BARASA

Department of Chemistry and Biochemistry, University of Eldoret

Signature………………………….   Date……………………………

PROF. SAMUEL LUTTA

Department of Chemistry and Biochemistry, University of Eldoret

Signature………………………….   Date……………………………

PROF. TERESA AKENGA

Department of Chemistry and Biochemistry, University of Eldoret

DEDICATION

Specially dedicated to;

The entire Lameck Akumu's Family

My dear wife Damaris,

Daughter Patience

and

Sons Praston and Powell.

ABSTRACT

Over the years, Fluoride has been identified as a contaminant of great global concern on drinking water safety. The need to prevent the population from consuming higher fluoride content in water lies in fluoride sensing. A number of the reported fluoride probes are water-insoluble and suffer from a longer time taken to respond thus, limiting application in real-time fluoride detection. To solve the above problems, new and accurate fluoride detectors with ability to detect very low Fluoride concentrations in water in the presence of other anions have been developed. Three novel sensors 7-O-tert-butyldimethylsylyl-3-cyano-4-methylcoumarin (**2**), 7-O-tert-butyldiphenylsylyl-3-cyano-4-methylcoumarin (**3**) and 7-O-tert-butyldimethylsylyl-2-(hydroxyimino)-4-methyl-2*H*-chromene-3-carbonitrile (**4**) were synthesized by introducing fluoride responsive *tert*-butyldimethylsilylchloride (TBDMS) and *tert*-butyldiphenylsilylchloride (TBDPS) moieties into the 3-cyano-7-hydroxy-4-methylcoumarin (**1**) derivatives and by modifying the lactone moiety of compound (**1**) by substituting the lactone carbonyl with a hydroxyimino group. The starting reagent (**1**) and the synthesized compounds 7-O-tert-butyldimethylsylyl-3-cyano-4-methylcoumarin (**2**), 7-O-tert-butyldiphenylsylyl-3-cyano-4-methylcoumarin (**3**) and 7-O-tert-butyldimethylsylyl-2-(hydroxyimino)-4-methyl-2*H*-chromene-3-carbonitrile (**4**) were characterised using GC-MS spectrometer (Micromass, Wythenshawe, Waters, Inc. UK), Bruker Avance NEO 500 MHz (TXO cryogenic probe) NMR spectrometer and Agilent 400 MHz -DD2 NMR spectrometers. The NMR spectral data were processed by MestreNova (v14.0.0) software. The absorption and fluorescence characteristics of these synthesized fluoride sensors were studied by use of UV-Vis spectrophotometer and Fluorospectrophotometer. An investigation on the response of the synthesized sensors **2**, 7-O-tert-butyldiphenylsylyl-3-cyano-4-methylcoumarin (**3**) and 7-O-tert-butyldimethylsylyl-2-(hydroxyimino)-4-methyl-2*H*-chromene-3-carbonitrile (**4**) to environmentally and biologically relevant anions revealed lower levels of background of fluorescence in the range of 2.1 to 3.9 AFU. However, their fluorescence responses were not considerably affected due to direct competition with the tested anions apart from fluoride. These results undoubtedly show that environmentally relevant groundwater anions found in do not impede with fluoride detection by the synthesized sensors 7-O-tert-butyldimethylsylyl-3-cyano-4-methylcoumarin (**2**), 7-O-tert-butyldiphenylsylyl-3-cyano-4-methylcoumarin (**3**) and 7-O-tert-butyldimethylsylyl-2-(hydroxyimino)-4-methyl-2*H*-chromene-3-carbonitrile (**4**). The detection limits of these sensors were established to be 4.5-8.5 μM in aqueous NaF solutions with 7-O-tert-butyldimethylsylyl-2-(hydroxyimino)-4-methyl-2*H*-chromene-3-carbonitrile (**4**) being the most sensitive. However, they confirmed their capability to determine TBAF concentrations as lower concentrations of between 0.18 μM and 1.9 μM. This is considered much lower than the current WHO guidelines for maximum fluoride concentration in potable water of 789.4 μM (1.5 mgL^{-1}). The second order rate constants for these sensors were between 1.4 x10 M^{-1}min^{-1} and 1.9 x10 M^{-1}min^{-1}. This demonstrates their ability to rapidly sense the existence of aqueous fluorides in potable water. The quantum yields of these sensors compared against quinine sulphate (standard) were established to be between 0.65 and 0.72. This indicates that all the synthesized sensors had higher efficiency of photon emission than Quinine sulphate which stands at 0.546.

TABLE OF CONTENTS

LIST OF TABLES

LIST OF FIGURES

LIST OF APPENDICES

LIST OF SYMBOLS AND ACCRONYMS

1D	One dimension
1D NMR	One dimension Nuclear magnetic Resonance
2D NMR	Two dimension Nuclear magnetic Resonance
Å	Angstrong
AA	Activated alumina
AAS	Atomic Absorption Spectroscopy
ACN	Acetonutrile
ACNTs	Alligned Carbon Nanotubes
ACQ	Aggregation-caused quenching
AIDAs	Allosteric indicator displacement assays
AIE	Aggregation-induced emission
BDE	Bond dissociation energy
BODIPY	dipyrrometheneboron difluoride
BTTPB	N-(3-(benzo[d]thiazol-2-yl)-4-($tert$-butyldiphenyl silyloxy)phenyl)-benzamide
CDCl$_3$	Deuterated chlorophorm
CNS	Central nervous system
CNTs	Carbon nanotubes
COSY	Correlation spectroscopy
CT	Charge transfer
CTAB	Cetyltrimethylammonium bromide
CTABr	Cetyltrimethylammonium bromide
DCM	Dichloromethane
DDAs	DimerDye disassembly assays

DDQ	2,3-Dichloro-5,6-dicyano-1,4-benzoquinone
DFT	Density-functional theory
DI	De-ionized
DICH	2-(3,5-dichloro-2,6-dihydroxy-phenyl)-benzoxazole-5-carboxylic acid
DNA	Deoxyribonucleic acid
DTA	differential thermal analysis
DVB	Divinylbenzene
EARS	East African Rift System
ED	Electrodialysis
EDGs	Electron donating groups
EDTA	Ethylenediaminetetraacetate
EET	Electronic energy transfer
eIDAs	Enantioselective indicator displacement assays
ER	Endoplasmic reticulum
ESI	Electrospray Ionization
ESIPT	Excited state intramolecular proton transfer
ET	Electron transfer
EthAc	Ethyl acetate
ETM	Electron transmission microscopy
EtOH	Ethanol
EWGs	Electron withdrawing groups
FC-A	Fluorescent chemodosimeter compound
FCs	Fluorinated compounds
FIDAs	Fluorescent indicator displacement assays
FISE	Fluoride ion-selective electrode

FRET	Fluorescence/ Förster resonance energy transfer
FS	Flurospectrometre
GO	Graphene oxide
HEPES	4-(2-hydroxyethyl)-1-piperazineethanesulfonic acid
HF	Hydroge fluoride
HMBC	Heteronuclear Multiple Bond Correlation
HOMO	Highest occupied molecular orbital
HOMO	Highest occupied molecular orbital
ICT	Intramolecular charge transfer
HPLC-PDA-ESI-MS	Highperformance liquid chromatography-photodiode array detection-electrospray ionisation mass spectrometry
HSQC	Heteronuclear single quantum coherence or Heteronuclear single quantum correlation
HS-SPME	Headspace solid phase microextraction
Hz	Hertz
ICP-MS	Inductively Coupled Plasma Mass Spectrometry
ICT	Internal Charge Transfer
IDAs	Indicator displacement assays
IE	Ion exchange
IIDAs	Intramolecular indicator displacement assays
IR	Infrared
ISC	Intersystem crossing
ISEs	Ion–selective electrodes
K	Kelvin
k_2	Second-order rate constant.

k_{obs},	Pseudo-first-order rate constant
LOD	Limit of detection
LUMO	Lowest unoccupied molecular orbital
LUMO	Lowest unoccupied molecular orbital
m/z	Charge mass ratio
MAS	Molecular Absorption Spectrophotometry
MC-IDAs	Mechanically controlled indicator displacement assays
MEC	Molar Extinction Coefficients Determination
MeOD	Deuterated methanol
MeOH	Methanol
MHz	Megaherts
mL	millilitre
MLCT	Metal–ligand charge transfer
MS	Mass Spectrometer
NF	Nano-filtration
NIR	Near infrared
NMR	Nuclear Magnetic Resonance
NOESY	Nuclear Overhauser Effect Spectroscopy
NOM	Natural organic matter
OLEDs	Organic light-emitting diodes
PDT	Photodynamic treatment
PET	Photoinduced electron transfer
PL	Photoluminescence
PNS	Peripheral nervous system
ppb	Parts per billion

ppm	Parts per million
PRE	Paramagnetic relaxation enhancement
PSs	Photosensitizers
pTLC	Preparative thin layer chromatography
PVC	Polyvinylchloride
QDAs	Quencher displacement assays
RIAs	Reaction-based indicator displacement assays
RNA	Ribonucleic acid
RO	Reverse osmosis
t	time
TBA	Tert-Butyl alcohol
TBAB	Tetra-n-butylammonium bromide
TBAF	Tetra-n-butylammonium fluoride
TBDMS	*tert*-butyldimethylsilyl
TBDMSCl	Tertbutyldimethylsilylchloride
TBDPS	*tert*-butyldiphenylsilyl
TBDPSF	*tert*-butyldiphenylsilylfluoride
TDDFT	Time-dependent density-functional theory
TF	Thylstrup and Fejerskov Fluorosis Index
TFA	Trifluoroacetic acid ()
TG	Thermo-gravimetric
THF	Tetrahydrofuran
TICT	Twisted intramolecular charge transfer
TLC	Thin layer chromatography
TMS	Tetramethylsilane

TP	Two-photon
TPA	Two photon absorption
TT	Triplet–Triplet
TTA	Triplet-Triplet attrition
UV	Ultraviolet
UV-Vis	Ultraviolet-Visible
v/v	Volume:volume ratio
v/v/v	Volume:volume:volume ratio
WHO	World Health Organisation
XAD-4	Amberlite
XRD	X-ray diffraction
δ	chemical shift
ε	Solvent permittivity
η	Refractive index

ACKNOWLEDGEMENTS

CHAPTER ONE

INTRODUCTION

This chapter discusses the sources and methods of exposure and health consequences of fluorides. The methods of fluoride detection and analysis have also been emphasized. This chapter concludes by identifying the gap in the literature that this study will fill through the problem statement and justification of this research.

1.0 Background of study

An elevated fluoride concentration in domestic water is a major health risk since it can cause fluorosis, which is a common and severe condition on the teeth and bone. Given the relevance of fluoride, an effort has been made to design and produce basic, cheap, and simple-to-use fluride sensors. A number of the reported fluoride probes are water-insoluble and usually suffer from a longer time taken to respond thus, limiting their application in real-time fluoride detection. This research work aimed at solving the aforementioned problems; by designing novel accurate fluoride detectors with ability to detect aqueous Fluoride ion concentrations below the WHO recommended fluride levels in the presence of other anions.

1.1   Fluorine

1.1.1   Occurrence

Fluorine is a natural element that ranks 13th in terms of abundance (Shahid, *et al.,* 2019). The Earth's crust contains approximately 0.08 % of Fluorides (Yadav, 2019). It highly dissolves in air, water and soil. Due to its high reactivity, Fluorine does not occur as an independent atom in nature, but bound to other elements as fluoride (Lacson *et al.,* 2020). In 2016, a study on dental caries Global Disease burden estimated that dental

caries of the permanent teeth was most prevalent. This accounts for about 2.4 billion people, out of which, about 486 million children suffer from primary teeth caries (Vos *et al.,* 2017).

Over the years, fluoride has been identified as a contaminant of great global concern in terms of drinking water safety (Barathi *et al.,* 2019). Fluorine commonly occurs in many rock-forming minerals and sedimentary rocks. Fluorine is the most abundant halogen in the sedimentary rocks. Classic sediments can contain higher levels of fluorine, while sediments that are either of life origin or/and chemical may contain more than 800 mg/kg fluorine (Ranjan & Yasmin, 2019). On average, fluoride content of rocks ranges between 100 milligram for every kilogram in ultramafic rock deficient in SiO_2 to 1000 milligrams for every kilogram in alkalic rock (Ranjan & Yasmin, 2019). Fluoride ions are released into groundwater from fluoride bearing minerals. These include; biotite, fluorite, fluoroapatite, among others (Adimalla *et al.,* 2018). Some parts of Africa especially Eastern and western are highly affected by fluoride contamination (Bhattacharya, 2020).

Fluoride is commonly observed in ground water due to natural and anthropogenic processes during its formation. Fluoride can get dissolved in groundwater after being leached out during the natural movement of water in the soil substrata. In many basement aquifers, high fluoride concentration is commonly found in calcium-deficient ground waters, these include; geothermal fluids, granite, and sedimentary basins among others. (Bhattacharya, 2020). When water passes through the rocks, there is ion exchange between F^- and OH^-, this leads to elevated amounts of fluoride in groundwater (Adimalla *et al.,* 2018).

Natural phenomenon includes mainly weathering of rocks, volcanoes and geothermal activities. The geological settings and types of rock are the two major contributors that influence the variation of groundwater fluoride ion concentrations. Fluorine concentrations in igneous and volcanic rocks vary from 100 mg/kg (ultramafic) to more than 1000 mg/kg (alkalic) while in sedimentary rocks it ranges from about 200 mg/kg in limestone to 1000 mg/kg in shales; metamorphic rocks' fluoride concentration range from about 100 mg/kg in regional metamorphism to a much higher than 5000 mg/kg in global/contact metamorphism (Bondu, 2020). Some of the most common Fluoride occurrences in the ecosystem are shown in Figure 1.1.
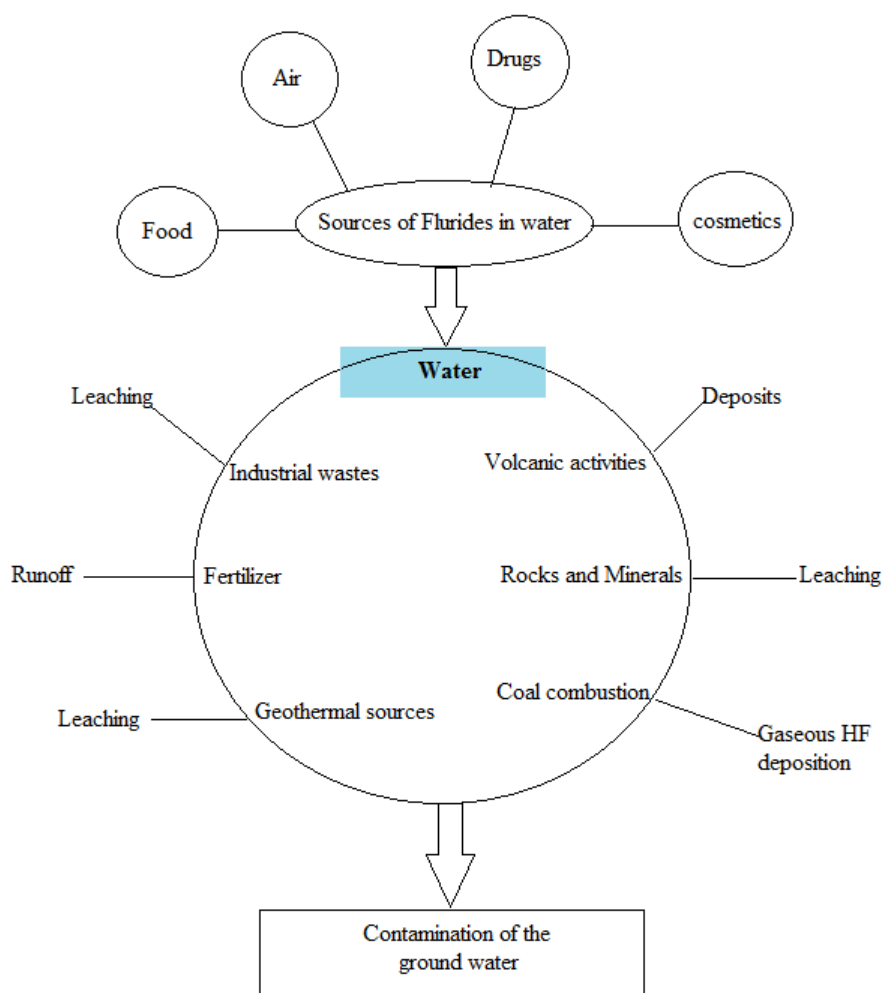
Figure 1.1: Some of the common sources of ground water fluoride contamination in the ecosystem.

The information on some of the fluoride-bearing minerals or rock with its chemical compositions is provided in table 1.1. Fluoride-rich groundwater may be found in several regions of the world, notably major parts of Middle East, Southern Asia (Sri Lanka, Bangladesh, and India, Pakistan), China and Africa (Keesari *et al.,* 2021). One of the most well-known continental high fluoride zones runs from Malawi to Eritrea along the East African rift system, as well as from Iraq to Turkey. Other countries include; India, Iran, Northern Thailand, China and Afghanistan (Dharmaratne, 2019; Dhilleswara *et al.,* 2021). Even though aquifer mineral has high concentration of fluoride, contact time or reaction time plays major role in ultimate concentration of fluoride in source water. High fluoride concentrations can build up due to longer reaction time. These types of aquifers are commonly associated with deep aquifer systems and zones where groundwater flow velocity is low (Saeed *et al.,* 2020).

Table 1.1: Natural sources of fluorides

Source	Formula	Fluoride Content
Sellaite	MgF_2	61%
Villiamnmite	NaF	55%
Cryolite	Na_3AlF_6	54%
Fluorspar	CaF_2	49%
Topaz	$Al_2 SiO_4 (F,OH)_2$	11%
Bastnaesite	$(Ce, La) (CO_3) F$	9%
Lepidolite	$K(Li,Al)_3(Si,Al)_4O_{10}(F, OH)_2$	4.9%
Phlogopite	$KMg_3(Si_3AlO_{10})(F,OH)_2$	4.5%
Fluorapatite	$Ca_3(PO_4)_3F$	4%

(Rubio *et al.,* 2020; Štepec, *et al.,* 2019).

Fluoride levels are typically low in shallow aquifers that are commonly infiltrated with rainfall. Variations can be found in other aquifers found in active volcanic regions that have been altered by hydrothermal activity. The fluoride solubility rises with rising temperature as well as the dissolution of HF gas (Ong *et al.,* 2020). Thus, groundwater with high fluoride concentration is associated with thegeochemistry of the region having neutral to alkaline pH of 7.6–8.9, low Ca, and high Na and HCO_3 concentrations (Subba *et al.,* 2020).

Further, the intrinsic groundwater fluoride content is determined by geological factors and the physicochemical features of the aquifer (temperature, pH, porosity, and chemical composition), and depth of the aquifer and intensity of weathering (Subba *et al.,* 2020). Some of the anthropogenic activities like agriculture, industrial operations (soils used in concrete/ceramic industry or coal burning) and phosphate-based fertilizer usage also greatly influence in increasing the groundwater fluoride concentration. Source includes liquid discharges from industries like glass, ceramic, brick, iron works, toothpaste, electroplating, and many more (Ankidawa *et al.,* 2020).

Fuel combustion byproduct fly ash contains high fluoride similar to volcanic fly ash. Every year, between 100 and 150 million tonnes of fly ash are released in the air globally as a result of coal combustion, particularly in electric power generation stations (Yousuf *et al.,* 2020). Fluoride gets leached into groundwater once fly ash is disposed of improperly. Atmospheric fluoride originates from fluoride-containing soils, gaseous industrial pollutants, coal fires and volcanic activity (Schlesinger *et al.,* 2020). At later stages, these atmospheric fluorides are deposited on ground and enter the hydrological cycle. Table 1.2 shows the five major natural sources of fluorides.

Table 1.2: Average fluoride concentration ranges in environment

Environment	Range	Unit
Ambient air (non-industrial zone)	0.01–0.4	$\mu g/m^3$
Ambient air (industrial zone)	5–111	$\mu g/m^3$
Precipitation (non-industrial zone)	1–89	$\mu g/L$
Precipitation (industrial zone)	0.1–1	mg/L
Ocean (increases with depth)	0.3–1.4	mg/L
Soil	90–980	mg/L
River	0.1–0.2	mg/L

(Ali, 2020).

1.1.2 Applications of fluorine

Fluorine as an element remains a key player in a larger number of biochemical processes. Due to its unique character in preventing caries and in the treatment of osteoporosis, it is commonly included as an important constituent in toothpaste. Other applications include pharmaceutical, beauty products and drinking water. Fluoride is required for suitable growth and protection of strong teeth and bones as well as healthy hair and nails. It is also applied in military science as nerve gas monitor as well as in nuclear weapon manufacture (Udhayakumari, 2020).

1.1.3 Health significance of fluorides

Water is considered to be the largest contributor for daily fluoride intake amounting to about 75–90% (Assunção *et al.,* 2018). Fluoride ion precence in domestic and particularly drinking water has always been a double-edge sword with both beneficial and detrimental effects on the population's health depending on the amounts of consumption. It is beneficial for older people since it reduces hardening of arteries,

stimulates bone formation, and helps in the treatment of osteoporosis (Johnston & Strobel, 2020).

Human exposure to fluoride is via drinking water, foods, products for dental cleanliness, absorption through the skin from chemicals and contact with certain wastes and emissions from industries (Villanueva *et al.,* 2014). Concentration of fluoride past the recommended World Health Organization (WHO) limit of 1.5 milligram for every litre (Cotruvo, 2017) is common in several regions within the African continent. Fluoride (F⁻) is consumed by millions of people globally through water uptake. According to the most recent estimates, more than 200 million individuals from 25 states worldwide suffer from effects caused by fluorosis. China and India, the world's two most populated countries, are the hardest affected (Rasool *et al.,* 2018).

The United States public health service has set its daily fluoride maximum uptake to be 1 milligram. On average, the human body contains about three milligrams of fluoride (Peckham and Awofeso, 2014). Fluorine as an element is exceedingly poisonous. Fluorosis (Wang *et al*., 2020), causes severe toxic effects to the tissues leading to grave neurodegenerative and related diseases (Esparza *et al.,* 2019; Grandjean, 2019). Furthermore, disorders of the kidney increased density of the bone, cancer and even death may be caused by consuming higher levels of fluorides (Udhayakumari, 2020). In 2017, a study by Malago *et al.,* showed that high fluoride levels occur in states such as Kenya, Tanzania, Uganda, Sudan, and Ethiopia within Eastern region of Africa, Malawi, and South Africa within the Southern side of Africa and Nigeria, Algeria, Ghana in Western side of Africa. The maximum known fluoride concentration so far

stands at 2,800 milligrams per litre of water in Lake Nakuru located in Kenya's central rift (Malago, 2017).

Another study by Wambu *et al.,* in 2014 estimated that 36% of children living in Bondo-Rarieda are at risk of fluorosis as they consume water from ground sources with fluoride levels above the recommended WHO limit (Wambu *et al.*, 2014). Soaring water fluoride levels is related to volcanic activities, especially the ones with high pH, volcanic gas emissions, granitic and gneissic rocks (Mengyan, 2020). The health significance of fluoride consumption at different levels is as shown in table 1.3.

Table 1.3: Health significance of fluoride consumption

Fluoride, mg/L	Impact
< 0.5	Tooth decay
0.5–1.5	Optimum dental health, works against dental caries
1.5–3	Dental fluorosis, blackening and enamel hypoplasia and teeth from long-term exposure, mottled enamel, Roentgenographic bone changes, polydipsia
3–8	Skeletal fluorosis, damages fetus, infant mortality due to calcification of blood vessels, low IQ in children, osteosclerosis, renal diseases, elevated serum alkaline phosphatase, stiffness of knees and hips, increased bone mineral density, bone and joint pains.
10–100	Gastroenteritis, skin irritation, deformation of bones and other skeletal abnormalities, thyroid changes, growth retardation, kidney damage, crippling

(Johnston & Strobel, 2020; Wang *et al.,* 2020)

The presence of F⁻ anions at concentrations above 1.5 mg/L is causes spotting and discoloration (mottling) of teeth. The long-term exposure may result in permanent grey to black discoloration of the enamel (dental fluorosis) (Khandare *et al.,* 2018). Children consuming water containing fluoride of 5 mg/L may develop pitting of the enamel. Further, consuming larger concentration of 30–50 mg/L may lead to deformation of bones and other skeletal abnormalities. Since fluoride affinity towards phosphate is high, 96–99% of consumed fluoride combines with bones. Optimum concentration of fluoride consumption (1.5 mg/L, according to WHO) helps to maintain dental health and appropriate bone density (Saeed *et al*., 2020).

Non-skeletal fluorosis causes gastrointestinal related ailments as well as neurological problems (Grandjean, 2019). From these facts, it is evident that fluoride has adverse impact on human health when it is consumed at higher concentrations and for longer duration. Reducing fluoride concentration from excess to safe levels is very essential. Different physicochemical methods are proposed to be practiced and investigated for fluoride elimination from water using chemicals, biosorbents, ion exchange resins, etc., which are synthesized or are naturally available (George, 2020).

Teeth fluorosis is the dental hard tissues pathology that occurs during the formation of the teeth (Simmer *et al.,* 2012). Endemic fluorosis incidence correlates with the environmental fluoride, particularly water (Mohammadi *et al.,* 2017). Endemic fluorosis is in more than a thousand zones in the world. The East African Rift System (EARS) states are highly exposed to high fluoride levels from their groundwater (Karunanidhi *et al.,* 2020). The general damages caused by fluorides in animals ranges from cells to

organs and even structures (Zhao *et al.,* 2018; Yadav, 2019; Jiménez-Córdova *et al.,* 2019; Wimalawansa, 2020).

Low concentration of Fluoride is favourable to healthy teeth. The WHO guidelines specifies a fluoride concentration limit of 1.5 milligrams for every litre of drinking water; lower than this, fluoride promotes the development of healthy teeth and strong and healthy bones However, beyond this concentration it is known to replaces apatite by chemical reaction in teeth (Mengyan, 2020). Calcified tissues, in particular, are a normal sinks for fluorides (Voicu *et al.,* 2020).

Incorporation of fluorides as fluoro(hydroxy)apatite in tooth enamel mediates its anticaries action (Iafisco *et al.,* 2018). Fluoride is known to play crucial role in teeth and bone mineralization (Walsh, *et al.,* 2019; (Saha, *et al.,* 2020), motility of sperms and fertility decline (Liang *et al.,* 2020), enzyme activation (Waugh, 2019) and the production of blood cells (Miranda *et al.,* 2018) among others. Fluorides at low levels also decrease the production of acid by inhibiting the breakdown of carbohydrates by bacteria (Zhao *et al.,* 2018).

Long-term interaction with excess fluorides lead to all forms of fluorosis (Wong & Stenstrom, 2018; Esparza *et al.,* 2019; Grandjean, 2019; Mengwei *et al.,* 2020; Zhang *et al.,* 2020). Skeletal fluorosis is considered in cases of extra bone growth accompanied by distended bone joints (Sellami *et al.,* 2020) leading to poor and unhealthy quality of the bones (Wu *et al.,* 2019). Acute fluoride toxicity includes nausea, vomiting, abdominal pain and diarrhoea (Amadeu de Oliveira *et al.,* 2018) (Jeffrey Kuo *et al.,* 2020).

The renal system is key in excreting excess ingested fluorides. On average, about half of the ingested fluorides' excretion is through the kidneys. Thus, the nephrons are highly exposed to Fluoride (Dharmaratne, 2019; Sivasubramanian *et al.,* 2019; Yazdi and Vosoogh, 2019). Those who continuously drink water with elevated fluoride levels are about five times more in danger of developing nephrolithiasis (Dissanayake and Chandrajith, 2019). Excess consumption of fluorides is also known to induce anomalies in chromosomes leading to genetic mutations (Johnston and Strobel, 2020). Even at a low concentration, fluorides have outstanding negative effects on protein as well as DNA and RNA biosynthesis and fragmentation (Sharma *et al.,* 2017).

1.2   Metabolism of fluoride

The human body absorbs approximately 90% of the fluoride that is ingested. As a result of the stomach's acidity, approximately 40% of ingested fluoride is taken up as HF by the walls of the stomach. The intestines absorb the rest of the fluoride, which is not affected by acidity. All absorbed fluoride is distributed throughout the body. The absorbed fluorides get incorporated into the Calcium-rich crystalline lattice regions especially the teeth and bones at a rate of 99%. Fluoride excretion is mostly through urine and sweat (Kabir *et al.,* 2020).

1.2.1   Effects on teeth

The impact of fluorides on teeth is determined by the doses including duration of exposure (Khandare *et al.,* 2018). Fluoride, at a reduced concentration, helps to reduce dental caries. Large quantities, on the other hand, cause dental fluorosis. This is condition is distinguished by yellowish or brown-like creases in tooth enamel. Fluoride

also decreases available Ca^{2+} and disrupts enamel calcification. The magnitude of tooth decay is determined by physical examination of the deposits mostly on front teeth. The Thylstrup and Fejerskov (TF) Fluorosis Index recommends a zero to five scale that shows the degree of tooth decay (Sezgin *et al.,* 2018).

1.2.2   Effects on bone

Bone is thought to be a perfect fluoride ion sink. Lengthy fluoride toxicity causes bone fluorosis (Wong & Stenstrom, 2018). Bone osteoporosis is caused by increased bone formation, which leads to greater bone mineral density and weight, as well as swollen joints. Despite increased bone density, a reduction of trabecular bone connection lowers bone quality (Wu *et al.,* 2019).

1.2.3   Effects on soft tissue

Excess fluoride intake harms the soft tissues of many organs. Several experiments have shown that certain results are linked to oxidative damage; however, the cause is largely unresolved (Jiménez-Córdova *et al.,* 2019).

By contrasting an edentulous subject panel (n = 9) to a completely dentate panel (n = 10), Zero and colleagues demonstrated the relevance and significance of oral soft tissue as the primary location of fluoride ion deposition and retention. They discovered no statistically significant difference in salivary flow rate seen between two panels for each operation. Salivary fluoride levels were higher in the edentulous panel than that of the dentate panel. However, the FD and FG treatments were statistically significant ($p <$ 0.05). Fluoride levels at particular soft-tissue locations were assessed during a sixty-minute period in a second research using absorbent discs implanted in distinct soft-

tissue oral regions. Fluoride levels were highest in the lower posterior vestibule and tongue, followed by that of the upper posterior buccal vestibule and upper anterior labial vestibule, and lowest in the lower anterior vestibule and floor of the mouth. This study group proposed a strong-to-moderate association of fluoride concentrations in total saliva and particular tissue (Zero *et al.,* 1992).

1.2.4   Gastrointestinal effects

The impact on gastrointestinal tract often is determined by ionic fluoride amounts in the belly instead of just the actual volume of fluorides consumed. Numerous severe gastrointestinal symptoms in animals, including humans, have been identified in cases of acute fluoride toxicity. This involves symptoms such as fatigue, vomiting, stomach problems, and diarrhea (Amadeu de Oliveira *et al.,* 2018; Jeffrey Kuo *et al.,* 2020).

1.2.5   Renal effects

The renal function is critical in discharging absorbed fluorides. The kidneys remove about half of the fluoride that is swallowed. Due to this, the nephrons are directly exposed to F^-. Following exposure to elevated fluoride levels in their drinking water, individuals are more likely to experience renal calculi, nephrolithiasis or urolithiasis (Dissanayake & Chandrajith, 2019).

1.2.6   Effects on the brain

Fluoride overexposure may have an effect mostly on the structure and operation of the CNS and PNS. Large amounts of fluoride accumulation in the hippocampus triggers neurodegeneration, reduces body creation of energy through the combustion in the presence of oxygen, and shifts in free radical metabolic processes. Fluorides often

improve the impact of aluminum on neuronal cytoskeleton metabolic processes (Esparza *et al.,* 2019; Grandjean, 2019).

1.2.7 Hepatic effects

One other primary functions of the liver of animals is the removal of both endogenous and exogenous contaminants. Numerous research findings have reported increases in the concentrations of liver-specific enzymes as a consequence of fluoride consumption. In addition, the rabbit liver cells undergo histopathological alterations in response to fluoride treatment. Incurable and pathological disruption has been observed in hepatocyte cells containing vacuoles (Mengwei *et al.,* 2020; Zhang *et al.,* 2020).

1.2.8 Cytotoxicity

Fluoride absorption causes chromosomal abnormalities and genetic defects in human cells. Fluorides have excellent influences on DNA and protein metabolism even at low doses. Fluorides in abundance can induce changes in cell morphology and DNA damage in nucleosomes (Johnston & Strobel, 2020).

1.3 Importance of Testing of Fluorides

In order to establish the level of fluorides in water, tests must be done. This is necessary to prevent the toxicity of fluorides to both terrestrial and aquatic biota. Fluorides accumulated in tissues find their way into the food chain through food (Darchen *et al.,* 2016). Biomagnification then occurs up the food chain (Banerjee *et al.,* 2019).

1.4   Methods of Fluoride Sensing

1.4.1   Mass Spectrometry (MS)

Fluoride sensing by MS depends on the gas–phase ions that are resolved based on the mass-charge ratio (m/z). However, the detection limit of this method stands at 0.5 mg L^- ^{1}, which is not satisfactory (Dhillon *et al.,* 2016). Kwon and Shin applied this method to detect fluoride in biological samples by using 2-(bromomethyl)naphthalene as a derivatizer, headspace solid phase microextraction (HS-SPME), and gas chromatography-tandem MS detection. Under these set reaction conditions, the LOD reported were 11 µg/L and 9 µg/L in 1.0 ml of urine and plasma respectively. At 0.1 mg/L and 1.0 mg/L concentrations, the intraday and interday relative standard deviations were recorded to be less than 7.7% (Kwon & Shin, 2015). This method also faces stability challenges that interfere with consistent detection of fluorides (Ünal *et al.,* 2019).

1.4.2   Inductively Coupled Plasma (MS)

The Inductively Coupled Plasma also referred to as ICP-MS is a prospective approach in analyzing fluorinated compounds (FCs). It has traditionally been known to be among the most accurate analytical tool. However, due to fluorine's high ionization potential and spectral and/or non-spectral interferences, direct detection of fluorine using this method is challenging. Several research works have documented adjustments to a standard ICP-MS analytical process on analysis and instrument optimization to improve the quality of results (Moirana *et al.,* 2021).

A superior F^- analytical technique ought to be able to efficiently execute non-targeted detection and quantification with little or no sample preparation steps. Several Fluoride

analytical techniques used currently need significant sample preparation while also not being capable of non-targeted analytes. With advancements in apparatus and procedure, ICP-MS has proven the capacity to fully perform non-targeted analysis at low LOD. Although significant sample preparation techniques are still required to prevent external interference during analysis, it is a promising technology. The hyphenation of ICP-MS to HPLC proven to become the most effective approach for determining and quantifying FCs, especially for noise reduction. Despite this, little research has been conducted on environmental analytes. Furthermore, recent advances in the identification and characterization of FCs in the positive mode of ICP-MS may be investigated in the negative mode of ICP-QMS for fluoride analysis (Moirana *et al.,* 2021).

This method atomizes samples using a plasma source. Although this method has lower detection sensitivity of about 110 µg L^{-1} and reduced interferences, it is costly, complex and requires high skilled operators (Ünal *et al.,* 2019). Guo *et al.,* (2017) determined the limit of detection (LOD) inductively coupled plasma quadrupole mass spectrometry (ICP-MS-MS) as 0.022µg mL^{-1} on total fluoride determination based on a mass-shift strategy (Guo *et al.,* 2017).

1.4.3 Atomic Absorption Spectroscopy (AAS) and Molecular Absorption Spectrophotometry (MAS)

This is a highly discriminatory and responsive analytical method. It involves absorption of radiation by gas-phase atoms. A study involving the determination of fluorine using a high-resolution continuum source electrothermal atomic absorption spectrometer reported a limit of detection of 0.105 ng (Ozbek & Akman, 2014). However, the

application of low resolution MAS is poor due to low resolution, absence of excitation frequencies, and incidence of spectral interferences (Ünal *et al.,* 2019).

1.4.4 Ultra Violet–Visible (UV-Vis) Spectroscopy

A number of straight forward and relatively cheap colorimetric or fluorescent sensors have been in use for fluoride detection in the past decades. However, this technique demonstrates a decline in the peak intensity with increase in the concentration of fluoride due to the collection of metal nanoparticles (Au, Ag and Cu) upon addition of fluoride ions (Ünal *et al.,* 2019).

1.4.5 Ion–selective electrodes

Ion–selective electrodes (ISEs) are used for both quantitative and qualitative analysis of several ions. Fluoride ion-selective electrode (FISE) is used for the quantitative determination of fluoride. The method's detection limits ranging from 0.001 mg/L to 20,000 mg/L is considered wide and is also affected by the interferences from sample colour, other ions, temperature variation, shift potential and ion activity (Ünal *et al.,* 2019; Goud *et al.,* 2020).

1.4.6 Fluorescence fluoride testing

Fluoride sensing fluorescent probe is required to contain two simple components: a receptor that recognizes the fluoride and a fluorophore that signals the identification by causing a visible physical wavelength shift. Several attempts to develop fluoride selective fluorescent probes have been made over the last decade. Inspite ofthis, obtaining realistic and cost–effective potential sensing probes is still a challenge (Ünal *et al.,* 2019).

The invention of superior analytical methods for fluoride sensing has received a lot of attention. Despite growing public interest, the production of fluoride probes has traditionally been difficult due to anion selectivity requirements. Several techniques used to detect and quantify fluoride exist, and these include electrolytic, colorimetric fluorescence and ^{19}F NMR studies (Dhillon *et al.,* 2016).

By utilizing unique chemical properties of fluoride, chemists have continuously designed fluoride specific colorimetric and fluorescent sensors. Due to the fluoride importance and toxicity, the creation of specific optical technique that can be used to analyse fluoride anion is getting prominence. Anion recognition and sensing by synthesis is of interest. Steps must be taken in this field directed in achieving optimal selectivity and sensitivity as well as solubility in aqueous systems by careful selection and modification of the fluorophores. Several mechanisms of action have been employed to achieve this (Johnston & Strobel, 2020).

1.5   Problem Statement

Clean water is a basic requirement for good health. An average teenage adult's overall body water content ranges between 50%–70% of the total body weight; (Naeem *et al.,* 2017). Potable water, on the other hand, is uncommon and safe water is rare in nature. Apart from particulate matter, water from natural sources includes various soluble salts. Surface and groundwater contain salts and minerals that originate from the soil and rocks with which they come into contact. Groundwater is the best for drinking in rural areas among the developing countries, including Kenya, where there is no piped water. The majority of surface waters in agricultural areas are polluted and contaminated,

putting direct users at risk of illness. As a result, relying on groundwater for drinking becomes essential.

Groundwaters in rift valley environment frequently have elevated fluoride levels. Knowledge on fluoride levels in potable water is crucial to systematically address water quality and extensively minimize human exposure to elevated fluoride concentration in drinking water.

The connection linking excessive fluoride intake and the occurrence of human fluorosis cannot be dismissed; fluorosis still affects people in many parts of the world. It persists due to the population's lack of choice of clean drinking water and food supplies, as well as the fact that a majority of first-world countries fluoridate their regionally centralized drinking water. Private water supply, food preferences, oral and pharmaceutical materials, factory emissions, and/or workplace exposure are only a few of the other causes. Depending on the primary source of exposure, steps such as eliminating fluoride from current water supplies and/or providing alternate water sources with low fluoride content, thus improving the way rainwater is captured can be taken to address this problem.

A number of known fluoride sensing systems focus on hydrogen bonding and Lewis acid/base relationships. These detectors, however, can only sense tetrabutylammonium fluoride in non-aqueous media. Despite the benefits, the majority of the probes documented is insoluble in water and hence have a long response period. As a result, their usage in real-time detection is minimal. Due to its dual position as a hazardous pollutant on the one hand and a beneficial addition in products consumed

by man as well as industrial processes products on the other, fluoride has become popular target for detection and sensing. Several publications have claimed the development of novel selective sensors for fluoride ion in the past, but only a handful of them have met the real conditions of high affinity and selectivity to be regarded.

More significantly, these molecular sensors function almost entirely in organic fluids or aqueous mixtures; fluoride sensing in water is only possible in a few exceptional cases, which is a critical need for broadening the area of use. Around 80% of the already existing anion receptors rely on H-bonding interactions for detection. In order to address these problems, this research intends to introduce novel fluoride sensors which are cheap, selective and respond fast to aquesous fluoride below the WHO set standards for maximum fluoride intake of not more than 1.5 mg/L.

Neutral, monotopic and simple hydrogen bonding fluoride detetors have exceptional strong affinity for fluoride in polar aprotic solvents, with K values as high as 107 M^{-1} in some cases, however they can't differentiate between fluoride anion and many other similarly basic anions. Under these conditions, these anions far too strongly interfere with fluoride sensing. With the exception of a few situations, building more sophisticated and multitopic frameworks do not always assist. Furthermore, in most situations, the presence of plar protic solvents, significantly decreases or even completely prevents binding. The use of more energetic binding driving factors, such as Lewis centre interactions, can improve sensing ability.

1.6   Justification

Fluoride can be harmful to the populations' health at elevated doses of (>1.5 mg/L), therefore it is a health concern to detect and quantify. Given the dangers of drinking water with elevated fluorides, considerable attention must be paid to the advancement of modern methods for fluoride sensing. Currently, WHO recommends two traditional fluoride-detecting methodologies. These techniques; Ion-selective electrodes and ion chromatography however, necessitate the use of professional, specialized equipment and skilled personnel. As a result, they are impossible to carry out in low-income or even middle-income economies round the Globe. Fluorescent fluoride probes that are simple to use, inexpensive, non-invasive, detect in real time, and are incredibly biased have piqued the interest of researchers (Liu *et al.,* 2018).

A number of different of defluoridation technologies, such as adsorption, reverse osmosis, precipitation-coagulation, nanofiltration, dialysis, and electrodialysis, and electrolytic defluoridation are capable of keeping fluoride concentration in potable water within acceptable limit. Adsorption is seen as a more feasible alternative for defluoridation due to its affordability and ease of design. Basically, this is a solid phase extraction approach that is suitable for a wide range of applications. The well-known Nalgonda method, which includes the use of lime and alum for fluoride adsorption and was developed in India, has been in use for a long time. However, there are some limitations to using the Nalgoda technique (Kimambo *et al.,* 2019). One major problem is the leaching of extra aluminum with a rise in the pH of treated water (Barathi *et al.,* 2019). Some of the well-studied adsorbents for fluoride removal include activated carbon from various sources, activated alumina, fly ash, and bone charcoal. Table 4 shows the advantages and disadvantages of several defluoridation techniques.

Because of fluorine's strong polarizing power and incredibly small size as an atom, several known fluoride sensing systems focus on hydrogen bonding and Lewis acid/base relationships (Han *et al.,* 2019). These detectors, however, can only sense tetrabutylammonium fluoride in non-aqueous media. Due to fluoride's large hydration enthalpy ($\Delta H_o = -504$ kJ/mol), their fluoride sensing has been shown to be extremely difficult in aqueous solutions (Zhan & Dixon, 2004).

Recently, a well-established technique for detecting fluoride in aqueous media has been developed, which is focused on the unusual chemical reactivity of silicon and fluoride in contrast to sensors based on non-covalent bonding and weak interactions. The probes that focus on complex reactions are more stable and selective (Han *et al.,* 2019).

Despite the benefits, the majority of the probes documented is insoluble in water and hence have a long response period. Furthermore, it is contradictory that the same hydrogen bonding that fails in abiotic systems is used by Nature to bind anions. High affinity is frequently achieved in by placing the binding site inside a hydrophobic pocket, a protected milieu where anion-sensing interactions are more favorable, in addition to meticulous customization of the active sites. As a result, their usage in real-time detection is minimal. Furthermore, a majority of these probes may be turned on or off with just a single-wavelength transition as the monitoring signal (Wu *et al.,* 2020). The detection precision is subjective to the environment and conditions such as the excitation energy, analyte concentration auto-fluorescence and self quenching. A variety of methods might be used to transfer this concept to aqueous systems. Because

water is a key competitor in the binding process, including one or more water molecules in the process might have certain advantages.

To resolve the aforementioned concerns, new and accurate fluoride detectors have been developed with ability to detect Fluoride ion concentrations below the WHO fluoride intake limits in water by introducing F^- responsive *tert*-butyldimethylsilyl (TBDMS) and *tert*-butyldiphenylsilyl (TBDPS) moieties into the coumarin derivatives (figures 5-7). These new fluoride detectors have ability to islate fluoride in the presence of other anions and respond instantly in the presence of fluorides.

A success in this research will assist governments in making correct environmental remediation choices, as well as establishing new health care plans and response needed to address fluoride-related health complications among its people.

1.7   Objectives

1.7.1   Overall Objective

To design, synthesise and characterize of novel fluorogenic 3-cyano-7-hydroxy-4-methylcoumarin derivative for rapid fluoride detection in potable water, based on TBAF-promoted desilylations.

1.7.2   Specific objectives

1. To design and synthesize novel derivatives 3-Cyano-7-hydroxy-4-methylcoumarin fluoride probe for rapid fluoride detection in household waters.

2. To identify the newly synthesized sensors using spectroscopic techniques such as MS, 1D NMR and 2D NMR.

3. To evaluate the sensitivity and selectivity of the synthesized scaffolds as fluoride sensors.

1.8   Research Questions

1. Is it possible to rationally design and synthesize novel derivatives of 3-Cyano-7-hydroxy-4-methylcoumarin fluoride sensors for rapid detection of fluorides in household waters at the point of use as mitigation for excess fluoride consumption by rural, low income households in Kenya?

2. Is it possible to carry out structure elucidation using spectroscopic techniques of the newly synthesized fluoride sensors?

3. Is it possible to evaluate the sensitivity and selectivity of the synthesized scaffolds as fluoride sensors?

CHAPTER TWO

LITERATURE REVIEW

This chapter provides a review of the literature on fluoride reduction, removal, and detection from/in water. This chapter also discusses the synthetic methods to fluoride sensors, as well as their limitations. The chapter goes on to discuss the gaps in the literature and how this research contributes to filling them.

2.1 Defluoridation Techniques

As part of plans to mitigate toxic health effects induced by fluorides, several governments and organizations have tried to come up with skilfully developed defluoridation methods in areas where clean water is not available (Dhillon *et al.*, 2017). Some of these technologies make use of the theory of coagulation, adsorption, bio-sorption, reverse osmosis (RO), electrodialysis (ED), ion exchange (IE) and nano-filtration (NF). However, these methods have serious drawbacks in terms of high costs, low efficiency and creation of residual pollutants (Mobeen & Kumar, 2017).

De-fluoridation can be categorized into three main groups: Adsorption using bone char, activated alumina and clay as packed media in columns which are used for a period of operation. These processes result in saturation of media which can be renewed or regenerated; Aluminum sulfate and lime in the Nalgonda technique (Naika *et al.*, 2020), poly aluminium chloride, lime and similar compounds act as co-precipitation chemicals to be added daily and in batches. Precipitation techniques produce a certain amount of sludge every day; Calcium and phosphate compounds are the so-called contact precipitation chemicals to be added to the water upstream of a catalytic filter bed. In contact precipitation, there is no sludge and no saturation of the bed, only the

accumulation of the precipitate in the bed; Other advanced treatment processes include reverse osmosis, electro-dialysis, electro-coagulation, distillation and many more (Geleta & Kebede, 2021). The stengths and weaknesses of some of the commonly used defluoridation techniques are given in table 2.1.

Table 2.1: Commonly used defluoridation techniques

Techniques	Merits	Shortcomings	Reference
Precipitation	Conventional and extensively implemented	Efficiency of 65-70%. A high amount of Aluminium sulphate (800-100 mg/L) and is leached into treated water	(Barathi *et al.*, 2019)
Ion-Exchange	High removal efficiency of between 90-95%.	Other anions interfere with process and expensive. The treated wate is highly acidic.	(Yadav, 2019)
Adsorption	Efficient and relatively cheap	Depends on pH. Other anions compete with fluoride. Regeneration is not possible	(Aoun *et al.*, 2018; Kalamkar, *et al.*, 2021)
Membrane processes	Efficiency of about 95%. Taste and colour of water is not affected.	Expensive and susceptible to contamination by bacteria.	(Damtie *et al.*, 2019)
Electrodialysis	Excellent. No need for any chemicals, No wastes are gererated.	Expensive and vital nutrients are lost during the process.	(Aliaskari & Schäfer, 2021)
Nalgoda technique	Colour, odour, pesticides and organic substance are also removed	Expensive, highly skilled and high chemical consumption	(Modi, 2013)

2.1.1 Coprecipitation

This is the transfer of trace constituents to a precipitate simultaneously with the deposition of primary substances present in a solution. It occurs when a solution is supersaturated with a substance forming the precipitates (Liu *et al.,* 2020).

2.1.2 Nalgonda Technique

It involves sequential addition of an alkali, chlorine and aluminum sulfate or aluminum chloride or both by employing several unit operations and processes which include rapid mixing, chemical process, flocculation, sedimentation, filtration, disinfection and sludge concentration to recover water and aluminum salts. Depending upon sulfate and chloride content in raw water aluminium sulfate or aluminum chloride is selected in order to avoid unnecessary increase in sulphate or chloride concentration above permissible limits (Srivastava *et al.,* 2020).

This technique is a cost-effective method which is extensively practiced in most of the developing countries. Though lime softening alone accomplishes fluoride removal, its high initial cost, dosage and alkaline pH of the treated water renders it unsuitable for field application as it requires pH adjustments for treated water and thereby increasing the overall treatment cost. The process is initiated by addition of lime to raw water and followed by rapid mixing. Alum is added and slowly mixed for 10 minutes. The flocs formed are settled out under quiescent condition. The addition of aluminum sulfate to water results in the formation of insoluble positively charged flocs of aluminum hydroxide. These charged particles attract negatively charged ions by electrostatic force and are removed from subsequent settling (Sahu *et al.,* 2020).

The function of lime or sodium carbonate is to hydrolyze alum completely. In order to disinfect water, bleaching powder is also applied simultaneously prior to the addition of alum. The reaction mechanism involves (i) aluminum dissolution, (ii) aluminium precipitation, (iii) co-precipitation and (iv) pH adjustments (Sahu *et al.,* 2020).

2.1.3 Bone Char and Contact Precipitation

The degreased and alkali-treated bones were employed initially in home filters. Later the material was discontinued due to odour problems and imparting taste into treated water. Investigators suggested using of bones after converting to charcoal to avoid odor and taste in treated water. In practice, the bone char is prepared from the animal or bird bones and teeth, which comes out as a waste from poultry or meat processing small to large scale industries. The bones before being charred are boiled, washed, dried and crushed to required size. The charring processes can be pyrolysis (without oxygen) or calcination (limited supply of oxygen). The crushed bones are converted to char in an oven or furnace at a temperature of 300–800 °C for duration of 1–3 hours (Minja, 2019; Alemayehu, 2020; Kikuchi *et al.,* 2020).

The char obtained is further pulverized to required sieve sizes and used for defluoridation process.The process of charring results in formation of three fragments (white, grey and black) depending upon the applied temperature. Each fragment exhibits difference in fluoride adsorption capacity. The composition range of compounds present in bone charcoal is presented in table 2.2.

Table 2.2: Major Components of Bone Charcoal.

Compounds	Range (%)
Calcium phosphate	57–80
Calcium carbonate	6–10
Carbon	7–10
Iron, aluminum	0.5–1
Magnesium	0.2–0.5
Nitrogen	0.8–1
Residue insoluble in acid	0.1–0.3

(Sahu *et al.,* 2020; Wang, 2020)

2.1.4 Adsorption and Ion Exchange

Ion exchange resins are another important class of molecules for the removal of aqueous ionic contaminants. Ion exchange is a fast, reversible stoichiometric method in which an ion that is removed from the polymeric resin surface is replaced by a counter ion in order to retain electroneutrality (Peng & Guo, 2020). These resins are divided into two types: cation exchange resins (Liu *et al.,* 2020) and anion exchange resins (Singh *et al.,* 2020). Cation exchange resins attract negatively charged functional groups, whereas anion exchange resins are attached to positively charged groups. This leads to an exchange of ions beteen the resins.

A cation exchange resin can be loaded with positively charged metal ions, which have a significant affinity for anions. The anion exchange capacity of most anion exchange materials drops in the following sequence, showing low affinity for fluoride ions in comparison to other anions; floride< acetate < formate< chloride < thiocyanide <

bromide < chromate< nitro <iodide< oxalate< sulfate < Citrate. To remove large amounts of fluoride, a strongly basic ion-exchange resin with quaternary ammonium moeities would be more efficient. Styrene–divinylbenzene copolymers (DVB) have been the most commonly utilized polymeric sorbents for heavy metal removal throughout the years, owing to their hydrophilic character and physicochemical stability (Simsek *et al.,* 2012).

Al-Amberlite resin, chelating resins like Indion FR 10 (Barathi *et al.,* 2019) and ceralite IRA 400 anion exchange resins (Pillai *et al.,* 2021) Metal (III)-loaded Amberlite resin (Paudyal *et al.,* 2018), Ion exchange fiber (Grzegorzek *et al.,* 2020), Zr immobilized resin (Wang *et al.,* 2017), and polystyrene encapsulated zirconium phosphate nanocomposite (Zhang *et al.,* 2017) have demonstrated fluoride removal efficacy in water.

Thiourea based Amberlite XAD-4 resin is renowned for defluoridating water in aqueous solution with 90% fluoride removal but the untreated resin efficiency stands at 30% at pH 7.0. The hydrogen interaction between the amide groups in thiourea and fluoride is responsible for fluoride's strong adsorption capability (He *et al.,* 2019).

2.1.5 Bio-polymer based materials

Due to their relative abundance, affordability, high stability and chemical reactivity, biodegradability, and sufficient reactive sites, biopolymer-based materials have received a lot of attention as an efficient adsorbent in water treatment. Among the different bio-adsorbents, chitin and chitosan derivatives exhibit substantial fluoride adsorption

capacity (Dehghani *et al.,* 2020). Table 2.3 shows the adsorption capacity of a number of chitosan modified metal biopolymers.

Table 2.3. Adsorption capacity of Chitosan based sorbents.

Adsorbent	Adsorption Capacity	Reference
La impregnated chitosan	1.27 mg/g	(Wimalasiri *et al.,* 2021)
Magnesia-chitosan	4440 mg/g	(Srivastava et al., 2020)
La incorporated chitosan flakes	1.27 mg/g	(Wimalasiri *et al.,* 2021)
La incorporated chitosan beads	4.7 mg/g	(Wimalasiri *et al.,* 2021)
Aluminium modified chitosan	1.73 mg/g	(Prabhu *et al.,* 2016)
Neodymium-modifies chitosan	11.4-22.3 mg/kg	(Yao *et al.,* 2009)
Carboxylated chitosan beads	1800 mg/kg	(Viswanathan *et al.,* 2009)
La-Carboxylated chitosan beads	4711 mg/kg	(Miretzky & Cirelli, 2011)
Zr-Carboxylated chitosan beads	4850 mg/kg	(Barathi *et al.,* 2019)
Fe-Carboxylated chitosan beads	4230 mg/kg	(Sengupta *et al.,* 2020)
Hydrotalcite/chitosan	1255 mg/kg	(Pandi *et al.,* 2017)
Chitosan coated silica	44.4 mg/kg	(Vijaya & Krishnaiah, 2009)
Ti-Al binary metal oxide supported chitosan	2.22 mg/kg	(Thakre *et al.,* 2010)
Magnetic chitosan	22.49 mg/kg	(Jaafari *et al.,* 2020)
Nanohydroxyapatite-chitin composite	2840 mg/kg	(Barathi *et al.,* 2019)

2.1.6 Carbonaceous materials and metal organic frameworks

Carbon based materials are well known for themselves in the field of water defluoridation. Activated carbon with suitable structural adjustments has been widely researched as an efficient adsorbent for water treatment to remove a wide variety of contaminants, taking into account economic aspects, large surface area, and the presence of excipients (Alemayehu, 2020).

Kumar and his colleagues examined fluoride adsorption onto lemon peel activated carbon. This was accomplished by studying the roles of various adsorption parameters (pH, adsorbent dosage, contact time, rotation speed). Kumar and colleagues' findings demonstrated that low-cost lemon peel activated carbon might be useful for fluoride removal from water. The results from this team revealed that fluoride adsorption is highest in the pH range of 4, and increasing the pH resulted in a drop in percentage adsorption. Maximum fluoride removal % was obtained after contact duration of two hours, as well as optimum defluoridation for an adsorbent dosage of 10 g/L (Kumar *et al.*, 2016).

2.1.7 Fluoride Remediation by Adsorption

Adsorption research promoters believe that the technique is cheap, effective, and generates high-quality water. Fluoride removal via adsorption techniques has received a lot of attention in recent times, and there's a great deal of information about functionalizing high-valency metals in sorbents. Absorption or transfer of fluoride ions to the exterior parts of the adsorbent from solution phase throughout the boundary separation enveloping the adsorbent molecule, known as the external mass transfer; the chemisorption of F^- anion on to adsorbent probe; and electrostatic interaction between

the adsorben and fluoride ions; based on the composition of solids, deposited fluoride ions interchange with other chemical components of the same kind within adsorbent particles, or the accumulated fluoride ions are transported to the interior surfaces of permeable materials/intra-particle transport (Tamrakar *et al.,* 2019).

Fluoride adsorption, like that of any other anion, is based on ions (adsorbate) in a solution spreading to that same surface of a solid, in which they either bind or are kept in place by weak intermolecular interactions. Studies have shown that adsorption efficiency, specificity for fluoride ions, regenerability, compatibility, particle and pore size, and cost are all important characteristics that determine adsorbent suitability for practical application, while fluoride removal efficiency is always dependent on the untreated water quality characteristics, that includes initial fluoride ion intensity, acidity, temperature, reaction time, and quantity of the adsorbent (Inglezakis *et al.,* 2020).

The selectivity of the adsorbent for fluoride ions appears to be a more critical process parameter. This is attributed to the ability of certain adsorbents' excellent performance in experimental determinations but fail in practical applications at the industrial water treatment plants due to a loss in effective adsorption power induced by adsorbent active sites being occupied by other similar and competing anions in the treated water (Jeyaseelan *et al.,* 2021). Selectivity is determined as the percentage of the component's potential at a particular fluorine concentration. As concentration declines, selectivity becomes constant. As a result, researchers and professionals must idesign and produce a low-cost, efficient, and environmentally friendly adsorbent with a relatively higher adsorption capacity (Gamaethiralalage *et al.,* 2021).

A wide variety of adsorbents and their modifications have been tested for the removal of fluoride from water. These include activated carbons (Alemayehu, 2020) activated alumina (Ahamad *et al.,* 2018), bauxite (Cherukumilli *et al.,* 2017), hematite (Kumar *et al.,* 2019), polymeric resins (Singh *et al.,* 2020), activated rice husk (Gebrewold *et al.,* 2019), brick powder (Singh *et al.,* 2020), pumice stone (Yousefi *et al.,* 2019), red soil, charcoal, brick, fly ash, serpentine (Sivarajasekar, 2017), seed extracts of *Moringa oleifera* (Kalavathy, 2017) granular ceramics (Chao *et al.,* 2019) chitin, chitosan and alginate (Nasrollahzadeh *et al.,* 2021), modified ferric oxide/hydroxide (Gogoi *et al.,* 2018), hydroxyapatite (HAP) (Nayak *et al.,* 2017), zirconium and cerium modified materials (He *et al.,* 2019), titanium-derived adsorbent (Al-Itawi, 2019), schwertmannite (Zhu *et al.,* 2020), modified cellulose (Gopakumar *et al.,* 2017), clays (Uddin *et al.,* 2019), zeolite (Aloulou *et al.,* 2021) and magnesium-modified sorbent (Al-Itawi, 2019). Different metal hydroxides and oxides, particularly ones produced in nano-form, offer the greatest performance and greater adsorption capabilities among the above-mentioned adsorbents.

Moreover, as fluoride concentrations fall, many adsorbents start losing their removal efficiency; the minimum significant limit for fluoride decrease by a number of adsorbents is 2 mg/L; as a result, they aren't really appropriate for use in drinking water, especially since many of them can just work at exceptional pH values, such as activated carbon, which only removes fluorides at a of pH of less than 3.0 (Fito, 2019).

Recently, Liu and co-workers have outlined the conceptual features of fluoride removal on by solid particles in three stages: diffusion and/or transport of F- anions to the

adsorbent's surface, and interchange of adsorbed fluoride anions with structural elements within the adsorbate molecules (Zhang *et al.,* 2018; Liu *et al.,* 2020).

In adsorption method, use of activated alumina (AA) has been a method of choice in developed countries. Activated alumina is an aluminum oxide that is highly porous and exhibits high surface area. It can be produced through different methods from aluminum salts. The main activated alumina (Millar *et al.,* 2017) phase used as an adsorbent is gamma alumina (γ-Al_2O_3). AA adsorption is a physicochemical process by which ions in water are removed by the available adsorption sites. AA is usually prepared through dehydration of precipitated $Al(OH)_3$ at high temperatures (300 – 600 °C) which consists of amorphous and gamma alumina oxide. This method is generally used as packed beds to remove fluoride, arsenic, selenium, silica and natural organic matter (NOM). The process involves simply passing the water continuously through one or more AA beds (Kumari *et al.*, 2020).

When the available adsorption sites are exhausted, the AA media may be regenerated with a strong base, NaOH, or simply disposed. Removal efficiency (Ahamad *et al.,* 2018) is noted to be more than 90% with the optimum adsorbent dosage of 1.6 g/L, for water having initial fluoride concentration of 20 mg F/L and has a wide range of working pH of 4–9. The fluoride adsorption capacity of untreated hydrated alumina (7 mg/g) and thermally treated hydrated alumina (23 mg/g) (Dessalegne *et al.*, 2018) were tested and observed that adsorption capacity is significantly higher compared to AA (1.8–1.9 mg/g). The crystal structure of alumina contains cation lattice with discontinuities giving rise to localized areas of positive charge and therefore alumina attracts various anionic species. As polymeric anion exchange resins, AA exhibits high

preference for fluoride ions compared to other anionic species according to series of selectivity (Millar *et al.,* 2017).

2.2   Adsorbents for Fluoride Removal

2.2.1   Oxides and Hydroxides

Many studies have documented defluoridation by use of various metal hydroxides and oxides with a large surface area. However, a number of these have applied Fe_2O_3 as an adsorbent to remove heavy metals, anions, and dangerous substances in wastewater (He *et al.,* 2019).

The use of hydrous titanium dioxide (TiO_2) nanoparticles as a specific adsorbent for fluoride anions, halogens and compounds of arsenic has been reported by researcher. (Bhattacharya, 2017; Patel *et al.,* 2021). These materials have shown the ability to selectively adsorb fluoride anions as well as the properties of the adsorption-desorption cycle with titanium tetrahydroxide, $Ti(OH)_4$.The jelly titanium oxysulfate $TiO(SO_4)$ particles were produced to use titanium hydroxide in an efficient equipment by filling the column with mesoporous particles to bind to fluoride anions. The jelly adsorbent has the same sorption power as $Ti(OH)_4$ particles. The adsorbent showed strong fluoride ion adsorption abilities even at low fluoride concentrations, as well as selectivity for fluoride anions with intervening anions like chloride, sulfate and nitrate. The adsorbent was able to reduce fluoride anions in wastewater to less than 0.8 mg/L (Chen *et al.,* 2012).

Adsorbents formed from $Ti(OH)_4$ displayed strong adsorption capability of more than 98% for fluoride anions, with remarkable selectivity even amidst competing ions like

chloride, nitrate, and sulfate. It was reported that with an average fluoride dose of 50 mg/L, the adsorbent effectively absorbed fluoride anions lower than 0.8 mg/L from the given solution (He *et al.,* 2019).

In 2017, Mukhopadhyay studied the capacity of abimetallic oxide nanopaticles adsorbent for the removal of F^- by use of NH_3 titration at rt by co-precipitation of Ti(IV) and Fe(II) sulfate solutions. The Implications of washing and drying techniques, calcination, variation in temperature, Fe/Ti molar ratio, crystallization, material composition, and interactive components were also studied. The Langmuir model revealed the potential of Fe–Ti bimetallic oxide adsorbent as 47.0 mg/g. This indeed was much greater than the adsorption capabilities recorded by separate Fe/Ti oxide adsorbents (Mukhopadhyay, 2017).

This resulted from synergistic relationship involving Fe–O–Ti bonds on the fluoride ions adsorbent surfaces and OH groups, which supplied binding sites for the bond formation in the Fe–O–Ti–F straucture. This provides a cost-effective fluoride removal mechanism from domestic/drinking water. Mukhopadhyay also investigated the effectiveness of fluoride and Arsenate (AsO_4^{3-}) ions removal by Fe and Al binary oxide ($FeAlO_xH_y$), aluminum oxyhydroxide (AlO_xH^y), and iron oxyhydroxide (FeOxHy) , as well as the effects of pH and Fe to Al ratios (Mukhopadhyay, 2017).

In a batch adsorption test carried out at 25 °C with AsO_4^{3-} and F- solutions with starting quantities of 0.2 mM and a pH level ranging from 4 to 9, it has been demonstrated that FeOxHy has a strong removal capacity for AsO_4^{3-} but limited effectiveness for F^- removal. When AsO_4^{-3} and F^- were concurrently eliminated at a pH range of between 4

and 11, AlOxHy exhibited high effectiveness, and thus the greatest effect was observed at a weakly acidic pH of 6 due to the impact of electrostatic force at a different pH conditions (Mukhopadhyay, 2017). In general, arsenic is better removed by up to 94.8 % by adsorbents. However, FeOxHy could only remove a maximum of 18.4 % of the original fluoride concentration while adding AlOxHy to FeOxHy raised the efficiency to 64.5 % (Kazi *et al.,* 2018).

A study on the application of magnesium nano-ferrihydrate in defluoridation evaluated the synthesised Magnesium-Doped Nano-ferrihydrite in the range of 0.4% to 1% derived from altering Mg concentration. The preliminary test revealed that the 0.4% to 1% rise in Magnesium concentration in nanoferrihydrate lead to a rise in defluoridation from 66% to 91%. Measurements on batch adsorption when done by various times ranging from 30 minutes to 8hours, with a starting pH of between 1.0 and 10 in a fluoride concentration of between 10 mg/L and 150 mg/L while the adsorbent concentration set at between 0.5 g/L and 4 g/L, temperature range of between 20 °C and 45 °C). The investigators also studied the effects of competing Cl^- and SO_4^{-2} anions up to 50 mg/L in this research (Mohapatra *et al.,* 2012).

When the Manesiumg-doped ferrihydrite is applied and time data are well-fitted to the pseudo rate equation of the 2nd order, the maximum fluorides absorption potential is above 60 mg/g. Characterization of the Magnesium-doped ferrihydrate by X-ray diffraction (XRD), Thermo-gravimetric (TG) Electron transmission microscopy (ETM), Differential thermal analysis (DTA) and Electron diffraction (ED) showed a higher degree of dispersion of particles after fluoride adsorption with improved crystalline phase and the fluoride existence of the loaded adsorbent was also verified. A desorption

test for fluoride anions indicated that almost 90% of all the fluorides may be desorbed under varied pHs as well as the incubation time. Recently, Dhilleswara and co-workers in 2021 studied the removal of fluoride in a fixed bed reactor employing customized aluminum iron oxides. Column experiments were carried out to assess the impact on breakthrough curves of varying substrate masses (Dhilleswara *et al.,* 2021).

A fixed bed study with the initial fluoride dose of 4 mg/l at a pH of about 6.0 as well as drinking water solution at a pH of about 7.0 was conducted with a flow rate of 1 mL/min, 2, 4 and 6 g Al-modified Fe_xO_y with bed depths correspondingly 3.5, 7.0 and 10.5 cm (Pillai *et al.,* 2020). The conclusions drawn demonstrate that, when more locations are available, the amount of F- or drinking water increases owing to a rise in the overall surface area of the adsorbent. Measurements reported indicate the eluted F^- solution mean pH of 7.2 for the model solution and 7.3 for the domestic/drinking water (Habuda-Stanić, *et al.,* 2014). Subsequently, earlier research reported that the optimum fluoride detection limits at the breakthroughs had been around 0.51 mg/g in a bed depth of 0.035 m and bed weight of 0.002 kg after 4 hours and 14 minutes as the fluoride solution was alloed to go through the column, and 0.296 mg/g in the same bed depth and bed weight as before but after 2 hours and 28 minutes when fluoridereach water was allowed to pass through the column (Saliu & Oladoja, 2020).

In 2019, Luo and colleagues examined the effectiveness and technique of heated Mg-Fe stacked double hydroxides for synchronous AsO_4^{-3} and F^- absorption from aqueous solution. They conducted adsorption tests to see how several parameters including material preparation, Mg/Fe molar ratio, and calcination temperature affected defluoridation effectiveness. He used adsorption isotherms to anticipate mechanisms of

adsorption and to find the best parameters for heated Mg-Fe stacked double hydroxides to remove the most F^- and AsO_4^{3-}. The highest defluoridation rate was recorded when Mg-Fe stacked double hydroxides were heated to about 400 °C, whereas optimum fluoride adsorption capacity was about 50 mg/g related to the adoption of the Langmuir isotherm model (Luo *et al.,* 2019).

Earlier research has also highlighted the importance of ion exchange interactions, surface adsorption and the rebuilding of the original stratified double hydroxide framework by intercalation of F^- and AsO_4^{3-} ions into the interlayer area for F^- adsorption (Wu *et al.,* 2017).

Bulk tests utilizing 10 mL of fluoride solution with an initial fluoride dose of 10 mg/L and varied quantities of adsorbent of between a minimum of 3 mg and a maximum of 500 mg revealed that the employed adsorbent had a good specificity for fluoride extraction. Up to 92% of fluoride was adsorbed from a solution with 10 mg/L under optimal conditions of 20 minutes contact time, pH = 5.5, and an adsorbent mass of 100 mg. Studies on adsorbent effectiveness in the existence of interdependent anions notably SO_4^{2-}, NO_3^-, NO_2^-, Br^-, and Cl^- in variable concentrations ranging from 1:1 to around 1:100 revealed that the percentage removal of F^- dd not change but remained well within the tolerance limit throughout the existence of a 10-fold dose of Br^-, and Cl^-, 50-fold of SO_4^{2-} anions and finally 100-fold of NO_2^- (Bhattacharya, 2017).

Water contaminated with fluoride average content of about 35 mg/L was also investigated an adsorption test. It was reported that this removed more than 90% of the residual fluoride content of about 3 mg/L. The advantages of generated zirconium (IV)-

metalloporphyrin-Fe_3O_4 nanoparticles were highlighted (Poursaberi *et al.,* 2012). The simplicity with which it can be separated by a magnetization, the ease with which it can be recovered after washing with a basic aqueous solution, and the fact that it may be reused for up to 5 times (Ahamad *et al.,* 2018).

A granulated zirconium-iron oxide (Dou, 2012) consisting of non-crystaline and nano-scale oxide was produced use of an extrusion method, and its adsorption profile owing to defluoridation was investigated. defluoridation was assessed using both F^- solution and actual F^- containing water specimens via batch and column procedures under a variety of operating conditions, including starting fluoride content of between 10 mg/L to 150 mg/L, pH value ofbetween 3.0 and 11.0, reaction time, and existance of other chemical species. The toxicity profile leaching technique was performed to assess the leaching potential of the employed particulate zirconium-iron oxide (Wu *et al.,* 2011).

With the exception of bicarbonate, co-existing chemicals such as Cl^-, SO_4^{2-}, NO_3^-, $[PO_4]^{3-}$, humic acids, and others seemed not to impede defluoridation in natural groundwater, demonstrating the excellent selectivity of the employed adsorbent for fluoride. In 2012, Dou used batch adsorption experiments to evaluate the efficiency of produced hydrous zirconium oxide, whereas surface titration, electrophoretic measurement, spectroscopic methods and surface complexation modelling were used to explore the defluoridation process. Batch isotherm tests were conducted with solutions with starting fluoride doses ranging from 2 mg/L to 120 mg/L, an adsorbent dosage of 0.3 g/L, and pH maintained between 7 and 4 at 25 °C for 24 hours. At pH = 7, kinetics studies were carried out at room temperature with aqueous samples containing starting

fluoride doses ranging from 20 mg/L to 100 mg/L, and an adsorbent dosage of 0.00003 kg/L (Dou, 2012).

In 2020, Singh and co-workers verified that aqueous ZrO_2 had fluoride adsorption capacities of between 124 mg/g and 68 mg/g at a pH range of betwee 4 and 7, respectively, after studying the impact of pH and co-existing anions on fluoride removal (Gan, 2019). Fluoride adsorption followed a pseudo-second-order rate curve, according to kinetic investigations. Fluoridation by aqueous zirconium oxides was discovered to be caused by the interchange between F^- and the OH groups as well as the electrostatic interaction seen between the charging surface and F^-, using spectroscopic techniques, surface complexation models, surface titration, and electrophoretic measurement. At the surface of aqueous zirconium oxide, neither surface deposition of NaF nor crystallization of ZrF_4 was detected (Buckley *et al.,* 2018).

It has often been observed that when the pH rises, the capacity of synthetic adsorbent decreases owing to variations mostly in pH-dependent electrostatic force between the sorbent surface and fluoride. At all levels, Cl^-, SO_4^{2-} and NO_3^- had a little influence on defluoridation, but $[PO_4]^{3-}$, AsO_4^{3-}, and HCO_3^- had a substantial inhibitory effect when present at a concentration of about 0.1 g/L (Sandoval *et al.,* 2021).

Zirconium or chromiun double hydroxide layered nitrate may be used for water defluoridation. The batch investigations of Fluoride absorption were performed using 1 g/L adsorbent when magnetically agitated continuously for a period of three hours at 600 rpm, with various starting fluoride concentration of between zero amd 100 mg/L. The maximum absorption of fluoride was recorded to be 31 mg/g, these acquired

findings showed an increase in the Zr/Cr double layered hydroxide load for synthesis of the adsorbent. The preference of specific monovalent anions and divalent anions in fluoride absorption tests was used to evaluate the effects of competing anions including sulfate SO_4^{2-}, phosphate (PO_4^{3-}), carbonate (CO_3^{2-}) and nitrate (NO_3^-) on defluoridation by absorption (Kanrar, 2020).

Column experiments employing polysulfone/zirconium-chromium layered double hydroxides with different doses of multilayer double hydroxides were used to investigate the possible use of adsorbents. The findings indicate that by using a composite material implied superior aqueous permeability than using charged multilayered double hydroxides, implying that polysulfone might be a good column composition. For composite materials known to contain 9 percent, 17 percent, and 38 percent of multilayer double hydroxides, the absorbtion abilities determined depending on the time, mass flow, as well as quantities up to the breakthrough points were 1.0, 1.7, and 6.9 mg/g, respectively, whereas the complete absorption powers were 1.8, 4.9, and 12.5 mg/g. A column investigation of fluoride absorption from actual water with fluoride content of about 12.6 mg/L indicated that almost all the anions were absorbed by the selected adsorbent at the early stage of about 20 minutes, suggesting poor specificity when natural environmental water samples were processed (Bhattacharya, 2017).

When 0.1 g of zirconium(IV)ethylenediamine hybrid sorbent was used with 100 ml of fluoride solution starting with fluoride level of 10 mg/L at a level of pH = 7.0 for one hour of adsorption, fluoride was eliminated up to 99%. The adsorption procedure was carried out and followed by pseudo 2nd order kinetics, with the actual and theoretical

adsorption capacities being quite near. Kirkendall phenomenon was used to determine the defluoridation effectiveness of CeO_2-ZrO_2 nanoparticle, as well as a structural analysis (Wu *et al.,* 2011).

The maximal potential of the permeable CeO_2-ZrO_2 nanoparticles was determined to be 175 mg/g at pH = 4.0 based on the findings of a batch adsorption investigation, and the Langmuir model accurately characterized the isotherm. When co-existing ions were tested, it was shown that large quantities of Cl^- and AsO_4^{3-} inhibit fluoride adsorption, whereas sulfate had no impact. The attention has been placed on the adsorption process of the F^- adsorbent which might entail anion exchange and electrostatic forces, depending on electrophoretic determination, spectroscopic techniques, as well as surface complexation simulations. By applying a 0.4 g/L adsorbent dosage, the effectiveness of synthetized CeO_2-ZrO_2 nanocages was tested with a groundwater sample naturally possessing high fluoride content (2.820 mg/L). After one hour of treatment, the residual fluoride concentration was 1.39 mg/L (Dou, 2012).

The adsorption of fluoride anions by powdered crystalline TiO_2 (metastable mineral form of TiO_2-Anatase) from water mainly with a contact area of 56 m^2/g, was investigated. The goal of the adsorption tests was to figure out the best adsorbent dose, as well as the influence of starting F^- concentration, co-existing competeing anions, contact time, ionic strength, and pH on fluoride absorption. As a result, aqueous fluoride solutions with beginning pH values ranging from 2.0 to 11.0 were employed, together with a variety of adsorbent doses ranging from 0.01 g to 2 g and initial F^- concentrations ranging from 5 mg/L to 20 mg/L (Mikrut *et al.,* 2019).

For water defluoridation, a Fe–Al–Ce trimetal hydroxide adsorbent was created by coating a Fe–Al–Ce nanoarticle dispersion over glass beads using acrylic–styrene copolymer latex binding. On particle strength properties and adsorption ability, the impacts of coat temperature, latex/Fe–Al–Ce ratios, as well as coat quantity were studied. Higher latex/Fe–Al–Ce ratio and greater coating temperatures following adsorbent production were also linked to a rise in bead strength and decreased adsorption ability. When the nanoparticles are encased at a temperature of 65 °C with a latex/Fe–Al–Ce ratio of 1:2, the maximum performance and maximal defluoridation of 2.77 mg/g of utilized Fe–Al–Ce trimetal hydroxide adsorbent was achieved. The specific fluoride adsorption efficiency was recorded when the starting fluoride content was 0.001 M and the initial pH at 7.0 (Bhattacharya, 2017).

In 2018, Zao and co-workers looked into granulated Fe-Al-Ce hydroxide made by ejection with a cross-linked polyvinyl alcohol binding. Fluoridated water solutions of various concentration level ranging from 10 mg/L to 250 mg/L at a pH level of 7.0, a column test with fluoridated tap water with an average average fluoride concentrations of 5.0 m/L at an average pH = of 7.9, and groundwater with naturally high F^- levels at an average fluoride concentration of 3.7 mg/L and an average pH of about 8.0 were used to examine the effectiveness of the derived trimetal absorbent. $NaAlO_2$ solution was also used in the rejuvenation trials (Zhao *et al.,* 2018).

At pH of 7.0, the Langmuir maximum adsorption potential of granular Fe–Al–Ce hydroxide was 51.3 mg/g residual F^- doses at the 1.0 mg/L. When fluoridated tap water was purified, column studies revealed an F^- anions adsorption capability of 5.7 mg/g and 3.2 mg/g when natural water with elevated F^- concentration was utilized. F^- anions

were spread equally in the bridge of the Fe–Al–Ce hydroxide utilized in the produced adsorbent, indicating that the majority of active sites inside the adsorbent were accessible for defluoridation. After four adsorption-regeneration cycles, regenerating experiments with $NaAlO_2$ revealed strong adsorbent efficiency and F^- anions retention of over 60% (Zhao *et al.,* 2018).

2.2.2   Biosorbents

Biosorption is a relatively new water-treatment technology that makes use of readily accessible natural resources. For fluoride elimination, a variety of natural biosorbents have been created including Chitin and chitosan which are appealing natural adsorbents due to their exceptional features, such as biocompatibility, low cost and biodegradability as well as their unique physicochemical properties, which are a consequence of chemically moieties in polymer chains (George, 2020).

Chitosan is commonly employed in the absorption process in terms of powders, which are less stable and produce a large drop in pressure, affecting filtering in potential application. The potential of unaltered chitosan to defluoridate was determined to be limited. These drawbacks exceed the benefits of biodegradability and nativeness. If chitosan could be changed in a way that might overcome the problems outlined above, defluoridation effectiveness would undoubtedly increase (Korde, 2020).

Chitosan particles with low fluoride absorbing ability when chemically changed by carboxylation and protonation to introduce versatile groups, namely $-NH_2$ and $-COOH$ entities, in order to use both hydroxyl and amine moeities for defluoridation. The highest defluoridation capability of protonated carboxylated chitosan particles was 1664

mg/kg, while raw chitosan particles had a considerably lower adsorption capability of 52 mg/kg. The adsorption mechanism was shown to be pH-independent, with the existence of other existing anions having a little impact (Dehghani *et al.,* 2018).

By optimizing different synthesis parameters, lanthanum integrated chitosan beads are produced for defluoridation application. These beads had a fluoride removal rate of 97 percent at pH = 5 and were able to overcome the disadvantages of traditional adsorbents. Lanthanum-incorporated chitosan particles may lower fluoride levels in water below the WHO permitted limit of 1.5 mg/L, making them an efficient adsorbent for defluoridation of drinking water (Srivastava *et al.,* 2020).

There have been defluoridation experiments utilizing chitin (Nehra *et al.,* 2019), chitosan, and chitosan with 20% lanthanum integrated chitosan. Lanthanum-chitosan adsorbents perform far superior than to chitosan and chitin in water defluoridation. The concentration and type of coexisting-anions, as well as the pH of the solution, all influence F^- adsorption on the surface of the adsorbent. It was discovered that anions, particularly CO_3^{2-} and HCO_3^- anions, had a negative impact on fluoride adsorption. The process of fluoride ion sorption on the chitosan nanoparticles from a batch water solution has been investigated. The maximum levels of adsorbed fluoride found were 20.96–23.98 mg/g, according to the findings. Chitosan's metal-binding ability is utilized to integrate titanium metal into an adsorbent for fluoride removal (Bhatnagar & Sillanpää, 2011).

In comparison to chitosan, titanium macro-particles have a relatively high defluoridation capability. Fluoride adsorption on titanium macroparticles is primarily

influenced by the solution acidity and the presence of coexisting anions. The absorption is relatively modest at alkaline pH above 7.0. Fluoride absorption is hampered by the presence of other coexisting anions in water, notably carbonate and bicarbonate. One of the most important parts of ecological engineering to meet biological, household as well as environmental circumstances is the biosorbent generated from shellfish waste materials (Habuda-Stanić *et al.,* 2014).

The use of Nd-modified chitosan as adsorbent materials for water defluoridation has recently been studied by Jiang and co-workers. The influence of several physico-chemical factors (adsorbent dosage, particle size, and the presence of co-anions) was investigated. The pH value was set to 7.0, wat a temperature of 50° C, and the crystallite size of 0.10 mm. Sorption process on fluoridated water containing 20 mg/L fluoride ions was 98.15 % at a dose of 2.0 g/L, 50 mg/L nitrate, 500 mg/L chloride and 500 mg/L sulphate in water, had no significant effect on defluoridation (Kusrini *et al.,* 2019; Sen *et al.,* 2020; Jiang *et al.,* 2021).

There is also a study on water defluoridation utilizing a hybrid material of Fe/Zr nanoparticles. In batch adsorption tests with 50 mL of fluoride solution, several physico-chemical parameters were investigated. The initial fluoride doses ranged from 2 mg/L to 50 mg/L, the pH was 2.0 to 12.0, and the adsorption period of not more than five hours. The desorption profile of the hybrid material revealed that at pH = 12, approximately 89 percent of fluoride could also be drained out, whereas at pH = 6.0, the maximal defluoridation took more than three hours. According to the results, the highest sorption potential for Fe/Zr nanoparticles was 0.981 mg/g (Wu *et al.,* 2017).

2.2.3 Carbon-based particles

For defluoridation investigations, a variety of carbon-based nanoparticles from various sources can be employed as adsorbents. The basic ingredients required to make carbon are commonly accessible. Any carbon-based substance with high carbon content may easily be chemically converted into activated carbon (Côrtes *et al.,* 2019).

Since charcoal made from softwoods is highly unstable, activated carbon made from hardwood is preferred for adsorption. Physicochemical activation is the most prevalent mechanism of making activated carbons. The activation technique used is also determined by the feedstock and the density of the required carbon product. Anaerobic calcination under 600 °C generates activated carbons produced by a slow rate substrate introduction. This eliminates volatiles, which is followed by physico-chemical activation. The activation processis completed by using either steaming water,O_2 gas or CO_2 gas as oxidizing agentst increased temperatures or chemical activating agents like Zinc chloride, phosphoric acid, sulphuric acid, potassium hydroxide, potassium sulphide and potassium thiocyanate (Côrtes *et al.,* 2019; Minami, 2021).

2.2.4 Industrial Products and By-Products

Studies of the factors that influence the rate of defluoridation, particularly the types of aluminum salt, the sample F^- anion concentration of between 2 mg/L and 20 mg/L, the adsorbent mass ranging from zero to 14 g/L as well as the time for adsorption ranging from zero to 72 h, revealed that the synthesized adsorbent recorded a relatively fast kinetics. when the fluoride io s inad a 10 mg/L and measurement done at a pH valueo of about 7.25, 10 g/L customized charred bone removed upto 97% of the fluoride. Customized bone char therefore has a promising future in real world applications for

defluoridation of fluoride rich drinking water (Delgadillo-Velasco, 2017; Alemayehu, 2020; Kikuchi *et al.*, 2020).

2.2.5   Structural materials as fluoride sorbents

A research by Yadav *et al.,* reported effectiveness of brick powder on groundwater fluoride removal. When the defluoridation efficacy of brick powder was compared to the commercially available activated charcoal laboratory reagent grade. The maximum fluoride adsorption by brick powder was reported to be around 50% in the pH range of between 6.0 and 8.0. However, it was noted that fluoride adsorption reduced with increasing pH in the case of commercially available activated charcoal. Under optimum pH conditions, brick powder's deflouridation capability was observed owing to the ionic interactions of fluoride with metal oxides. Other ions had no effect on the deflouridation efficiency of brick powder. When the contact duration was prolonged from 15 to 120 minutes, the percent defluoridation from synthetic sample improved from 29.8 to 54.4 and 47.6 to 80.4 percent for brick powder and commercially available activated carbon respectively (Yadav *et al.,* 2018).

2.2.6   Nano-sorbents for defluoridation of water

Nanotechnology is a promising technology in a variety of sectors (Priestly *et al.,* 2007). Similarly, the use of nanoparticles as sorbents for water purification (Plotnikov *et al.,* 2015) for example carbon nanotubes (CNTs) has received a lot of interest in recent years. They have sparked a great deal of curiosity. Because of their tiny size, vast surface area, great mechanical strength, and exceptional electrical conductivities, they are prospective substances for a broad spectrum of potential applications (Barathi *et al.,* 2019).

Alligned Carbon Nanotubes (ACNTs) created by the catalytic breakdown of xylene with ferrocene as a catalyst, was tested for defluoridation efficacy. The surface and interior cavities of ACNTs were discovered to be fluoride sorption optimal at a pH range of between 3 and 9. At a pH of 7.0 and a F- anion content of 15 mg/L, ACNTs had a optimum sorption capacity of 4.5 mg/g (Li *et al.,* 2003).

2.3 Mechanisms of Fluorescent Fluoride sensing

2.3.1 Photoinduced electron transfer (PET)

A PET process as illustrated in figure 2.1 is indeed a messaging expression used to describe the quenching or stimulation of radiation. Fluorescent sensors that depend on PET are typically composed of a fluorophore, receptor and spacer. The receptor comprises of interacting atoms that possess comparatively high energy non-bonding electrons that can pass an electron to the HOMO including its activated fluorophore, resulting in quenching (Tang *et al.,* 2020).

As the electron pair is active throughout the interaction of metal ions, the receptor's reduction potential becomes boosted, causing the fluorophore to be higher in energy the associated HOMO; as a result, the PET mechanism from the receptor to the fluorophore is disallowed, resulting in increased emission spectra. Furthermore, depending on the surrounding orbitals added, an interaction between the receptor and analytes causes PET from the fluorophore's excited LUMO to the receptor's HOMO, culminating into quenching. As a result, it is commonly seen in sensors for fluorescent detection of charged or neural samples. Covalently connected fluorescent sensors are usually made up of a receptor and a fluorophore that seem to be electrically separated (Magri, 2021).

Figure 2.1: PET mechanisms for fluorescent fluoride sensors

2.3.2   Intramolecular charge transfer (ICT)

Intramolecular charge transfer (ICT) probes involve the conjugation of electron donating groups (EDGs) and electron withdrawing groups (EWGs) groups into a single atom. This results into a 'push-pull' on pi-electron system in its activated form. As the fluorophore is excited, electron density redistribution occurs, leading to the formation of a significant dipole and ICT from donor to acceptor. The attachment of active site to the basic group slows the ICT process due to reduced electron-donating power, resulting in a shift towards shorter wavelengths in absorbance. As samples bind to the acidic group, an obvious shift to the longer wavelengths on absorbance is detected owing to enhanced ICT activity (Kodlady, *et al.,* 2021).

2.3.3   Fluorescence/ Förster resonance energy transfer (FRET)

FRET is a non-radiative emission process in which an activated donor loses energy to a ground-state acceptor via long-dipole correlations. The FRET output refers to the likelihood of transfer of the emitted energy. This is heavily comparative to the space between the two fluorophores, the similarity between emitter and absorber, as well as

the comparative dipole orientation of the donor and acceptor. In FRET schemes, the donor output must have effective spectral similarity mostly with acceptor absorption wavelength (Mizuta *et al.,* 2021).

PET fluorescent fluoride sensors consist of a set-up of fluorophore-spacer-receptor. The fluorophore and receptor are completely distinguished by a short aliphatic spacer. Even so, the receptors need a non-bonded fairly excited electron pair. Once an electron in the Highest Occupied Molecular Orbital (HOMO) is activated, it transits to the Lowest Unccupied Molecular Orbital (LUMO). A swift intramolecular transfer of electrons occurs in the unbound state between the HOMO (receptor) and the LUMO (excited fluorophore). In "off" state B (Figure 2.1), the probe is quenched. The linked receptor, on the other hand, allows the electron pair to coordinate to F^-. As a result, the HOMO of the receptor shrinks in comparison to the fluorophore. The attached receptor, on the other hand, enables the electron pair to coordinate to F^-. As a result, the receptor's HOMO gets smaller as compared to the fluorophore. The PET process can be slowed or even turned off by reducing the redox at the receptor. This causes fluorescence "turned on" (Jiao *et al.,* 2015).

Before binding with fluoride, the energy level of the receptor's HOMO is lower than the reporter. One electron is promoted to the LUMO upon excitation and can freely transit back to the ground state and release energy in the form of fluorescence. However, the HOMO energy level of the receptor becomes higher when fluoride binds at the receptor. Similarly, one electron on the receptor's HOMO upon excitation transfers to the empty position of the reporter's HOMO before the LUMO electron of the reporter relaxes back to the ground state. This significantly quenches fluorescence. The degree of

fluorescence quenching can be monitored by instruments and correlated to the amount of fluoride in solution (Ashokkumar, *et al.,* 2014).

In 2020, Yang *et al.,* recorded a photo-induced and excited state Intramolecular Proton Transfer (ESIPT) mechanism for a novel 2-(3,5-dichloro-2,6-dihydroxy-phenyl)-benzoxazole-5-carboxylic acid (DICH) compound. They managed to monitor and regulate ESIPT behaviour in the DICH system in varried solvent polarities. The deprotonation reaction from fluoride anion, which inhibits the primary ESIPT process of DICH, is the justification for the hypothesis on fluoride sensing mechanism for DICH system. As a result, new UV-Vis spectra occur, which play a role in fluorescence activity. Upon binding with fluoride, the fluorescence of these sensors is significantly quenched due to PET. The selectivity of this type of sensor arises from its hydrogen donating property. Due to the PET process, these types of fluoride sensors are usually "turn-off" sensors and hence the sensitivity is usually limited (Yang, *et al.,* 2020).

2.3.4 Hydrogen-Bond Interaction Based Fluoride Sensors.

A hydrogen bond is predominantly an electrostatic interaction between hydrogen (H) and a more electronegative atom like oxygen (X), nitrogen, fluorine, or and possibly another neighboring atom with a lone pair of electrons. Hydrogen bonds are essential in many biochemical pathways. They are characterized by the H-X framework. Associated liquids are liquids that exhibit hydrogen bond character. O-H bond is amongst the most potent hydrogen bond donors. Intramolecular hydrogen bonds exist more often than the intermolecular ones. Fluoride is perhaps the most common substrate for anion identification in various receptors as a hydrogen bond acceptor. In the orders of $CF_3 <$

$CHF_2 < CH_2F_2$, the strength of hydrogen bond formation for fluorinated substituents applied to a certain molecular system reduces (Yang *et al.,* 2020).

Since hydrogen bonds remain lateral, it is possible to create sensors with complex shapes that are able to discern among anionic species of various geometrical setups. There have been two elements of hydrogen-bonding that work together. The first involves entities with several bonds. These are commonly referred to as a resonance enabled hydrogen bonds; secondly, there is one associated with recurrent strings or loops of hydrogen-bonded organic compounds possessing the donor as well as acceptor moeties. These electrostatic interactions may be combined to create an appropriate anion receptor (Yang *et al.,* 2020).

Fluoride forms stronger hydrogen bonds compared to oxygen and nitrogen. In the past, designing these fluoride sensors depended on fluoride receptors like urea (Xia *et al.,* 2021), thiourea (Li & Zhongzhen-Tian, 2020), sulphonamide (Zimmerman *et al.,* 2018), amide (Patel *et al.,* 2020), Schiff base (Saini *et al.,* 2018) and many more. The sensors have a reporter that consists of a chromophore/fluorophore, a fluoride receptor which is the hydrogen donor and a spacer or linker to connect the reporter and fluoride receptor. Binding of fluoride to these receptors will cause a change in the electron density surrounding the reporter, known as the photoinduced electron transfer (PET) process (Figure 2.1) and hence the absorption and emission spectrum of the reporter will change accordingly (Ashokkumar *et al.,* 2014).

Lewis bases, like F^-, would hydrogen bond with Hydrogen-bond donors such hydroxyl and amine groups by deprotonation that generally follows their coordination. Because

of the existence of coordinated amines, hydroxyl groups, or even (thio)ureas, such compounds end up detecting fluoride ions. In the year 2013, Mahapatra and research team reported a deprotonation of the hydroxyl group in ACN allows the Bis(coumarin)methylene chemosensor to detect fluoride ions (Mahapatra *et al.,* 2013).

Mahapatra and co-workers further observed that the inclusion of fluoride resulted in a distinct colorimetric as well as fluorescent shifts. The process was considered to occur by forming a hydrogen-bonded contact when one equivalent of fluoride ions was added followed by the deprotonating the phenolic group when the next equivalent is added. This second phase was shown to be crucial to the observable chromogenic effect (Mahapatra *et al.,* 2013).

In 2016, Li and co-workers reported that coumarin dimer can recognize fluoride ions in DMF. The nonfluorescent molecule dramatically changed to a strongly fluorescenceing chemosensor by the introduction of fluoride ions coming from an initial fluoride coordination, accompanied by deprotonation. The molecule, meanwhile, was not just selective to fluoride ions alone as it fluoresced brightly in the presence of Mg^{2+} ions and Zn^{2+}, coordinating the dimer both through the phenol and imine heteroatoms (Li *et al.,* 2016).

In the same year 2016, Tian and co-workers reported a diarylethene-coumarin derivative fluoride sensor whore detection mechanism was based on deprotonating the phenol in ACN in an identical way. The PET effect with the closed diarylethene resulted in either an open state (fluorescencing) or a closed state (non-fluorescencing) molecule when the state of the diarylethene photoswitch was modulated. It was also

reported that the presence of Zn^{2+}, the identical detector exhibited its fluorescence amplification (Tian *et al.,* 2016). In 2017, a fluoride ion chemosensor built on a coumarin-pyrazole-pyridine framework was reported by Alkış and co-workers. Introducing fluoride ions to the chemosensor was noticed to cause an ON-OFF shift in DMSO, which could also be reverted by introducing trifluoroacetic acid (TFA) (Alkış *et al.,* 2017).

In another separate work, fluorescence quenching in the presence of fluoride ions has been recorded to be affected by the breakdown of the pyrazole hydrogen bridge. A related molecule, which lacked the pyridine unit but rather included a phenyl group, responded in such a comparable pattern; thet is through deprotonation and hydrogen-bridge disturbance. This molecule did, however, exhibit significant fluorescent decrease in the presence of AcO⁻ (Babür *et al.,* 2015)

In theyear 2017, Yeap and a team of researchers designed a fluoride ion chemosensor based on chalconea and equipped with coumarin and naphthol for the selective detection of fluoride ions. Due to the extreme deprotonation of the hydroxyl group, the probe could identify fluoride ions with a fluorescence amplification reaction thereby increasing an intermolecular charge transfer (ICT) activity (Yeap *et al.,* 2017).

Fluoride ion detection can indeed be accomplished not just by deprotonation and coordination of phenol protons, but as well as through the deprotonation and coordination of many Nitrogen-based electron deficient protons. Park and co-workers designed a chromogenic chemosensor capable of detecting both F⁻ and Al^{3+} through nitrogen ligand coordination and deprotonation. It changed colour from yellow to pink

as a result of the dye's enhanced push and pull nature following chemical deprotonation (Park *et al.,* 2014).

Incidentally, when different concentrations of fluoride ios are added to acetonitrile/dimethyl sulfoxide (CH₃CN/DMSO), coumarincarbohydrazone and coumarin-carbohydrazone display an ON→OFF→ON fluorescence. First, a complex with a 1:1 stoichiometry between the compounds and fluoride is produced; resulting in a reduction in fluorescence, whereas adding additional equivalents resulted in a partial restoration of blue-shifted fluorescence (Biswas *et al.*, 2016).

Lastly, the Ma and the research team presented a fluoride ion fluorescence probe that applies a PET quenching method. In the presence of an excess of fluoride ions, the initial strong fluorescence in THF solvent was reorded to be completely quenched, owing to a PET effect seen between the coumarin moiety and deprotonated group (Ma *et al.,* 2017).

2.3.5   π-electron delocalization induced by hydrogen bond

The delocalization of pi-electrons and, as a result, the electron motion inside the formed loop results in the synchronization of suitable bonds. The transfer of electron density in resonance-aided hydrogen bond structures appears to be crucial for the photochemical characteristics of these groups. The migration of electrons from its Lewis base entity to the Lewis acid end is quite well documented for intermolecular H-bonds. The varying types and strengths of H-bonds influence pi-electron migration in the remaining structure. These can include not only the pi-electron spacer but also conjugated systems within the structure. Especially with regard to the relationships seen between aromatic

component of the system's pi-electron migration as well as the form including its H-bond, aromaticity indicators could be used for every reason, which will define pi-electron delocalization as well as compare respective intensities to quantities for well-known aromatic structures (Liu *et al.,* 2021).

2.3.6 Lewis acid-base interactions

Lewis philosophy employed transfer of electrons rather than just proton movement and claimed explicitly how an acid embraces an electron pair using its empty orbital while a base make a contribution of its non-bonding electron pairs, culminating in a coordinate bond. Soft acids tend to associate more with soft bases while the hard acids prefer to connect to hard bases. Lewis acid cores with fewer electrons will connect to anions through orbital overlapping. This results in an interaction between bonds. As a result, several novel anion hosts from various transition metals have been synthesized (Chen *et al.,* 2021).

2.3.7 Displacement Assays

Displacement assessments are already extensively used in the development of anions' visual probes. The attachment of the specific anion to recognition pocket of the molecular group not only leads in the relocation of the triggering receptor but also a major visual shift in the relocation strategy. The binding of the specific anion to the active sites results in the relocation of the sensing subunit and a dramatic visual shift in this technique. The identification of the resulting anion is caused by the difference in optical properties between the independent receiver as well as the coordinated sensor. One intriguing assumption of this approach has been that the majority of synthesized

structures exhibit signalling functionality in aqueous or organic/aqueous mixtures, leading to the establishment of practical sensing schemes (Sedgwick *et al.,* 2021).

2.3.8 Metal Ion Displacement Mechanism.

The metal ion displacement method can also identify fluoride ions. Mg^{2+}, Gd^{3+}, Cu^{2+}, and Al^{3+} are some of the the metal complexes that have been widely described thus far. The intense blue fluorescence, which is structurally identical to the presence of cyanide ion (CN^-), is reportedly substantially suppressed by Cu^{2+} in acetonitrile (ACN), but when fluoride ions was added, the fluorophore was liberated and the vivid blue fluorescence was restored (Razi *et al.,* 2015; Sarkar *et al.,* 2017; Wang *et al.,* 2017). Interestingly, the complex primarily demonstrated a significant sensitivity to fluoride ions, notwithstanding the high affinity of S^{2-} and CN^- for Cu^{2+}. Repeated cycles of sequentially adding copper (II) ions and fluoride ions to a solution, totally quenched the solution, followed by a restoration of the fluorescence verified the process decomplexation preceeded by a complexation reaction. In an aqueous solution containing DMSO (approximately 17%), the coumarin hydrazine derivative was recorded to display an inverted fluorescence response; exhibiting a very considerable rise in fluorescence following complexation with Al^{3+} ions alone. The fluorescence was noted to be suppressed in the presence of fluoride ions owing to the increase affinity of fluoride ions for Al^{3+} cations (Wang *et al.,* 2017).

The initial strong fluorescence of gadolinium(III)-coumarin complex (Figure 2.2) (Sarkar *et al.,* 2017) is dramatically quenched, however the presence of fluoride ions in an aqueous solution containing ACN (approximately 30%) was reported to restore the fluorescence attributed to the creation of a gadolinium-fluoride complex as a

consequence of the suppression of the PET mechanism in the non-complexed fluorophore. A magnesium complex (Figure 2.3) has been reported to produce intense red fluorescence, but the introduction of fluoride ions causes the magnesium complex to undergo decomplexion reaction, thereby suppressing the fluorescence owing to the revival of the PET mechanism in the liberated fluorophore.
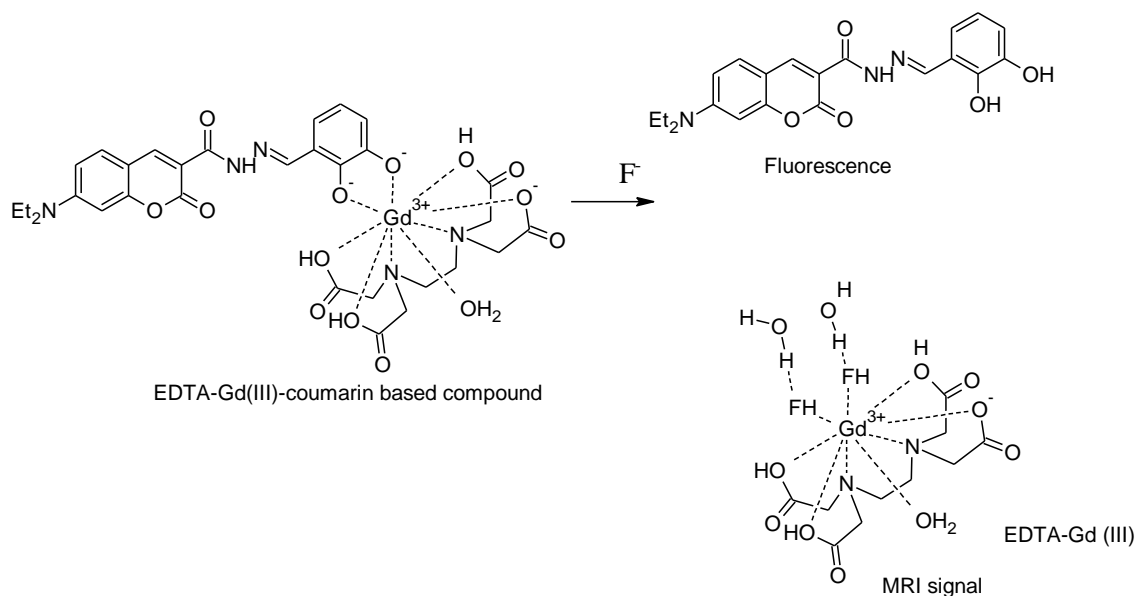
Figure 2.2: Proposed binding mode of fluoride ions on EDTA-Gd(III)-Coumarin based compound
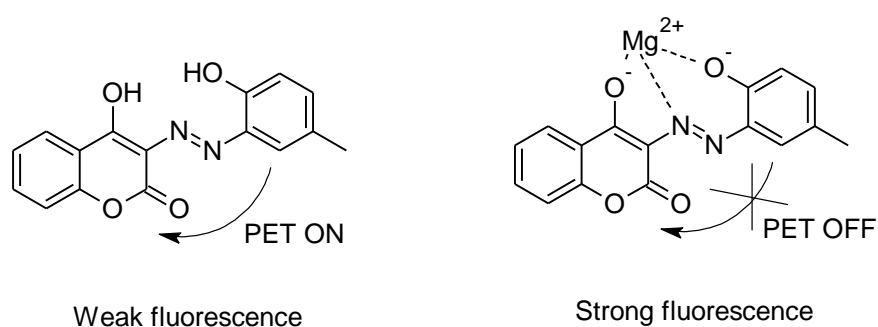
Figure 2.3: Proposed reaction mechanism of magnesium complex fluoride sensor

2.3.9 Use of Chemodosimeter

The chemodosimeter method makes use of permanent chemical change brought about by an anion. This results in variations in emission or change in colour. Relevant chemical processes arise in these methods that necessarily contain the shattering as well as establishment of many covalent bonds. Chemodosimeters (Figure 2.4) may react rather selectively towards specific anions in aqueous or mixed organic-aqueous mixtures. Chemodosimeters primarily use the nucleophilic attack on the target electrophilic species, resulting in a reconfiguration of electric field throughout the whole structure accompanied by colour enhancement. Furthermore, some metal complexes that, on coordination with another ligand or anion, modify the metal complex's fluorescence signal that in turn favours detection and identification (Padghan *et al.,* 2021).
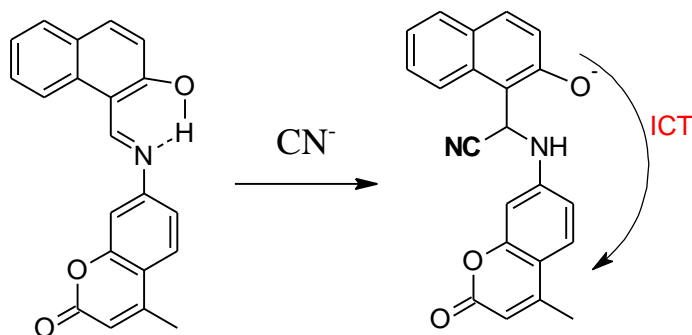
Figure 2.4: Cyanide selective chemodosimeters (Padghan *et al.,* 2021).

2.3.10 Fluoride-Boronic Acid Moieties Interaction Sensors

Boronic acid-based sensors have been designed as fluoride ion sensors attributed to the reason that trivalent boron forms strong covalent bonds fluoride ions. Because the Boron–Oxygen bond in aromatic boronic acids is labile under protic circumstances, the introduction of fluoride causes a series of equilibria in which boron participates in an

OH⁻/F⁻ exchange mechanism. Tetrahedral boronate anions generally quench the fluorescence of fluorophores attached to them by way of an ICT process. This mechanism operates in emitting probes that like boron–fluoride complexes (Avinash *et al.,* 2020).

The boronic acid group's affinity to hard bases, such as fluoride has been used to develop fluoride sensors based on the relationship between the fluorescence or absorbance and the electronic properties of the boron centre upon fluoride binding (Guo *et al.,* 2012). Triarylboranes are strong Lewis acids. This property enables them to be used as nucleophilic anions sensors. The fluorescent character of triarylboranes promotes their use as visual sensors (Avinash *et al.,* 2020).

Fluoroborate anions are usually formed when fluoride ions are added to triarylboranes. The reaction between fluoride ions and boron cluster depends on the changes in the electronic structure of the substituent. This property (Figure 2.5) has been exploited in the development of visual fluoride sensors (Zhou *et al.,* 2014). This is an off-on sensor in which the fluorescein derivative is initially put out through a PET process. However, upon reacting with fluoride, the sensitivity of this sensor is greatly improved and the fluorescence is turned on (Figure 2.6). In this type of sensor, the boron centre has to compete with water to react with fluoride and the concentration of the sensors used for the assay is usually in the low micromolar range, making competition with water (55 M) difficult, (Guo *et al.,* 2012). Boron-containing chemosensors are at the forefront but despite significant development, there have been no reports of fluoride-specific boron based fluoride detectors that can be efficiently applied in aqueous systems.
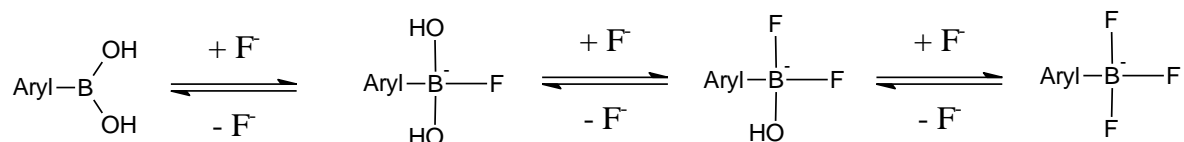
Figure 2.5: Mechanism for fluoride binding with boronic acids
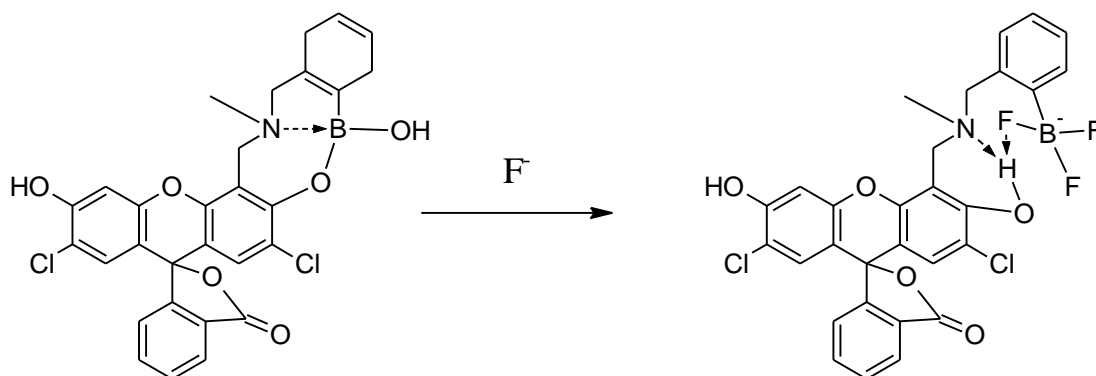
Figure 2.6: An example of fluoride binding with boronic acids (Guo *et al.,* 2012).

2.3.11 Fluoride Promoted Desilylation Sensors

The affinity of fluoride to silicon is one other attribute that make it stand out from other anions. The fluoride-silicon bond is much more stable as shown by its bond dissociation energy (BDE) at 141 kcal/mol which is higher than the bond dissociation energy (BDE) of carbon-silicon at 69 kcal/mol and oxygen-silicon bond dissociation energy (BDE) at 103 kcal/mol. Several oxygen-silicon bond and carbon-silicon based F⁻ sensors have been reported (Zhou *et al.,* 2014).

These sensors have an electron acceptor: (fluorophore/chromophore) that contains an electron withdrawing group) in addition to a fluoride receptor that contains one/more oxygen-silicon or carbon-silicon moieties. However, unlike the PET process, the receptor and reporter are usually linked through a conjugated linker or directly attached

to each other. The sensors by themselves are normally non-fluorescent or weakly fluorescent because of the free bond rotation of the silicon moieties (Zhou *et al.,* 2014).

Upon fluoride reacting with the sensor, the silicon moieties leave and the receptor becomes a strong electron donating group. The charge can be transferred into the fluorophore, thereby greatly enhancing the "push-pull" effect of the fluorophore and in turn lowering the HOMO-LUMO energy gap, making the excitation and emission wavelength red-shifted and improving the quantum yield. This process is known as the ICT process (Figure 2.7).

Figure 2.7: ICT mechanism in designing fluorogenic probes (Akumu *et al.,* 2021).

With tert-butyldiphenylsilyl (Hossein *et al.,* 2020), ether (Ghate *et al.,* 2005) or triisopropylsilyl ether (Grimm *et al.,* 2013) as the reactive group, these compounds are reported to be extremely sensitive fluoride sensors, with fluorescence increasing upto more than 700-times when the F⁻ anion is added.

Si-O bonds can be permanently broken by fluoride ion due to the higher bond strength of a Si-F bond over a Si-O bond. Due to the extreme reactivity of 2-(trimethylsilyl)ethyl ether group as reported by Mahoney and coworkers, fluoride ion may easily activate aryl phthalate esters (Figure 2.8). When the silyl coupler is deprotected, the phthalate monoester that results cyclizes, freeing the coumarin and increasing fluorescence intensity. When the Silyl Bridge is deprotected, the phthalate monoester that results

cyclizes, releasing the coumarin and increasing fluorescence intensity (Mahoney *et al.,* 2013).
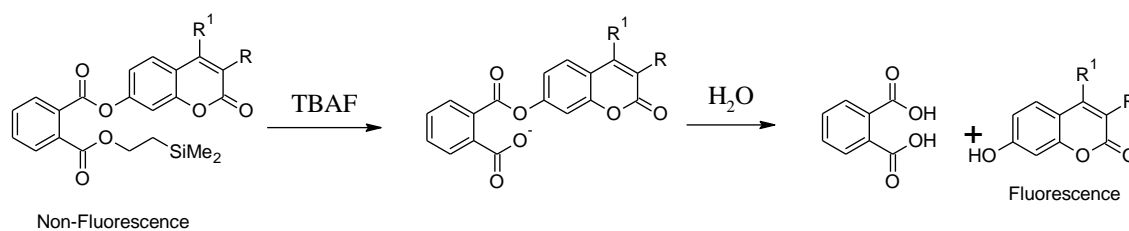
Figure 2.8: Molecular structure of an aryl phthalate ester and proposed binding mode to fluoride ion.

To detect fluoride ions, Huang and co-workers employed an innovative self amplifcation method. The activation of the sensor, followed by the 1,6-elimination of the 4-hydroxybenzyl alcohol binder, resulted in the generation of two more equivalents of fluoride ions (Figure 2.9).
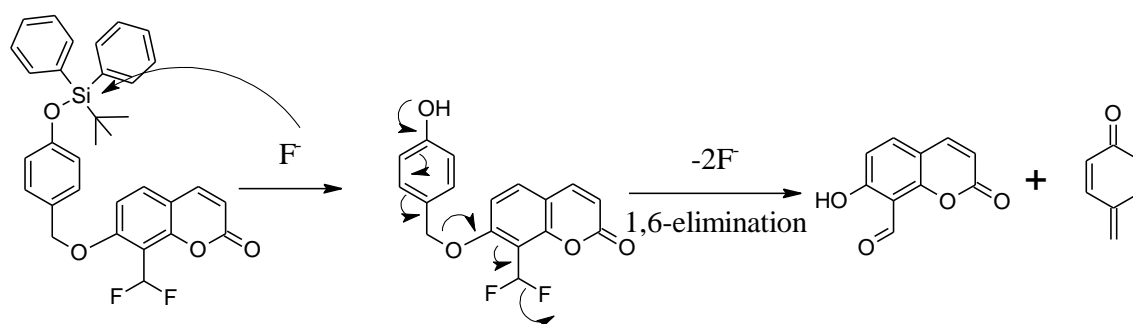
Figure 2.9: Sensor self inducing signal amplifcation process the presence of fluoride ions.

When these compounds are investigated in the presence of acetonitrile-pyridine-water (94/1/1) (v/v/v) solution, to establish an extremely wide range in LOD of between 0.5-238 pM among analogues, with the ones that lack self-amplification process rcording

higher LODs. This clearly illustrates the advantage of the self amplification (Mahoney *et al.,* 2013; Feng *et al.,* 2019).

Figure 2.10: shows an example of a fluoride chemosensor relying on the substitution of tert-butyldiphenylsilyl, which activates Förster resonance energy-transfer (FRET). As a reulst, this leads to abathochromic shift in fluorescence from 464 nm (blue) to 523 nm (green). Breaking the Si-O bond lowers the potency of the ICT process; as a result such compounds undergo a ratiometric reaction to fluoride ions (Shen *et al.,* 2018).

.
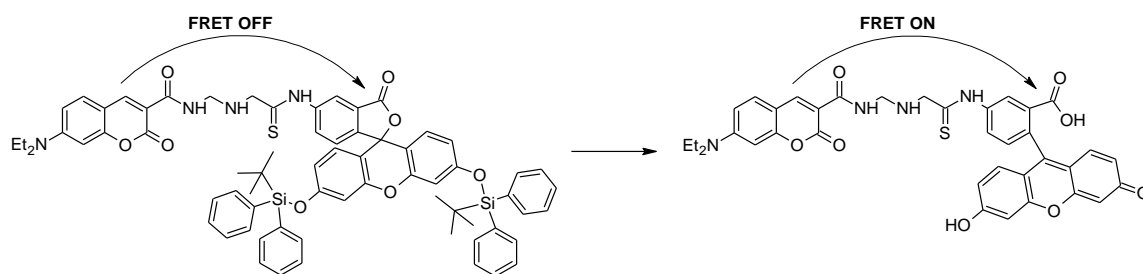
Figure 2.10: An example of a fluoride chemosensor relying on the substitution of tert-butyldiphenylsilyl.

These types of sensors usually undergo an off-on process upon reacting with fluoride. The success of this type of sensors depends on the rate of fluoride breaking the Oxygen-Silicon or Carbon-Silicon bond and the quantum yield and molar extinction coefficient of the reporter. These factors determine the sensors' detection limit. Since these types of sensors are reaction based, their selectivity to fluoride is usually very good. Also, they usually exhibit a turn-on process upon reacting with fluoride increasing the sensitivity compared with other types of sensors. By taking advantage of these two main

superiorities, many research groups have designed this type of sensor to detect fluoride in living cells (Zhou *et al.,* 2015).

2.4   Synthetic Approaches to Fluoride Sensors

Synthetic chemical sensors have attracted a lot of research interest (Gale & Caltagirone, 2018). By and large, most common receptors for anions include -OH,-NH$_2$, -COX, imidazole, benzimidazole, urea, pyrrole and thiourea, among others. A number of reports are available where fluorogenic and chromogenic responses to fluorides have been studied. The reported fluorescent fluoride sensors are famous either for quenching or fluorescence intensity enhancement after binding to specific receptors (Han *et al.,* 2019). Different synthetic strategies have been used to obtain sensitive and selective novel fluoride (Udhayakumari, 2020).

Some fundamental photophysical mechanisms that might be beneficial in the creation of novel chemosensors remain undiscovered (Wu *et al.,* 2011). These include:

2.4.1   Interference of triplet excited states

Triplet photosensitizers (PSs) are chemicals with an ability to be effectively excited to the triplet excited state and then serve as photochemical catalysts. The term was PSs obtained from chemicals that were utilized to transmit triplet energy to other compounds with a low inherent triplet state output. Triplet PSs are utilized for photo - catalytic biochemical systems, photodynamic treatment (PDT), photoinduced hydrogen generation from water, and triplet-triplet attrition (TTA) upconversion, in addition to triplet energy transfer. A good PS should have highly excited uponabsorbing light absorptio coupled with high intersystem crossing (ISC) yield for rapid triplet state

generation, and a long triplet lifespan to allow for interaction with a reactant molecule (Zhao *et al.,* 2013).

Many metal complexes exhibit rapid ISC but have low molar absorption coefficients within the visible spectral range and temporary triplet excited states, making them inappropriate for use as triplet PSs. The challenge in forecasting the ISC of chromophores, particularly organic compounds lacking heavy atoms, is one barrier to the creation of novel triplet PSs. Some photophysical mechanisms, including triplet–triplet transfer of energy and phosphorescence, can benefit from the influence of triplet excited states (Zhao *et al.,* 2013).

2.4.2   Triplet–triplet (TT) transfer of energy.

An effective gap of about 10 Å for energy transfer between triplet states indeed is substantially lower than the Forster radius which stands at 100 Å in the case of FRET as compared to the traditional singlet–singlet (SS) energy transfer. The TT energy transfer rate constant is anticipated to drop gradually as the space in between the high energy donor and the unexcited (lowr energy) acceptor grows, according to the Dexter mechanism (Wu *et al.,* 2011).

The benefit of TT transition is that even little intervention involving the donor and acceptor leads to a large shift in photophysical propeties. As a result, TT energy transfer based chemosensors have a significant distance dependency on analytes. The restricted contact mehanisms are critical in a wide range of compound electronic components as well as biochemical pathways, including DNA analysis and photosynthesis. Intermolecular TT transfer of energy is routinely used in organic light-emitting diodes

(OLEDs); nevertheless, its applicability in chemical probes is limited furthermore, it warrants more investigation (Wu *et al.,* 2011).

2.4.3   Delayed fluorescence.

The modification of organic molecules' triplet excited state has been applied in designing time-modulated chemosensors. Due to minimal energy gap involving the first excited singlet (S_1) and the first excited triplet (T_1) coupled with a long lifespan, reverse ISC from T_1 to S_1 can occur. This produces energy release reflecting the spectrum structure just like conventional fluorescence even though with a significantly more time for decay (Wu *et al.,* 2011).

2.4.4   Up-conversion fluorescence

Up-conversion Fluorescence is described as excitation upon absorption of photons with low energy, mostly in the nesr infra-red range, followed by an emission at a higher energy typically in the visible range of the spectrum. This is a rate and very unique mechanism in which long wavelengths are 'transformed' to shorter wavelengths. An up-conversion fluorescence method therefore is ideal for studying photoinduced intramolecular interactions such as proton transfer, charge transfer and intermolecular processes (Wu *et al.,* 2011).

Photoactive yellow protein and blue fluorescent protein have been reported as being used in the research of light-driven biological processes. Furthermore, up-conversion fluorescence microscopy with absorbance in the near-infrared range is utilized to biological cells and tissues imaging. This method offers many benefits, along with no photodamage to live organisms, much less autofluorescence, excellent recognition, as

well as a significant high spatial contrast in deep tissues. This mechanism is applicable both inside and outside living organism epifluorescence studies. Yet, fluorescence-based probes relying on sequential uptake of photons leading to higher energy emission process remain uncommon; however, two photon absorption (TPA), has lately received a lot of interest. Several organic compounds have indeed been targeted on the basis of TPA. However, TPA sensors are still in the process since a number of TPA probes have tiny 2-photon active intersections, which limit their application in TPA. Any prospective studies in this field should indeed be centered on this (Shen, 2016).

2.4.5 Proximity effect

The closeness of the n–pi* and pi–pi* singlet states, speeds up the IC to the lowest energy state. This phenomenon, also known as the proximity effect, occurs from n–pi* and pi–pi* nonadiabatic coupling. The mutual effect may be used to detect polarity micropolarity in cells (Wu *et al.,* 2011).

2.4.6 Fluorescence polarization

This mechanism provides information on compound's orientation as well as its movement. It is particularly handy in the investigation of receptor–ligand bond relations, protein– deoxyribonucleic acid interrelationships, peptide bonds hydrolysis reactions, lipid bilayer viscosity and contraction of the muscle. Furthermore, polarization fluorescence-based chemosensors may be a superior alternative for chiral sensing (Zhou *et al.,* 2018).

2.4.7 Exciplex formation

Collisional intermolecular interactions between excited states generate unstable dimers and complexes, resulting in lower energy excimer/exciplex emission, that can only be distinguished from photoluminescence (PL) caused by monomeric molecules (Garci *et al*., 2020).

Even though excimer creation is extensively used in the development of chemosensors, just a few models are based on electronic excitation of a complex of known stoichiometry. Since excimer/exciplex production follows identical non-chemical photoexcitation propeties, and numerous natural esources have been recorded as having an ability to produce an exciplex, it is expected that additional exciplex-based fluorescent chemosensors (Figure 2.11) will emerge in the near future. Photophysical processes may be used to create sensors that use novel indicator methods for specific chemical structures held by intermoleculat forces and conditions for sensitivity to fulfill specific needs in various uses. Further to this, novel sensing methods are likely to be introduced in the future (Zhou *et al.,* 2018).
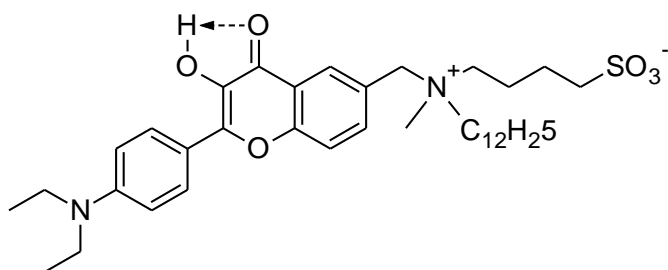
Figure 2.11: Molecular structure of an exciplex-based fluorescent chemosensor

2.4.8 Conventional signal mechanisms

On the basis of several fundamental photophysical interactions, conventional signal mechanisms were increasingly recognized. Only a basic categorization of these mechanisms has been provided here. Among these traditional methods, Electron transfer (ET), primarily by photo-induced electron transfer (PET), has been the most frequently used in fluorescent chemosensors. The emission of a fluorophore is usually reduced through a PET mechanism, but it can be restored by inhibiting this operation using molecular recptors. Secondly, charge transfer (CT) mechanisms include twisted intramolecular charge transfer (TICT), metal–ligand charge transfer (MLCT) ans intramolecular charge transfer (ICT) (Zhou *et al.,* 2018).

Enhancing or suppressing any ICT mechanism can result in a bathochromic or hypsochromic effects in the emission spectrum of an ICT-based chemosensor. This results in a ratiometric signal that can eradicate most discrepancies by self-calibration of two emission bands and allow quantitation in more complex applications, such as imaging in living cells. Alternatively, MLCT is often found in transition metal complexes. It may also be utilized to construct chemosensors based on analytes' effect on the MLCT energy level (Zhou *et al.,* 2018).

TICT is a powerful intramolecular CT that occurs in the excited state and includes relaxation due to the surrounding molecule, resulting in a continuous rotation of the electron donor/acceptor. The intramolecular rotation aswell as the charge separation in the TICT state does not require organic solvent relaxation. Fluorescence characteristics are extremely responsive to very low polarity and/or steric bulk for structure rotations (Zhou *et al.,* 2018). TICT inhibition may greatly boost the luminance of fluorophores.

Accurate TICT estimation is thus essential for the quantitative development of efficient fluorophores (Wang *et al.,* 2020).

Depending on the contact distance between the energy donor and energy acceptor, energy transfer (ET) can be categorized as electronic energy transfer (EET) or fluorescence resonance energy transfer (FRET). In order to be effective, EET, also known as Dexter electron transfer, requires a distance of less than 10 Å between the acceptor and the donor, whereas. FRET needs a specific level in overlap involving the emission and absorption spectra of the donor and acceptor respectively. For effective FRET, the desirable space between the acceptor and donor is expected to range between 10 Å and 100 Å. As a result, chemical probes that operate on the processes involving energy transfer are highly gap sensitive. When a fluorophore in the excited state differs from its ground state, the resulting complex is an excimer/exciplex (Mukherjee *et al.,* 2020).

When compared to the monomer, the emission spectra of an excimer/exciplex that has undergone bathochromic shift, and dual emission from the monomer is frequently detected. As a result sensing may be accomplished simply by monitoring the excimer/exciplex band from its production or deformation during contact with an acceptor. However, this remains an area of much research interest as very few chemosensors functioning exciplex have been developed (Şenkuytu, 2018).

2.5   Promising signaling methods

Because of the fast growth of chemical probes made up of a distinct number of structures, several basic photoemissive processes are drawing interest for the

development of novel sensing systems. A stiff fluorophore promotes radiative relaxation whereas a flexible design promotes relaxation to lower energy states with very little or no emission; sp^2 carbon isomerization absorbs energy while increasing non-radiative relaxation; in the excited state, the rate of proton transfer is significantly larger than that of electron transport (Wu *et al.,* 2011). Furthermore, the most basic nonradiative decay mechanism that causes emission and fluorescence quenching is intramolecular rotation in certain components leading to emission (Abebe *et al.,* 2018).

A noticeable fluorescence fluctuation is therefore predicted if such an intramolecular rotation is partially or fully blocked (Wu *et al.,* 2011). Because molecular rotation reduces emission if form of fluorescence, it is therefore realistic that a limitation on molecular rotations decreases the non-radiative mechanism character and results in to a higher fluorescence intensity. Several novel designs based on photophysical mechanism are in use as fluorescent chemosensors (Khan & Kumar, 2021). Even though the knowledge on these novel processes is currently limited in comparison to traditional mechanisms, they do offer some recommendations for developing new supramolecular systems for detecting analytes (Asiri *et al.,* 2019).

2.5.1 Aggregation-induced emission (AIE)

This mechanism is commonly recognised in organofluorophores whose emissions are frequently reduced when they are gathered together; this results into an aggregation-caused quenching (ACQ). Due to the extreme ACQ effect, several organic fluorophores have been seriously restricted in their usage in organic light-emitting diodes (OLEDs) and as chemosensing materials (Zhang *et al.,* 2019). To counteract the ACQ effect, branching chains and ring species are covalently bonded to the fluorophores to prevent

aggregation formation. However, certain organic compounds that are nearly non-fluorescent in have demonstrated ability to be converted into highly fluorescencing materials following the unusual characteristin in aggregation (Wang *et al.,* 2020). The aggregation-induced emission (AIE) process greatly multiplies the quantum yield of fluorophores, transforming it from virtually non-fluorescent to highly fluorescent species. It was later reported that AIE phenomena is also seen in a range of tetraphenylethene, diphenyl dibenzofulvenes, substituted olefins, and pyran derivatives (Chen *et al.,* 2019).

2.6   Mechanisms for anion sensing

The following anion sensing mechanisms may be used during synthesis to be applied in sensing studies for anions including fluorides through bond donation ability (Kaur *et al.,* 2017).

2.6.1   π-electron delocalization induced by hydrogen bond

The delocalization of pi- electrons and, as a result, the electron motion inside the formed loop results in the synchronization of suitable bonds. The transfer of electron density in resonance-aided hydrogen bond structures appears to be crucial for the photochemical characteristics of these groups. The migration of electrons from its Lewis base entity to the lewis acid end is quite well documented for intermolecular H-bonds (Ma *et al.,* 2017). The varying types and strengths of hydrogen bonds influence pi-electron migration in the remaining structure. These can include not only the pi-electron spacer but also conjugated systems within the structure. Especially with regard to the relationships seen between aromatic component of the system's pi-electron migration as well as the form including its H-bond, aromaticity indicators could be used

for every reason, that will define pi-electron delocalization as well as enable compare respective intensities to quantities for well-known aromatic structures (Liu *et al.,* 2021).

2.6.2 Lewis acid-base interactions

Lewis philosophy employed transfer of electrons rather than just proton movement and claimed explicitly how an acid embraces an electron pair using its empty orbital while a base make a contribution of its non-bonding electron pairs, culminating in a coordinate bond. Soft acids tend to associate more with soft bases while the hard acids prefer to connect to hard bases. Lewis acid cores with fewer electrons will connect to anions through orbital overlapping. This results in an interaction between bonds. As a result, several novel anion hosts from several transition metals have been synthesized (Chen *et al.,* 2021).

2.6.3 Photoinduced electron transfer (PET)

Photoinduced electron transfer (PET) is indeed a messaging expression used to describe the quenching or stimulation of radiation. Fluorescent sensors that depend on PET are typically composed of a fluorophore, receptor and spacer. The receptor comprises of interacting atoms that possess comparatively high energy non-bonding electrons that can pass an electron to the HOMO including its activated fluorophore, resulting in quenching (Tang *et al.,* 2020).

As the electron pair is active throughout the interaction of metal ions, the receptor's reduction potential becomes boosted, causing the fluorophore to be higher in energy the associated HOMO; as a result, the PET mechanism from the receptor to the fluorophore is disallowed, resulting in increased emission spectra. Furthermore, depending on the

surrounding orbitals added, an interaction between the receptor and analytes causes PET from the fluorophore's excited LUMO to the receptor's HOMO, culminating into quenching. As a result, it is commonly seen in sensors for fluorescent detection of charged or neural samples. Covalently connected fluorescent sensors are usually made up of a receptor and a fluorophore that seem to be electrically separated (Magri, 2021).

2.6.4   Intramolecular charge transfer (ICT)

Intramolecular charge transfer (ICT) probes involve the conjugation of electron donating groups (EDGs) and electron withdrawing groups (EWGs) into a single atom. This results into a 'push-pull' on pi-electron system in its activated form. As the fluorophore is excited, electron density redistribution occurs, leading to the formation of a significant dipole and ICT from donor to acceptor. The attachment of active site to the basic group group slows the ICT process due to reduced electron-donating power, resulting in a shift towards shorter wavelengths in absorbance. As samples bind to the acidic group, an obvious shift to the longer wavelengths on absorbance is detected owing to enhanced ICT activity (Kodlady *et al*., 2021).

2.6.5   Excited-state intramolecular proton transfer (ESIPT)

High enegy protons are absorbed or emitted by a molecule at higher rates than the low energy states in ESIPT systems. When compared to electron transfer, ESIPT is a rapid process, with reported values ranging from fractions of picoseconds to tens of picoseconds (Dong *et al.,* 2018). The pace of proton transfer is affected by the environment, and it becomes considerably slower in the nanocavities of cyclodextrin or in an emulsion, taking nanoseconds to occur. In steady-state spectra, the ESIPT process

is easily identified: the absorbance is typically comparable to the original chromophore, but the emission is substantially altered (Dhanunjayarao *et al.,* 2014).

Because ESIPT dyes have a strong absorption shift, they're ideal for deployment as fluorescence markers since they don't interact with other fluorescent elements in the sample. Due to the extreme large Stokes shift, ESIPT dyes have almost little spectrum overlap across absorption and emission, making them ideal for use in fluorescence sensors (Chen *et al.,* 2014; Sedgwick e*t al.,* 2018).

Jun-Sheng Chen's research on the sensing mechanism of the fluoride chemosensor *N*-(3-(benzo[*d*]thiazol-2-yl)-4-(*tert*-butyldiphenylsilyloxy)phenyl)-benzamide (BTTPB) in water using DFT/TDDFT methods revealed a desilylation reaction accompanied by a reasonable transition activation energy of 17.6 kcal/mol as well as the ESIPT of the desilylation reaction product (3-BTHPB) that concurrently work in the fluorescence emission. The built potential energy curves between the optimized 3-BTHPB and 3-BTHPB-e geometries on the S_0 and S_1 states revealed that the ESIPT is a low barrier process (0.1 kcal/mol), and the optimized geometries' energies revealed that the ESIPT process is exothermic (Chen *et al.,* 2014).

2.6.6 Fluorescence/ Förster Resonance Energy Transfer (FRET)

FRET is a non-radiative emission process in which an activated donor loses energy to a ground-state acceptor via long-dipole correlations. The FRET output refers to the likelihood of transfer of the emitted energy. This is heavily comparative to the space between the two fluorophores, the similarity between emitter and absorber, as well as the comparative dipole orientation of the donor and acceptor (Venkataraj *et al.,* 2018);

(Xiong *et al.,* 2019). In FRET schemes, the donor output must have effective spectral similarity mostly with acceptor absorption wavelength (Mizuta *et al.,* 2021).

Bo Qiu and colleagues proposed and synthesized Cou-FITC-Si, a Förster resonance energy-transfer (FRET)-based ratiometric fluorescent indicator toward fluoride ion by combining coumarin unit and fluorescein derivative as energy donor and acceptor, respectively. TBDPCl-Si was used to cap the fluorescein unit. The indicator emits emission responses depending on the activation of the FRET mechanism, which is activated by desilylation mediated by the fluoride ion. After the addition of fluoride ion, the fluorescence emission spectra of Cou-FITC-Si exhibit a substantial bathochromic shift of 59 nm, with up to a 180-fold increase in the fluorescence intensity ratio. The Cou-FITC-Si indicator system's LOD for fluoride ion was calculated to be 3300 ppm. Additionally, this indicator has already been used effectively to measure the fluoride ion concentrations in commercially products like toothpaste (Qiu *et al.,* 2018).

2.6.7   Displacement Assays

Displacement assessments are already extensively used in the development of anions' visual probes. The attachment of the specific anion to recognition pocket of the molecular group not only leads in the relocation of the triggering receptor but also a major visual shift in the relocation strategy. The binding of the specific anion to the active sites results in the relocation of the sensing subunit and a dramatic visual shift in this technique. The identification of the resulting anion is caused by the difference in optical properties between the independent receiver as well as the coordinated sensor. One intriguing assumption of this approach has been that the majority of synthesized

structures exhibit signalling functionality in aqueous or organic/aqueous mixtures, leading to the establishment of practical sensing schemes (Sedgwick *et al.,* 2021).

Indicator displacement assays (IDAs) are a novel and cutting-edge technique in structural sensing. IDAs identify a variety of physiologically and ecologically significant species, as well as providing a mechanism for detecting complex analytes and determining and discriminating unknown mixed sample. These characteristics are frequently inaccessible to typical molecular sensors, such as reaction-based probes. The pioneers of IDA; Inouye, Shinkai, and Anslyn encouraged scholars all over the world to create numerous expansions of this concept. The field of indication displacement assays has grown since their early work. Allosteric indicator displacement assays (AIDAs), Reaction-based indicator displacement assays (RIAs), Enantioselective indicator displacement assays (eIDAs), intramolecular indicator displacement assays (IIDAs), quencher displacement assays (QDAs), Fluorescent indicator displacement assays (FIDAs), DimerDye disassembly assays (DDAs), and mechanically controlled indicator displacement assays (MC-IDAs) are examples of current research in this field. The ease of use of these IDAs, combined with their affordability, high sensitivity, andhigh performance on automation analysis, has resulted in their widespread use in molecular sensing, together with other popular strategies such as responsive sensors and chemosensors (Sedgwick *et al.,* 2021).

2.6.8   Use of Chemodosimeter

The chemodosimeter method makes use of permanent chemical change brought about by an anion. This results in variations in emission or change in colour. Relevant chemical processes arise in these methods that necessarily contain the shattering as well

as establishment of many covalent bonds. Chemodosimeters may react rather selectively towards specific anions in aqueous or mixed organic-aqueous mixtures. Chemodosimeters primarily use the nucleophilic attack on the target electrophilic species (Martínez-Máñez & Sancenón, 2006; Wu *et al.,* 2018), resulting in a reconfiguration of electric field throughout the whole structure accompanied by colour enhancement. Furthermore, some metal complexes that, on coordination with another ligand or anion, modify the metal complex's fluorescence signal that favours detection and identification (Padghan *et al.,* 2021).

Yang together with his research team designed and synthesised a new merocyanine-based chemodosimeter capable of detecting aqueous F⁻ anions. The discovery of this highly selective and sensitive colorimetric fluorescent fluoride sensing chemodosimeter, with a rapid reaction to fluoride within a few minutes, has led to a novel and extremely promising sensor for quick detection of aqueous F⁻ anions (Yang *et al.,* 2013).

Changyao and co-workers reported a self-assembly of fluorescent chemodosimeter compounds on a graphene oxide (GO) layer that overcome these sensing difficulties by utilizing GO's outstanding chemical catalysis and nanocarrier functionalities. A novel fluoride specific fluorescent chemodosimeter compound, FC-A, and the GO self-assembly framework of GO/FC-A were produced. The reported reaction rate constant of GO/FC-A for fluoride ion was about five times more than that of FC-A, thus the response time was reduced from four hours to around 30 minutes, but the response sensitivity of GO/FC-A for fluorideion was more than twice higher than that of FC-A. Furthermore, because of the nanocarrier role of GO for cells, GO/FC-A demonstrated higher bioimaging performance for fluoride ion than FC-A (Changyao *et al.,* 2014).

Kai and colleagues efficiently developed a new chemo-dosimeter for fluoride ions relying on Fluoride ion-triggered double Si–O bond breakage of distyrylbenzene compounds with excellent selectivity and sensitivity against fluoride anions via 'turn-on'chromogenic and fluorogenic double modes. For the detection of fluoride ion a simple and affordable test strip utilizing a chemodosimeter can easily bedesigned and developed (Kai *et al.,* 2016).

Cao and colleagues developed a new fluorescent chemosensor array for multi-anion detection using pyrenylboronic acid-based probes. Fluorescence quenching or enhancement was seen in pyrenylboronic acid derivatives owing to PET caused by anion binding. Fluorescence titrations and electrospray ionization mass spectrometry were used to evaluate the recognition abilities. Fluorescence titrations and electrospray ionization mass spectrometry were used to evaluate the recognition abilities. Because the array is made up of cross-reactive probes, the combination of differential binding affinities for anions and pattern recognition techniques such as linear discriminant analysis resulted in successful simultaneous anion detection with a classification rate of 100%. Moreover, utilizing a support vector machine, the chemosensor array enabled quantitative prediction of oxalate, malonate, and citrate in mixes. Furthermore, as probes, the array technology makes use of cheap, commercially accessible chemicals (Cao *et al.,* 2020).

2.7   Coumarins

The evolution of coumarin science may be traced to approximately over 200 years back. Vogel and Guibourt separately discovered this intriguing oxygen-containing

heterocyclic compound from tonka beans and the flowers of sweet clover in the year 1820. In 1868, Perkin who also pioneered the Perkin reaction became the first synthetic chemist to synthesize coumarin by heating the sodium salt of salicyaldehyde with acetic acid. Since 1872, the structure of coumarin proposed by Fittig, Strecker, and Tiemann as 1-benzopyran-2-one is widely regarded as accurate (Cao *et al.,* 2019).

In 1941, Rama was the first to study the crystal structure of coumarin, while the initial entry in the Cambridge structural database (CSD) was done in 1973 by Myasnikova and co-workers. Today more than one thousand structures of coumarin derivatives have already been deposited in the CSD (Cao *et al.,* 2019).

2.7.1   Coumarins Structural Features and Chemistry

Coumarin is a two-ring system with a phenyl group joined to a pyrone ring having six exterior C-H sites, as well as a C=O and a stiff C=C subunit from the position of molecular architecture. The C=C bond adopts s cis-conformation, which aids in preventing the trans-cis transition of typical C=C bonds in vinylic molecules and leads to coumarins' high fluorescence emissivity and resistance to photochemical degradation. Coumarins are organic heterocycles represented by benzopyrone (2*H*-1-benzopiran-2-one). The nomenclature is based on the International Union of Pure and Applied Chemistry (IUPAC) (El-Sawy *et al.,* 2021). The general structure of coumarin is given in figure 2.12.
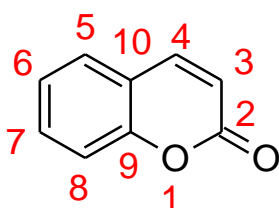

Figure 2.12: Basic coumarin structure.

The synthesis of coumarin compounds has received much interest from organic and medicinal chemists since many natural compounds include the coumarin heterocycle. While post functionalization is possible at all six C-H sites and the C=C unit, the 6th and 7th positions of the phenyl group and the 3rd and 4th the vinyl group are more appealing and chemically accessible to derivatization. Incidentally, virtually all natural coumarins have oxygen substituents at the 7th position, however the most significant fluorescent coumarins, have an amino or hydroxyl substituent at the 7th position. The Pechmann reaction (Monga *et al.,* 2020), Knoevenagel condensation (Lončarić *et al.,* 2020), and the Perkin condensation (Salem *et al.,* 2018) are the most common synthetic methods for coumarin derivatives, However, the searchfornew coumarin based compounds has also spurred the identification of totally novel approaches, like metal-catalyzed cyclization reactions (Bhatia *et al.,* 2018).

As a result, new methods including use of microwave (Mamidala *et al.,* 2021) and ultrasonic waves (Ghomi & Akbarzadeh, 2018), novel catalysts (Farahi *et al.,* 2017), and enviromentally safe solvents (Molnar *et al.,* 2020) have emerged in recent years to synthesize coumarins in a more efficient and environmentally friendly manner. Because coumarin is not a common hypothetical starting material in organic synthesis, its direct chemical functionalization has been explored frequently for specific synthetic purposes. In other words, rather than postfunctionalizing the coumarin skeleton, most coumarins have been synthesized or developed from start. In certain 7-amino or 7-hydroxyl coumarins, the direct electrophilic bromination (Gouda *et al.,* 2020) and Vilsmeier formylation (Jain *et al.,* 2020) reactions have been noticed to selectively occur.

However, direct addition of alcohols, ketones, and carboxylic acids, on the other hand, has not always been effective (Cao *et al.,* 2019).

The synthetic modification of coumarins into different heterocyclic compounds containing a coumarin backbone has also been produced. Furthermore, the coumarin ring system's benzene subunit is less reactive than a typical benzene derivative, but the C=C bonding between C-3 and C-4 is extremely reactive. Furthermore, the addition of one or more electrons to a photoexcited species or the photochemical hydrogenation of coumarins, which always occurs at this C=C bond, have been successfully determined (Cao *et al.,* 2019).

2.7.2   Classification of Coumarins

Coumarins are classified according to their chemical variety as well as complexity. Simple coumarins, biscoumarins, pyranocoumarins (both angular and linear), furanocoumarins, isocoumarins and phenylcoumarins are examples of this class of compounds (Table 2.4) (Zhu & Jiang, 2018). These compounds do have many appealing properties, including lower molecular weight, simplicity in structure, significant bio-availability, good solubility across most organic solvents, and excellent biocompatibility, which, combined with their multidimensional biological functions, ensures that they play an essential part as lead molecules in therapeutic applications (Zhu & Jiang, 2018) and fluorescence related studies (Carneiro *et al.,* 2021).

Besides their bioactivity, coumarins have yet another essential property that is being studied by the industry: potential luminous qualities. The inherent charge transfer characteristics cause the luminescence of certain analogues by electron-rich conjugated
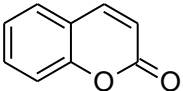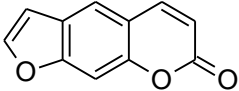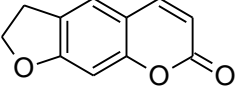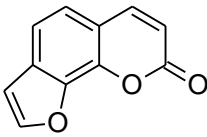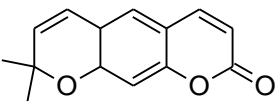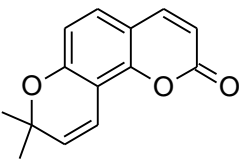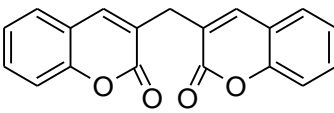
pi-systems (Pereira *et al.,* 2018). These compounds have a wide range of uses, such as photo-cleavable protecting moieties and fluorescent detectors (Tasior *et al.,* 2015).

2.7.3 Natural Coumarins and their Application

Coumarin derivatives play an important role in a number of biochemical processes. Coumarins are a large family of phytochemicals that are naturally occurring polyphenolics and are found throughout the plant kingdom. Coumarin derivatives play an important role in a number of biochemical processes (Harborne, 1982).

Since their first discovery, coumarins have attracted a large number of organic and medicinal chemistry researchers over a long period of time, and their separation from natural sources, chemical synthesis, and assessment of their uses has remained a fast expanding field in research. Coumarins have long served as a key structural component in a wide range of biologically active compounds, including antibacterial (Sahoo, 2021), antifungal (Ali, 2021), antiviral (Shan, 2021), anti-HIV (Srivastav, 2017; Wadhwa, 2018), anti-inflammatory (Emam, 2021), antioxidant (Khalil, 2020), anticancer (Al-Warhi, 2020), Antiproliferative (Erşatır, 2020), anticoagulant (Kraimi, 2021), antineurodegenerative (Chen, 2018; Erşatır, 2020), and photosensitization (Guerrero, 2021). In recent years, these various pharmacological characteristics have sparked a lot of attention. A few classes of coumarins have emerged as preferred scaffolds in drug development (Alshibl *et al.,* 2020).

Table 2.4: Natural coumarins classification

Coumarin class	General structure	Reference
Simple coumarins		(Önder, 2020)
Furanocoumarins		(Sumorek-Wiadro *et al.,* 2020)
Pyranocoumarins		(Joshi, 2021)
Biscoumarins		(Asgari *et al.,* 2019)

In the hunt for novel research candidates, this structure serves as a key foundation for the construction of chemical libraries. In addition, an overview of the most prevalent synthetic pathways used to create basic coumarins is offered, along with a discussion of alternative, creative, and green synthesis approaches.

2.7.4 Pi-Expanded coumarins

Coumarins have always piqued the interest of people. We are surrounded by them, from the fragrance of newly cut grass to laser dyes and fluorescent probes. More than that, we wear them like dyes along. Coumarins have captivated mankind since the dawn of time. Coumaris are everywhere ranging from the fragrance of newly cut grass to laser dyes and fluorescent detectors. Moreover, we commonly use them as optical brighteners. Coumarins in the company of additional aromatic or heterocyclic rings combined with chromen-2-one, were produced for the first time by Pechmann in 1842, they certainly didn't make their way to conventional photonic-oriented use until very recent times (Mirosanloo *et al.,* 2018).

Because of their distinctive photophysical and biological characteristics, benzocoumarins and heterocycle-fused coumarin derivatives have indeed been exploited in a variety of study areas.They have been utilized to create fluorescent probes and markers, photo-labile substances, and biologically active compounds (Jung *et al.,* 2018).

2.7.5 Coumarins as Photocleavable Protecting Groups (PPGs)

The creation of an appropriate design is a critical stage in the development of novel functional medicines. The development of innovative tactics aiming at selectively releasing the bioactive in a specific area at a precise moment to enhance efficacy while minimizing off-target undesirable effects constitutes a very active research lead. Several stimuli-responsive devices, comprising endogenous triggers; that is pH, enzymes, redox processes among others and exogenous stimuli, have also been studied in treatment modalities to govern the delivery of therapeutic content (Hennig *et al.,* 2020).

Because of their remarkable non-invasiveness and spatiotemporal pinpoint accuracy when a specificelective light-irradiationfrequency is used, light-mediated therapeutic approaches have displayed superior performance and achieve on-demand new treatments and optical techniques for investigating and detailed review of biochemical mechanisms in specific areas. The employment of photolabile "protecting" groups at crucial spots is one approach for controlling chemical activities with light. Ideally, this alteration fully inhibits any molecule's activity and only recovers it with light (Bardhan & Deiters, 2019).

Coumarins, specifically 4-hydroxymethyl analogues, have been shown to photolyze (Lin *et al.,* 2018). Coumarins, specifically 4-hydroxymethyl analogues (Figure 2.13), have been shown to photolyze (Lin *et al.,* 2018).Many biomolecules of importance have indeed been connected to the coumarin core, primarily as acyl equivalents. The biomolecules can be unleashed into the biosystems after being exposed to UV light. Various aspects such as the mechanism of fusion, the chemical composition of extra rings, and the availability of electron-donating and electron-withdrawing functional group all influence the photophysical characteristics of the produced analogues (Hu *et al.,* 2018).
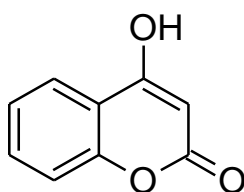

Figure 2.13: 4-hydroxymethyl coumarin

Fournier and colleagues presented a family of methyl-coumarins with bathochromic shift in absorption in 2013. Three compounds (Figure 2.14), in particular were easily synthesized and displayed a substantial reaction broad swath for uncaging with blue-cyan light, however their uncaging capability in the UV frequency domain was minimally maintained in order to prevent photo-activation when correctly tailored UV lighting was used (Fournier *et al.,* 2013).
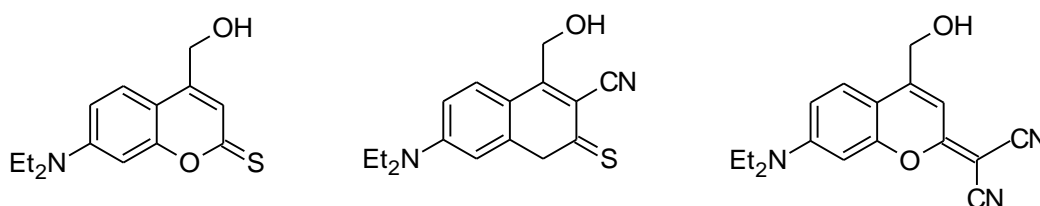
Figure 2.14: Structure of a few coumarin photoclavable protecting groups

Fournier and colleagues demonstrated that same year that a molecule containing a thiocarbonyl group was indeed a suitable blue-absorbing caging group due to its highly donating conjugated group. Furthermore, the researchers proved that this caging set could be employed in zebrafish embryos for developmental biology to execute chromatic orthogonal photo-activation of two bioactive species (Fournier *et al.,* 2013).

Gandioso and coworkers in 2017 reported the creation of green/red-absorbing fluorescent dyes based on coumarin scaffolds which could be used as photocleavable protective groups (Gandioso *et al.,* 2017).

2.7.6   Coumarins Photoproperties

The uses and characteristics of coumarin scaffold are quite diverse. Coumarin-based compounds have been used as active pharmaceutical, agrochemical components, beauty and colors for a variety of applications ranging from laser technology to organic photoredox catalysis, epifluorescence and photocleavable protecting groups (Passos *et al.,* 2021).

2.7.7   Fluorescent Coumarin Probes

Coumarins are electron-rich and highly conjugated systems with charge transfer (CT) properties, coumarin-based fluorophores are therefore extensively applied in assessing a wide range biochemical processes (Annunziata *et al.,* 2020). Many coumarin compounds have been suggested and studied for ion detection in a variety of applications, ranging from cellular imaging to environmental studies (Annunziata *et al.,* 2020).

Long and his team of researchers developed a coumarin-based fluorescent probe that was previously efficient in detecting glutathione in Cu^{2+} ionic solution. They extended its capability to detect hypochlorite ions with excellent selectivity and sensitivity. In reaction to hypochlorite, this sensor displayed stunning fluorescence intensity in detection of ClO^- in living cells through intracellular fluorescence imaging (Long *et al.*, 2018).

Due to the relevance of hypochlorite ions in both living systems (as one of the biologically most significant reactive oxygen species) and the environment (due to its usage as a disinfectant), Shangguan and his rearch team suggested a new sensor (Figure

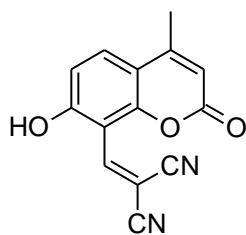2.15) based on coumarin dye and malononitrile for hypochlorite ion (Shangguan *et al.,* 2019).

Figure 2.15: Hypochlorite ion coumarin based fluorescent sensor

The probe's fluorescence response at 459 nm to ClO^- ions steadily increased with increasing ClO- concs, leading to a 45-fold fluorescence amplification. In addition, the sensor demonstrated great accuracy for quantification of hypochlorite ions in aqueous samples with a potential to be utilized as a chemosensor for the detection of ClO^- in various aqueous systems (Shangguan *et al.,* 2019).

Tang and colleagues also worked on a coumarin-based fluorescent probe capable of swiftly distinguishing ClO^- and Cu^{2+} ions in various aqueous systems. It was observed that the reaction with ClO^- caused a significant blue shift in the fluorescence wavelength, as well as observable changes in loss of colour from from a yellowish to colorless. Furthermore, it demonstrated a clear fluorescence quenching response to Cu^{2+} ions with chromogenic measurement ranging from dull yellow to brilliant yellow (Tang *et al.,* 2019).

Starzak and colleagues conducted an important study on the interaction between coumarin-based ionic detectors and hypochlorite ions. The studies determined a linear drop in fluorescence with a rise in ClO^- quantities in distinct coumarin compounds,

which were chosen due to the presence of the 7-diethylamino group and the 3-substituted lactone ring, which are well-known structural patterns responsible for fluorescence properties. A varied reactivity pattern was found to depend on the pH levels, most likely owing to the variable reactivity of hypochlorite ions due to the change of the salt's dissociation at different pH values. Later, the possibility of the production of chlorinated derivatives was investigated: The presence of chlorinated derivatives was shown by HPLC-PDA-ESI-MS studies, proving that the chlorination process was responsible for the linear fluorescence deterioration. The findings imply that these coumarin ionic detectors can be used to detect and quantify hypochlorite species in aqueous systems (Starzak *et al.,* 2019).

Bekhradnia and coworkers described a coumarin fluorescent probe based on a nitro-3-carboxamide derivative for selective Cu^{2+} ions detection. At a wavelength of 320 nm, the compound displayed the greatest emission intensity in Cu^{2+} ions compared to a range of hazardous and heavy metal ions (Bekhradnia *et al.,* 2016).

In 2018, He and coworkers explored another technique for the specific detection of copper (II) ions, basing the fluorescent sensor on a coumarin-Schiff base derivative. In the presence of numerous other ions, this probe proved to be especially selective for Cu^{2+} ions (He *et al.,* 2019).

Saravana together with his research team developed BENZEPYR, a coumarin hydrazine-based fluorescent probe for the detection of Cu^{2+} ions based on a condensation process. This chemosensor recognizes Cu^{2+} among other bothersome metal ions, leading in a strong response and a noticeable colorimetric shift.

Furthermore, the limit of detection (LOD) was determined to be 40 nM (Annunziata *et al.,* 2020).

2.7.8 Photophysical properties of Coumarins

Despite the fact that the basic coumarin has no or very weak fluorescence, a large number of appropriately substituted coumarin derivatives have sufficient fluorescence in the visible range. Since the 1980s, researchers have been working on coumarin sensors in order to achieve ahigh fluoresence efficiency at the desired frequency. The photophysical characteristics of coumarin-based dyes have been widely studied in order to better understand and improve them. Due to their high fluorescent quantum yields (Chen *et al.,* 2017), adjustable emission frequencies (Avhad *et al.,* 2018), and responsiveness to the polarity effects (Islam *et al.,* 2021) in their microsurroundings, several coumarin dyes have been synthesized as active components in optical brighteners (Ingalagondi *et al.,* 2019), dispersed fluorescence dyes (Atta-Eyison, 2020) and laserdyes (Abdel-Mottaleb *et al.,* 2018).

Hundreds of coumarins classified as laser dyes still are commercially available, despite the fact that most of the dye lasers documented have never been utilized. The photophysical characteristics of fluorescent coumarins have been studied extensively in the past, revealing key structure-property correlations that have aided in the development of fluorescent chemosensors. The coumarin group was substituted, resulting in hypsochromic or bathochromic shift in fluorescence. Red shifted emission is caused by EDGs in the 6th or 7th positions (Godugu *et al.,* 2020) or EWGs in the 3rd or 4th position (Pajk *et al.,* 2020). The substitution sequence of the amine group has a

significant impact on the fluorescence quantum yield of 7-aminocoumarins (Kitamura *et al.,* 2007).

The development of a model for these coumarins' non-radiative decay was made possible by measuring their fluorescence quantum yield and lifetimes in solvents with a wide range of polarity. It was suggested that a planar emissive ICT excited state corresponds to a nonfluorescent TICT state (Senthilkumar, 2004), resonance develops for the two geometries, and consequently avoiding this twisting mechanism enhances the fluorescence quantum yield by a significant amount. A push-pull effect occurs via a rigid planar arrangement with charge-separated excited configurations, resulting in outstanding fluorescence emission characteristics (Zhu *et al.,* 2015). As a result, structural limitation boosts fluorescence quantum yields significantly. After the ICT-TICT interconversion, the activity of these polar excited-state compounds has drawn a lot of interest and is widely recognized (Nad *et al.,* 2003).

2.8   Coumarin Fluorescent probes and dyes

Fluorescent dyes are critical for studying molecular interactions and are extensively utilized as investigative probes in biomedical aswell as environmental sciences. The highest absorption wavelength of typical coumarin dyes is in the UV-Vis range. Absorption of the high energy range can induce autofluorescence as well as photo-damage in tissue imaging. As a result of their pi-extended characteristic, benzocoumarins are predicted to alleviate the difficulties associated with tissue fuorescence imaging. Benzocoumarins with favorable characteristics would be more photostable than π-extended coumarins extended by sp^2 hybridised carbon systems.

Coumarins act as dipolar dyes when they have electron-donating groups in the proper substitution point (Cao *et al.,* 2019).

The coumarin moiety can be combined with other functional receptors to create coumarin-derived fluorescent chemosensors. Because of the increased charge transfer character arising from this substitution pattern, an amino group or hydroxyl at the 7th position and acetyl moiety at the 3rd position is frequently used as the desirable fluorophore scaffold. Because of quenching effects like the photoinduced electron transfer (PET) process, isomerization, as well as other factors, certain chemosensors are weaker fluorophores. Such quenching effects are reduced upon interactions with a range of different analytes and a bright fluorescence is later restored. Different chemosensors in the chemodosimeter category associated with chemical bond breakage, which releases a highly fluorescent molecule, or the formation of new chemical bonds, which causes wavelength shifts (Cao *et al.,* 2019)..

2.8.1   Two-photon (TP) probes based on benzocoumarins and their analogues.

When compared to coumarins, the molecular architectures of π-extended benzocoumarins are predicted to give greater two-photon absorption capacity with a red shift in both excitation and emission. As two photon dyes, benzo-coumarins are of special relevance due to the predicted photochemical stability, in addition to the other benefits stated above. Moreover, some few instances show that benzocoumarin dyes have the ability to be two-photon absorbent materials for applications in bio-imaging (Cao *et al.,* 2019).

2.8.2 Photo-caging benzocoumarins

One of the intriguing uses of benzocoumarin compounds is as a photocaging device. A compound of biological relevance is "caged" by covalently attaching a photo-labile caging group to a reactive group of the compound. This caged compound remains inert until exposed to light, in a biological environment (Cao *et al.,* 2019).

Coumarins, especially 4-hydroxymethyl derivatives, have been shown to photolyze. A number of biomolecules of importance have been presented as a result of this finding; most notably as acyl derivatives that can be liberated in biological systems when exposed to UV light (Cao *et al.,* 2019).
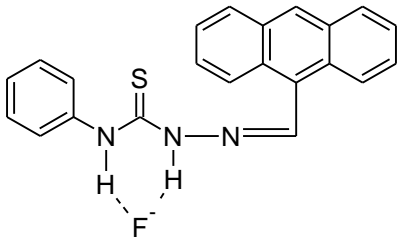
2.8.3 Electron and energy transfer

A wide range of coumarins have been employed in the fabrication of artificial light capturing devices. Gryko and colleagues coated corrole, a carbon short equivalent of porphyrin, with ethynyl-biscoumarins. The corrole-coumarin dyads were created via condensation of dipyrromethane and an aldehyde having protective acetylene functionality, accompanied by oxidation by DDQ. Ultra-violet light excitation of the dyad resulted in total quenching of the coumarin fluorescence, but the corrole luminescence was still equal to that of an optical corrole solution ussed as a reference. This demonstrated an excellent (almost 100 percent) energy transfer from coumarin to the corrole subunit, which was confirmed by time-dependent fluorescence experiments (Gryko, 2002).

2.9   Synthetic Fluoride Sensors

2.9.1   Anthracene Floride sensors

Anthracene is a class of aromatic hydrocarbons made up of three merged rings of benzene whose derivatives are well-known fluorophores due to their luminescence properties and stability. Anthracene is a basic and easy-to-make chromogenic fluoride sensor based on thiourea substituents that performs both as a linking and a signalling component (Udhayakumari *et al.,* 2015). These sensors have a strong selectivity and an excellent limit of detection (LOD) of about 8μM. An example of Anthracene fluoride sensor and its limit of detection is shown in table 2.5.

Table 2.5: Structure of Anthracene fluoride sensor based on hydrogen bonding
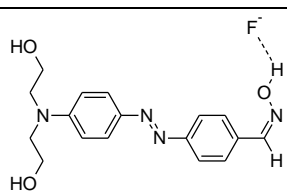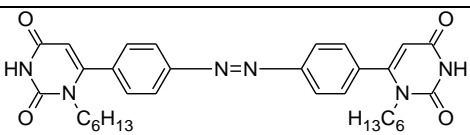
Sensor structure	Mechanism	Limit of Detection (LOD) (F^-)	Reference
	Hydrogen bonding	8μM	(Udhayakumari *et al.,* 2015)

Deprotonation of –NH bonds results in the presence of fluoride ions forming hydrogen-fluoride composite associated with the visible color alteration (Udhayakumari, 2020).

2.9.2 Azo Floride ion sensor

Azo as a functional group is a chromophore. The alkyl groups in azo compounds may either be aromatic or aliphatic. The alkyls often stabilize the azo group as an extended delocalized system. Azo compounds show intense ICT in the visible region. This makes them ideal for colorimetric chemosensors (Sivamani & Siva, 2017). The acidic hydrogen in carboxylic acid group interacts with fluorides through hydrogen bonding. The limit of detection of these sensors range between 0.1 μM to 10 μM [F$^-$] (Balamurugan & Lee, 2015; Sivamani & Siva, 2017; Arabahmadi, 2019). The structures of Azo fluoride sensors and their limits of detection is shown in table 2.6.

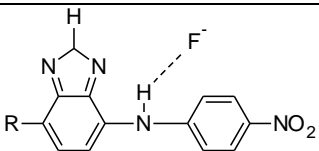**Table 2.6: Structure of Azo fluoride sensor based on hydrogen bonding**
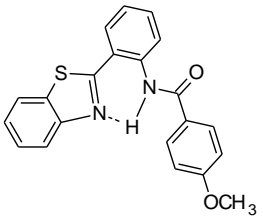
Sensor structure	Mechanism	Limit of Detection (LOD) (F$^-$)	Reference
	Hydrogen bonding	0.1 μM	(Balamurugan & Lee, 2015)
	Hydrogen bonding	3.95 μM	(Sivamani & Siva, 2017)

2.9.3   Benzothiazole Fluoride sensors

Benzothiazoles are thiazole containing fused heterocyclic rings. Benzothiazole derivatives are fluorophores widely used in photoelectrical materials (Guan *et al.,* 2019).

These types of fluorophores demonstrate intense fluorescence with a large molar extinction coefficient and excellent stability. Benzothiazole receptor is a selective reversible fluoride sensor over other anions. Sensitivity of benzothiazole based fluoride sensors depends on the aromatic π-π^* electronic transitions and the azomethine(C=N) n-π^* electronic transitions. The addition of F^- to these probes, leads to a shift in the absorption band to a new intense band at lower frequencies. The strong hydrogen bonding interaction deprotonates the amidic proton leading to enhanced π delocalization, which reduces the frequency in the π - π^* electronic transition. The variation in the limit of detection of these sensors is large (Wu *et al.,* 2016)**.** The structures of Benzothiazole fluoride sensors and their limits of detection are shown in table 2.7.
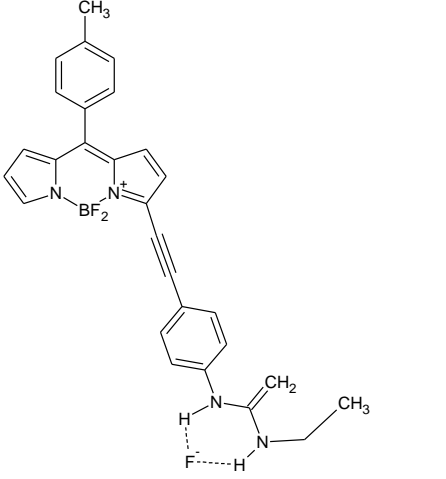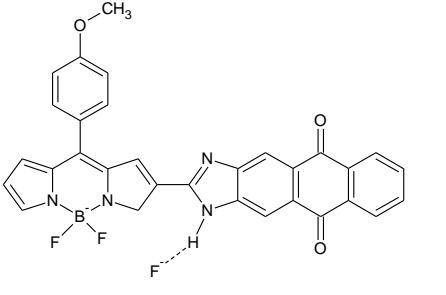
Table 2.7: Structure of Benzothiazole fluoride sensor based on hydrogen bonding

Sensor structure	Mechanism	Limit of Detection (LOD) (F$^-$)	Reference
	Hydrogen bonding	0.86 µM	(Wu *et al.*, 2016)
	Hydrogen bonding	87µM	(Dhaka *et al.*, 2016)

2.9.4   Boron dipyrromethenes (BODIPY) Fluoride sensors

BODIPYs fluorophores have wavelength constricted but relatively intense fluorescence in addition to high quantum yields and stability. This is because of their low chemical reactivity. When linked with a urea group, BODIPY receptor can sense fluoride ions even in the presence of other anions at very low F$^-$concentrations through a bathochromic shifted band. The addition of fluoride ions into the receptor induces ICT (Dixit & Agarwal, 2017). Table 2.8 presents structure of selected BODIPY fluoride sensors based on hydrogen bonding.
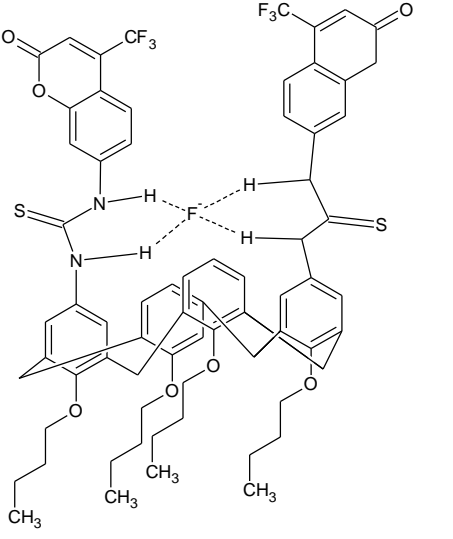
Table 2.8: Structure of BODIPY fluoride sensor based on hydrogen bonding

Sensor structure	Mechanism	Limit of Detection (LOD) (F⁻)	Reference
	Hydrogen bonding	0.74 μM	(Liu *et al.,* 2015)
	Hydrogen bonding	4.39 μM	(Dixit & Agarwal, 2017)

2.9.5   Arene Fluoride sensors

Supramolecular networks founded on arenes (Calixarenes/thiacalixarenes) are appropriate for the development of molecular receptors. When different receptors capable of sensing F⁻ are added into the substrates, the arene structure takes on an advanced layout of electronic systems. A calixarene receptor linked with coumarin and thiourea in the presence of F⁻ shows a detection limit of about 3.5 μM both as colorimetric and fluorescent probes. The colorless receptor red shifts in the presence of visible light but quenches under the ultra-violet frequencies (Wang *et al.,* 2017). Table 2.9 presents structure of selected arene-based fluoride sensor and the modes of action.

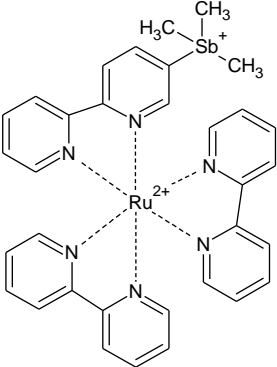**Table 2.9: Structure of Arenes fluoride sensor based on hydrogen bonding**
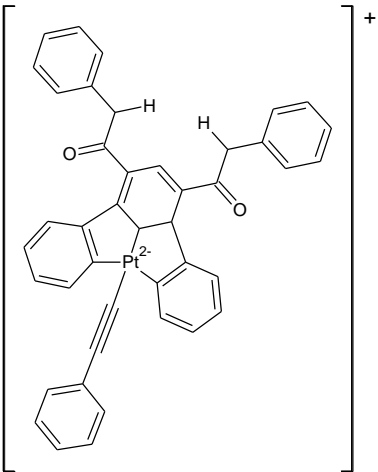
Sensor structure	Mechanism	Limit of Detection (LOD) (F⁻)	Reference
	Hydrogen bonding	3.5 μM	(Li *et al.,* 2018)

2.9.6 Complex based Fluoride probes

Coordination compounds based on Schiff bases are effective fluoride probes. The receptor is set free from the M-complex in the presence of fluorides. This leads to colour change based upon metal-centred transitions (Christianson & Gabbaï, 2017). Table 2.10 presents a sample of Complex fluoride sensor and its mode of action.
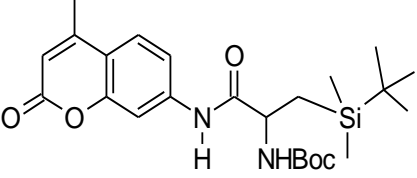
Table 2.10: Structure of Complex fluoride sensor

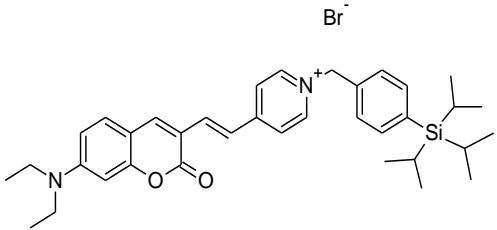| Sensor structure	Mechanism	Limit of Detection (LOD) (F$^-$)	Reference
	Lewis Acid-base interraction	7.28 μM	(Christianson & Gabbaï, 2017)
	Hydrogen bonding	5.75 μM	(Yeung *et al.,* 2014)

2.9.7 Coumarin fluoride sensors

Coumarin receptors are useful in the development of an array of optical and fluorescent sensors. This is due to the fact that they are biologically compatible and have beneficial photoexcitation properties such as massive change in stoke shift (Singhal & Jha, 2019). These sensors apply different mechanisms for sensing fluorides; ICT (Shen *et al.,* 2018) and PET (Gonçalves *et al.,* 2016) among others. Table 2.11 presents structures of selected Coumarin fluoride sensors.

Table 2.11: Structure of Coumarin fluoride sensors
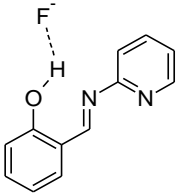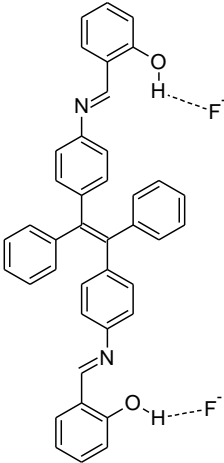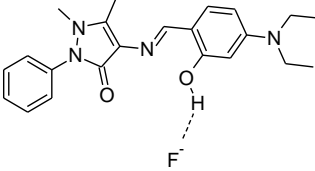
Sensor structure	Mechanism	Limit of Detection (LOD) (F⁻)	Reference
	ICT	12 nM	(Shen *et al.*, 2018)
	PET	33 μM	(Gonçalves *et al.*, 2016)

There are a few types of chemosensors for F⁻ ion based on coumarin derivatives: hydrogen bond reactions, Metal ion displacement processes, silicon-oxygen bond breaking, and F⁻ ion intitiated silicon-oxygen bond breaking.

2.9.8 Schiff base fluoride sensors

Schiff bases (azomethines or imine) are reasonably stable sensors with intense colour emissions. They are easy to synthesize as per the requisite as selective anion sensors (Ghosh, *et al.,* 2016). These sensors use different mechanisms to detect fluoride ions such as ESIPT (Alam *et al.,* 2016) and hydrogen bonding (Sen *et al.,* 2017). Table 2.12 present structures of selected Schiff base fluoride sensors.
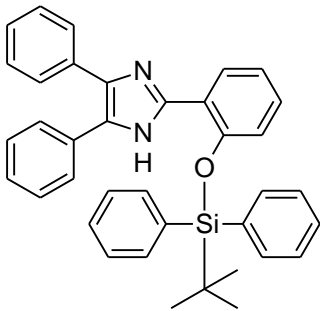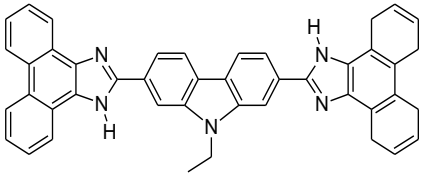
Table 2.12: Structure of Schiff base fluoride sensors

Sensor structure	Mechanism	Limit of Detection (LOD) (F^-)	Reference
	ESIPT	14.0 pM	(Alam *et al.,* 2016)
	Hydrogen bonding & ESIPT	0.5 μM	(Sen *et al.,* 2017)
	Hydrogen bonding	12 μM	(Na *et al.,* 2015)

2.9.9 Imidazole based Fluoride sensor

Imidazole fluorescence properties make its derivatives easy to be applied in fluorescence detection as it easily forms bonds with other anions capable of hydrogen bonding. The nitrogen atoms in the ring exhibit high quantum efficiency as well as outstanding electronic transitions (Udhayakumari, 2020). As an optical sensor, imidazole determines the presence of fluoride anions by ESIPT (Jayasudha *et al.,* 2016) and ICT (Beneto & Siva, 2017) mechanisms among others. The structures of Imidazole fluoride sensors and their limits of detection are shown in table 2.13.
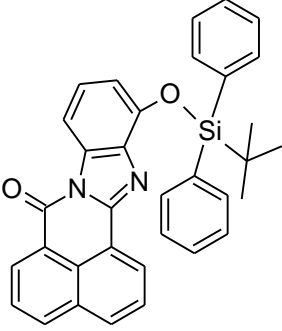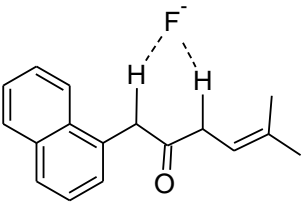
Table 2.13: Structure of Imidazole fluoride sensors

Sensor structure	Mechanism	Limit of Detection (LOD) (F$^-$)	Reference
	ESIPT	1.2 μM	(Jayasudha *et al.,* 2016)
	ICT	2.8 μM	(Beneto & Siva, 2017)

2.9.10 Naphthalene fluoride sensors

Naphthalene receptors have already been synthesized and they usually display outstanding fluorescence and robust chemical and heat stability. Their derivatives sense fluorides through a variety of mechanisms notable desilylation (Li *et al.,* 2017) and excited state proton transfer (Basheer *et al.,* 2017). Table 2.14 shows two of the already synthesized Naphthalene fluoride sensors with their limits of detection and mechanism of detection.

Table 2.14: Structure of Naphthalene fluoride sensors

Sensor structure	Mechanism	Limit of Detection (LOD) (F$^-$)	Reference
	Desilylation reaction	3.2 nM	(Li *et al.,* 2017)
	ESIPT	12.8 μM	(Basheer *et al.,*2017)

2.9.11 Naphthalimide based F- ion sensor

As synthetic fluoride probes, derivatives of naphthalimide are excellent and extremely flexible. This is due to their chemical stability, complemented by a significant stokes shift and a high quantum yield. These compounds, considered as macrocycles with two donor groups detect F$^-$ even in the presence of other anions and at very low concentrations (Chen *et al.,* 2017). Table 2.15 shows two of the already synthesized Naphthalimide fluoride sensors with their limits of detection and mechanism of detection.

Table 2.15: Structure of Naphthalimide fluoride sensors

Sensor structure	Mechanism	Limit of Detection (LOD) (F$^-$)	Reference
	PET	0.55 μM	(Fu *et al.,* 2017)
	Desilylation reaction	5.27 μM	(Yuan *et al.,* 2017)

2.9.12 Diketopyrrolopyrrole fluoride sensors

Diketopyrrolopyrrole pigments are good electron-deficient groups. They can be used to synthesize receptors for molecular recognition. In the presence of fluorides, diketopyrrolopyrrole derivatives undergo a colour change as a result of the ICT channel.

Table 2.16: Structure of diketopyrrolopyrrole fluoride sensors

Sensor structure	Mechanism	Limit of Detection (LOD) (F$^-$)	Reference
	ICT	0.15 μM	(Tao *et al.,* 2019)
	Hydrogen bonding and PET	10 nM	(Zhang *et al.,* 2018)
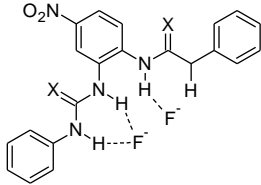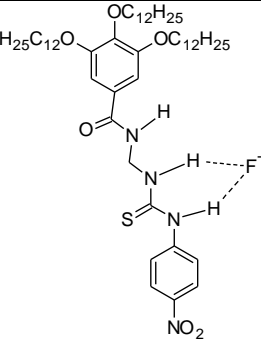
Their fluorescence off-on mechanism involves ICT and PET process among other mechanisms between Sp^2 and Sp^3 hybrid systems in boron (Tao *et al.,* 2019). Table 16 shows two of the already synthesized diketopyrrolopyrrole fluoride sensors with their
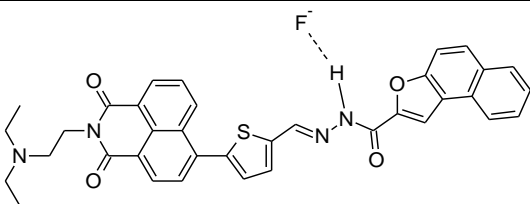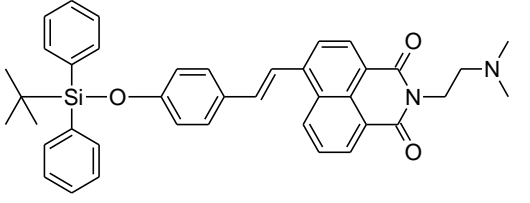
limits of detection and mechanism of detection. Table 2.16 shows the structure of selected diketopyrrolopyrrole fluoride sensors and their limits of detection and mechanism of detection.

2.9.13 Urea based Fluoride sensors

Table 2.17 shows two of the already synthesized Urea fluoride sensors and their limits of detection and mechanism of detection.

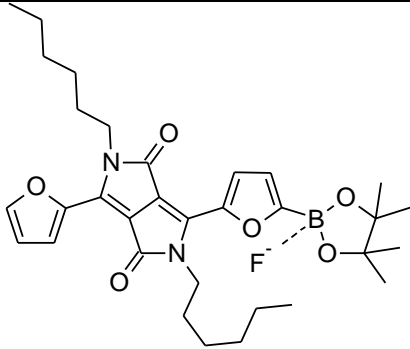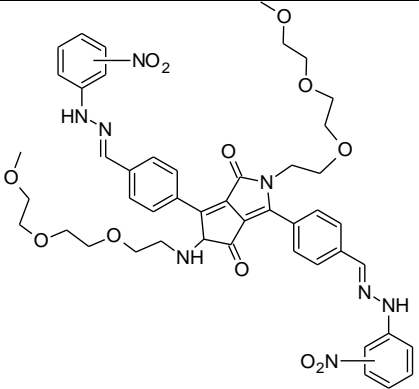**Table 2.17: Structure of Urea fluoride sensors**

Sensor structure	Mechanism	Limit of Detection (LOD) (F^-)	Reference
	Hydrogen bonding	3.1 μM	(Saikia *et al.,* 2016)
	Hydrogen bonding	5.09 μM	(Cao *et al.,* 2018)
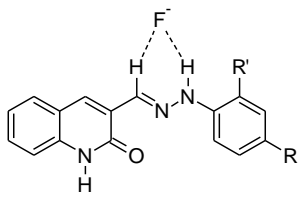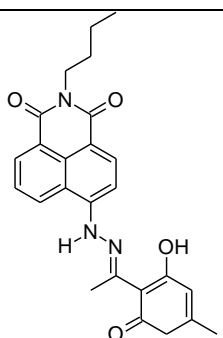
The presence of nitrogen in Urea/thiourea makes them excellent hydrogen bond donors. This makes them excellent candidates for synthesis of receptors for the discriminatory detection of a number of anions. A fluoride acts as a go-between in breaking the Si-O

bonds upon addition. This culminates in the creation of a new compound signalled by colour change (Udhayakumari, 2020).

2.9.14 Hydrazone based Fluoride sensors

Hydrazones, a subclass of imines, are widely used in the synthesis of fluoride sensors capable of distinguishing fluorides even in the existence of many other anions. Hydrazone-based receptors are synthesized through a basic condensation technique (Nikolaeva *et al.,* 2016). Table 2.18 shows two of the already synthesized Hydrazone fluoride sensors and their limits of detection and mechanism of detection.

Table 2.18: Structure of Hydrazone fluoride sensors

Sensor structure	Mechanism	Limit of Detection (LOD) (F⁻)	Reference
	Hydrogen bonding	1.42 µM	(Saini *et al.,* 2018)
	Hydrogen bonding	0.023 µM	(Dhanunjayarao *et al.,* 2016)

2.10   Novel approaches to anion sensing

There are several instances of anion binding proteins that are inspirational in terms of anion recognition. Kubik and colleagues have analyzed several of these intriguing biological systems from the perspective of organic chemistry principles (Kubik *et al.,* 2005). A comprehensive structural study of the Protein Data Bank (PDB) and the Cambridge Structural Database (CSD) databases, focusing on phosphate recognition in biological systems, was also recently completed. According to the findings of this latter investigation, binding sites consisting of uncharged amino acids are most of the time embedded within the protein structure rather than being exposed to the solvent. These results suggest that placing the binding site in a protected site has great importance in establishing water binding, particularly in the case of weak H-bonding interactions. This might be one of the explanations why relatively few neutral abiotic sensors have been identified to far that succeed in binding with anions only through H-bonding interactions (Hirsch *et al.,* 2007).

The enthalpic contribution to the binding is unavoidably reduced when the two interacting partners, the receptor with its binding site and the anion, are strongly solvated. Despite a developing knowledge of how biological systems execute their tasks, which began with Fisher's explanation of the "lock and key" idea in the late nineteenth century. The synthesis of artificial protein-like specific receptors continues to be a problem. As a result, new techniques must be investigated. In accordance with the ahallenge above, it may be prudent to discover a way to design the receptor's molecular structure in such a manner that the receptor site is, relatively protected from the majority of water molecules (Hirsch *et al.,* 2007).

Li and co-workers examined the thiourea derivative (Figure 2.16), which in MeCN is compatible with everything aforementioned about urea and thiourea derivatives in organic media. The affinity for acetate by the receptor when studied in various H_2O–MeCN mixtures, and based on the available thermodynamic data on anion transfer to acetonitrile from water, it was discovered that the theoretical optimum threshold of one hundred and sixty times decrease in the association constant was only a ten times decrease in practical terms (Li *et al.,* 2010).
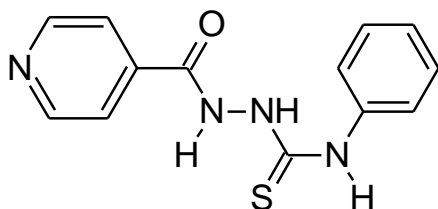
Figure 2.16: MeCN compatible Thiourea derivative

In highly aqueous solutions, the receptor is likely to assume a contractive conformation, creating a hydrophobic microenvironment around the binding site.The greater affinity for acetate is due to the highly guarded microenvironment, while van der Waals interactions seen between $–CH_3$ from $RCOO^-$ and the aromatic systems may also play a role. Jeong's group created the nicely crafted indolocarbazole-based receptor (Figure 2.17), which works on the same basis. In water, the receptor acquires a twisted helical conformation that creates a pocket that is protected from the solvent and has all of the NH binding sites directed inwards (Suk & Jeong, 2008).
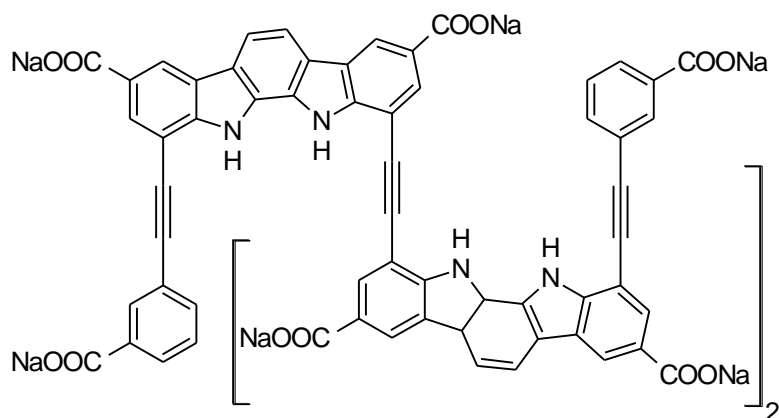
Figure 2.17: Indolocarbazole-based anion receptor (Suk & Jeong, 2008).

The Cl⁻, F⁻, and Br⁻ anions are coupled, with constants ranging from 65 M^{-1} for Cl⁻ to 19 M^{-1} for Br⁻ ion. Considering the low affinities (K = 46 M^{-1}) and lack of F⁻ selectivity, the fact that unfoldable do not bind under the same circumstances suggested that the formation of a guarded microenvironment may lead to F⁻ ion attachment to water by a neutral hydrogen bonding receptor. In addition to their relevance in structural mimicking of natural systems, foldable oligomers can be used to create foldameric receptors with enhanced binding capacities (Gillies *et al.,* 2007).

In heterogeneous environments, similar anion recognition may be accomplished, leading to the world of functional materials.This category includes high-resolution sensor array for anions in water. This team of researchers presented a system made up of a variety of sensor molecules, all of which include pyrrolic hydrogen bond donor atoms and are mixed in a polyurethane crosslinked water insoluble hydrophilic polymer. This method has been demonstrated to be capable of distinguishing fluoride content amongst different common fluoride containing toothpastes. This amazing method, which allows for the actual use of synthetic anion receptors, is made feasible when a fluoride anion penetrating the hydrogel encounters a different environment than the

bulk, resulting in a change in its hydration that makes it even more accessible to bonding (Palacios *et al.,* 2007).

A previously disclosed microporous material produced by the combination of Tb(III) and benzene-1,3,5-tricarboxylate as building block units is another exciting example of a functional material utilized for anion identification. This material has 1D channels through which ligand molecules may be coordinated to Tb(III) metal centers. The introduction of F^- to CH_3OH enhances the photoluminescence intensity. The authors explain this by assuming that the F and Tb(III)-CH_3OH molecules interact. As a result, the system functions as a binding site that accepts F^- in methanol exclusively through hydrogen bonding interactions. This may look odd, but the reason is probably in the specific context in which the attachment occurs. The microporous tunnels provide a safe environment in which a metal-bound ligand (methanol) may compete for a fluoride F^- anion through hydrogen bonding with the far more bulky components. Mesoporous silica, which has nanometer-scale pores of 7.5 nm in diameter, may be appropriately derivatized to produce comparable effects. Chemical processes can sequester the anthraquinone derivative (Figure 2.18), which in acetonitrile does not display any appreciable fluorescence wavelength shift when halides and sulfate are added as TBA salts) (Kim *et al.,* 2008).
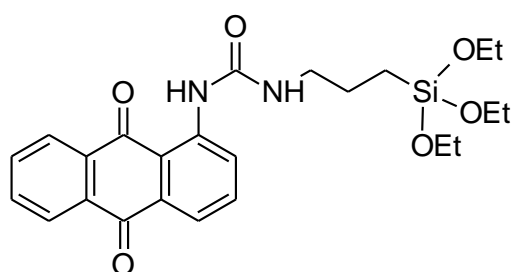
Figure 2.18: Anthraquinone anion sensor

It can detect water soluble anions under these parameters, and it even has considerable selectivity for fluoride anion. The coupling of a receptor component and a shielded environment allows hydrogen bonding interactions to be used to bind fluoride from water. In the past, there has been a lot of interest in low-molecular-weight of any substance capable of forming a gel (gelator) and that can produce stimuli sensitive gel-phase systems. The receptor might be included inside the gel phase, or the gelator molecule can function as the receptor. In DMSO solution and the ethanolic gel phase, the anthraquinone oxalamide organic gelator (Figure 2.19) may preferentially bind fluoride ions (Maeda, 2008).
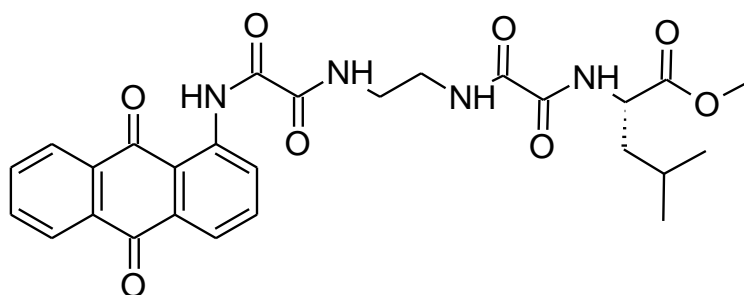
Figure 2.19: Anthraquinone oxalamide organic gelator

The preceding examples demonstrate that, despite their inherent weakness and solvent competition, hydrogen bonding interactions may be successful in polar protic media and in water, if the binding site is located in closed systems. Nothing prevents using this technique when the binding contact is not the same, such as a Lewis acid–base interaction. The uranyl (UO_2^{2+}) center has already been demonstrated to have a significant attraction for Lewis bases as fluoride ions (Cametti *et al.,* 2008).

Nevertheless, the association constant K of about 106 M^{-1} observed in DMSO is significantly decreased in protic solvents such as methanol, where it has been reported to be as low as approximately 300 M^{-1}. If the uranyl complex (Figure 2.20) was water-soluble, it is logical to anticipate it to be of the same order of magnitude if not less) in aqueous solutions. The authors found that the UO_2-complex dissolves in CTABr micelles and that the resulting UO_2-complex-CTABr system attaches itself to fluoride in water with a remarkably high affinity of K ca. 104 M^{-1}. As a result, an aggregate may also be seen as a protective shell that protects around the binding site.
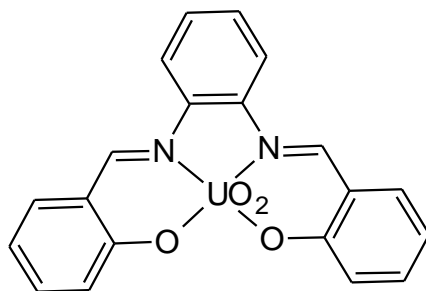
Figure 2.20: Uranyl complex

The UO_2 complex may be thought of as a supramolecular system that fully integrates two different components, the micelle and the receptor. While they do not operate as independent units, their assembly has the greatest fluoride affinity for a neutral receptor in aqueous systems. PRE (paramagnetic relaxation enhancement) and NOESY NMR experiments reveal that Uranyl complex has a preferred geometry inside the micelle, proving that the protected salophen–UO_2 complex is more efficient. This approach may be extended to any other receptors that are insoluble in water but have a high affinity for fluoride in non-aqueous solutions (Cametti *et al.,* 2009).

While these examples come from different fields of study, such as material science, organic and inorganic chemistry, they all show that successful fluoride binding in hypercompetitive media is dependent on the presence of a binding site engrained in a protected micro - environment, which is similar to what happens with biological binding systems, such as proteins. F^- ion is very soluble in water, having a hydration free energy of around 100–110 kcal mol^{-1}. A number of research groups have offered a highly complicated view of fluoride hydration, and it indicates that over least fifteen water molecules in rapid exchange are required to create an inwardly solvated fluoride. The situation can be significantly less complex in the solid form An investigation in the CSD yields valuable information on the solid-state hydration zone of the fluoride anion. There are two X-ray structures of simple tetraalkylammonium fluoride salts with distinct cation–anion pairs and completely hydrated fluoride anion (Cametti *et al.,* 2009).

In both cases, the systemic study indicates a tetrahydrated fluoride anion with very low hydroxyl-fluoride contact distances. The shortest contact, 1.738 Å, equates to a 35% reduction in the sum of the Van der Waals (vdW) radii of the F and H atoms. In one example, the coordination sphere is slightly distorted square planar, whereas in the other, it is deformed tetrahedral (Borah *et al.,* 2016).

The fluoride anion and water have strong interactions, thus it's possible that a receptor that can bind the aqueous fluoride ions while holding onto one or more water molecules in the anion's hydration sphere saves energy. Furthermore, dealing with a hydrated species eliminates the need and associated difficulties for numerous binding sites to concentrate around the tiny bare fluoride. This might also offer you access to novel

structural ideas that haven't been considered before. However, because each water molecule not discharged upon connection may have an entropic effect, an ideal balance should be achieved. A review of the literature on receptor–fluoride complexes in the solid state finds several intriguing cases in which the species actively bonded is hydrated fluoride ions rather than fluoride. A multicharged cryptand, bonds two fluoride ions in the solid state by strong $N^+H\text{-}F^-$ electrostatic hydrogen bonding interactions. The two fluorides share a water molecule, allowing them to remain hydrated. The discovered species F^-—H_2O—F^- is an adduct in which the water molecule serves as a structural unit in the binding process. According to a distance analysis, the NH—F^- and OH—F^- contact distances are short, 1.695 Å and 1.891 Å, respectively, equivalent to a 35 and 30% decrease in total vdW radii. A monohydrated fluoride H_2O—F^- unit is bound by a smaller cryptand counterpart. The anion becomes tetrahedrally coordinated and firmly bound by hydrogen bonding to three NH_2^+ groups and water inside the cavity. Chloride, Sulfate, and acetate ions are further instances of hydrated anion interactions in which a receptor molecule interacts directly with the water molecule (s) (Borah *et al.,* 2016).

Some of these complexes could have been used as examples of how to design water molecules into bond formation. A number of metallic and non-metallic components like the molecular analogues of zeolite act as fluoride cages that fit properly. Although these structures have not been explored for anion identification and their application as such is still speculative, they provide a perfect architectural environment for fluoride encapsulation. Crystal engineering has fast become a key field for the development of functional materials, and it will have an influence on anion identification as well (Rissanen, 2008).

In the presence of an anion, competitive crystallization of single or multiple molecular tectons results in the selective encapsulation of an anion into crystalline material based on its design. Metal organic frameworks (MOFs), which are made up of organized metal–ligand networks, have been proposed as potential possibilities for developing selective anion isolation via straightforward crystallization (Custelcean & Moyer,2007).

The ultimate objective is to counteract the inherent solvation of the selected anion and isolate it selectively into the crystalline solid phase, in a clear liquid/liquid anion partition thermodynamics, which may be qualitatively represented by the empirical lyotropic series. In order to build a system that can bind the desired anion into its created solid-state assembly, the structure, size, and all other unique features of the desired anion must be factored in. Although several cases of MOFs and other non-metallated compounds which prefer a specific anion from a solution by competitive crystallization, no reports of fluoride bonding have been identified, and a bias for lipophilic anions is frequently seen. Interestingly, certain evidences of anti-Hofmeister behavior for the efficient capture of SO_4^{-2} anion have been demonstrated, making this method highly promising (Kim *et al.,* 2010).

The most effective examples of fluoride binding compounds are charged species, such as polyprotonated cryptands, however the low pH required and sluggish exchange dynamics limit their actual use.

CHAPTER THREE

MATERIALS AND METHODS

The techniques of analysis for testing the study's research questions have been explained in this chapter. Every reagent has been described in terms of its source and purity. The analytical procedure and instrumentation has been specified and described. Each compound's design and synthesis method, as well as the reaction mechanisms, have also been illustrated.

3.1   Equipment and Reagents

Magnetic stirrer and magnetic stir bar

Bk-F93 F2000 Fluorospectrophotometer (FS)

MRC-UV-Vis Spectrophotometer-UV-(11S/N; UEB1011006)

GC micromass spectrometer (Micromass, Wythenshawe, Waters, Inc. UK)

Bruker Avance NEO 500 MHz (TXO cryogenic probe) NMR spectrometers

Agilent 400 MHz -DD2 NMR spectrometer

 MestreNova (v14.0.0) software.

UV-lamp (UV303$_D$)

3-cyano-4-methylcoumarin (Sigma-Aldrich 97%)

Imidazole (Sigma-Aldrich 99.5%)

Dichloromethane (DCM) - Sigma-Aldrich 99.8%

Tetrahydrofuran (THF) - Sigma-Aldrich 99.9%

Tert-butyldimethylsilylchloride (TBDMSCl) - Sigma-Aldrich 97%

Tert-butyldimethylsilylchloride (TBDPSCl) - Sigma-Aldrich 97%

Tetra-n-butylammonium fluoride (TBAF) - Sigma-Aldrich 97%

Tetra-n-butylammonium chloride (TBAC) - Sigma-Aldrich 97%

Tetra-n-butylammonium bromide (TBAB) - Sigma-Aldrich 97%

Hydroxylamine hydrochloride ($NH_2OH.HCl$) – AR/ACS 99%

Sodium hydroxide (NaOH) - Sigma-Aldrich Analytical, Puriss

TBAF 1.0 M in THF

HEPES 1 M in H_2O

Cetyltrimethylammonium bromide, (CTAB) - Sigma-Aldrich Calbiochem® 98%

TLC Silica gel 60 F_{254} (Merck, Darmstadt, Germany) on pre-coated Aluminium sheets

Silica gel 60 (230-400 mesh) and G-HR for TLC

3.2   Rational design

Among the three sensing mechanisms described in chapter one, the fluoride induced cleavage of oxygen-silicon bonds stands out as a selective approach for fluoride detection. To increase the response of this system even more, a fluorophore with reasonable quantum yield is needed and more importantly, higher affinity for fluoride. Since fluoride has the highest electronegativity of the halogens, 3-Cyano-7-hydroxy-4-methylcoumarin scaffold was employed as electron deficient conjugated systems with higher quantum yield than quinine sulphate (0.54) towards fluoride sensing.

Based on the ICT mechanism, the synthesis of a 3-Cyano-7-hydroxy-4-methylcoumarin protected by TBDPS/TBDMS was considered. This research anticipated that the cleavage of the TBDPS/TBDMS groups by fluoride would to lead to a swift formation of a fluorescent species. 3-Cyano-7-hydroxy-4-methylcoumarin fluorophore was included as a moiety to promote fluorescence via an ICT mechanism. The response of these compounds in 1 millimole of aqueous tetra-n-butylammonium fluoride (TBAF)

solution in dioxane was investigated. Energy changes in excitation and emissions were observed as TBAF was added to the solutions. This produced a desilylated fluorescent product. With this the relation between the quantities of substances that take part in the reaction between each compound and F⁻ was determined, further demonstrating a recognition method as F⁻ reacts with each of these compounds to generate non-fluorescent TBDPSF/TBDMSF and fluorescent specie(s) O⁻-Aryl. Figure 31 shows athe structures of the sensors designed.
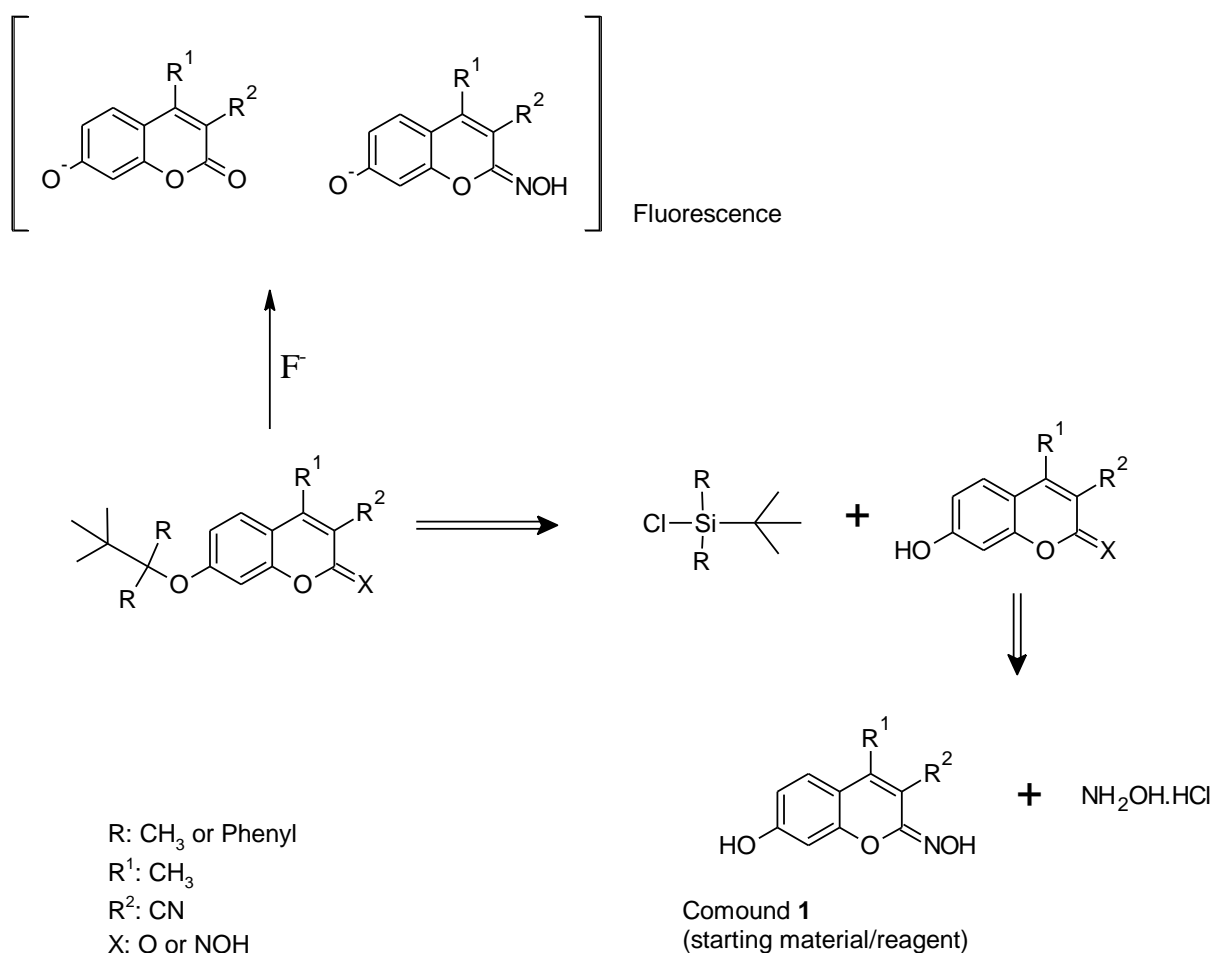

R: CH₃ or Phenyl
R¹: CH₃
R²: CN
X: O or NOH

Comound **1**
(starting material/reagent)

Figure 3.1: structures of the designed compounds (fluoride sensors)

3.3 General Experimental Procedures for Synthesis of fluoride sensors

3.3.1 Synthesis of compound 2: 7-O-tert-butyldimethylsylyl-3-cyano-4-methylcoumarin

3-cyano-4-methylcoumarin (30 g, 0.15 moles) also referred to here as compound **1** and imidazole (20.4g, 0.3 moles) was dissolved in a 600 mL mixture (3:1) of dry dichloromethane (DCM)-Tetrahydrofuran (THF) solvent. This solution was then continuously stirred in an inert atmosphere of N_2 gas until the solution became clear. Tert-butyldimethylsilylylchloride (TBDMS, 22.6 g, 0.15 moles) in 60 mL of dichloromethane was slowly added dropwise for three continuous hours. This process was allowed to take place for an extra 2 hours at room temperature with agitation and in an inert environment.

This was followed by filtration through a short bed celite and washed three times with 600 mL of purified and deionized water, supplemented by 200 mL of aqueous NaCl. The non-polar fraction was then dried by exposure to anhydrous sodium sulphate, filtered and concentrated using a Buchi rotavapour under reduced temperature of below 40°C and below atmospheric pressure to get an unpurified product. Further purification was done by means of column chromatography using DCM:THF as a mobile phase in varying concentrations. The result obtained at this stage was a bright yellow crystalline solid. These crystals were again subjected to further purification through another column using DCM:THF solvent system. This second column purification was done more cautiously, and only the central portions of the three fractions were selected and concentrated following analysis by TLC. Upon concentration and drying under decreased pressure and high vacuum of 5 mbar per 3 minutes at a pressure of 10 mbar for an extended period of time, the product was collected as a bright and shiny yellow

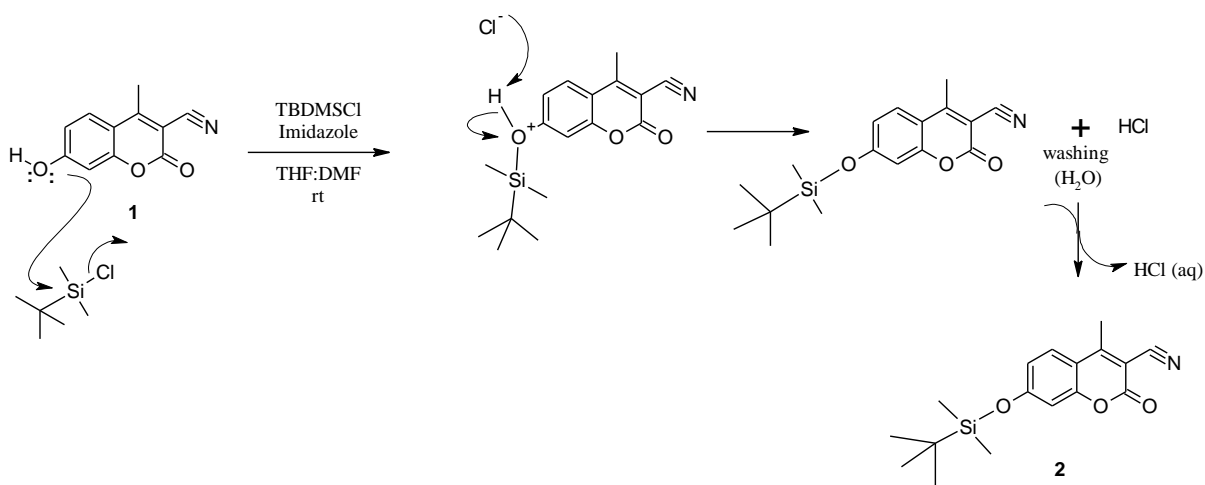solid, 24.67 g (82.24% yield). A scheme of how compound **2** was synthesized is as shown in figure 3.2.

Figure 3.2: Proposed reaction mechanism for the synthesis of compound 2.

3.3.2 Synthesis of compound 3: 7-O-tert-butyldiphenylsylyl-3-cyano-4-methylcoumarin

3-cyano-4-methylcoumarin (30 g, 0.15 moles) also referred to here as compound **1** and imidazole (20.14 g, 0.3 moles) were dissolved in a 600 mL mixture (3:1) of dry dichloromethane (DCM)-Tetrahydrofuran (THF) solvent. This solution was then continuously stirred in an inert atmosphere of N_2 gas until the solution became clear. Tert-butyldimethylsilylchloride (TBDPS, 41.3g, 0.15 moles) solution in 100 mL of dichloromethane was slowly added dropwise over a period of one hour.

The reation process was allowed to take place for an extra 2 hours at room temperature with agitation and in an inert environment. This followed by filtration through a short celite bed and washed three times with 600 mL of purified and de-ionized water, supplemented by 200 mL of aqueous NaCl. The non-polar fraction was then dried by

exposure to anhydrous sodium sulphate, filtered and concentrated using a Buchi rotavapour under reduced temperature and pressure to get an impure product. Further purification was done by means of column chromatography using DCM:THF as a mobile phase in varying concentrations starting from 100 % DCM and slowly varying the polarity by adding 5 mL of THF while serially reducing the volume of DCM by 5 mL upto 100% THF. The result obtained at this stage was a bright yellow crystalline solid. These crystals were again subjected to further purification through another column using DCM : THF solvent system. This second column purification was done more cautiously, and only the central portions of the three fractions were selected and concentrated following analysis by TLC. Upon concentration and drying under decreased pressure and high vacuum for an extended period of time, the product was collected as a bright yellow solid, 52.47 g (79.57% yield). A scheme of how compound **3** was synthesized is as shown in figure 3.3:
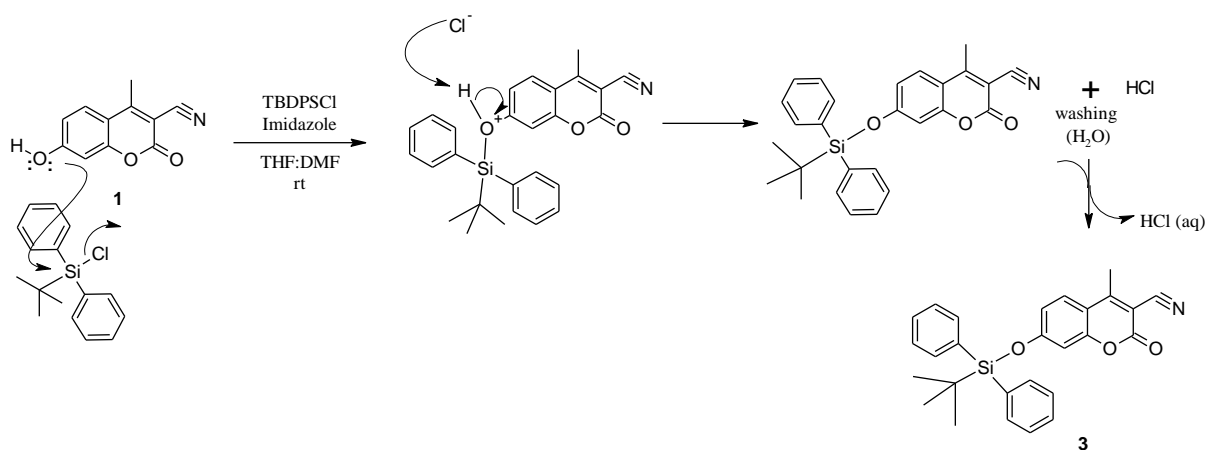

Figure 3.3: Schematic for the synthesis of compounds 3.

3.3.3 Synthesis of compound 4: 7-O-tert-butyldimethylsylyl-2-(hydroxyimino)-4-methyl-2*H*-chromene-3-carbonitrile

6.3 g (0.02 moles) of compound **2** was introduced into a reagent bottle containing 100 mL mixture (3:1) of dry dichloromethane (DCM)-Tetrahydrofuran (THF) solvent, filled with nitrogen gas and closed. A separate solution was made by dissolving 1.4 g (0.02 moles) of hydroxylamine hydrochloride ($NH_2OH.HCl$) in 100 ml distilled and de-ionized water. The solution was stirred with a glass rod until it became clear. 0.8 g (0.02 moles) NaOH in 100 mL of distilled and de-ionized water was then added to this solution and stirred until it became clear. The two solutions were mixed in a reagent bottle and placed on a shaker for 12 hours. The mixture was further filtered using a Whatman filter paper. The non-polar fraction was then dried by exposure to anhydrous sodium sulphate, filtered and concentrated using a Buchi rotavapour under reduced temperature and pressure to get an impure product. Further purification was done by means of impure product.

The compound obtained was a bright yellow crystalline solid. These crystals were again subjected to further purification through another column chromatogarphy using DCM : THF solvent system starting from 100 % DCM and slowly varying the polarity by adding 5 mL of THF while serially reducing the volume of DCM by 5 mL upto 100% THF. This second column purification was done more cautiously, and only the middle portions of the three fractions were selected and concentrated following analysis by TLC.

Upon concentration and drying under decreased pressure and high vacuum for an extended period of time, the product was collected as a bright yellow thread-like solid.

This product was subjected to a further purification by pTLC in a 1:3 DCM:THF solvent mixture. The collected mass was (2.59 g) with a 41.1 % yield. A scheme of how compound **4** was synthesized is as in figure 3.4.
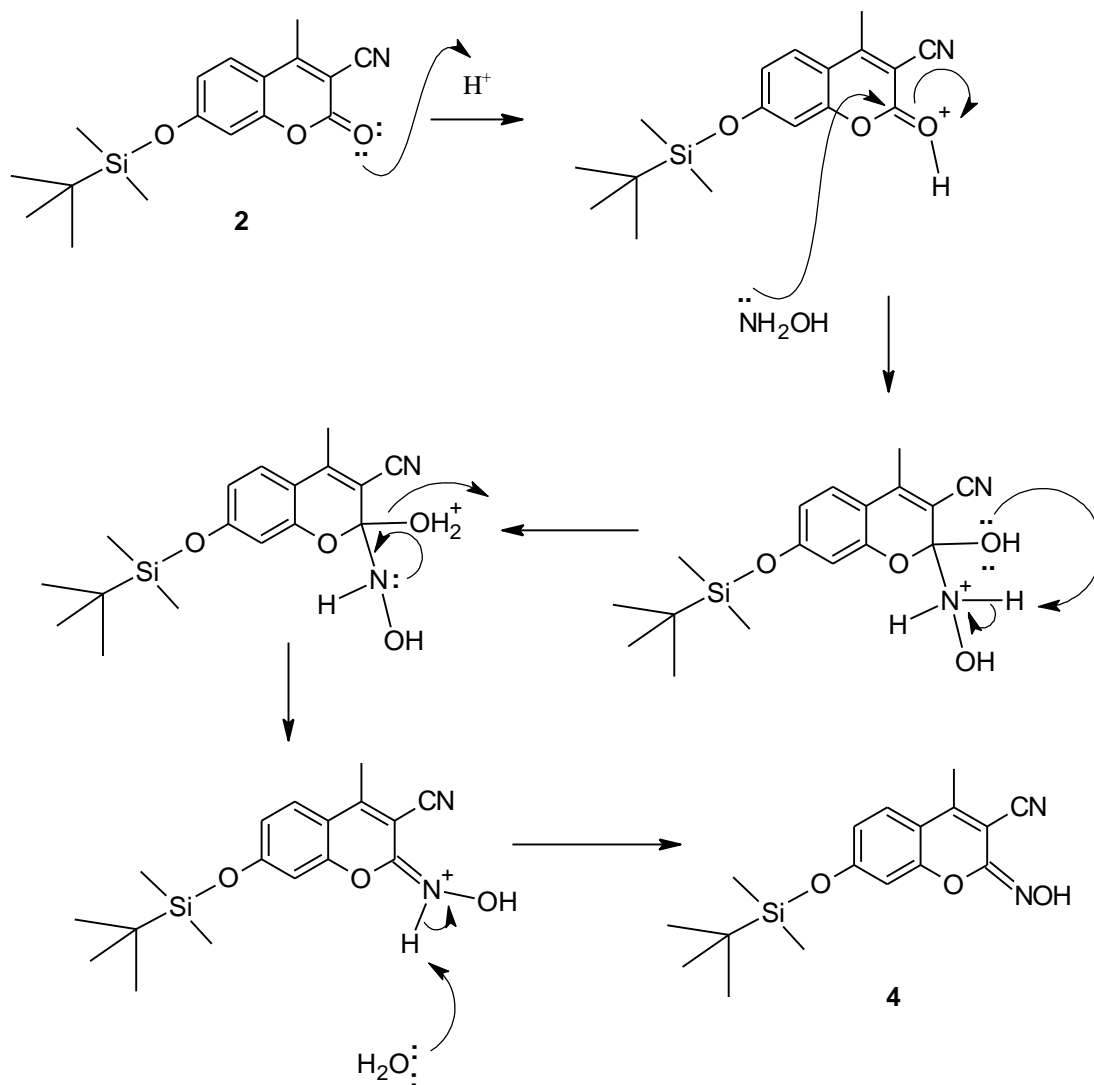

Figure 3.4: Proposed reaction mechanism for the synthesis of compounds 4.

3.4 Physical measurements

3.4.1 Spectroscopic studies

NMR spectra of the synthesized sensors were acquired using a Bruker Avance NEO (TXO cryogenic probe) spectrometer 500 MHz for compounds **1**and **2** while the 400MHz was used for compounds **3** and **4**. The acquired spectra were subjected to processing via the MestreNova software (version 14.0.0). Referencing of both the ^{13}C NMR and ^{1}H NMR chemical shifts was done with internal standard as deuterated solvents; methanol-d_4 with peaks expected at δ_H 3.32 and δ_C 49.00 while the CDCl$_3$ peaks were set at δ_H 7.26 and δ_C 77.16). Assignments were based on proton, carbon-13, spin-spin coupling between neighbouring protons (COSY), an extension of COSY (TOCSY), direct attachment of hydrogen atoms to carbon atoms by analyzing the Heteronuclear Single Quantum Coherence Spectroscopy (HSQC), Heteronuclear Multiple Bond Correlation; correlations between hydrogen atoms and carbon atoms and that are separated by 2, 3...and, sometimes in conjugated systems (HMBC), and cross-correlation between atoms (NOESY) NMR spectra. Chemical shifts were recorded in ppm (δ) downfield from TMS. The *J*-Couplings were recorded in frequencies (Hz). The single diode array and Mass spectra were obtained by means of LC-MS in an ESI. This was linked to an Agilent gradient pump system (1100 series) and a C18 Atlantis T3 column (3.0 × 50 mm, 5 μm), using Milli-Q water-acetonitrile at the ratio of 5:95 to 95:5, with 1 % formic acid and a flow rate of 0.75 mL/min for 7 minutes. Fluorescence measurements were conducted using Biobase-BKF93 Model F2000 fluorospectrometer at room temperature. UV spectra were acquired by UV-(11S/N; UEB1011006) MRC – UV-Vis spectrophotometer. To track the purification processes, thin layer chromatography (TLC) was performed on silica gel 60 F254 on aluminium pre-coated plates. TLC plates were developed using suitable processing solvent systems and

visualized under UV light (below 365 nm) and by charring with 5 % H_2SO_4/H_2O solution. pTLC was done by means of silica Gel G-HR.

3.4.2   Fluoride Testing.

The interaction between the synthesized compound, (**2, 3,** and **4**) and fluoride ions were investigated in dioxane solution through fluorescent analysis. A set of test samples of each of the synthesized compounds were formulated with differing fluoride concentrations ranging from 0.1 to 100 mg/L by dissolving 22.1 mg of TBAF in 1 L of de-ionized (DI) water and diluting to the desired concentration. 1 mL of a 4 percent solution of each of the synthesized compounds contained in dioxane was then added to 40 mL of test samples. These solutions were incubated for 20 minutes at room temperature in 1:1 (v/v) 10 mM HEPES-dioxane mixture maintained at a pH of 7.4. Fluorescence studies in terms of excitation and emission frequencies were done for each of these solutions with three replicates being tested for each compound. Figures 3.5-3.7 show the interaction between the synthesized compound, (**2, 3** and **4**) and fluoride ions in dioxane.
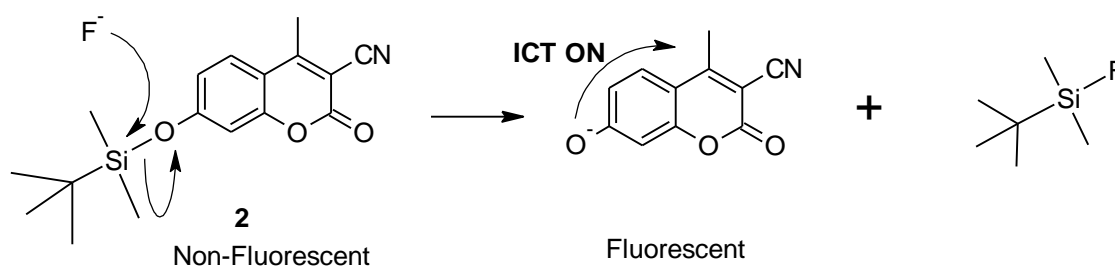

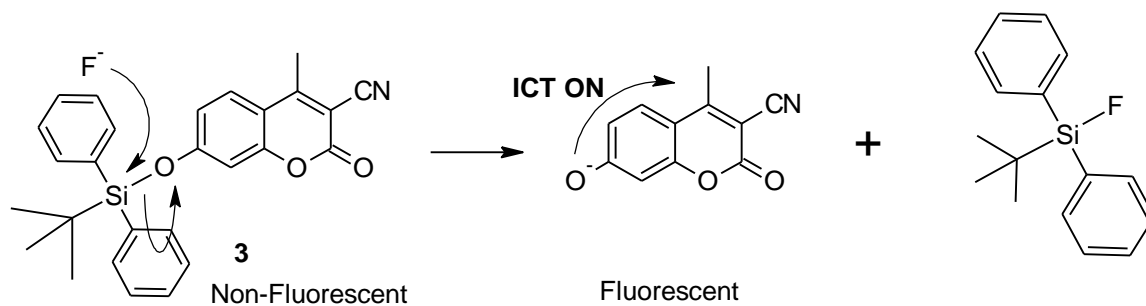**Figure 3.5: ICT initiated by of desilylation of compound 2 by fluoride ions.**

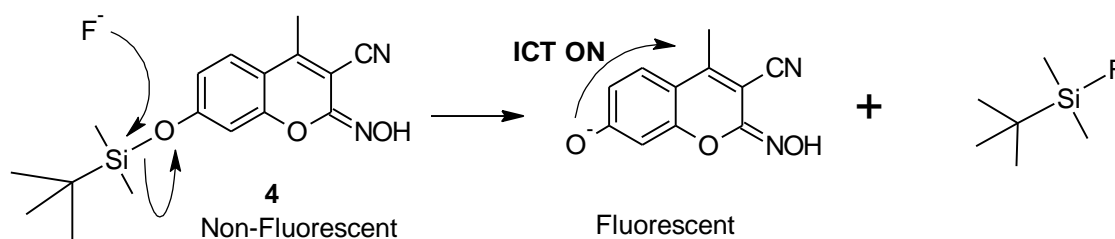**Figure 3.6: ICT initiated by of desilylation of compound 3 by fluoride ions.**

Figure 3.7: ICT initiated by desilylation of compound 4 by fluoride ions.

3.4.3 Selectivity studies

Selectivity studies were done according to a method by (Zhou *et al.,* 2015). Solutions of a number of selected anions; chloride, bromide, iodide, nitrate and sulphate at a concentration of 200 μM were prepared as well as TBAF and NaF (200 μM). The studies were done in a solution of a pH maintained at 7.4 by 1:1 (v/v) 10 mM HEPES : dioxane mixture. A series of test samples of each of the synthesized fluoride sensors (**2**, **3**, and **4**) with [F⁻] ranging from 0.1 to 100 mg/L were made by dissolving 22.1mg (TBAF) in 1 L of distilled and de-ionized water and diluted as per the selected concentrations. 1 mL of a 4 percent solution of each of the synthesized compounds contained in dioxane was then added to 40 mL of test samples. These solutions were incubated for 20 minutes at room temperature in 1:1 (v/v) 10 mM HEPES-dioxane mixture maintained at a pH of 7.4. Fluorescence studies in terms of excitation and

emission frequencies were done for each of these solutions with three replicates of each of the synthesized compounds **2**, **3** and **4** being tested.

3.4.4 Molar Extinction Coefficients Determination (MEC).

The Molar Extinction Coefficients were determined according to a method by (Zhou *et al.,* 2015). Solutions of compounds **2, 3** and **4** with varied concentrations (0, 10, 20, 40, 80 and 160 μM) were made by serial dilution. The absorbance of each of these solutions was measured after being allowed to react for 5 minutes. A plot of linear correlation between the absorbance and the concentrations was used to resolve the MEC.

3.4.5 Quantum Yield Measurements.

Quantum Yield Measurements were done according to the method described by (Nawara & Waluk, 2019). A series of concentrations (0.02, 0.04, 0.06, 0.08 and 0.10 mg/L) of each of the synthesized sensors and standard were separately made. Both absorbance and emission spectra for each sensor and standard were recorded. Compounds **2**, **3** and **4** and standard intensity fluorescence was integrated (that is, the area under the fluorescence spectrum). Linear plots of integrated intensity of fluorescence and absorbance for each of the compounds **2**, **3** and **4** were made. This resulted into a linear graph with intercept = **0** and whose gradients **m**, were equated to the quantum yield for each compounds **2**, **3** and **4**.

The fluorescence quantum yields ($\Phi_{2, 3, 4}$) of the synthesized fluoride sensors (**2, 3** and **4**) + **F-** were determined using equation 3.1.

$$\Phi_X = \Phi_{ST} \left(\frac{Grad_x}{Grad_{ST}}\right)\left(\frac{\eta_x^2}{\eta_{ST}^2}\right) \dots\dots\dots\dots\dots\text{equation (3.1)}$$

Where Φ = quantum yield

η = refractive index of the solvent.

$Grad_X$ = compound gradient.

$Grad_{ST}$ = standard gradient.

The low concentrations with Absorbance ≤ 0.05 were used throughout the fluorescence emission studies. This was to prevent self-quenching. The emission intensities for each of the compounds **2, 3** and **4** were recorded at their excitation wavelengths. The standard used for this study was Quinine sulphate dihydrate in 0.1M perchloric acid (Nawara & Waluk, 2019). The Φ of this standard was 0.54 at an excitation and emission of 310 nm and 455 nm respectively. The Φ was calculated by measuring the absorbance at 455 nm as described by Nawara and Waluk, 2019. A plot of absorbance against the area for each of the test compounds **2**, **3** and **4** was evaluated against that of the standard quinine sulphate. This data was used to calculate the quantum yield.

3.4.6 Rate Constant Determination

A method described by Zhou *et al.,* 2015 was used to determine the rate constants. 20 μM of each of the compounds **2, 3** and **4** (fluoride sensors) in a 1:1 (v/v) of 10 mM HEPES as a buffer maintaining the pH at 7.4) and dioxane as a solvent was introduced into 200, 400, 600, 800, 1000 μM of NaF solutions. A plot of fluorescence intensity with increase in time was made. The rates of reactions for each of the compounds **2, 3** and **4** were obtained for each concentration above by using equation (3.2).

$$\text{Fluorescence} = 1 - \exp(-k_{obs}t) \quad ....\text{equation (3.2)}$$

Where; **t** = time in minutes.

k_{obs}, = pseudo-first-order rate constant

A plot of k_{obs} against fluoride concentration was used to calculate the second-order rate constant equation (3.3).

$$k_{obs} = k_2[NaF] \text{...equation (3.3)}$$

Where; k_2 = second-order rate constant.

3.4.7   Paper disc Tests.

Paper discs were made by cutting Whatman filter paper (20 μm) into discs using a paper punch. The discs were immersed into a 1:3 mixture of dichloromethane (DCM): Tetrahydrofuran (THF) solution containing varied concentrations (100 μM, 80 μM, 60 μM, 40 μM and 20 μM of each of the synthesized fluoride sensors (**2, 3** and **4)** and dried in air. A blank was also prepared and taken through the same process. The pre-treated discs were immersed into an un-buffered distilled and de-ionised aqueous solution containing two millimolar cetyltrimethylammoniumbromide, (CTAB) for ten seconds and exposed to dry for five minutes. Images of emission intensity from the treated discs were taken as the discs were illuminated by a handheld UV-lamp (UV303$_D$) below 365 nm.

CHAPTER FOUR

RESULTS

In this chapter the findings of this study has been described. Where appropriate use chemical structures tables, graphs and charts have been used to support the presentation of these results.

4.1   Rational Design

The fluoride induced oxygen-silicon bond cleavage was selected as most selective approach for aqueous fluoride detection based on ICT mechanism. Figure 3.1 show the structures of the sensors designed.

4.2   Structural elucidation

4.2.1   Compound 1

The spectral analysis on compound **1** was done by acquiring the following; Proton Nuclear Magnetic Resonance (^{1}H NMR) - Appendix I, C-13 Nuclear Magnetic Resonance (^{13}C NMR) **-** Appendix II, Correlation spectroscopy (COSY) **-** Appendix III, Heteronuclear Single Quantum Coherence Spectroscopy (HSQC) **-** Appendix IV, Heteronuclear Multiple Bond Correlation (HMBC) **-** Appendix V, Total Correlation Spectroscopy (TOCSY) - Appendix VI, Nuclear Overhauser Effect Spectroscopy (NOESY) - Appendix VII, Diode Array chromatograph - Appendix VIII and Mass spectrum- Appendix IX.

4.2.2   Compound 2

The spectral analysis on compound **2** was done by acquiring the following; Proton Nuclear Magnetic Resonance (^{1}H NMR) - Appendix X, C-13 Nuclear Magnetic

Resonance (^{13}C NMR) **-** Appendix XI, Correlation spectroscopy (COSY) **-** Appendix XII, Heteronuclear Single Quantum Coherence Spectroscopy (HSQC) **-** Appendix XIII, Heteronuclear Multiple Bond Correlation (HMBC) **-** Appendix XIV, Total Correlation Spectroscopy (TOCSY) - Appendix XV, Nuclear Overhauser Effect Spectroscopy (NOESY) - Appendix XVI, Diode Array chromatograph - Appendix XVII and Mass spectrum- Appendix -XVIII.

4.2.3   Compound 3

The spectral analysis on compound **3** was done by acquiring the following; Proton Nuclear Magnetic Resonance (^{1}H NMR) - Appendix XIX, C-13 Nuclear Magnetic Resonance (^{13}C NMR) **-** Appendix XX, Correlation spectroscopy (COSY) **-** Appendix XXI, Heteronuclear Single Quantum Coherence Spectroscopy (HSQC) **-** Appendix XIII, Heteronuclear Multiple Bond Correlation (HMBC) **-** Appendix XXII, Diode Array chromatograph - Appendix XXIII and Mass spectrum- Appendix -XXIV.

4.2.4   Compound 4

The spectral analysis on compound **4** was done by acquiring the following; Proton Nuclear Magnetic Resonance (^{1}H NMR) - Appendix XXV, C-13 Nuclear Magnetic Resonance (^{13}C NMR) **-** Appendix XXVI, Correlation spectroscopy (COSY) **-** Appendix XXVII, Heteronuclear Single Quantum Coherence Spectroscopy (HSQC) **-** Appendix XXVIII, Heteronuclear Multiple Bond Correlation (HMBC) **-** Appendix XXIX, Diode Array chromatograph - Appendix XXX and Mass spectrum- Appendix -XXXI.

4.3 Excitation and Emission

4.3.1 Compound 2

The absorption and emission spectra of compound **2** (200 μM) in fluoride free solution
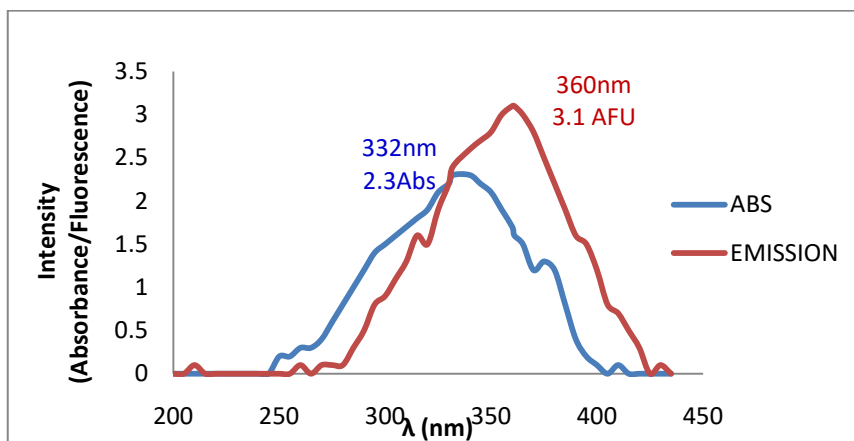is given in figure 4.1.

**Figure 4.1. Absorption and Emission spectra of compound 2 (200 μM) in F⁻ free
solution.**

4.3.2 Compound 3

The absorption and emission spectra of compound **3** (200 μM) in fluoride free solution
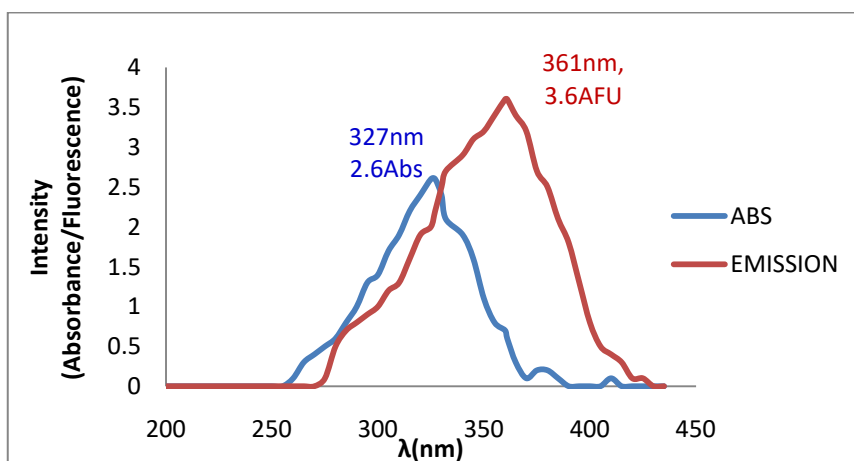is given in figure 4.2.

**Figure 4.2: Absorption and Emission spectra of compound 3 (200 μM) in F⁻ free
solution.**

4.3.3 Compound 4

The absorption and emission spectra of compound **4** (200 μM) in fluoride free solution

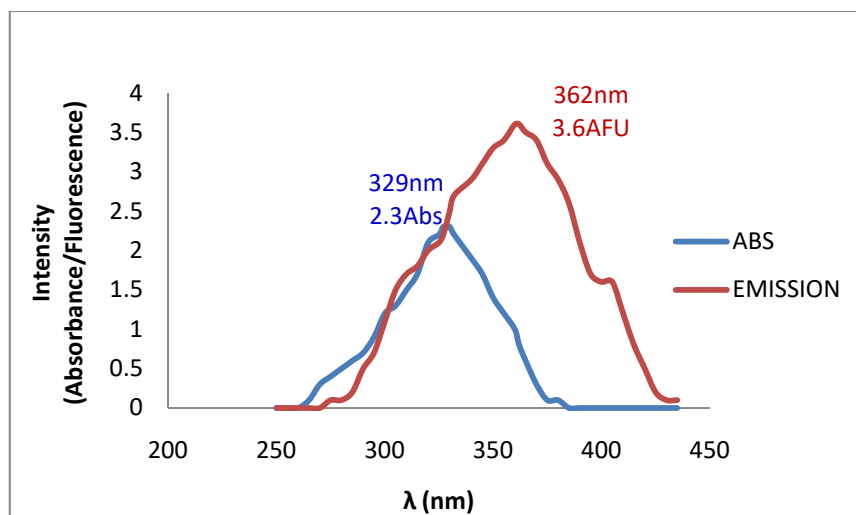is given in figure 4.3.

Figure 4.3: Absorption and Emission spectra of compound 4 (200 μM) in F⁻ free

        solution.

4.4   Time-dependent fluorescence intensity of the synthesized compounds (sensors) in fluoridated solution.

4.4.1   Compound 2

The variation of fluorescence intensity (AFU) of compound **2** with time (seconds) in the presence of fluoride ions is given in figure 4.4.

Figure 4.4: Time-dependent fluorescence intensity of compound 2 in fluoridated solutions

4.4.2   Compound 3

The variation of fluorescence intensity (AFU) of compound **3** with time (seconds) in the presence of fluoride ions is given in figure 4.5.

Figure 4.5: Time-dependent fluorescence intensity of compound 3 fluoridated solutions

4.4.3 Compound 4

The variation of fluorescence intensity (AFU) of compound **4** with time (seconds) in the
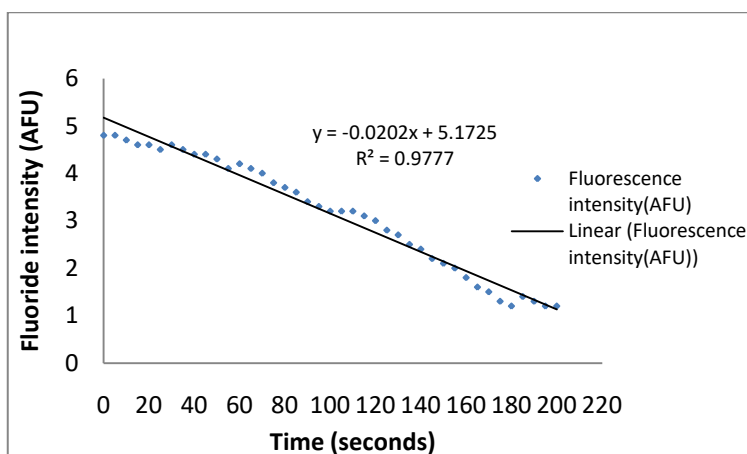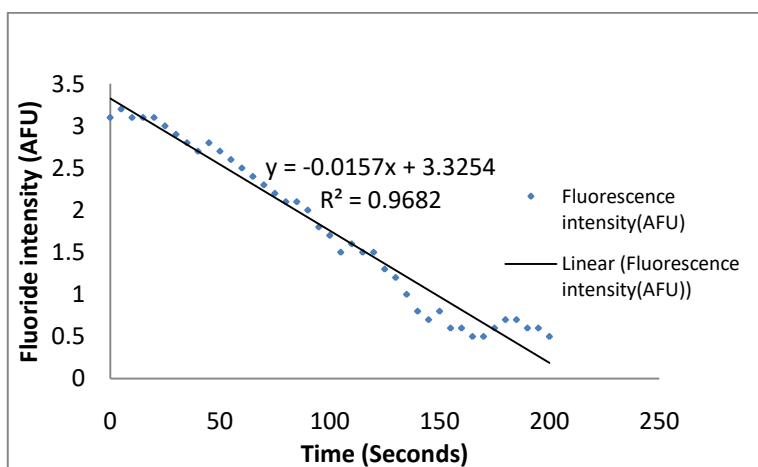
presence of fluoride ions is given in figure 4.6.

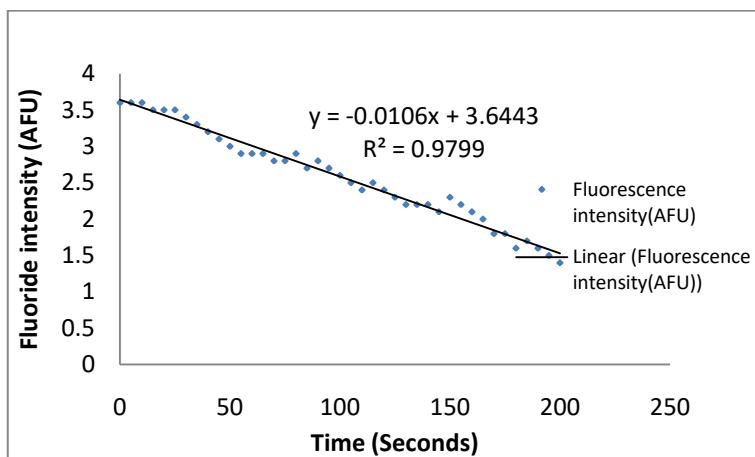**Figure 4.6: Time-dependent fluorescence intensity of compound 4 fluoridated**

solutions

4.5   Sensors fluorescence response in the presence of other anions

4.5.1   Compound 2

The fluorescence response of compound **2** (20 μM) in the presence of fluoride ions and other anions is given in figure 4.7.

Figure 4.7: Selectivity of compound 2 (20 μM) for fluoride in the existence of other anions

4.5.2 Compound 3

The fluorescence response of compound **3** (20 μM) in the presence of fluoride ions and other anions is given in figure 4.8.

Figure 4.8. Selectivity of compound 3 (20 μM) for fluoride in the existence of other anions

4.5.3 Compound 4

The fluorescence response of compound **2** (20 μM) in the presence of fluoride ions and other anions is given in figure 4.9.
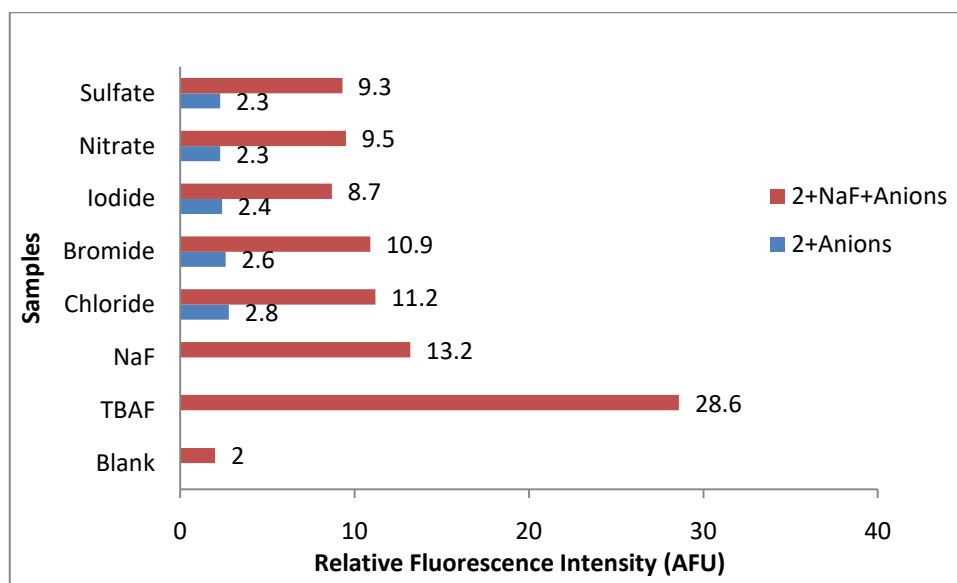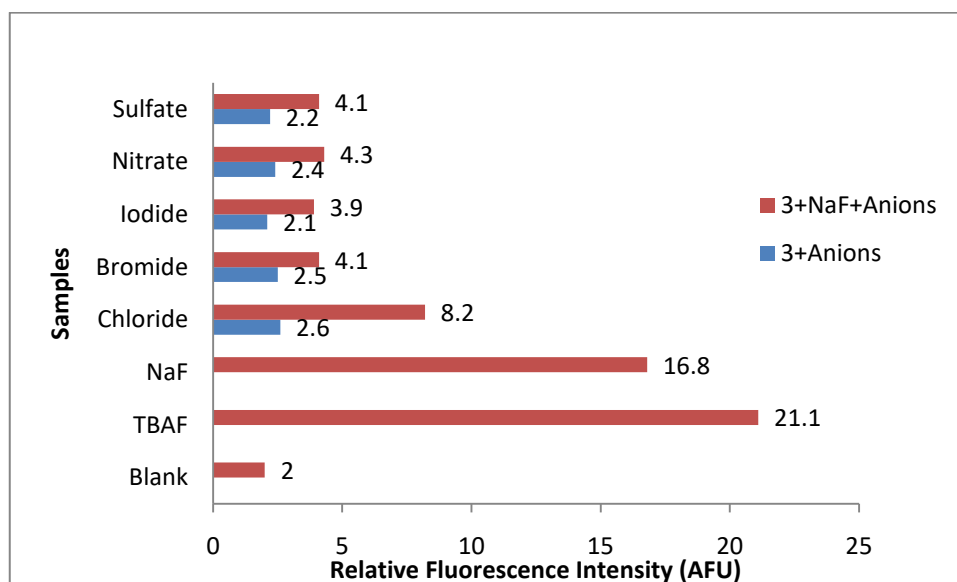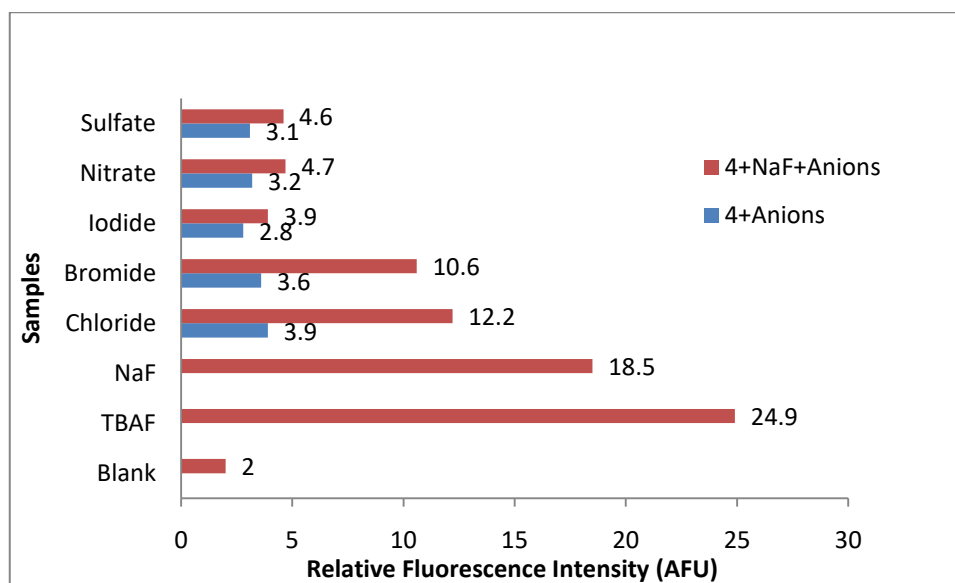

Figure 4.9: Selectivity of compound 4 (20 μM) for fluoride in the existence of other anions

4.6   Effects of fluorophore concentration on intensity of fluorescence

4.6.1   Compound 2

Figure 4.10 shows the variation of fluorescence intensity of sensor **2** (20 µM) with increase in concentrations of NaF (200 µM to 1000 µM) over time in HEPES buffer solution (10 mM, pH = 7): dioxane (1:1 v/v).
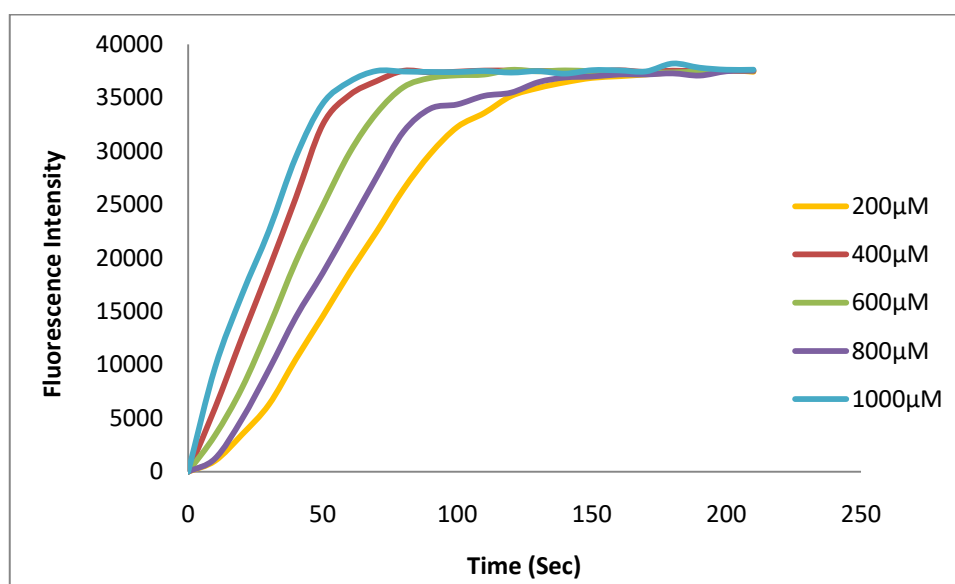
Figure 4.10: The variation of fluorescence intensity of sensor 2 (20 µM) with increase in concentrations of NaF (200 µM to 1000 µM) over time in HEPES buffer solution (10 mM, pH = 7): dioxane (1:1 v/v).

4.6.2 Compound 3

Figure 4.11 shows the variation of fluorescence intensity of sensor **3** (20 μM) with increase in concentrations of NaF (200 μM to 1000 μM) over time in HEPES buffer solution (10 mM, pH = 7): dioxane (1:1 v/v).
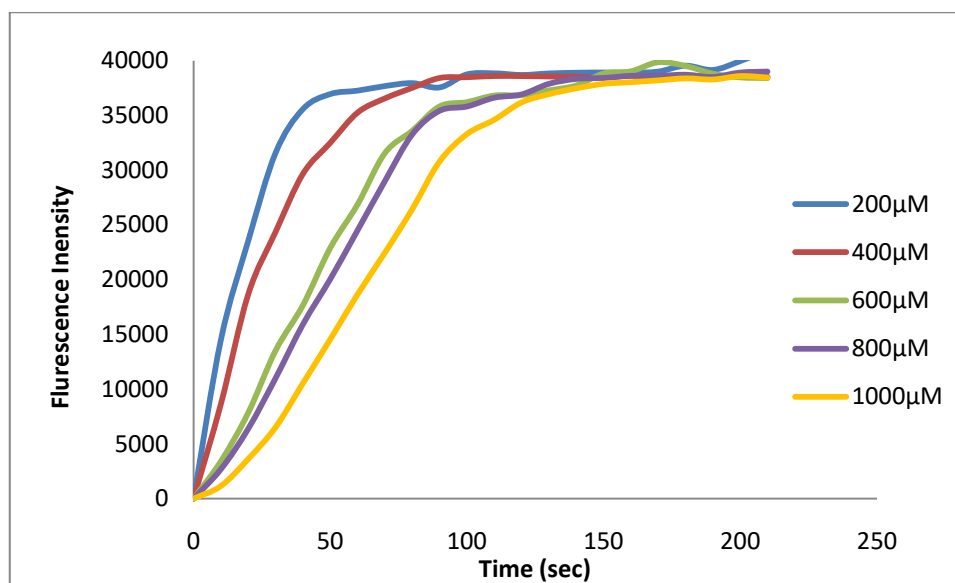
Figure 4.11: The variation of fluorescence intensity of sensor 3 (20 μM) with increase in concentrations of NaF (200 μM to 1000 μM) over time in HEPES buffer solution (10 mM, pH = 7): dioxane (1:1 v/v).

4.6.3 Compound 4

Figure 4.12 shows the variation of fluorescence intensity of sensor **4** (20 μM) with increase in concentrations of NaF (200 μM to 1000 μM) over time in HEPES buffer solution (10 mM, pH = 7): dioxane (1:1 v/v).
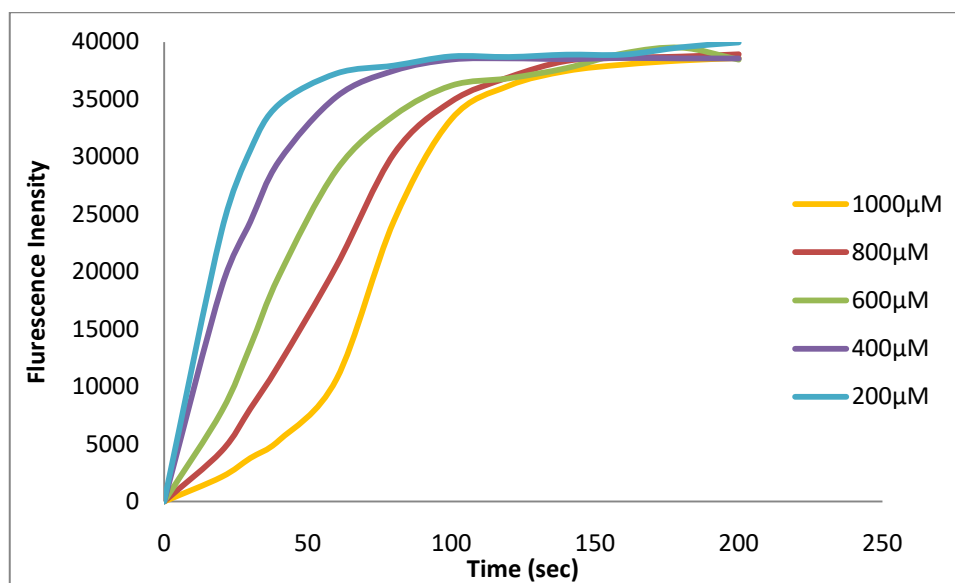
Figure 4.12: The variation of fluorescence intensity of sensor 4 (20 μM) with increase in concentrations of NaF (200 μM to 1000 μM) over time in HEPES buffer solution (10 mM, pH = 7): dioxane (1:1 v/v).

4.7   Rate constants

A pseudo-first-order rate constant plot for the synthesized fluoride sensors as a function

of [NaF] is shown in figures 4.13-4.15 while the second rate constants (extracted from

figures 4.13-4.15) are as shown in table 4.1.

Table 4.1: Second order rate constants

Fluoride sensor	Linear fit equation	R^2 value	2nd order rate constants
2	y = 0.0019x - 0.294	$R^2 = 0.9881$	$1.9 \times 10 \ M^{-1}min^{-1}$.
3	y = 0.0018x - 0.174	$R^2 = 0.9748$	$1.8 \times 10 \ M^{-1}min^{-1}$.
4	y = 0.0014x - 0.1275	$R^2 = 0.9722$	$1.4 \times 10 \ M^{-1}min^{-1}$.

4.7.1   Compound 2

A plot pseudo-first-order rate constant as a function of [NaF] for compound **2** is given

in figure 4.13.
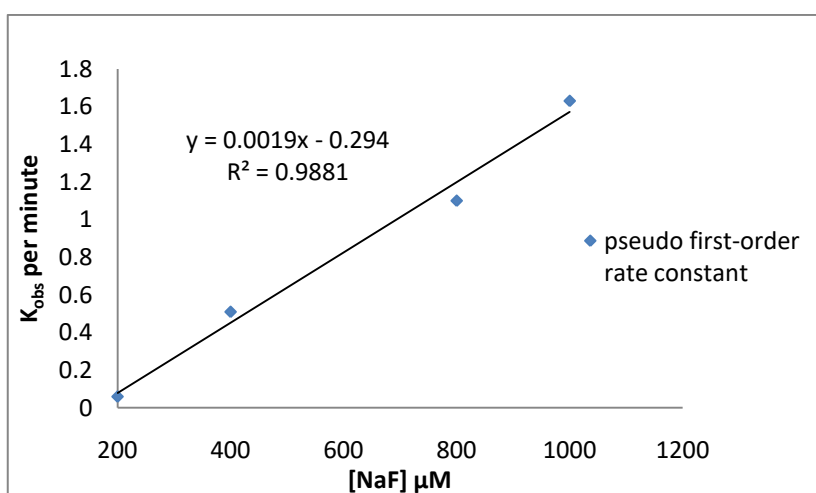
Figure 4.13: A pseudo-first-order rate constant plot for compound 2 as a function

of [NaF].

4.7.2 Compound 3

A plot pseudo-first-order rate constant as a function of [NaF] for compound **3** is given in figure 4.14.
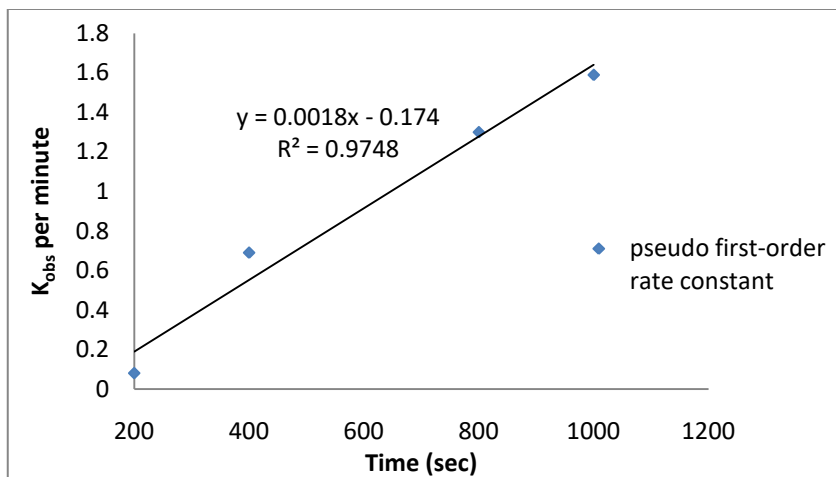
Figure 4.14: A pseudo-first-order rate constant plot for compound 3 as a function of [NaF].

4.7.3 Compound 4

A plot pseudo-first-order rate constant as a function of [NaF] for compound **4** is given in figure 4.15.
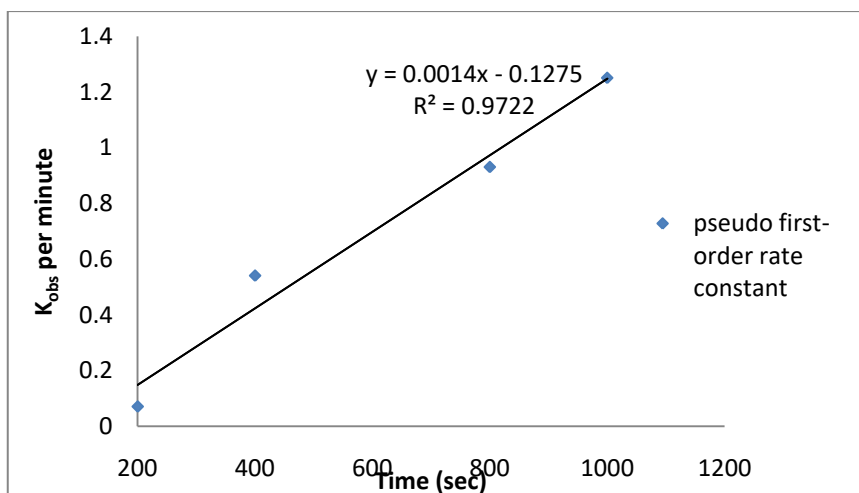
Figure 4.15: A plot of the pseudo-first-order rate constant for sensor 4 as a function of [NaF].

4.8   Selectivity studies.

The emission of the synthesized fluoride sensors (**2**, **3** and **4**) as a response for fluoride

detection in NaF is shown in figures 4.17-4.19.

4.8.1   Selectivity studies on Compound 2 in various concentrations of NaF

The emission of compound **2** (20 µM) in various [NaF] in a solution maintained at a pH

of 7 by 1:1 (v/v) 10 mM HEPES:dioxane is given in figure 4.16

Figure 4.16: Emission of 20 µM of compound 2 in various [NaF] in a solution

maintained at a pH of 7 by 1:1 (v/v) 10 mM HEPES:dioxane

4.8.2 Selectivity studies on Compound 3 in various concentrations of NaF

The emission of compound **3** (20 μM) in various [NaF] in a solution maintained at a pH of 7 by 1:1 (v/v) 10 mM HEPES:dioxane is given in figure 4.17

Figure 4.17: Emission of 20 μM of compound 3 in various [NaF] in a solution maintained at a pH of 7 by 1:1 (v/v) 10 mM HEPES:dioxane

4.8.3 Selectivity studies Compound 4 in various concentrations of NaF

The emission of compound **4** (20 μM) in various [NaF] in a solution maintained at a pH of 7 by 1:1 (v/v) 10 mM HEPES:dioxane is given in figure 4.18.

Figure 4.18: Emission of 20 μM of compound 3 in various [NaF] in a solution maintained at a pH of 7 by 1:1 (v/v) 10 mM HEPES:dioxane

The emission of the synthesized fluoride sensors (**2**, **3** and **4**) as a response for fluoride detection in TBAF is as shown in figures 4.19 and 4.21.

4.8.4 Selectivity studies Compound 2 in various concentrations of TBAF

The emission of 20 μM of compound **2** (Log AFU) in various [TBAF] in a solution maintained at a pH of 7 by 1:1 (v/v) 10 mM HEPES:dioxane in given in figure 4.19.
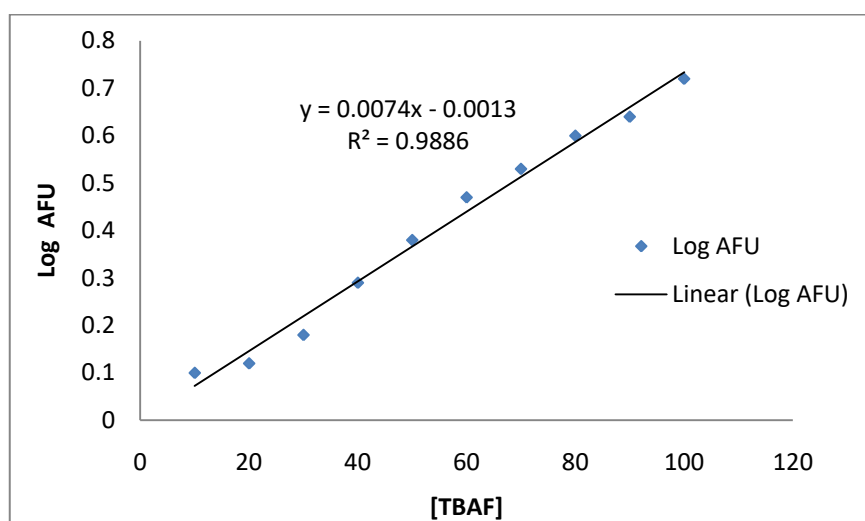
Figure 4.19: Emission of 20 μM of compound 2 in various [TBAF] in a solution maintained at a pH of 7 by 1:1 (v/v) 10 mM HEPES:dioxane.

4.8.5 Selectivity studies Compound 3 in various concentrations of TBAF

The emission of 20 μM of compound **3** (Log AFU) in various [TBAF] in a solution maintained at a pH of 7 by 1:1 (v/v) 10 mM HEPES : dioxane in given in figure 4.20.
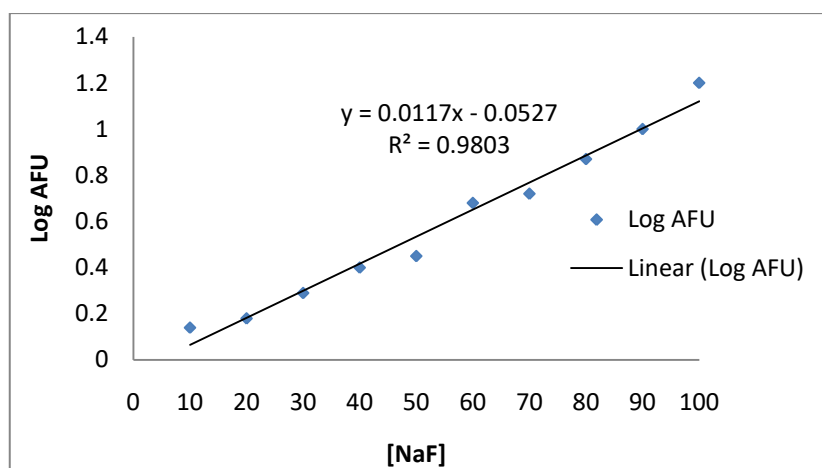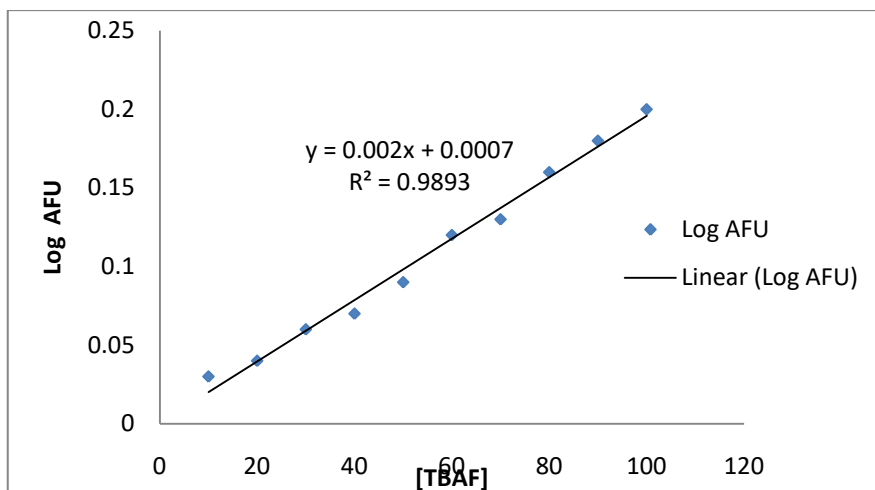
Figure 4.20: Emission of 20 μM of compound 3 in various [TBAF] in a solution maintained at a pH of 7 by 1:1 (v/v) 10 mM HEPES:dioxane.

4.8.6   Selectivity studies Compound 4 in various concentrations of TBAF

The emission of 20 μM of compound **4** (Log AFU) in various [TBAF] in a solution maintained at a pH of 7 by 1:1 (v/v) 10 mM HEPES:dioxane in given in figure 4.21.
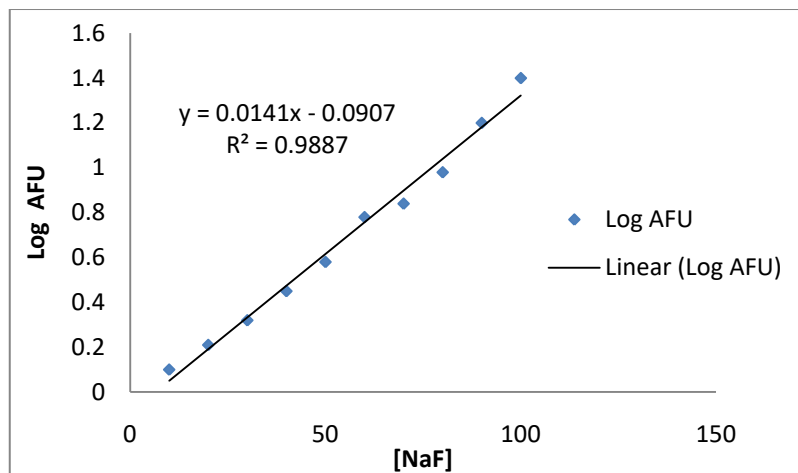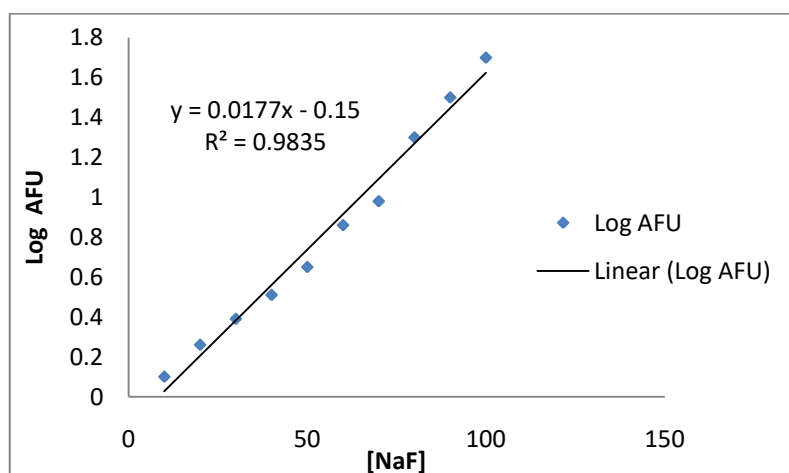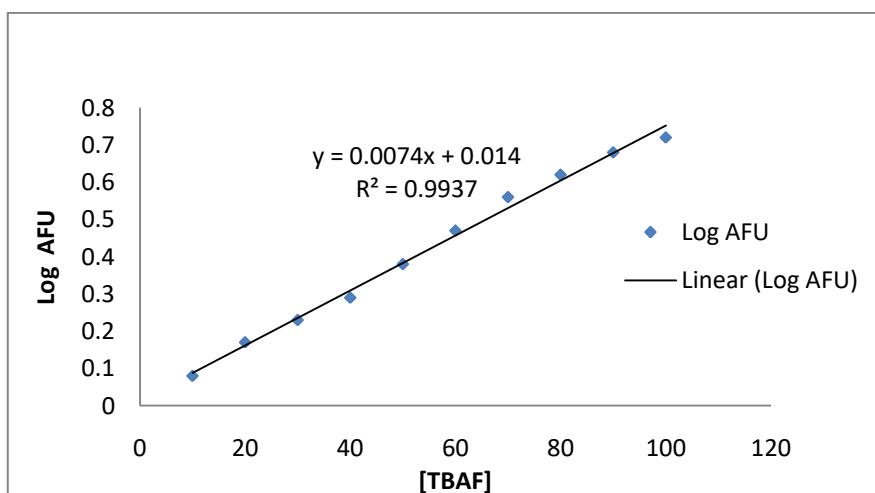

Figure 4.21: Emission of 20 μM of compound 4 in various [TBAF] in a solution maintained at a pH of 7 by 1:1 (v/v) 10 mM HEPES:dioxane

4.9 Quantum yield

Table 4.2: Calculated sensors 2-4 quantum yields using standard (quinine sulfphate in 0.1M perchloric acid).

Sample	Standard (quinine) refractive index	Sample Ref index	Standard quantum yield	Standard gradient	Sample gradient	Sample quantum yield
Sensor **2**	1.33	1.38	0.54	28.81	32.44	**0.6546**
Sensor **3**	1.33	1.39	0.54	28.81	35.28	**0.7228**
Sensor **4**	1.33	1.42	0.54	28.81	33.9	**0.7243**

4.9.1 Integrated fluorescence intensity of Compound/sensor 2 compared to standard quinine (350 nm)

A plot of integrated Fluorescence intensity of sensor **2** at 360 nm against the corresponding absorbance for the standard (quinine sulphate) at 350 nm is given in figure 4.22.
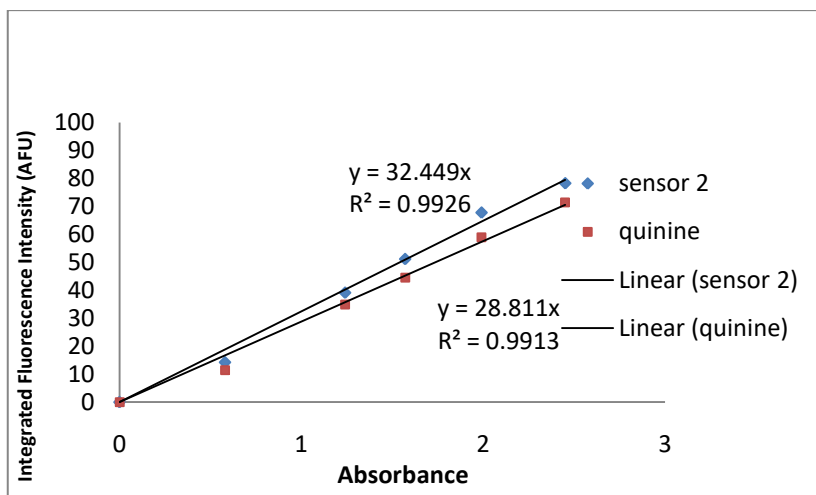
Figure 4.22: Plot of integrated Fluorescence intensity of sensor 2 at 360 nm versus the corresponding absorbance for the standard (quinine sulphate) at 350 nm.

4.9.2 Integrated fluorescence intensity of Compound/sensor 3 compared to standard quinine (350 nm)

A plot of integrated Fluorescence intensity of sensor **3** at 361 nm against the corresponding absorbance for the standard (quinine sulphate) at 350 nm is given in figure 4.23.
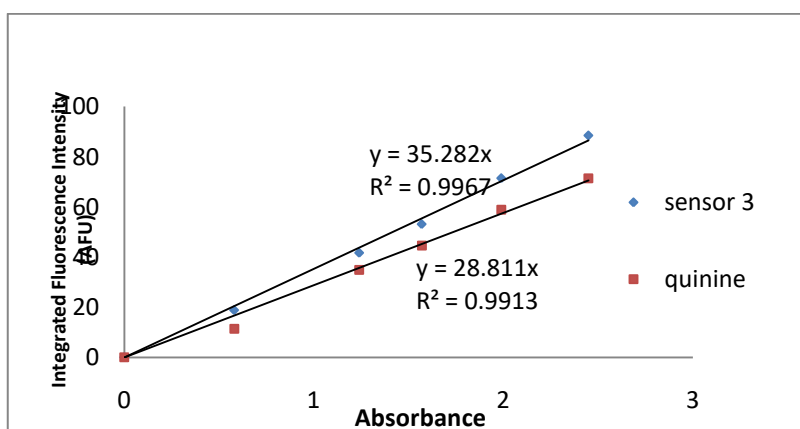
Figure 4.23: Plot of integrated Fluorescence intensity of sensor 3 at 361 nm versus the corresponding absorbance for the standard (quinine sulphate) at 350 nm.

4.9.3 Integrated fluorescence intensity of Compound/sensor 4 compared to standard quinine (350 nm)

A plot of integrated Fluorescence intensity of sensor **4** at 362 nm against the corresponding absorbance for the standard (quinine sulphate) at 350 nm is given in figure 4.24.
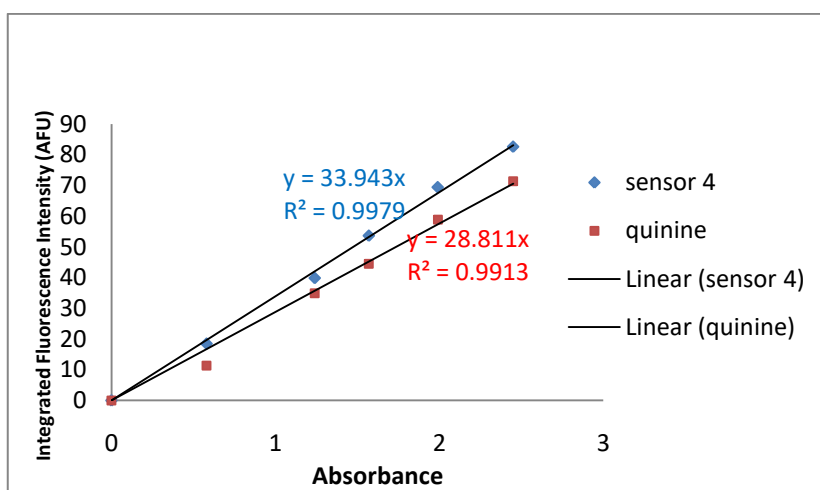
Figure. 4.24: Plot of integrated Fluorescence intensity of sensor 4 at 362 nm versus the corresponding absorbance for the standard (quinine sulphate) at 350 nm.

4.10   Paper disc test

The variation of fluorescence intensity of compounds **2**, **3** and **4** on paper discs with a decrease in the concentration of fluoride ions is shown in figure 4.25.
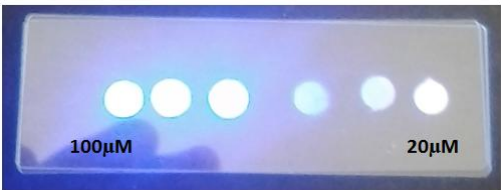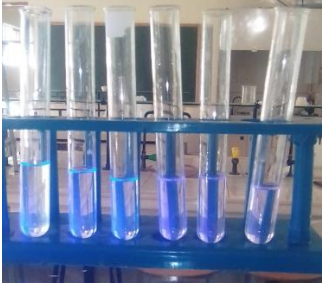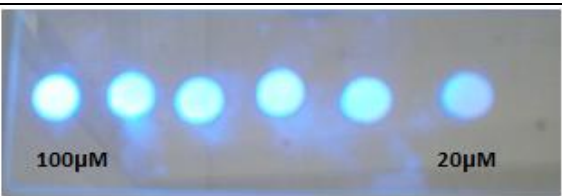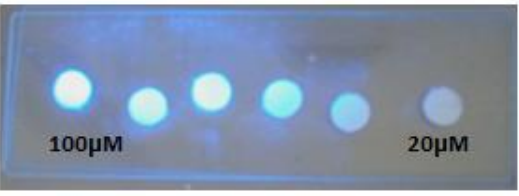
SENSOR	STRIP TEST FLUORESCENCE	FLUORESCENCE OF SENSORS IN TBAF SOLUTION
Blank		
Sensor 2		
Sensor 3		
Sensor 4		

Figure 4.25: Fluorescence of test-trips containing the synthesised sensors 2, 3 and 4 in the presence of decreasing aqueous [TBAF].

CHAPTER FIVE

DISCUSSION

In this chapter the findings of this study have been discussed. A detailed explanation on spectral analysis has been covered and where necessary, the explanations have been accopannied by relevant figures and tables. An explanation on relevance of all findings on this research work has been presented. The contribution and implications of the findings on previous studies have been outlined as a conclusion. Finally, and recommendations for future research have been presented.

5.1 Rational Design

Out of the sensing mechanisms described in chapter two, the fluoride induced oxygen-silicon bond cleavage stands out as most selective approach for aqueous fluoride detection. To promote the sensitivity of this approach, a fluorophore with a high quantum yield is necessary. Since fluoride has the highest electronegativity, a conjugated fluorophore with several electrophilic centres was used to induce resonance once the oxygen-silicon bond is cleaved upon reaction with fluoride. 3-cyano-7-hydroxy-4-methylcoumarin scaffold distinguished itself as an electron deficient conjugated system and could give reasonably high quantum yield. Therefore the ability of some 3-cyano-7-hydroxy-4-methylcoumarin derivatives as fluoride sensors was investigated. Based on the ICT mechanism, the synthesis of a TBDMS and TBDPS protected 3-cyano-7-hydroxy-4-methylcoumarin and its derivatives (see figure 6) were envisioned. The breaking away of TBDMS/TBDPS by fluoride as well as the conversion of the coumarin carbonyl into hydroxyimino functional group would induce faster resonance into the fluorophore resulting into fluorescence.

5.2   Structural elucidation

5.2.1   Compound 1

A single diode array chromatograph peak at 2.93 retention time (see appendix VIII) on this compound confirms its purity. The Mass spectrum (see appendix IX) revealed an M^+ + 1 at 202.2. The molecular mass of compound (**1**) matches with 3-cyano-4-methylcoumarin which was used as the starting reagent for the synthesis. The ^{1}H NMR (500 MHz, MeOD) spectrum (Appendix I) showed different multiplicities.   The aliphatic protons resonate at δ 2.73 (s, 3H), while the aromatic protons at 7.80 (d, J = 8.9 Hz, 1H), 6.75 (d, J = 2.3 Hz, 1H). 6.92 (dd, J = 8.9, 2.3 Hz, 1H) as assigned in table 5.1.

The [1]H–[1]H coupling is observed between δ 7.8 and δ 6.75 (J = 8.9Hz) while two-bond coupling ([1]H–C–[1]H) is between δ 6.75 and δ 6.92 (J = 2.3 Hz). The multiplicity provided in figure 5.1 indicates the aromatic proton at δ 6.92 is coupled to the two other protons at δ 7.8 and δ 6.75, thus the signal at δ 6.92 is a double duplet. The aromatic proton at δ 7.8 only shows coupling with another at 6.75 hence is a duplet.
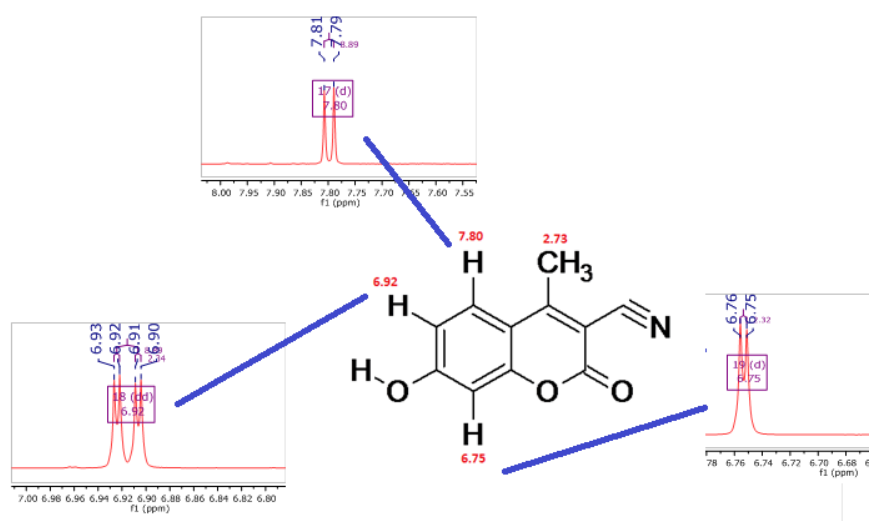
Figure 5.1: Proton chemical shifts and expanded ^{1}H NMR Signal multiplicities of the aromatic protons

The ^{13}C NMR: (500 MHz, MeOD) spectrum (Appendix II) signals were observed at δ 15.75, 101.29, 109.84, 112.89, 113.23, 127.17, 154.71, 157.32, 162.55 and 163.82. Mohamed and co-workers in a study synthesized a related 4-methyl-7-hydroxycoumarin (coumarin–OH). ^{1}H and ^{13}C nuclear magnetic resonance spectroscopy confirmed the structure of the synthesised compound 4-methyl-7-hydroxycoumarinas follows; ^{1}H NMR (500 MHz, DMSOd$_6$, δ, ppm): 2.40 (s, 3H, CH$_3$), 3.70 (s, 1H, OH), 6.08 (s, ^{1}H, CH), 6.87 (d, 2H, CH), 7.45 (s, 1H, CH) while the ^{13}C NMR (125 MHz, CDCl$_3$, δ ppm): 18.3 (CH$_3$), 163.1 (C=O) (Mohamed *et al.*, 2015). Comparing this data with spectra (Appendix I and II), the methyl at carbon-4 and the OH at carbon-7 on compound **1** can be confirmed as their chemical shift match with the ones indicated by Mohammed and his team.

The off-diagonal correlations in the ^{1}H-^{1}H COSY (**CO**rrelated **S**pectroscop**Y**) indicate that the aromatic protons 13, 14 and 12, 13 are *J*-coupled (Fig. 5.2 and Appendix III). All atom positions in the structure are as assigned by the MestreNova (v14.0.0) software.

Figure 5.2: COSY correlation of compound 1

The correlations between a carbon and its attached protons are shown in the HSQC (Heteronuclear Single Quantum Coherence Spectroscopy) spectrum (Figure 5.3 and appendix IV). The HSQC spectrum clearly shows that proton 12 is directly bonded to carbon 4, proton 13 is directly bonded to carbon 5, proton 14 is directly bonded to carbon 3 and finally the protons at position 15 are bonded to carbon 15. The long range correlations between carbons and protons that are separated by multiple bonds are as shown in figure 5.3 and table 5.1. All atom positions in the structure are as assigned by the MestreNova (v14.0.0) software.
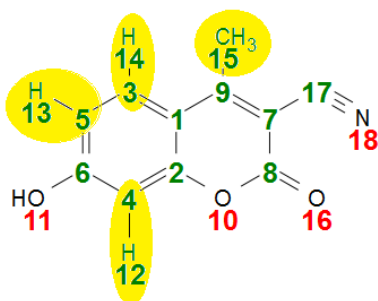
Figure 5.3: HSQC correlation of compound 1
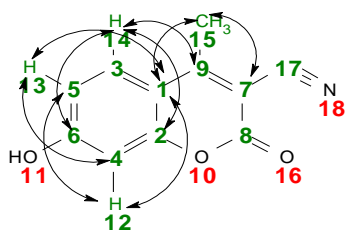
Figure 5.4: HMBC correlation of compound 1

The NOESY (**N**uclear **O**verhauser **E**ffect **S**pectroscopy) revealed through-space interactions leading to cross-relaxations between the aromatic protons 13, 14 and 12, 13 as shown in appendix III and VII. The cross peaks observed in the NOESY spectrum (appendix VII) shows a strong NOESY correlation of the signal at 6.92 ppm and the proton at 7.80ppm. The rest of the protons from this structure are as assigned in table 5.1.

Table 5.1: NMR Spectral data for compound 1

Position	Atom type	δ_H (ppm), H, m (J, Hz)	δ_C(ppm)	COSY	HSQC (C-H direct connectivity)	HMBC(long range C-H connectivity)
1	C	-	112.86	-	-	12,13,15
2	C	-	154.71	-	-	14
3	CH	-	127.17	-	14	-
4	CH	-	109.84	-	12	13
5	CH	-	112.89	-	13	-
6	C	-	157.32	-	-	14
7	C	-	101.29	-	-	15
8	C	-	162.55	-	-	-
9	C	-	163.82	-	-	14
10	O	-	-	-	-	-
11	O	-	-	-	-	-
12	H	6.92,dd, 1H, (8.9, 2.3)	-	13	-	-
13	H	6.75, d, 1H, (2.3)	-	12, 14	-	-
14	H	7.80,d, 1H (8.9)	-	13	-	-
15	CH$_3$	2.73, s, 3H	15.75	-	15	-
16	O	-	-	-	-	-
17	C	-	113.23	-	-	-
18	N	-	-	-	-	-

5.2.2   Compound 2

A single diode array chromatograph peak at 2.92 retention time (appendix XVII) on this compound confirms its purity.   The Mass spectrum revealed an $M^+ + 1$ at 315.4 (Appendix XVIII). The molecular mass of compound (**2**) matches with the expected mass of the synthesised compound 7-O-tert-butyldimethylsylyl-3-cyano-4-methylcoumarin as shown in appendix XVIII. The ^{1}H NMR (500 MHz, MeOD) spectrum (Appendix X) showed different multiplicities. The aliphatic protons resonate at δ_H 1.38 (6H, s), 2.16 (9H, s) and 2.73 (3H, m), while the aromatic protons at 6.92 (1H, dd, J = 7.7, 1.5 Hz), 6.76 (1H, d, J = 1.5, 0.5 Hz), 7.79 (1H, d, J = 7.7, 0.5 Hz) as assigned in table 5.2.

The ^{1}H–^{1}H coupling is observed between δ 7.79 and δ 6.92 while two-bond coupling (^{1}H–C–^{1}H) is between δ 6.76 and δ 6.92. The multiplicity provided in figure 5.5 below indicates the aromatic proton at δ 6.92 is coupled to the two other protons at δ 7.79 and δ 6.76, thus the signal at δ 6.92 is a double duplet. The aromatic proton at δ 7.79 only shows coupling with another at 6.76 hence is a duplet. Figure 5.5 shows that all the non-aromatic protons at δ 1.38, δ 2.16 and δ 2.73 show no coupling and appear as singlets.
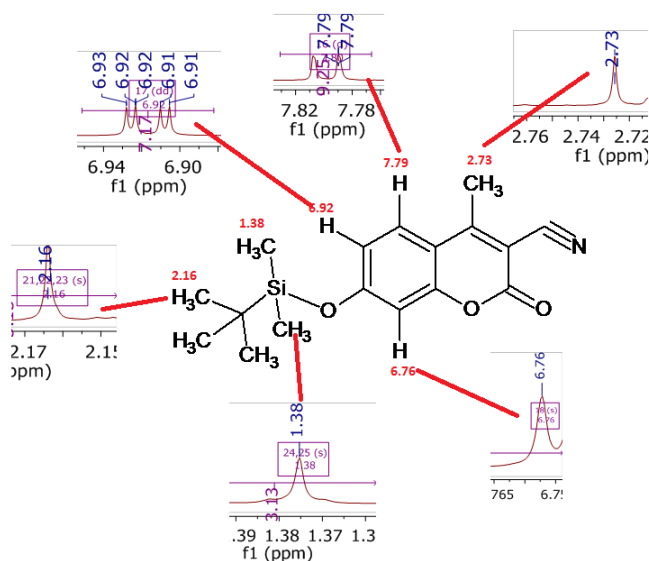
Figure 5.5: Expanded ^{1}HNMR Signal multiplicities of compound 2 protons

These signals correspond to ^{13}C NMR: (500 MHz, MeOD) spectrum (Appendix XI) signals at δ 1.66, 15.36, 15.76, 28.51, 101.28, 110.01, 112.88, 113.22, 127.18, 154.70, 157.33, 162.57 and 163.78 as assigned in table 5.2.

The off-diagonal correlations in the ^{1}H-^{1}H COSY (**CO**rrelated **S**pectroscop**Y**) indicate that the aromatic protons 13, 14 and 12, 13 are *J*-coupled. The off-diagonal correlations in the ^{1}H-^{1}H COSY (**CO**rrelated **S**pectroscop**Y**) indicate that the aromatic protons 16 and 17 are J-coupled (Figure 5.6 and appendix XII). All atom positions in the structure are as assigned by the MestreNova (v14.0.0) software.
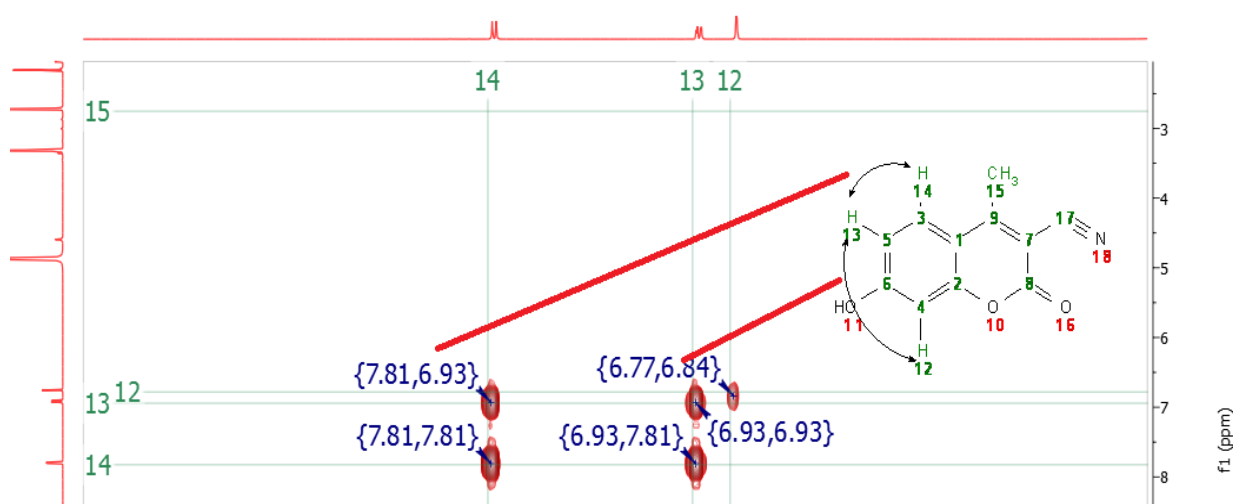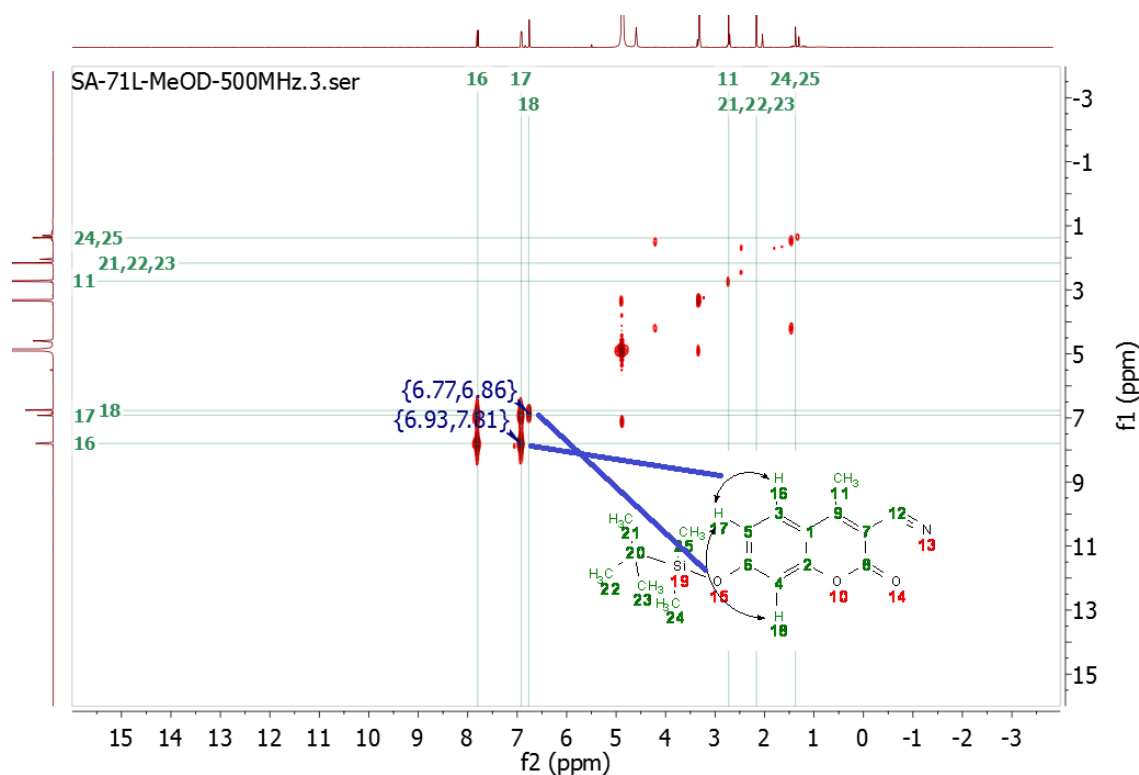

Figure 5.6: COSY correlation of compound 2

NOESY NMR spectrum (appendix XVI) at 500 MHz, MeOD indicate that the aromatic protons 16 and 17 are J^2-coupled. The chemical shifts of carbon atoms to which the protons are directly bonded are as shown in the HSQC spectrum (appendix XIII). The cross peaks observed in the NOESY spectrum (appendix XVI) shows a strong NOESY correlation of the signal at δ_H 6.92 ppm and the proton at δ_H 7.79ppm. The assignment H-17 is in accordance with the multiplicity of this signal due to one vicinal coupling with H-16 (*J*=7.7Hz) and one long-range coupling with H-18(*J*=0.5). HMBC correlations are as shown in figure 5.7. The rest of the protons from this structure are as assigned by their mutual NOESY correlations as shown in table 5.2. All atom positions in the structure are as assigned by the MestreNova (v14.0.0) software.

Figure 5.7: HMBC correlation of compound 2

Table 5.2: NMR Spectral data for compound 2

Position	Atom	δ_H (ppm),H, m(*J*, Hz)	δ_C(ppm)	COSY	HSQC	HMBC
1	C	-	112.88	-	-	17,18
2	C	-	154.68	-	-	16
3	CH	-	127.18	-	16	-
4	CH	-	101.28	-	18	17
5	CH	-	123.46	-	17	18
6	C	-	157.31	-	-	-
7	C	-	110.01	-	-	11
8	C	-	162.56	-	-	-
9	C	-	163.77	-	-	16
10	O	-	-	-	-	-
11	CH$_3$	2.73, 3H, m	15.76	-	11	-
12	C	-	113.22	-	-	-
13	N	-	-	-	-	-
14	O	-	-	-	-	-
15	O	-	-	-	-	-
16	H	7.79,H, d (7.7, 0.5)	-	17	-	-
17	H	6.92, H, dd (7.7, 1.5)	-	16	-	-
18	H	6.76, H, s,(1.5, 0.5)	-	17	-	-
19	Si	-	-	-	-	-
20	C	-	15.36	-	-	-
21,22,23	CH$_3$	2.16, 9H, s	28.51	-	21,22,23	24,25
24,25	CH$_3$	1.38, 6H, s	-1.66	-	24,25	21,22,23

5.2.3 Compound 3

A single diode array chromatograph peak (appendix XXIII) at 2.92 retention time on this compound confirms its purity. The Mass spectrum revealed an $M^+ + 1$ at 439.5 (appendix XXIV). The molecular mass of compound (**3**) matches with the expected mass of the synthesised compound 7-O-tert-butyldiphenylsylyl-3-cyano-4-methylcoumarin (Appendix XXIV). The ^{1}HNMR (400 MHz, DMSO-d_6) spectrum (Appendix XIX) showed different multiplicities with aliphatic protons resonating at 2.62 (s, 3H) while the aromatic protons resonate at δ_H 7. 93 (dd, J = 8.8 Hz, 1H), 7.77(d, J = 8.8 Hz, 1H), 7.76 (d, J = 7.3 Hz, 1H), 7.14 (s, 1H), 6.87 (dd, J = 8.9, 2.3 Hz, 1H), 6.71 (d, J = 2.3 Hz, 1H).

The ^{1}H–^{1}H coupling is observed between δ_H 7.91 and δ_H 6.85 while two-bond coupling (^{1}H–C–^{1}H) is between δ_H 6.87 and δ_H 6.71. The multiplicity provided in figure 5.8 indicates the aromatic proton at δ_H 6.87 is coupled to the two other protons at δ_H 7.93 and δ_H 6.71, thus the signal at δ_H 6.87 is a double duplet. The aromatic proton at δ_H 7.93 only shows coupling with another at δ_H 6.87 hence is a duplet. All the non-aromatic protons at δ_H 2.62 show no coupling and appear as singlet. Other aromatic protons at δ 7.14 appear as abroad singlet while δ_H 7.77 and δ_H 7.76 are duplets as shown in figure 5.8. All atom positions in the structure are as assigned by the MestreNova (v14.0.0) software.

Figure 5.8: Expanded ^{1}H NMR Signal multiplicities of compound 3 protons

The ^{13}C NMR (400 MHz, DMSO-d_6) (Appendix XX) δ_C 165.14, 163.85, 157.92, 155.59, 135.48, 129.29, 121.69, 115.24, 114.84, 110.98, 102.84, 96.43, 18.37 as assigned in table 5.3). The chemical shifts of carbon atoms to which the protons are directly bonded are as shown in the HSQC spectrum (Figure 5.9 and appendix XXI) while the correlations between protons and carbons that are separated by multiple bonds (HMBC) are as shown in figure 5.10. The rest of the protons from this structure are as assigned in table 5.3. All atom positions in the structure are as assigned by the MestreNova (v14.0.0) software.

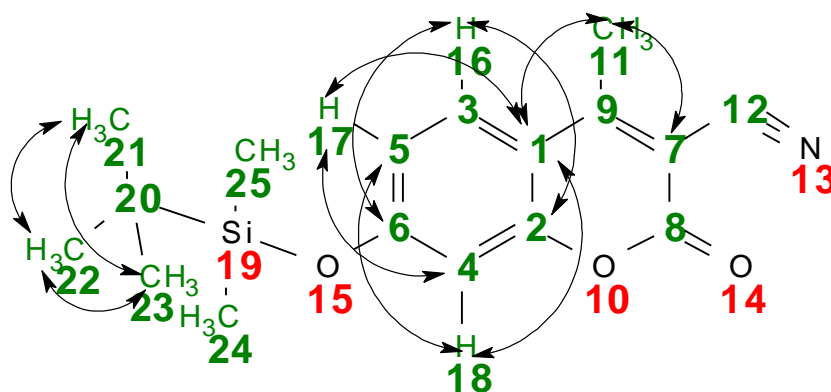**Figure 5.9: HSQC correlation of compound 3**

Figure 5.10. HMBC correlation of compound 3

Table 5.3: NMR Spectral data for compound 3

No	Atom	δ H, (ppm), m	δ C	HSQC	HMBC
1	C	-	110.9	-	33, 37, 38
2	C	-	155.6	-	36
3	CH	-	121.7	36	-
4	CH	-	115.2	38	37
5	CH	-	121.7	37	38
7	C	-	96.4	-	33
9	C	-	165.1	-	36
12	CH$_3$	-	18.4	33, 34, 35	-
18	CH$_3$	2.60 (s)	18.4	18	19, 20
19	CH$_3$	2.60 (s)	18.4	19	18, 20
20	CH$_3$	2.60 (s)	18.4	20	19. 19
21	C	-	129.3	-	40, 43
22	CH	-	114.8	42	39, 41
23	CH	-	114.8	41	39, 42
24	CH	-	102.8	43	40
25	CH	-	102.8	40	43
26	CH	-	129.3	39	41, 42
27	C	-	129.3	-	46
28	CH	-	114.8	45	48
29	CH	-	114.8	44	44
30	CH	-	102.8	46	47
31	CH	-	102.8	47	46
32	CH	-	129.3	48	44, 45

5.2.4 Compound 4

A single diode array chromatograph peak (appendix XXX) at 2.92 retention time on this compound confirms its purity. The Mass spectrum revealed an M$^+$ + 1 at 330.4 (Appendix XXXI). The molecular mass of compound (**3**) matches with the expected mass of the synthesised compound 7-*O*-tert-butyldimethylsylyl-2-(hydroxyimino)-4-methyl-2*H*-chromene-3-carbonitrile. The ^{1}H NMR (500 MHz, DMSO-d_6) spectrum (Appendix XXV) showed different multiplicities with aliphatic protons resonating 7.79 (s, 1H), 2.56 (s, 9H), 1.84 (s, 6H). While the aromatic protons at δ 7.72 (s, 1H), 6.89 (d, *J* = 8.9 Hz, 1H), 6.83 (dd, *J* = 8.9, 2.3 Hz, 1H) (Figure 5.11). All atom positions in the structure are as assigned by the MestreNova (v14.0.0) software.
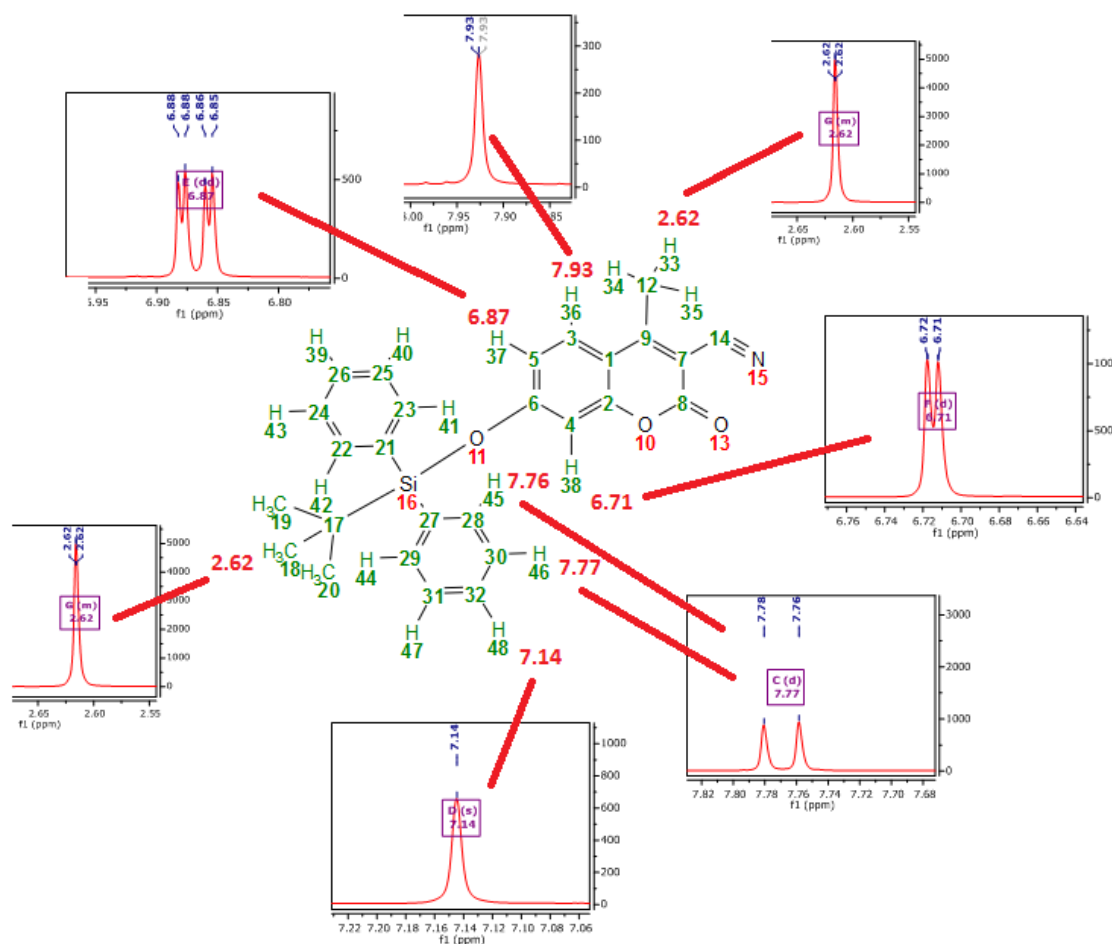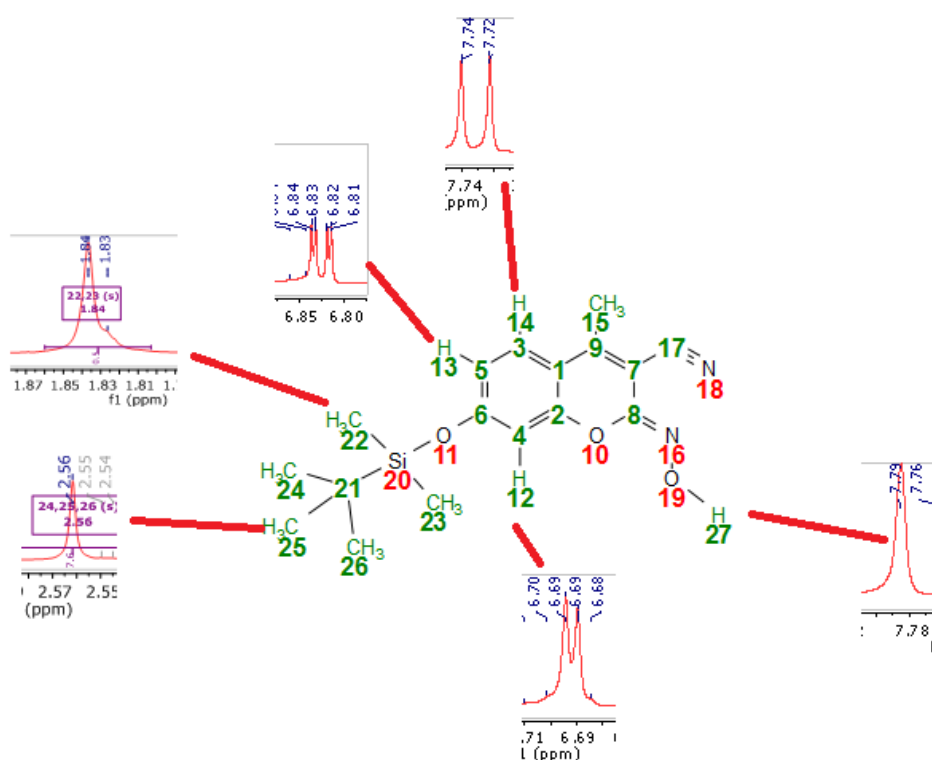

Figure 5.11: Expanded 1HNMR Signal multiplicities of compound 3 protons

The ^{13}C NMR (500 MHz, DMSO-d_6) (Appendix XXVI)chemical shifts (δ_C) for compound 4 was found to be located at 165.02 , 163.92 , 157.94 , 155.58 , 135.38 , 129.32 , 121.68 , 118.42 , 115.24 , 114.78 , 111.02 , 102.83 , 96.45 , 30.70 , 28.24 , 18.36 . The off-diagonal correlations in the ^{1}H-^{1}H COSY (500 MHz, DMSO-d_6) indicate that the aromatic protons **13**, **14** (Figure 5.12 and appendix XXVII) are *J*-coupled.

The chemical shifts of carbon atoms to which the protons are directly bonded are as shown in the HSQC spectrum (Figure 5.13 and appendix XXVIII) while the correlations between protons and carbons that are separated by multiple bonds (HMBC) are as shown in figure 5.14 and appendix XXIX. The rest of the protons from this structure are as assigned by their mutual correlations as shown in table 5.4. All atom positions in the structure are as assigned by the MestreNova (v14.0.0) software.
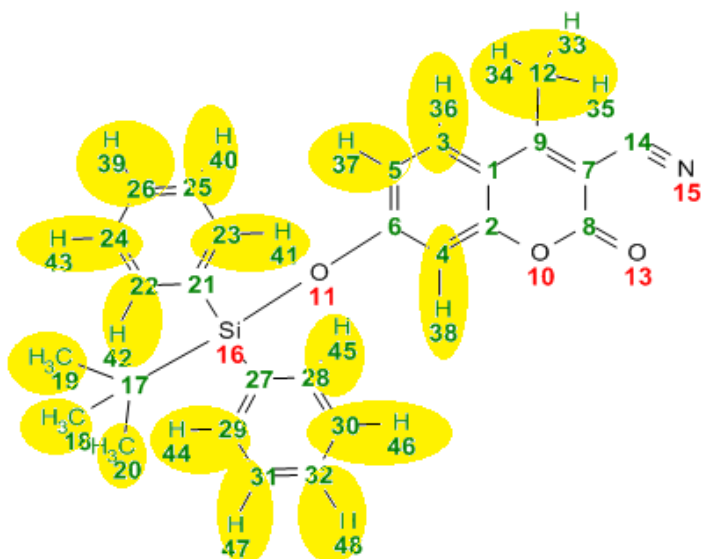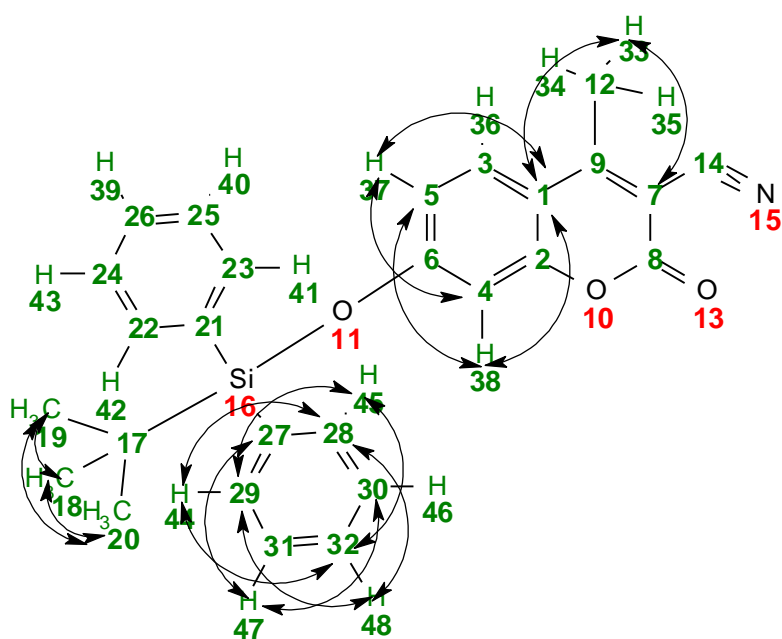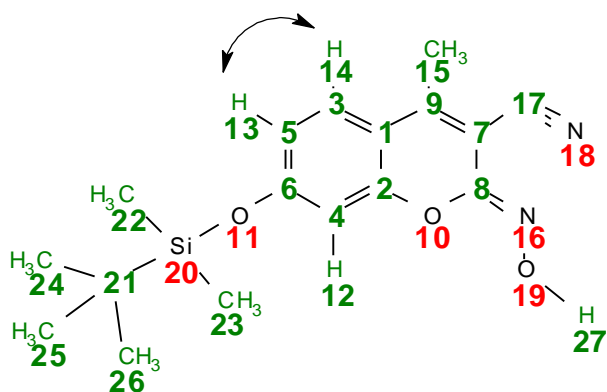

Figure 5.12: COSY correlation of compound 4
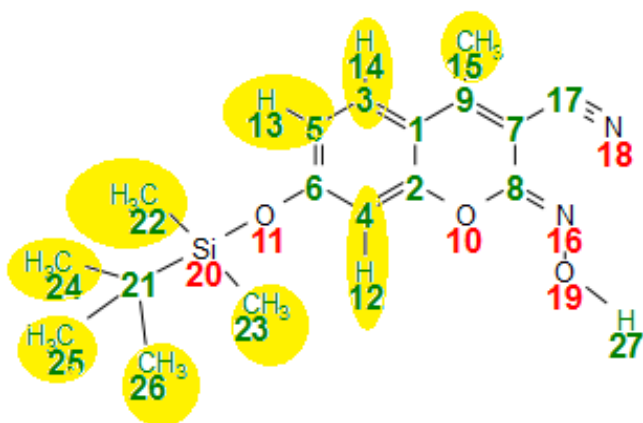
Figure 5.13: HSQC correlation of compound 4
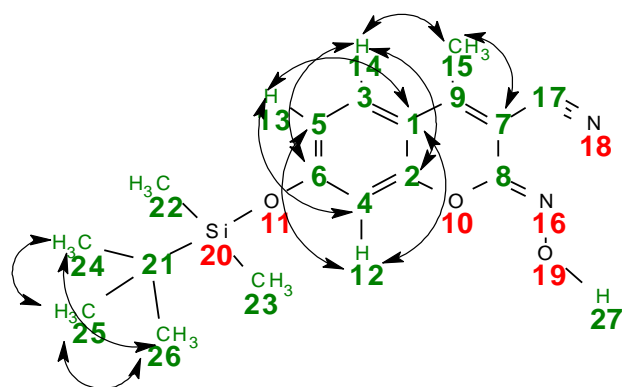
Figure 5.14: HMBC correlation of compound 4

Table 5.4: NMR Spectral data for compound 4

Position	δ_H (ppm), H, (*J*, Hz)	δ_C(ppm)	COSY	HSQC	HMB
1	-	114.78	-	-	12, 13
2	-	157.94	-	-	14
3	-	129.32	-	13	-
4	-	102.83	-	12	13
5	-	121.68	-	13	12
6	-	165.02	-	-	-
7	-	96.45	-	-	15
8	-	163.92	-	-	-
9	-	155.58	-	-	-
12	6.83, dd (8.86, 2.35)	-	13	-	-
13	6.83, dd (8.86, 2.35)	-	12, 14	-	-
14	7.73, d (8.85)	-	13	-	-
15	-	18.36	-	15	-
17	-	111.02	-	-	-
21	-	18.36	-	-	-
22	1.84, s	0.74	-	22	-
23	1.84, s	0.74	-	23	-
24	2.56, s	28.24	-	24	-
25	2.56, s	28.24	-	25	-
26	2.56, s	28.24	-	26	-

5.3   Excitation and Emission

Fluorophores are known to possess distinct and distinguishing spectra for absorption /excitation and emission, owing to due to their original electronic systems. These absorption and emission spectra show relative Intensity of fluorescence against the wavelength. The wavelength(s) of maximum, also called the excitation maximum were determined by recording intensity of absorbance over a range of wavelengths as shown in figures 4.1-4.3. The λ_{max} for both the excitation and emission for compounds **2, 3** and **4** are presented in figures 4.1-4.3.

Compound **2** registered the lowest stokes shift of 28 nm while compounds **3** and **4** registered stokes shift of 34 nm and 33 nm respectively. This implies that the change in electronic property (dipole moment) in ground and excited state of compound **2** is smaller as compared to that of compounds **3** and **4**. These large Stokes shifts (28-34 nm) indicate the presence of excited state reactions, especially the excited state proton transfer while purely vibrational shifts that arise from displacement of the potential energy curve in the excited state with respect to the ground state, are small. The large stokes shift may also indicate a fast relaxation from the initial state to the emissive state due to ICT leading to a significant red shift. Comparing both excitation and emission spectra for the samples **2, 3** and **4,** it can be observed that the spectra appear to obey Kasha's Rule (Deng *et al.,* 2019) as these spectra appear to be identical (Figures 4.1-4.3).

5.4   Time-dependent fluorescence study

Time-dependent fluorescence measurements were used as a quantitative method for determining dissociation constants to study receptor–ligand interactions. The ability and

extent of fluoresence or phosphorescence depends on intrinsic structure of a molecule and the nature of substituent group both electrn donating groups (EDG's) and electron withdrawing groups (EWG's). Rigid structures show no fluorescence as the lone pair of electrons enter triplet state ($S_1 \rightarrow T_1$) by intersystem crossing. The fluorescence intensity at 200 seconds for compounds **2**, **3** and **4** were calculated by substituting time in seconds into the linear equations in figures 4.4-4.6. Compound 4 recorded the highest fluorescence intensity of 1.52 AFU followed by compound **2** with 1.13 AFU and finaly compound **3** recorded the least fluorescence intensity of 0.19 AFU at 200 seconds (Table 5.5). This confirms that the conversion of the lactone carbonyl to hydroxyimino group reduces the rigidity of the fluorophore. An induction of resonance from the hydroxyimino group reduces the ability of the O-Si bond cleavage. This explains why the initial fluorescence intensity at t=0 sec is lowest in compound **3**.

Table 5.5: Fluorescence Intensity cof compounds 2, 3 and 4 in AFU at 200 seconds

Compound	Equation	Time(sec)	Y-value (Intensity in AFU at 200 sec)
2	y = -0.0202x + 5.1725	200	1.13
3	y = -0.0157x + 3.3254	200	0.19
4	y = -0.0106x + 3.6443	200	1.52

5.5 Sensors fluorescence response in the presence of other anions

The ability of compounds **2, 3** and **4** to detect fluorides by fluorescence was studied by exploring the influence of other anionic analytes on its detection: NO_3^- (from potassium nitrate), SO_4^{2-} (from sodium sulfate), I^- (from potassium iodide), Br^- (from tetrabutylammonium bromide), and Cl^- (from tetrabutylammonium chloride). An investigation on the response of compounds **2, 3** and **4** to environmentally and biologically relevant anions revealed lower levels of background of fluorescence in the range of 2.1 AFU to 3.9 AFU. However, the fluorescence response of compounds **2, 3** and **4** were not considerably affected due to direct competition with the tested anions apart from fluoride ions (Figures 4.7-4.9). The results undoubtedly show that environmentally relevant anions present in groundwater have negligible interference to fluoride sensing using compounds **2, 3** and **4**.

5.6 Effects of fluorophore concentration on intensity of fluorescence

Figures 4.10-4.12 confirm the effects of concentration of a fluorophore on fluorescence intensity**.** Fluorescence decreases with increase in fluorophore concentration due to

inner filler effects. Enhanced increase in concentration of the sensors bring about an adjustment in the fluorescence spectrum profile as shorter wavelength emissions is absorbed by other neighbouring species of the same electronic systems.

5.7   Rate constants

The second order rate constants for compounds **2**, **3** and **4** were calculated from the linear fit equations $y = mx + c$ (Figures 4.13-4.15), where **m** is the 2nd order rate constant. These were established to range from 1.4 x10 $M^{-1}min^{-1}$ to 1.9 x10 $M^{-1}min^{-1}$. These rate constant (Figures 4.13-4.15) demonstrate the ability of compounds **2**, **3** and **4** to rapidly detect the presence of aqueous fluorides in portable water as compared to a range of 0.54 $M^{-1}min^{-1}$ to 116 $M^{-1}min^{-1}$ for most fluoride sensors (Zheng *et al.,* 2016).

The fluorescence intensity changes were studies to understand the progress of the reaction over time. The effects of concentration on pseudo first order rate constants, and subsequently the second order rate constants were studied and recorded. From the results, it is evident that the polar groups have a significant effect on the reaction rate with fluoride in water. This is expected if water solubility is a key factor on sensitivity of the fluoride sensors. The results indicate that the water solubility difference introduced by the polar groups seems to be directly correlated to the probe reactivity toward fluoride detection in potable water.

5.8   Selectivity studies.

The limit detection was calculated from the linear fit equations y = mx + c from figures 4.16-4.18 where **x** is the detection limit and y=0 is as summarised in table 5.6.

Table 5.6: Detection limits of the synthesized Fluoride Sensors

Compound	Linear fit equations		Limit detection	
	NaF	TBAF	NaF	TBAF
Sensor **2**	y = 0.0117x - 0.0527	y = 0.0074x - 0.0013	4.5 µM	0.18 µM
Sensor **3**	y = 0.0141x - 0.0907	y = 0.002x + 0.0007	6.4 µM	0.35 µM
Sensor **4**	y = 0.0177x - 0.15	y = 0.0074x + 0.014	8.5 µM	1.9 µM

The response of sensors **2-4** to diminishing aqueous concentrations of NaF in a 1:1 (v/v) solution of H_2O : dioxane resulted into detection limits of 4.5 µM, 6.4 µM, and 8.5 µM in aqueous NaF solutions (Figures 4.16-4.18). This study demonstrated the capability of these sensors to resolve fluorides in TBAF at lower concentrations of 0.18 µM, 0.35 µM and 1.9 µM for sensors **2, 3** and **4** respectively (Figures 4.19-4.21). This is without a doubt lower than present WHO guidelines for fluoride concentration for water intake of 1.5 mgL^{-1} equivalent to 789.4 µM.

5.9   Quantum yield

The quantum yield of sensors **2, 3** and **4** (Table 5.7) were all higher than that of the standard (quinine sulfphate). These were worked out by integrating Fluorescence intensity of each sample in dioxane (refractive index η = 1.42) against quinine sulphate in 0.1M perchloric acid (refractive index η = 1.33) as standard. The gradients of the

standard (quinine sulfate in 0.1M perchloric acid) and the synthesised samples/sensors

(Figures 4.12-4.14) were substituted into equation (4.1);

$$Q_S = Q_R\left[\left(\frac{m_S}{m_R}\right) X \left(\frac{n_S}{n_R}\right)^2\right]$$...(4.1) (Nawara & Waluk, 2019).

Where;

Q_R: quantum yield of the standard/reference fluorophore (quinine sulphate).

Q_S: quantum yield of the sample.

m_R: The slope of a plot of integrated fluorescence intensity against the absorbance of the reference fluorophore (quinine sulphate).

m_S: The slope of a plot of integrated fluorescence intensity against the absorbance of the sample.

n_R: Refractive Index of the reference fluorophore (quinine sulphate)

n_S: Refractive Index of the sample

The quantum yields obtained were 0.6546, 0.7228 and 0.7243 for sensors **2**, **3** and **4** respectively as shown in table 5.7. This indicates that all the synthesized sensors had higher efficiency of photon emission than Quinine sulphate.

Table 5.7: Calculated sensor 2, 3 and 4 quantum yields using standard (quinine sulfphate in 0.1 M perchloric acid).

Sample	Standard (quinine) refractive index	Sample Ref index	Standard quantum yield	Standard gradient	Sample gradient	Sample quantum yield
Sensor **2**	1.33	1.38	0.54	28.81	32.44	**0.6546**
Sensor **3**	1.33	1.39	0.54	28.81	35.28	**0.7228**
Sensor **4**	1.33	1.42	0.54	28.81	33.9	**0.7243**

5.10   Paper disc test

Since this study targeted portable water, it applied test strips as fluoride probes because of low cost and easy accessibility. This was done by monitoring the fluorescence changes in the probe. The addition of TBAF to a solution containing sensors **2**, **3** and **4** resulted in vivid changes in fluorescence intensity with increase in fluoride (TBAF) concentrations of 20 µM, 40 µM, 60 µM, 80 µM, 90 µM and 100 µM as shown in figure 4.15.

The paper disc based assay was capable of selectively detecting fluoride in the existence of other anions (Cl^-, Br^-, I^-, NO_3^-, and SO_4^{2-}). These results are an indication of the potential of compounds 2-4 scaffolds as versatile fluoride sensing probes. In the long term, the paper disc-based assay as illustrated above can be attached to the agile, cheap and portable fluorescence probes to facilitate the swift and affordable fluoride detection.

CHAPTER SIX

RECOMMENDATIONS AND CONCLUSION

6.1 CONCLUSION

Three novel fluoride sensors (**2**, **3** and **4**) were successfully designed, synthesized and structures determined by MS and NMR spectroscopic technique. The sensitivity, selectivity and quantum yields of each of the synthesized compounds were also determined. An investigation on the response of the synthesized sensors **2**, **3** and **4** to environmentally and biologically relevant anions revealed lower levels of background of fluorescence in the range of 2.1 to 3.9. However, their fluorescence responses were not considerably affected due to direct competition with the tested anions apart from fluoride. These results undoubtedly show that environmentally relevant groundwater anions do not impede the fluoride sensing by sensors **2**, **3** and **4**. The detection limits of sensors **2**, **3** and **4** were established to be 4.5 µM (8.5 mg/L), 6.4 µM (1.2×10^{-1} mg/L) and 8.5 µM (1.6×10^{-1} mg/L) respectively in aqueous NaF solutions. However, they confirmed the capacity to determine TBAF at lower concentrations of 0.18 µM (3.4×10^{-3} mg/L), 0.35 µM (6.6×10^{-3} mg/L) and 1.9 µM (3.6×10^{-2} mg/L) respectively**.** This is lower than the present WHO advice for fluoride concentration in domestic water for consumption of 789.4 µM equivalent to 1.5 mgL^{-1}. The second order rate constants for sensors **2**, **3** and **4** were 1.9 x10 M^{-1}min^{-1}, 1.8 x10 M^{-1}min^{-1} and 1.4 x10 M^{-1}min^{-1} demonstrating their ability to rapidly detect the existence of aqueous fluorides in potable water. The quantum yields of sensors **2**, **3** and **4** compared against quinine sulphate (standard) were established to be 0.65, 0.72 and 0.72 respectively. This indicates that all the synthesized sensors had higher efficiency of photon emission than Quinine sulphate.

6.2   RECOMMENDATIONS

Although sensors **2**, **3** and **4** have shown remarkable sensitivity and selectivity for fluoride testing in portable water, there is need to carry out toxicity studies on them before being developed into commercial products. Since sensors **2**, **3** and **4** are new compounds, there is need for repurposing into a variety of applications especially bioactivity against selected pathogens, epifluorescence and many more.

REFERENCES

Abdel-Mottaleb, M. S. A., Hamed, E., Saif, M., & Hafez, H. S. (2018). Binding, and thermodynamics of β-cyclodextrin inclusion complexes with some coumarin laser dyes and coumarin-based enzyme substrates: a simulation study. *Journal of Inclusion Phenomena and Macrocyclic Chemistry*, **92**(3), 319-327.

Abebe, F., Sutton, T., Perkins, P., & Shaw, R. (2018). Two colorimetric fluorescent turn-on chemosensors for detection of Al^{3+} and N_3^- : Synthesis, photophysical and computational studies. *Luminescence*, **33**(7), 1194–1201.

Adimalla, N., Vasa, S. K., & Li, P. (2018). Evaluation of groundwater quality, Peddavagu in Central Telangana (PCT), South India: An insight of controlling factors of fluoride enrichment. *Modeling Earth Systems and Environment*, **4**(2), 841–852.

Ahamad, K. U., Singh, R., Baruah, I., Choudhury, H., & Sharma, M. R. (2018). Equilibrium and kinetics modeling of fluoride adsorption onto activated alumina, alum and brick powder. *Groundwater for Sustainable Development*, **7**, 452–458.

Akumu, E. O., Barasa, S., Lutta, S., & Akenga, T. A. (2021). Potable Water Fluoride Rapid Detection Based on TBAF Desilylation by a Novel Fluorogenic 7-O-tert-butyldimethylsilyl-3-cyano-4-methylcoumarin Compound. *African Journal of Education, Science and Technology*, **6**(3).

Ali, A. (2020). Fluoride concentration and other elements in tooth structure and its effect on dental caries in Kirkuk, Iraq. *Iraqi Geological Journal*, **53**(2), 1–11.

Ali, E. M., Alkuwayti, M. A., Aldayel, M. F., & Abdallah, B. M. (2021). Coumarin derivative, 5′-hydroxy-auraptene, extracted from Lotus lalambensis, displays

antifungal and anti-aflatoxigenic activities against Aspergillus flavus. *Journal of King Saud University-Science*, **33**(1), 101216

Aliaskari, M., & Schäfer, A. I. (2021). Nitrate, Arsenic and Fluoride removal by electrodialysis from brackish groundwater. *Water Research*, **190**, 116683.

Al-Itawi, H. I. (2019). Removal of fluoride from wastewater by calcined gypsum: adsorption and kinetics study, **14**, 13.

Alkış, M., Pekyılmaz, D., Yalçın, E., Aydıner, B., Dede, Y., & Seferoğlu, Z. (2017). H-bond stabilization of a tautomeric coumarin-pyrazole-pyridine triad generates a PET driven, reversible and reusable fluorescent chemosensor for anion detection. *Dyes and Pigments*, **141**, 493-500.

Aloulou, H., Ghorbel, A., Aloulou, W., Ben Amar, R., & Khemakhem, S. (2021). Removal of fluoride ions (F−) from aqueous solutions using modified Turkish zeolite with quaternary ammonium. *Environmental technology*, **42**(9), 1353-1365.

Alshibl, H. M., Al-Abdullah, E. S., & Alkahtani, H. M. (2020). Coumarin: a promising scaffold for design and development of bioactive agents. *Current Bioactive Compounds*, *16*(**6**), 837-852.

Al-Warhi, T., Sabt, A., Elkaeed, E. B., & Eldehna, W. M. (2020). Recent advancements of coumarin-based anticancer agents: An up-to-date review. *Bioorganic Chemistry*, 104163.

Amadeu de Oliveira, F., MacVinish, L. J., Amin, S., Herath, D., Jeggle, P., Mela, I., Pieri, M. 2018). The effect of fluoride on the structure, function, and proteome of intestinal epithelia. *Environmental Toxicology*, **33**(1), 63–71.

Ankidawa, B. A., Audu, D. S., Inuwa, A. M., & Vanke, I. (2020). Assessment of fluoride concentration in groundwater in hong and environs, adamawa state, northeastern nigeria, **5**(2), 12.

Annunziata, F., Pinna, C., Dallavalle, S., Tamborini, L., & Pinto, A. (2020). An overview of coumarin as a versatile and readily accessible scaffold with broad-ranging biological activities. *International Journal of Molecular Sciences*, **21**(13), 4618.

Aoun, A., Darwiche, F., Hayek, S. A., & Doumit, J. (2018). The Fluoride Debate: The Pros and Cons of Fluoridation. *Preventive Nutrition and Food Science*, **23**(3), 171–180.

Asgari, M. S., Mohammadi-Khanaposhtani, M., Kiani, M., Ranjbar, P. R., Zabihi, E., Pourbagher, R. & Rahimi, R. (2019). Biscoumarin-1,2,3-triazole hybrids as novel anti-diabetic agents: Design, synthesis, in vitro α-glucosidase inhibition, kinetic, and docking studies. *Bioorganic Chemistry*, **92**, 103206.

Ashokkumar, P., Weißhoff, H., Kraus, W., & Rurack, K. (2014). Test-Strip-Based Fluorometric Detection of Fluoride in Aqueous Media with a BODIPY-Linked Hydrogen-Bonding Receptor. *Angewandte Chemie International Edition*, **53**(8), 2225–2229.

Asiri, A. M., Al-Ghamdi, N. S. M., Dzudzevic-Cancar, H., Kumar, P., & Khan, S. A. (2019). Physicochemical and Photophysical investigation of newly synthesized carbazole containing pyrazoline-benzothiazole as fluorescent chemosensor for the detection of Cu2+, Fe3+ & Fe2+ metal ion. *Journal of Molecular Structure*, **1195**, 670–680.

Assunção, C. M., Schlueter, N., Rodrigues, J. A., Carvalho, T. S., & Lussi, A. (2019). Do fluoride toothpastes have similar preventive effect in permanent and

primary teeth against erosive tooth wear?. *International journal of paediatric dentistry*, **29**(2), 228-236.

Atta-Eyison, A. A. (2020). Performance Evaluation of Fluorescence and Photostability of Coumarin Disperse Yellow 82. *Journal of Materials Science and Chemical Engineering*, **8**(1), 11.

Avhad, K. C., Patil, D. S., Chitrambalam, S., Sreenath, M. C., Joe, I. H., & Sekar, N. (2018). Viscosity induced emission of red-emitting NLOphoric coumarin morpholine-thiazole hybrid styryl dyes as FMRs: consolidated experimental and theoretical approach. *Optical Materials*, **79**, 90-107.

Avinash, I., Parveen, S., & Anantharaman, G. (2020). Backbone Boron-Functionalized Imidazoles/Imidazolium Salts: Synthesis, Structure, Metalation Studies, and Fluoride Sensing Properties. *Inorganic Chemistry*, **59**(8), 5646–5661.

Babür, B., Seferoğlu, N., & Seferoğlu, Z. (2015). A ratiometric fluorescence chemosensor based on a coumarin–pyrazolone hybrid: the synthesis and an investigation of the photophysical, tautomeric and anion binding properties by spectroscopic techniques and DFT calculations. *Tetrahedron Letters*, **56**(17), 2149-2154.

Banerjee, A., Singh, A., & Roychoudhury, A. (2019). Spermidine application reduces fluoride uptake and ameliorates physiological injuries in a susceptible rice cultivar by activating diverse regulators of the defense machinery. *Environmental Science and Pollution Research*, **26**(36), 36598–36614.

Barathi, M., Kumar, A. S. K., & Rajesh, N. (2019). Impact of fluoride in potable water – An outlook on the existing defluoridation strategies and the road ahead. *Coordination Chemistry Reviews*, **387**, 121–128.

Bardhan, A., & Deiters, A. (2019). Development of photolabile protecting groups and their application to the optochemical control of cell signaling. *Current Opinion in Structural Biology*, **57**, 164–175.

Bekhradnia, A., Domehri, E., & Khosravi, M. (2016). Novel coumarin-based fluorescent probe for selective detection of Cu(II). *Spectrochimica Acta Part A: Molecular and Biomolecular Spectroscopy*, **152**, 18–22.

Bhatia, R., Pathania, S., Singh, V., & Rawal, R. K. (2018). Metal-catalyzed synthetic strategies toward coumarin derivatives. *Chemistry of Heterocyclic Compounds*, **54**(3), 280-291.

Bhatnagar, A., & Sillanpää, M. (2011). A review of emerging adsorbents for nitrate removal from water. *Chemical Engineering Journal*, **168**(2), 493–504.

Bhattacharya, A. K. (2020). A Comprehensive Analysis of Fluoride Contamination in Global Groundwater, **32**.

Biswas, S., Gangopadhyay, M., Barman, S., Sarkar, J., & Singh, N. P. (2016). Simple and efficient coumarin-based colorimetric and fluorescent chemosensor for F^- detection: an ON1–OFF–ON2 fluorescent assay. *Sensors and Actuators B: Chemical*, **222**, 823-828.

Bondu, R., Cloutier, V., Rosa, E., & Roy, M. (2020). An exploratory data analysis approach for assessing the sources and distribution of naturally occurring contaminants (F, Ba, Mn, As) in groundwater from southern Quebec (Canada). *Applied Geochemistry*, **114**, 104500.

Borah, N., Gogoi, A., & Das, G. (2016). Competitive anion binding aptitude of benzimidazole and amide functionality of a non-symmetrical receptor in solid state and solution phase. *Supramolecular Chemistry*, **28**(3-4), 275-283.

Buckley, H. L., Molla, N. J., Cherukumilli, K., Boden, K. S., & Gadgil, A. J. (2018). Addressing technical barriers for reliable, safe removal of fluoride from drinking water using minimally processed bauxite ores. *Development Engineering*, **3**, 175–187.

Cametti, M., Dalla Cort, A., Mandolini, L., Nissinen, M., & Rissanen, K. (2008). Specific recognition of fluoride anion using a metallamacrocycle incorporating a uranyl-salen unit. *New Journal of Chemistry*, **32**(7), 1113-1116.

Cao, D., Liu, Z., Verwilst, P., Koo, S., Jangjili, P., Kim, J. S., & Lin, W. (2019). Coumarin-based small-molecule fluorescent chemosensors. *Chemical reviews*, **119**(18), 10403-10519.

Cao, Z., Cao, Y., Kubota, R., Sasaki, Y., Asano, K., Lyu, X., & Zhang, Z. (2020). Fluorescence Anion Chemosensor Array Based on Pyrenylboronic Acid. *Frontiers in Chemistry*, **8**, 414.

Carneiro, A., Matos, M. J., Uriarte, E., & Santana, L. (2021). Trending Topics on Coumarin and Its Derivatives in 2020. *Molecules*, **26**(2), 501.

Chao, C., Zhao, Y., Song, Q., Min, J., Wang, Z., Ma, H., & Li, X. (2019). Volcanic rock-based ceramsite adsorbent for highly selective fluoride removal: function optimization and mechanism. *Journal of Chemical Technology & Biotechnology*, **94**(7), 2263-2273.

Chen, J. X., Liu, W., Zheng, C. J., Wang, K., Liang, K., Shi, Y. Z., & Zhang, X. H. (2017). Coumarin-based thermally activated delayed fluorescence emitters with high external quantum efficiency and low efficiency roll-off in the devices. *ACS applied materials & interfaces*, **9**(10), 8848-8854.

Chen, J.-S., Zhou, P.-W., Zhao, L., & Chu, T.-S. (2014). A DFT/TDDFT study of the excited state intramolecular proton transfer based sensing mechanism for the aqueous fluoride chemosensor BTTPB. *RSC Adv.*, **4**(1), 254–259.

Chen, L., He, S., He, B.-Y., Wang, T.-J., Su, C.-L., Zhang, C., & Jin, Y. (2012). Synthesis of Iron-Doped Titanium Oxide Nanoadsorbent and Its Adsorption Characteristics for Fluoride in Drinking Water. *Industrial & Engineering Chemistry Research*, **51**(40), 13150–13156.

Chen, L., Wu, L., Duan, W., Wang, T., Li, L., Zhang, K., & Xiong, F. (2018). Photoredox-catalyzed cascade radical cyclization of ester arylpropiolates with CF_3SO_2Cl to construct 3-trifluoromethyl coumarin derivatives. *The Journal of organic chemistry*, **83**(15), 8607-8614.

Chen, Y., Lam, J. W. Y., Kwok, R. T. K., Liu, B., & Tang, B. Z. (2019). Aggregation-induced emission: Fundamental understanding and future developments. *Materials Horizons*, **6**(3), 428–433.

Cherukumilli, K., Delaire, C., Amrose, S., & Gadgil, A. J. (2017). Factors Governing the Performance of Bauxite for Fluoride Remediation of Groundwater. *Environmental Science & Technology*, **51**(4), 2321–2328.

Côrtes, L. N., Druzian, S. P., Streit, A. F. M., Sant'anna Cadaval Junior, T. R., Collazzo, G. C., & Dotto, G. L. (2019). Preparation of carbonaceous materials from pyrolysis of chicken bones and its application for fuchsine adsorption. *Environmental Science and Pollution Research*, **26**(28), 28574–28583.

Cotruvo, J. A. (2017). 2017 WHO Guidelines for Drinking Water Quality: First Addendum to the Fourth Edition. *Journal—American Water Works Association*, **109**, 44–51.

Custelcean, R., & Moyer, B. A. (2007). Anion separation with metal–organic frameworks. *European Journal of Inorganic Chemistry*, **2007**(10), 1321-1340.

Damtie, M. M., Woo, Y. C., Kim, B., Hailemariam, R. H., Park, K.-D., Shon, H. K., & Park, C. (2019). Removal of fluoride in membrane-based water and wastewater treatment technologies: Performance review. *Journal of Environmental Management*, **251**, 109524.

Darchen, A., Sivasankar, V., Prabhakaran, M., & Bharathi, CH. B. (2016). Health Effects of Direct or Indirect Fluoride Ingestion. In V. Sivasankar (Ed.), *Surface Modified Carbons as Scavengers for Fluoride from Water,* 33–62. Cham: Springer International Publishing.

Dehghani, M. H., Farhang, M., Alimohammadi, M., Afsharnia, M., & Mckay, G. (2018). Adsorptive removal of fluoride from water by activated carbon derived from CaCl$_2$-modified *Crocus sativus* leaves: Equilibrium adsorption isotherms, optimization, and influence of anions. *Chemical Engineering Communications*, **205**(7), 955–965.

Sivamani, J., & Siva, A. (2017). Self-assembly,"turn-on" fluorescent detection of fluoride ion using uracil based azo derivatives and their application in imaging of living cells. *Sensors and Actuators B: Chemical*, **242**, 423-433.

Dehghani, M. H., Karri, R. R., Lima, E. C., Mahvi, A. H., Nazmara, S., Ghaedi, A. M., & Fazlzadeh, M. (2020). Regression and mathematical modeling of fluoride ion adsorption from contaminated water using a magnetic versatile biomaterial & chelating agent: Insight on production & experimental approaches, mechanism and effects of potential interferers. *Journal of Molecular Liquids*, **315**, 113653.

Delgadillo-Velasco, L., Hernández-Montoya, V., Cervantes, F. J., Montes-Morán, M. A., & Lira-Berlanga, D. (2017). Bone char with antibacterial properties for fluoride removal: preparation, characterization and water treatment. *Journal of environmental management*, **201**, 277-285.

Deng, X., Zhuang, Z., Liu, H., Qiu, P., & Wang, K. (2019). Measurement of 3-photon excitation and emission spectra and verification of Kasha's rule for selected fluorescent proteins excited at the 1700-nm window. *Optics Express*, **27**(9), 12723.

Dessalegne, M., Zewge, F., Mammo, W., Woldetinsae, G., & Diaz, I. (2018). Effective fluoride adsorption by aluminum oxide modified clays: Ethiopian bentonite vs commercial montmorillonite. *Bulletin of the Chemical Society of Ethiopia*, **32**(2), 199-211.

Dhanunjayarao, K., Mukundam, V., & Venkatasubbaiah, K. (2014). A highly selective ratiometric detection of F^- based on excited-state intramolecular proton-transfer (imidazole) materials. *J. Mater. Chem. C*, **2**(40), 8599–8606.

Dharmaratne, R. (2019). Exploring the role of excess fluoride in chronic kidney disease: A review. *Human & Experimental Toxicology*, **38**(3), 269–279.

Dhilleswara, Rao, Vaddi, & Venkata Subba. (2021). Use of Aluminium Metal Embedded ThujaOccidentalis Leaves Carbon (AMETLC) for Fluoride Removal from Water: Equilibrium and Kinetic Studies. *Journal of Environmental Treatment Techniques*, **9**(2), 480–490.

Dhillon, A., Nair, M., & Kumar, D. (2016). Analytical methods for determination and sensing of fluoride in biotic and abiotic sources: A review. *Analytical Methods*, **8**(27), 5338–5352.

Dissanayake, C. B., & Chandrajith, R. (2019). Fluoride and hardness in groundwater of tropical regions—Review of recent evidence indicating tissue calcification and calcium phosphate nanoparticle formation in kidney tubules. *Ceylon Journal of Science*, **48**(3), 197.

Dong, H., Zhao, J., Yang, H., & Zheng, Y. (2018). The mechanism of ratiometric fluoride sensing and the ESIPT process for 2,6-dibenzothiazolylphenol and its derivative. *Organic Chemistry Frontiers*, **5**(8), 1241–1247.

Dou, X. (2012). Remediating fluoride from water using hydrous zirconium oxide. *Chemical Engineering Journal*, 10.

El-Sawy, E. R., Abdelwahab, A. B., & Kirsch, G. (2021). Synthetic Routes to Coumarin(Benzopyrone)-Fused Five-Membered Aromatic Heterocycles Built on the α-Pyrone Moiety. Part 1: Five-Membered Aromatic Rings with One Heteroatom. *Molecules*, **26**(2), 483.

Emam, S. H., Sonousi, A., Osman, E. O., Hwang, D., Kim, G. D., & Hassan, R. A. (2021). Design and synthesis of methoxyphenyl-and coumarin-based chalcone derivatives as anti-inflammatory agents by inhibition of NO production and down-regulation of NF-κB in LPS-induced RAW264. 7 macrophage cells. *Bioorganic Chemistry*, **107**, 104630.

Erşatır, M., Yıldırım, M., Giray, E. S., & Yalın, S. (2020). Synthesis and antiproliferative evaluation of novel biheterocycles based on coumarin and 2-aminoselenophene-3-carbonitrile unit. *Monatshefte für Chemie-Chemical Monthly*, **151**(4), 625-636.

Esparza, J. L., Gómez, M., & Domingo, J. L. (2019). Role of Melatonin in Aluminum-Related Neurodegenerative Disorders: A Review. *Biological Trace Element Research*, **188**(1), 60–67.

Farahi, M., Karami, B., Keshavarz, R., & Khosravian, F. (2017). Nano-Fe$_3$O$_4$@ SiO$_2$- supported boron sulfonic acid as a novel magnetically heterogeneous catalyst for the synthesis of pyrano coumarins. *RSC Advances*, **7**(74), 46644-46650.

Feng, A., Jia, Y., Huang, L., Wang, L., Zhou, G., Wang, S., & Liu, P. (2019). 1, 6- Elimination reaction induced detection of fluoride ions in vitro and in vivo based on a NIR fluorescent probe. *Spectrochimica Acta Part A: Molecular and Biomolecular Spectroscopy*, **220**, 117108.

Fito, J., Said, H., Feleke, S., & Worku, A. (2019). Fluoride removal from aqueous solution onto activated carbon of Catha edulis through the adsorption treatment technology. *Environmental Systems Research*, **8**(1), 1-10.

Fournier, L., Gauron, C., Xu, L., Aujard, I., Le Saux, T., Gagey-Eilstein, N., & Maurin, S. (2013). A Blue-Absorbing Photolabile Protecting Group for *in Vivo* Chromatically Orthogonal Photoactivation. *ACS Chemical Biology*, **8**(7), 1528–1536.

Gale, P. A., & Caltagirone, C. (2018). Fluorescent and colorimetric sensors for anionic species. *Coordination Chemistry Reviews*, **354**, 2–27.

Gamaethiralalage, J. G., Singh, K., Sahin, S., Yoon, J., Elimelech, M., Suss, M. E., & Liang, P. (2021). Recent advances in ion selectivity with capacitive deionization. *Energy & Environmental Science*, **14**(3), 1095–1120.

Gan, Y., Wang, X., Zhang, L., Wu, B., Zhang, G., & Zhang, S. (2019). Coagulation removal of fluoride by zirconium tetrachloride: performance evaluation and mechanism analysis. *Chemosphere*, **218**, 860-868.

Guan, J., Tu, Q., Chen, L., Yuan, M. S., & Wang, J. (2019). A benzothiazole-rhodol based luminophor: ESIPT-induced AIE and an application for detecting Fe^{2+}

ion. *Spectrochimica Acta Part A: Molecular and Biomolecular Spectroscopy*, *220*, 117114.

Nonell, S., Gandioso, A., Contreras, S., Melnyk, I., Oliva, J., Velasco Castrillo, D. & Marchán Sancho, V. (2017). Development of green/red-absorbing chromophores based on a coumarin scaffold that are useful as caging groups. *Journal of Organic Chemistry.* **8**(10) 5398-5408.

Garci, A., Beldjoudi, Y., Kodaimati, M. S., Hornick, J. E., Nguyen, M. T., Cetin, M. M., & Stern, C. L. (2020). Mechanical-Bond-Induced Exciplex Fluorescence in an Anthracene-Based Homo[2]catenane. *Journal of the American Chemical Society*, **142**(17), 7956–7967.

Gebrewold, B. D., Kijjanapanich, P., Rene, E. R., Lens, P. N. L., & Annachhatre, A. P. (2019). Fluoride removal from groundwater using chemically modified rice husk and corn cob activated carbon. *Environmental Technology*, **40**(22), 2913–2927.

Geleta Ebsa, D., & Kebede, A. B. (2021). Defluoridation of drinking water by modified natural zeolite with Cationic surfactant, in case of Ziway town, Ethiopia. *Drinking Water Engineering and Science Discussions*, 1-14.

George, A. M., & Tembhurkar, A. R. (2020). Taguchi experimental design for adsorptive removal of fluoride from water using novel Ficus Glomerata Bark-developed biosorbent. *International Journal of Environmental Science and Technology*, **17**, 4829-4840.

Ghate, M., Kusanur, R. A., & Kulkarni, M. V. (2005). Synthesis and in vivo analgesic and anti-inflammatory activity of some bi heterocyclic coumarin derivatives. *European journal of medicinal chemistry*, **40**(9), 882-887.

Ghomi, J. S., & Akbarzadeh, Z. (2018). Ultrasonic accelerated Knoevenagel condensation by magnetically recoverable MgFe$_2$O$_4$ nanocatalyst: A rapid and green synthesis of coumarins under solvent-free conditions. *Ultrasonics sonochemistry*, **40**, 78-83.

Gillies, E. R., Deiss, F., Staedel, C., Schmitter, J. M., & Huc, I. (2007). Development and Biological Assessment of Fully Water-Soluble Helical Aromatic Amide Foldamers. *Angewandte Chemie International Edition*, **46**(22), 4081-4084.

Godugu, K., Gundala, T. R., Bodapati, R., Yadala, V. D. S., Loka, S. S., & Nallagondu, C. G. R. (2020). Synthesis, photophysical and electrochemical properties of donor–acceptor type hydrazinyl thiazolyl coumarins. *New Journal of Chemistry*, **44**(17), 7007-7016.

Gogoi, C., Saikia, J., Sarmah, S., Sinha, D., & Goswamee, R. L. (2018). Removal of Fluoride from Water by Locally Available Sand Modified with a Coating of Iron Oxides. *Water, Air, & Soil Pollution*, **229**(4), 118.

Gopakumar, D. A., Pasquini, D., Henrique, M. A., de Morais, L. C., Grohens, Y., & Thomas, S. (2017). Meldrum's Acid Modified Cellulose Nanofiber-Based Polyvinylidene Fluoride Microfiltration Membrane for Dye Water Treatment and Nanoparticle Removal. *ACS Sustainable Chemistry & Engineering*, **5**(2), 2026–2033.

Goud, K. Y., Teymourian, H., Sandhu, S. S., Tostado, N., Mishra, R. K., Moore, L. C., & Harvey, S. P. (2020). OPAA/fluoride biosensor chip towards field detection of G-type nerve agents. *Sensors and Actuators B: Chemical*, **320**, 128344.

Gouda, M. A., Hussein, B. H., El-Demerdash, A., Ibrahim, M. E., Salem, M. A., Helal, M. H., & Hamama, W. S. (2020). A review: Synthesis and medicinal

importance of coumarins and their analogues (Part II). *Current Bioactive Compounds*, **16**(7), 993-1008.

Grandjean, P. (2019). Developmental fluoride neurotoxicity: an updated review. *Environmental Health*, **18**(1), 1-17.

Grimm, J. B., Heckman, L. M., & Lavis, L. D. (2013). The chemistry of small-molecule fluorogenic probes. *Progress in molecular biology and translational science*, **113**, 1-34.

Gryko, D. T. (2002). Recent advances in the synthesis of corroles and core-modified corroles. *European Journal of Organic Chemistry*, **2002**(11), 1735-1743.

Grzegorzek, M., Majewska-Nowak, K., & Ahmed, A. E. (2020). Removal of fluoride from multicomponent water solutions with the use of monovalent selective ion-exchange membranes. *Science of the Total Environment*, **722**, 137681.

Guerrero, T., Vázquez-Ortega, F., Lagunes, I., Ortiz-Blanco, E., Sosa-Ortiz, G., Tovar-Miranda, R., & Trigos, Á. (2021). Antagonistic activity of hydroxycoumarin-based antioxidants as possible singlet oxygen precursor photosensitizers. *Dyes and Pigments*, **192**, 109447.

Guo, W., Jin, L., Hu, S., & Guo, Q. (2017). Method Development for the Determination of Total Fluorine in Foods by Tandem Inductively Coupled Plasma Mass Spectrometry with a Mass-Shift Strategy. *Journal of Agricultural and Food Chemistry*, **65**(16), 3406–3412.

Habuda-Stanić, M., Ravančić, M., & Flanagan, A. (2014). A Review on Adsorption of Fluoride from Aqueous Solution. *Materials*, **7**(9), 6317–6366.

Han, J., Zhang, J., Gao, M., Hao, H., & Xu, X. (2019). Recent advances in chromo-fluorogenic probes for fluoride detection. *Dyes and Pigments*, **162**, 412–439.

Harborne, J. B. (1982). The natural coumarins: occurrence, chemistry and biochemistry. *Plant, Cell & Environment*, **5**(6), 435-436.

He, G., Hua, X., Yang, N., Li, L., Xu, J., Yang, L., & Wang, Q. (2019). Synthesis and application of a "turn on" fluorescent probe for glutathione based on a copper complex of coumarin hydrazide Schiff base derivative. *Bioorganic Chemistry*, **91**, 103176.

He, J., Hong, B., Bian, M., Jin, H., Chen, J., Shao, J., & Zhang, F. (2019). Docosahexaenoic acid inhibits hepatic stellate cell activation to attenuate liver fibrosis in a PPARγ-dependent manner. *International Immunopharmacology*, **75**, 105816.

He, Y., Zhang, L., An, X., Wan, G., Zhu, W., & Luo, Y. (2019). Enhanced fluoride removal from water by rare earth (La and Ce) modified alumina: Adsorption isotherms, kinetics, thermodynamics and mechanism. *Science of the Total Environment*, **688**, 184–198.

Hennig, A.-L. K., Deodato, D., Asad, N., Herbivo, C., & Dore, T. M. (2020). Two-Photon Excitable Photoremovable Protecting Groups Based on the Quinoline Scaffold for Use in Biology. *The Journal of Organic Chemistry*, **85**(2), 726–744.

Hirsch, A. K., Fischer, F. R., & Diederich, F. (2007). Phosphate recognition in structural biology. *Angewandte Chemie International Edition*, **46**(3), 338-352.

Hossein Javadi, S., Zareyee, D., Monfared, A., Didehban, K., & Mirshokraee, S. A. (2020). Silica-coated Fe_3O_4 magnetic nanoparticles-supported sulfonic acid as a highly active and reusable catalyst in chemoselective deprotection of tert-butyldimethylsilyl (TBDMS) ethers. *Phosphorus, Sulfur, and Silicon and the Related Elements*, **195**(1), 7-12.

Hu, C., Su, T.-R., Lin, T.-J., Chang, C.-W., & Tung, K.-L. (2018). Yellowish and blue luminescent graphene oxide quantum dots prepared *via* a microwave-assisted hydrothermal route using H_2O_2 and $KMnO_4$ as oxidizing agents. *New Journal of Chemistry*, **42**(6), 3999–4007.

Iafisco, M., Degli Esposti, L., Ramírez-Rodríguez, G. B., Carella, F., Gómez-Morales, J., Ionescu, A. C., & Brambilla, E. (2018). Fluoride-doped amorphous calcium phosphate nanoparticles as a promising biomimetic material for dental remineralization. *Scientific Reports*, **8**(1), 17016.

Ingalagondi, P. K., Patil, O., Sankarappa, T., & Hanagodimath, S. M. (2019, April). Spectroscopic studies of synthesized coumarins. In *AIP Conference Proceedings,* **2100**(1), 20112. AIP Publishing LLC.

Inglezakis, V. J., Balsamo, M., & Montagnaro, F. (2020). A Fractal-Based Correlation for Time-Dependent Surface Diffusivity in Porous Adsorbents. *Processes*, **8**(6), 689.

Islam, M. R., Warsi, F., Alam, M. S., & Ali, M. (2021). Solvatochromic behaviour of coumarin 102 in PEGs+ ionic liquid/water solutions: Role of solute-solvent or solvent-solvent interactions. *Journal of Molecular Liquids*, **334**, 116483.

Jaafari, J., Barzanouni, H., Mazloomi, S., Amir Abadi Farahani, N., Sharafi, K., Soleimani, P., & Haghighat, G. A. (2020). Effective adsorptive removal of reactive dyes by magnetic chitosan nanoparticles: Kinetic, isothermal studies and response surface methodology. *International Journal of Biological Macromolecules*, **164**, 344–355.

Jain, A., Gupta, R., & Agarwal, M. (2017). Instantaneous and Selective Bare Eye Detection of Inorganic Fluoride Ion by Coumarin–Pyrazole-Based Receptors. *Journal of Heterocyclic Chemistry*, **54**(5), 2808-2816.

Jeffrey Kuo, C.-F., Wang, H.-Y., Prasannan, A., Lai, J.-Y., Wang, J.-S., Chang, H.-M., & Tsai, H. C. (2020). *In vivo* degradation study of polyvinylidene fluoride/polybutylene succinate/modified organic montmorillonite nanocomposite films implanted in the gastrointestinal tract. *Polymer Degradation and Stability*, **172**, 109058.

Jeyaseelan, A., Naushad, Mu., Ahamad, T., & Viswanathan, N. (2021). Design and development of amine functionalized iron based metal organic frameworks for selective fluoride removal from water environment. *Journal of Environmental Chemical Engineering*, **9**(1), 104563.

Jiang, Y., Chen, H., Yang, X., & Feng, W. (2021). Neodymium Modified Chitosan/PMMA Integrated Thin-Core Fiber for Trace Fluoride Ion Detection. *IEEE Sensors Journal*, **21**(3), 2559–2564.

Jiao, Y., Zhu, B., Chen, J., & Duan, X. (2015). Fluorescent Sensing of Fluoride in Cellular System, **5**(2), 15.

Jiménez-Córdova, M. I., Sánchez-Peña, L. C., Barrera-Hernández, Á., González-Horta, C., Barbier, O. C., & Del Razo, L. M. (2019). Fluoride exposure is associated with altered metabolism of arsenic in an adult Mexican population. *Science of The Total Environment*, **684**, 621–628.

Johnston, N. R., & Strobel, S. A. (2020). Principles of fluoride toxicity and the cellular response: A review. *Archives of toxicology*, **94**(4), 1051-1069.

Joshi, P. P. (2021). A Review on Biological Activities of Linear Pyranocoumarins, **4**, 8.

Jung, Y., Jung, J., Huh, Y., & Kim, D. (2018). Benzo[g]coumarin-Based Fluorescent Probes for Bioimaging Applications. *Journal of Analytical Methods in Chemistry*, **2018**, 1–11.

Kabir, H., Gupta, A. K., & Tripathy, S. (2020). Fluoride and human health: Systematic appraisal of sources, exposures, metabolism, and toxicity. *Critical Reviews in Environmental Science and Technology*, **50**(11), 1116–1193.

Kai, Ji, Wu, H., Chen, J., Shen, J., Wang, X., Wu, H., & Liu, C. (2016). A selective chromofluorogenic chemodosimeter for fluoride ions based on distyrylbenzenes derivatives containing dual Si–O groups. *Luminescence*, **31**(4), 924-928.

Kalamkar, S., Kalambe, A., Doye, M., & Shende, N. (2021). A Review of Various Techniques for Removal of Fluoride from Water, **10**(2), 7.

Kalavathy, S. (2017). Low Cost Adsorbents for Removal of Fluoride from Water—An Overview, 5.

Kanrar, S. (2020). One-pot synthesis of Cr(III)-incorporated Zr(IV) oxide for fluoride remediation: A lab to field performance evaluation study. *Environ Sci Pollut Res*, 16.

Karunanidhi, D., Aravinthasamy, P., Deepali, M., Subramani, T., & Roy, P. D. (2020). The effects of geochemical processes on groundwater chemistry and the health risks associated with fluoride intake in a semi-arid region of South India. *RSC Advances*, **10**(8), 4840–4859.

Kaur, N., Kaur, G., Fegade, U. A., Singh, A., Sahoo, S. K., Kuwar, A. S., & Singh, N. (2017). Anion sensing with chemosensors having multiple NH recognition units. *TrAC Trends in Analytical Chemistry*, **95**, 86–109.

Kazi, T. G., Brahman, K. D., Baig, J. A., & Afridi, H. I. (2018). A new efficient indigenous material for simultaneous removal of fluoride and inorganic arsenic species from groundwater. *Journal of Hazardous Materials*, **357**, 159–167.

Keesari, T., Pant, D., Roy, A., Sinha, U. K., Jaryal, A., Singh, M., & Jain, S. K. (2021). Fluoride Geochemistry and Exposure Risk through Groundwater Sources in Northeastern Parts of Rajasthan, India. *Archives of Environmental Contamination and Toxicology*, **80**(1), 294–307.

Khalil, R. R., & Mustafa, Y. F. (2020). Phytochemical, antioxidant and antitumor studies of coumarins extracted from Granny Smith apple seeds by different methods. *Syst Rev Pharm*, **11**(2), 57-63.

Khan, S. A., & Kumar, P. (2021). Photophysical and Physicochemical Investigation of Newly Synthesized Polycyclic Pyrazoline-Benzothiazole as Fluorescence Chemosensor for the Detection of Cu $^{2+}$ Metal Ion. *Polycyclic Aromatic Compounds*, **41**(3), 576–592.

Khandare, A. L., Validandi, V., Gourineni, S. R., Gopalan, V., & Nagalla, B. (2018). Dose-dependent effect of fluoride on clinical and subclinical indices of fluorosis in school going children and its mitigation by supply of safe drinking water for 5 years: An Indian study. *Environmental Monitoring and Assessment*, **190**(3), 110.

Kikuchi, M., Arioka, Y., Tafu, M., & Irie, M. (2020). Changes in fluoride removal ability of chicken bone char with changes in calcination time. *International Journal of Ceramic Engineering & Science*, **2**(2), 83–91.

Kim, E., Kim, H. J., Bae, D. R., Lee, S. J., Cho, E. J., Seo, M. R., & Jung, J. H. (2008). Selective fluoride sensing using organic–inorganic hybrid nanomaterials containing anthraquinone. *New Journal of Chemistry*, **32**(6), 1003-1007.

Kim, J. I., Juwarker, H., Liu, X., Lah, M. S., & Jeong, K. S. (2010). Selective sulfate binding induces helical folding of an indolocarbazole oligomer in solution and solid state. *Chemical communications*, **46**(5), 764-766.

Kimambo, V., Bhattacharya, P., Mtalo, F., Mtamba, J., & Ahmad, A. (2019). Fluoride occurrence in groundwater systems at global scale and status of defluoridation – State of the art. *Groundwater for Sustainable Development*, **9**, 100223.

Kitamura, N., Fukagawa, T., Kohtani, S., Kitoh, S. I., Kunimoto, K. K., & Nakagaki, R. (2007). Synthesis, absorption, and fluorescence properties and crystal structures of 7-aminocoumarin derivatives. *Journal of Photochemistry and Photobiology A: Chemistry*, **188**(2-3), 378-386.

Kodlady, S. N., Narayana, B., Sarojini, B. K., Gauthama, B. U., & Manjunatha, J. G. (2021). Colorimetric sensor based on hydrazine moiety for rapid and selective detection of fluoride ion via intramolecular charge transfer. *International Journal of Environmental Analytical Chemistry*, 1–19.

Korde, S. (2020). Novel mesoporous chitosan-zirconia-ferrosoferric oxide as magnetic composite for defluoridation of water. *Journal of Environmental Chemical Engineering*, 10.

Kraimi, A., Belboukhari, N., Sekkoum, K., & Aboul-Enein, H. Y. (2021). Chiral Anticoagulants Drugs Based on Coumarin. *Aditum Journal of Clinical and Biomedical Research*, **2**(1).

Kubik, S., Reyheller, C., & Stüwe, S. (2005). Recognition of anions by synthetic receptors in aqueous solution. *Journal of inclusion phenomena and macrocyclic chemistry*, **52**(3), 137-187.

Kumar Patel, R., Kumar Chawla, A., Loulergue, P., Teychene, B., & Pandey, J. K. (2019). 3D printed microchannel loaded with hematite nanoadsorbent for fluoride removal from water. *Materials Letters*, **254**, 190–193.

Kumar, G. K., Kamath, M. S., & Mallapur, P. S. (2016). Defluoridation of water by using low cost activated carbon prepared from lemon peels. *J. Basic Appl. Eng. Res*, **3**, 658-660.

Kumari, U., Siddiqi, H., Bal, M., & Meikap, B. C. (2020). Calcium and zirconium modified acid activated alumina for adsorptive removal of fluoride: Performance evaluation, kinetics, isotherm, characterization and industrial wastewater treatment. *Advanced Powder Technology*, **31**(5), 2045–2060.

Kusrini, E., Paramesti, S. N., Zulys, A., Daud, N. Z. A., Usman, A., Wilson, L. D., & Sofyan, N. (2019). Kinetics, isotherm, thermodynamic and bioperformance of defluoridation of water using praseodymium-modified chitosan. *Journal of Environmental Chemical Engineering*, **7**(6), 103498.

Kwon, S.-M., & Shin, H.-S. (2015). Simple determination of fluoride in biological samples by headspace solid-phase microextraction and gas chromatography–tandem mass spectrometry. *Journal of Chromatography A*, **1407**, 216–221.

Lacson, C. F. Z., Lu, M.-C., & Huang, Y.-H. (2020). Fluoride network and circular economy as potential model for sustainable development-A review. *Chemosphere*, **239**, 124662.

Li, A. F., Wang, J. H., Wang, F., & Jiang, Y. B. (2010). Anion complexation and sensing using modified urea and thiourea-based receptors. *Chemical Society Reviews*, **39**(10), 3729-3745.

Li, D. & ZhongzhenTian. (2020). Benzimidazole-isoquinolinone functioned thiourea for selective and reversible recognition of fluoride ion. *Journal of Molecular Structure*, **1206**, 127631.

Li, L. I., Yun, S. H. E. N., Yuan-Hui, Z. H. A. O., Lan, M. U., Xi, Z. E. N. G., Redshaw, C., & Gang, W. E. I. (2016). A single chemosensor for multiple

analytes: Fluorogenic and ratiometric absorbance detection of Zn^{2+}, Mg^{2+} and F−, and its cell imaging. *Sensors and Actuators B: Chemical*, **226**, 279-288.

Li, Y.-H., Wang, S., Zhang, X., Wei, J., Xu, C., Luan, Z., & Wu, D. (2003). Adsorption of fluoride from water by aligned carbon nanotubes. *Materials Research Bulletin*, **38**(3), 469–476.

Liang, C., He, Y., Liu, Y., Gao, Y., Han, Y., Li, X., & Zhao, Y. (2020). Fluoride exposure alters the ultra-structure of sperm flagellum via reducing key protein expressions in testis. *Chemosphere*, **246**, 125772.

Lin, Q., Yang, L., Wang, Z., Hua, Y., Zhang, D., Bao, B., & Bao, C. (2018). Coumarin Photocaging Groups Modified with an Electron-Rich Styryl Moiety at the 3-Position: Long-Wavelength Excitation, Rapid Photolysis, and Photobleaching. *Angewandte Chemie International Edition*, **57**(14), 3722–3726.

Liu, S., Zhang, L., Zhou, P., Yang, Y., & Wu, W. (2018). Distinctive fluoride fluorescent probes with ratiometric characteristics combinate desilylation, hydrogen bond and ESIPT process: Spectral and mechanistic studies. *Sensors and Actuators B: Chemical*, **255**, 401–407.

Liu, W.-G., Wei, S., Zhang, J., Ao, C., Liu, F.-T., Cai, B., Zhou, & H.-Y. (2020). An improved separation scheme for Sr through fluoride coprecipitation combined with a cation-exchange resin from geological samples with high Rb/Sr ratios for high-precision determination of Sr isotope ratios. *Journal of Analytical Atomic Spectrometry*, **35**(5), 953–960.

Lončarić, M., Sušjenka, M., & Molnar, M. (2020). An Extensive Study of Coumarin Synthesis via Knoevenagel condensation in Choline Chloride Based Deep Eutectic Solvents. *Current Organic Synthesis*, **17**(2), 98-108.

Ma, L., Leng, T., Wang, K., Wang, C., Shen, Y., & Zhu, W. (2017). A coumarin-based fluorescent and colorimetric chemosensor for rapid detection of fluoride ion. *Tetrahedron*, **73**(10), 1306–1310.

Ma, L., Leng, T., Wang, K., Wang, C., Shen, Y., & Zhu, W. (2017). A coumarin-based fluorescent and colorimetric chemosensor for rapid detection of fluoride ion. *Tetrahedron*, **73**(10), 1306-1310.

Maeda, H. (2008). Anion-responsive supramolecular gels. *Chemistry–A European Journal*, **14**(36), 11274-11282.

Magri, D. C. (2021). Logical sensing with fluorescent molecular logic gates based on photoinduced electron transfer. *Coordination Chemistry Reviews*, **426**, 213598.

Mahapatra, A. K., Maiti, K., Sahoo, P., & Nandi, P. K. (2013). A new colorimetric and fluorescent bis (coumarin) methylene probe for fluoride ion detection based on the proton transfer signaling mode. *Journal of luminescence*, **143**, 349-354.

Mahoney, K. M., Goswami, P. P., & Winter, A. H. (2013). Self-immolative aryl phthalate esters. *The Journal of organic chemistry*, **78**(2), 702-705.

Malago, J. (2017). Fluoride Levels in Surface and Groundwater in Africa: A Review. *American Journal of Water Science and Engineering*, **3**(1), 1.

Mamidala, S., Peddi, S. R., Aravilli, R. K., Jilloju, P. C., Manga, V., & Vedula, R. R. (2021). Microwave irradiated one pot, three component synthesis of a new series of hybrid coumarin based thiazoles: Antibacterial evaluation and molecular docking studies. *Journal of Molecular Structure*, **1225**, 129114.

Mikrut, P., Kobielusz, M., & Macyk, W. (2019). Spectroelectrochemical characterization of euhedral anatase TiO_2 crystals – Implications for photoelectrochemical and photocatalytic properties of {001} {100} and {101} facets. *Electrochimica Acta*, **310**, 256–265.

Millar, G. J., Couperthwaite, S. J., Dawes, L. A., Thompson, S., & Spencer, J. (2017). Activated alumina for the removal of fluoride ions from high alkalinity groundwater: New insights from equilibrium and column studies with multicomponent solutions. *Separation and Purification Technology*, **187**, 14–24.

Minami, N., & Wajima, T. (2021). Preparation of fluoride adsorbent from zircon sand using mechanochemical treatment, and its application for fluoride removal. *International Journal*, **20**(81), 118-124.

Minja, R. (2019). Practical Approach for Removal of Natural Organic Matter and defluoridation of Maji ya Chai river Water: Use of Acid Pre-treated Bone Char and Coagulants. *Tanzania Journal of Engineering and Technology*, **38**(2), 204–206.

Miranda, G. H. N., Gomes, B. A. Q., Bittencourt, L. O., Aragão, W. A. B., Nogueira, L. S., Dionizio, A. S., & Buzalaf, M. A. R. (2018). Chronic Exposure to Sodium Fluoride Triggers Oxidative Biochemistry Misbalance in Mice: Effects on Peripheral Blood Circulation. *Oxidative Medicine and Cellular Longevity*, 1–8.

Miretzky, P., & Cirelli, A. F. (2011). Fluoride removal from water by chitosan derivatives and composites: A review. *Journal of Fluorine Chemistry*, **132**(4), 231–240.

Mirosanloo, A., Zareyee, D., & Khalilzadeh, M. A. (2018). Recyclable cellulose nanocrystal supported Palladium nanoparticles as an efficient heterogeneous catalyst for the solvent-free synthesis of coumarin derivatives via von Pechmann condensation: Heterogeneous nanocatalyst. *Applied Organometallic Chemistry*, **32**(12), e4546.

Yuan, X., Xu, X., Zhao, C., Zhang, F., Lu, Y., Shen, Y., & Wang, C. (2017). A novel colorimetric and fluorometric fluoride ion probe based on photoinduced electron transfer signaling mechanism. *Sensors and Actuators B: Chemical*, **253**, 1096-1105.

Mizuta, T., Sueyoshi, K., Endo, T., & Hisamoto, H. (2021). Lipophilic Fluorescent Dye Liquids: Förster Resonance Energy Transfer-Based Fluorescence Amplification for Ion Selective Optical Sensors Based on a Solvent Polymeric Membrane. *Analytical Chemistry*, **93**(9), 4143–4148.

Mobeen, N., & Kumar, P. (2017). Defluoridation techniques - A critical review. *Asian Journal of Pharmaceutical and Clinical Research*, **10**(6), 64.

Modi, Dr. S. (2013). Merits and Demerits of different technologies of defluoridation for drinking water. *IOSR Journal of Environmental Science, Toxicology and Food Technology*, **3**(2), 24–27.

Mohamed, M. G., Hsu, K. C., & Kuo, S. W. (2015). Bifunctional polybenzoxazine nanocomposites containing photo-crosslinkable coumarin units and pyrene units capable of dispersing single-walled carbon nanotubes. *Polymer Chemistry*, **6**(13), 2423-2433.

Mohammadi, A. A., Yousefi, M., Yaseri, M., Jalilzadeh, M., & Mahvi, A. H. (2017). Skeletal fluorosis in relation to drinking water in rural areas of West Azerbaijan, Iran. *Scientific Reports*, **7**(1), 17300.

Mohapatra, M., Hariprasad, D., Mohapatra, L., Anand, S., & Mishra, B. K. (2012). Mg-doped nano ferrihydrite—A new adsorbent for fluoride removal from aqueous solutions. *Applied Surface Science*, **258**(10), 4228–4236.

Moirana, R. L., Kivevele, T., Mkunda, J., Mtei, K., & Machunda, R. (2021). Trends towards Effective Analysis of Fluorinated Compounds Using Inductively

Coupled Plasma Mass Spectrometry (ICP-MS). *Journal of Analytical Methods in Chemistry*, **2021**, 3-11.

Molnar, M., Lončarić, M., & Kovač, M. (2020). Green chemistry approaches to the synthesis of coumarin derivatives. *Current Organic Chemistry*, **24**(1), 4-43.

Monga, P. K., Sharma, D., Bhasin, S., & Dubey, A. (2017). Environmentally positive and energy proficient synthesis of coumarin by the Pechmann reaction via microwave irradiation.

Mukherjee, S., Betal, S., & Chattopadhyay, A. P. (2020). Luminescence sensing, DFT, extraction and monitoring of Cr^{3+} and Al^{3+} *via* the application of first derivative fluorescence spectroscopy. *New Journal of Chemistry*, **44**(29), 12692–12703.

Mukhopadhyay, K., Ghosh, A., Das, S. K., Show, B., Sasikumar, P., & Ghosh, U. C. (2017). Synthesis and characterisation of cerium (IV)-incorporated hydrous iron (III) oxide as an adsorbent for fluoride removal from water. *RSC advances*, **7**(42), 26037-26051.

Nad, S., Kumbhakar, M., & Pal, H. (2003). Photophysical properties of coumarin-152 and coumarin-481 dyes: unusual behavior in nonpolar and in higher polarity solvents. *The Journal of Physical Chemistry A*, **107**(24), 4808-4816.

Naeem, M., Khalil, K.-R., Danish, Z., Sufian, M., & Saleem, W. (2017). Bacteriological analysis of drinking water in urban areas of district peshawar, khyber pakhtunkhwa, **25**(1), 3.

Naika, K., Ravikumar, P., & Prakash, K. L. (2020). An investigation of fluoride contamination in groundwater of Yadgir district, Karnataka, 8.

Nasrollahzadeh, M., Sajjadi, M., Iravani, S., & Varma, R. S. (2021). Starch, cellulose, pectin, gum, alginate, chitin and chitosan derived (nano)materials for sustainable water treatment: A review. *Carbohydrate Polymers*, **251**, 116986.

Nayak, B., Samant, A., Patel, R., & Misra, P. K. (2017). Comprehensive Understanding of the Kinetics and Mechanism of Fluoride Removal over a Potent Nanocrystalline Hydroxyapatite Surface. *ACS Omega*, **2**(11), 8118–8128.

Nehra, S., Raghav, S., & Kumar, D. (2019). Rod–shaped Ca–Zn@Chitin composite for fluoride removal studies by adsorption and statistical experiments. *Environmental Nanotechnology, Monitoring & Management*, **12**, 100264.

Önder, A. (2020). Anticancer activity of natural coumarins for biological targets. *Studies in Natural Products Chemistr,* **64**, 85–109.

Ong, T.-C., Sarvghad, M., Lippiatt, K., Griggs, L., Ryan, H., Will, G., & Steinberg, T. A. (2020). Review of the solubility, monitoring, and purification of impurities in molten salts for energy storage in concentrated solar power plants. *Renewable and Sustainable Energy Reviews*, **131**, 110006.

Ozbek, N., & Akman, S. (2014). Determination of fluorine in milk and water via molecular absorption of barium monofluoride by high-resolution continuum source atomic absorption spectrometer. *Microchemical Journal*, **117**, 111–115.

Padghan, S. D., Wang, L.C., Lin, W.C., Hu, J.W., Liu, W.C., & Chen, K.Y. (2021). Rational Design of an ICT-Based Chemodosimeter with Aggregation-Induced Emission for Colorimetric and Ratiometric Fluorescent Detection of Cyanide in a Wide pH Range. *ACS Omega*, **6**(8), 5287–5296.

Pajk, S., Majaron, H., Novak, M., Kokot, B., & Štrancar, J. (2019). New coumarin-and phenoxazine-based fluorescent probes for live-cell STED nanoscopy. *European Biophysics Journal*, **48**(5), 485-490.

Palacios, M. A., Nishiyabu, R., Marquez, M., & Anzenbacher, P. (2007). Supramolecular chemistry approach to the design of a high-resolution sensor array for multianion detection in water. *Journal of the American Chemical Society*, **129**(24), 7538-7544.

Pandi, K., Periyasamy, S., & Viswanathan, N. (2017). Remediation of fluoride from drinking water using magnetic iron oxide coated hydrotalcite/chitosan composite. *International Journal of Biological Macromolecules*, **104**, 1569–1577.

Park, G. J., Jo, H. Y., Ryu, K. Y., & Kim, C. (2014). A new coumarin-based chromogenic chemosensor for the detection of dual analytes Al^{3+} and F^-. *RSC Advances*, **4**(109), 63882-63890.

Passos, S. T. A., Souza, G. C., Brandão, D. C., Machado, D. F. S., Grisolia, C. K., Correa, J. R., & da Silva, W. A. (2021). Plasma membrane staining with fluorescent hybrid benzothiadiazole and coumarin derivatives: Tuning the cellular selection by molecular design. *Dyes and Pigments*, **186**, 109005.

Patel, A. M., Ray, D., Aswal, V. K., & Ballabh, A. (2020). Probing the mechanism of gelation and anion sensing capability of a thiazole based amide gelator: A case study. *Colloids and Surfaces A: Physicochemical and Engineering Aspects*, **607**, 125430.

Paudyal, H., Inoue, K., Kawakita, H., Ohto, K., Kamata, H., & Alam, S. (2018). Removal of fluoride by effectively using spent cation exchange resin. *Journal of Material Cycles and Waste Management*, **20**(2), 975–984.

Peckham, S., & Awofeso, N. (2014). Water Fluoridation: A Critical Review of the Physiological Effects of Ingested Fluoride as a Public Health Intervention. *The Scientific World Journal*, **2014**, 1–10.

Peng, H., & Guo, J. (2020). Removal of chromium from wastewater by membrane filtration, chemical precipitation, ion exchange, adsorption electrocoagulation, electrochemical reduction, electrodialysis, electrodeionization, photocatalysis and nanotechnology: A review. *Environmental Chemistry Letters*, **18**(6), 2055–2068.

Pereira, T. M., Franco, D. P., Vitorio, F., & Kummerle, A. E. (2018). Coumarin Compounds in Medicinal Chemistry: Some Important Examples from the Last Years. *Current Topics in Medicinal Chemistry*, **18**(2), 124–148.

Pillai, P., Dharaskar, S., Pandian, S., & Panchal, H. (2021). Overview of fluoride removal from water using separation techniques. *Environmental Technology & Innovation*, **21**, 101246.

Plotnikov, E., Martemianova, I., Martemianov, D., Zhuravkov, S., Voronova, O., Korotkova, E., & Vladimir, S. (2015). Water Purification with Natural Sorbents: Effect of Surface Modification with Nano-structured Particles. *Procedia Chemistry*, **15**, 219–224.

Poursaberi, T., Hassanisadi, M., Torkestani, K., & Zare, M. (2012). Development of zirconium (IV)-metalloporphyrin grafted Fe_3O_4 nanoparticles for efficient fluoride removal. *Chemical Engineering Journal*, **189**, 117–125.

Prabhu, S. M., Subaramanian, M., & Meenakshi, S. (2016). A simple one-pot in-situ method for the synthesis of aluminum and lanthanum binary oxyhydroxides in chitosan template towards defluoridation of water. *Chemical Engineering Journal*, **283**, 1081–1089.

Priestly, B. G., Harford, A. J., & Sim, M. R. (2007). Nanotechnology: A promising new technology — but how safe? *Medical Journal of Australia*, **186**(4), 187–188.

Qiu, B., Zeng, Y., Hu, R., Chen, L., Chen, J., Yu, T., & Yang, G. (2018). Förster Resonance Energy-Transfer-Based Ratiometric Fluorescent Indicator for Quantifying Fluoride Ion in Water and Toothpaste. *ACS Omega*, **3**(12), 18153–18159.

Ranjan, S., & Yasmin, S. (2019). Geological Source of Fluoride in Fluoride Endemic Region of Gaya District, Bihar, India. *Bioscience Biotechnology Research Communications*, **12**(4), 1165–1172.

Rasool, A., Farooqi, A., Xiao, T., Ali, W., Noor, S., Abiola, O., & Ali, S. (2018). A review of global outlook on fluoride contamination in groundwater with prominence on the Pakistan current situation. *Environmental Geochemistry and Health*, **40**(4), 1265–1281.

Razi, S. S., Srivastava, P., Ali, R., Gupta, R. C., Dwivedi, S. K., & Misra, A. (2015). A coumarin-derived useful scaffold exhibiting Cu^{2+} induced fluorescence quenching and fluoride sensing (On–Off–On) via copper displacement approach. *Sensors and Actuators B: Chemical*, **209**, 162-171.

Rissanen, K. (2008). Halogen bonded supramolecular complexes and networks. *CrystEngComm*, **10**(9), 1107-1113.

Rubio, C., Rodríguez, I., Jaudenes, J. R., Gutiérrez, A. J., Paz, S., Burgos, A., & Hardisson, A. (2020). Fluoride levels in supply water from a volcanic area in the Macaronesia region. *Environmental Science and Pollution Research*, **27**(11), 11587–11595.

Saeed, M., Malik, R. N., & Kamal, A. (2020). Fluorosis and cognitive development among children (6–14 years of age) in the endemic areas of the world: A review and critical analysis. *Environmental Science and Pollution Research*, **27**(3), 2566–2579.

Saha, D., Goswami, R., Majumdar, K. K., Sikdar, N., & Pramanik, S. (2021). Evaluating the Association Between Dental Fluorosis and Polymorphisms in Bone Development and Mineralization Genes Among Population from a Fluoride Endemic Region of Eastern India. *Biological trace element research*, **199**(1), 1-8

Sahoo, C. R., Sahoo, J., Mahapatra, M., Lenka, D., Sahu, P. K., Dehury, B., & Paidesetty, S. K. (2021). Coumarin derivatives as promising antibacterial agent (s). *Arabian Journal of Chemistry*, **14**(2), 102922.

Sahu, S., Mallik, L., Pahi, S., Barik, B., Sahu, U. K., Sillanpää, M., & Patel, R. K. (2020). Facile synthesis of poly o-toluidine modified lanthanum phosphate nanocomposite as a superior adsorbent for selective fluoride removal: A mechanistic and kinetic study. *Chemosphere*, **252**, 126551.

Saini, N., Prigyai, N., Wannasiri, C., Ervithayasuporn, V., & Kiatkamjornwong, S. (2018). Green synthesis of fluorescent N,O-chelating hydrazone Schiff base for multi-analyte sensing in Cu^{2+}, F^- and CN^- ions. *Journal of Photochemistry and Photobiology A: Chemistry*, *358*, 215–225.

Salem, M. A., Helal, M. H., Gouda, M. A., Ammar, Y. A., El-Gaby, M. S. A., & Abbas, S. Y. (2018). An overview on synthetic strategies to coumarins. *Synthetic Communications*, **48**(13), 1534-1550.

Saliu, T. D., & Oladoja, N. A. (2020). Assessing the suitability of solid aggregates for nutrient recovery from aqua systems. *Journal of Water Process Engineering*, **33**, 101000.

Sandoval, M. A., Fuentes, R., Thiam, A., & Salazar, R. (2021). Arsenic and fluoride removal by electrocoagulation process: A general review. *Science of the Total Environment*, **753**, 142108.

Sarkar, D., Ghosh, P., Gharami, S., Mondal, T. K., & Murmu, N. (2017). A novel coumarin based molecular switch for the sequential detection of Al^{3+} and F^-: application in lung cancer live cell imaging and construction of logic gate. *Sensors and Actuators B: Chemical*, **242**, 338-346.

Schlesinger, W. H., Klein, E. M., & Vengosh, A. (2020). Global biogeochemical cycle of fluorine. *Global Biogeochemical Cycles*, **34**(12), 6722.

Sedgwick, A. C., Brewster, J. T., Wu, T., Feng, X., Bull, S. D., Qian, X., & Sessler, J. L. (2021). Indicator displacement assays (IDAs): The past, present and future. *Chemical Society Reviews*, **50**(1), 9–38.

Sellami, M., Riahi, H., Maatallah, K., Ferjani, H., Bouaziz, M. C., & Ladeb, M. F. (2020). Skeletal fluorosis: Don't miss the diagnosis! *Skeletal Radiology*, **49**(3), 345–357.

Sen, K., Sharma, P., & Chauhan, K. (2020). Chloroacetyl-Mediated Modification of Chitosan by Tannic Acid to Synthesize Economical Tanninate-Chitosan and Its Use in Fluoride Ions Adsorption from Aqueous Solution. *ChemistrySelect*, *5*(6), 2023–2034.

Sengupta, P., Saha, S., Banerjee, S., Dey, A., & Sarkar, P. (2020). Removal of fluoride ion from drinking water by a new $Fe(OH)_3$ / nano CaO impregnated chitosan composite adsorbent. *Polymer-Plastics Technology and Materials*, **59**(11), 1191–1203.

Şenkuytu, E. (2018). A high selective "Turn-Off" aminopyrene based cyclotriphosphazene fluorescent chemosensors for Fe^{3+} /Cu^{2+} ions. *Inorganica Chimica Acta*, **479**, 58–65.

Senthilkumar, S., Nath, S., & Pal, H. (2004). Photophysical Properties of Coumarin-30 Dye in Aprotic and Protic Solvents of Varying Polarities. *Photochemistry and photobiology*, **80**(1), 104-111.

Sezgin, B. I., Onur, Ş. G., Menteş, A., Okutan, A. E., Haznedaroğlu, E., & Vieira, A. R. (2018). Two-fold excess of fluoride in the drinking water has no obvious health effects other than dental fluorosis. *Journal of Trace Elements in Medicine and Biology*, **50**, 216–222.

Shahid, M. K., Kim, J. Y., & Choi, Y.-G. (2019). Synthesis of bone char from cattle bones and its application for fluoride removal from the contaminated water. *Groundwater for Sustainable Development*, **8**, 324–331.

Shan, L. P., Zhou, Y., Yan, M. C., Liu, L., Chen, J., & Chen, J. P. (2021). A novel antiviral coumarin derivative as a potential agent against WSSV infection in shrimp seedling culture. *Virus Research*, **297**, 198387.

Shangguan, M., Jiang, X., Lu, Z., Zou, W., Chen, Y., Xu, P., & Pan, Y. (2019). A coumarin-based fluorescent probe for hypochlorite ion detection in environmental water samples and living cells. *Talanta*, **202**, 303–307.

Sharma, D., Singh, A., Verma, K., Paliwal, S., Sharma, S., & Dwivedi, J. (2017). Fluoride: A review of pre-clinical and clinical studies. *Environmental Toxicology and Pharmacology*, **56**, 297–313.

Shen, Y., Shuhendler, A. J., Ye, D., Xu, J. J., & Chen, H. Y. (2016). Two-photon excitation nanoparticles for photodynamic therapy. *Chemical Society Reviews*, **45**(24), 6725-6741.

Shen, Y., Zhang, X., Zhang, Y., Li, H., & Chen, Y. (2018). An ICT-modulated strategy to construct colorimetric and ratiometric fluorescent sensor for mitochondria-

targeted fluoride ion in cell living. *Sensors and Actuators B: Chemical*, **258**, 544-549.

Simmer, J. P., Richardson, A. S., Hu, Y.-Y., Smith, C. E., & Ching-Chun Hu, J. (2012). A post-classical theory of enamel biomineralization… and why we need one. *International Journal of Oral Science*, **4**(3), 129–134.

Simsek, E. B., Duranoglu, D., & Beker, U. (2012). Heavy Metal Adsorption by Magnetic Hybrid-Sorbent: An Experimental and Theoretical Approach. *Separation Science and Technology*, **47**(9), 1334–1340.

Singh, S., German, M., Chaudhari, S., & Sengupta, A. K. (2020). Fluoride removal from groundwater using Zirconium Impregnated Anion Exchange Resin. *Journal of Environmental Management*, **263**, 110415.

Sivarajasekar, N. (2017). Defluoridation of water using adsorbents—A concise review, *6*(1), 13.

Sivasubramanian, V., Jetty, K., & Kumar, S. S. (2019). Correlation of HbA1c with urinary ACR, serum creatinine and eGFR in type-2 diabetes mellitus at Puducherry, South India. *International Journal of Research in Medical Sciences*, **7**(5), 1924.

Srivastav, V. K., & Tiwari, M. (2017). QSAR and docking studies of coumarin derivatives as potent HIV-1 integrase inhibitors. *Arabian Journal of Chemistry*, **10**, S1081-S1094.

Srivastava, A., Kumari, M., Ramanathan, A., Selvaraj, K., Prasad, B., & Prasad, K. S. (2020). Removal of fluoride from aqueous solution by mesoporous silica nanoparticles functionalized with chitosan derived from mushroom. *Journal of Macromolecular Science, Part A*, **57**(9), 619–627.

Starzak, K., Matwijczuk, A., Creaven, B., Matwijczuk, A., Wybraniec, S., & Karcz, D. (2019). Fluorescence Quenching-Based Mechanism for Determination of Hypochlorite by Coumarin-Derived Sensors. *International Journal of Molecular Sciences*, **20**(2), 281.

Štepec, D., Tavčar, G., & Ponikvar-Svet, M. (2019). Fluorine in vegetation due to an uncontrolled release of gaseous fluorides from a glassworks: A case study of measurement uncertainty, dispersion pattern and compliance with regulation. *Environmental Pollution*, **248**, 958–964.

Subba Rao, N., Sunitha, B., Adimalla, N., & Chaudhary, M. (2020). Quality criteria for groundwater use from a rural part of Wanaparthy District, Telangana State, India, through ionic spatial distribution (ISD), entropy water quality index (EWQI) and principal component analysis (PCA). *Environmental Geochemistry and Health*, **42**(2), 579–599.

Suk, J. M., & Jeong, K. S. (2008). Indolocarbazole-based foldamers capable of binding halides in water. *Journal of the American Chemical Society*, **130**(36), 11868-11869.

Sumorek-Wiadro, J., Zając, A., Maciejczyk, A., & Jakubowicz-Gil, J. (2020). Furanocoumarins in anticancer therapy – For and against. *Fitoterapia*, **142**, 104492.

Tamrakar, S., Verma, R., Kumar Sar, S., & Verma, C. (2019). Cost effective natural adsorbents for the removal of fluoride: a green approach. *Rasayan Journal of Chemistry*, **12**(02), 455–463.

Tang, Y., Li, Y., Han, J., Mao, Y., Ni, L., & Wang, Y. (2019). A coumarin based fluorescent probe for rapidly distinguishing of hypochlorite and copper (II) ion

in organisms. *Spectrochimica Acta Part A: Molecular and Biomolecular Spectroscopy*, **208**, 299–308.

Tang, Z., Bai, T., & Zhou, P. (2020). Sensing Mechanism of a Fluorescent Probe for Cysteine: Photoinduced Electron Transfer and Invalidity of Excited-State Intramolecular Proton Transfer. *The Journal of Physical Chemistry A*, **124**(34), 6920–6927.

Tasior, M., Kim, D., Singha, S., Krzeszewski, M., Ahn, K. H., & Gryko, D. T. (2015). π-Expanded coumarins: Synthesis, optical properties and applications. *Journal of Materials Chemistry C*, **3**(7), 1421–1446.

Thakre, D., Jagtap, S., Sakhare, N., Labhsetwar, N., Meshram, S., & Rayalu, S. (2010). Chitosan based mesoporous Ti–Al binary metal oxide supported beads for defluoridation of water. *Chemical Engineering Journal*, **158**(2), 315–324.

Tian, Z., Cui, S., & Pu, S. (2016). A highly selective fluorescent sensor for dual detection of Zn^{2+} and F^- based on a new diarylethene. *Tetrahedron Letters*, **57**(25), 2703-2707.

Uddin, M. K., Ahmed, S. S., & Naushad, Mu. (2019). A mini update on fluoride adsorption from aqueous medium using clay materials. *Desalination and Water Treatment*, **145**, 232–248.

Udhayakumari, D. (2020). Detection of toxic fluoride ion via chromogenic and fluorogenic sensing. A comprehensive review of the year 2015–2019. *Spectrochimica Acta Part A: Molecular and Biomolecular Spectroscopy*, **228**, 117817.

Öztürk, E. İ., Kenar, A., Aksu, M. L., & Taştekin, M. (2019). Spectrophotometric methods for the determination of fluoride ion using indole-3-acetic acid interaction with iron (III). *Turkish Journal of Chemistry*, **43**(2), 415-423.

Velazquez-Peña, G. C., Solache-Ríos, M., & Martínez-Miranda, V. (2015). Competing Effects of Chloride, Nitrate, and Sulfate Ions on the Removal of Fluoride by a Modified Zeolitic Tuff. *Water, Air, & Soil Pollution*, **226**(1), 2236.

Venkataraj, R., Sarkar, A., Girijavallabhan, C. P., Radhakrishnan, P., Nampoori, V. P. N., & Kailasnath, M. (2018). Fluorescence resonance energy-transfer-based fluoride ion sensor. *Applied Optics*, **57**(15), 4322.

Verma, S., Aute, S., Das, A., & Ghosh, H. N. (2015). Hydrogen Bond and Ligand Dissociation Dynamics in Fluoride Sensing of Re(I)–Polypyridyl Complex. *The Journal of Physical Chemistry B*, **119**(47), 14952–14958.

Vijaya, Y., & Krishnaiah, A. (2009). Sorptive Response Profile of Chitosan Coated Silica in the Defluoridation of Aqueous Solution. *E-Journal of Chemistry*, **6**(3), 713–724.

Villanueva, C. M., Kogevinas, M., Cordier, S., Templeton, M. R., Vermeulen, R., Nuckols, J. R., & Nieuwenhuijsen, M. J. (2014). Assessing Exposure and Health Consequences of Chemicals in Drinking Water: Current State of Knowledge and Research Needs. *Environmental Health Perspectives*, **122**(3), 213–221.

Viswanathan, N., Sairam Sundaram, C., & Meenakshi, S. (2009). Development of multifunctional chitosan beads for fluoride removal. *Journal of Hazardous Materials*, **167**(1–3), 325–331.

Voicu, G., Ciobanu, C., Istrate, I. A., & Tudor, P. (2020). Emissions Control of Hydrochloric and Fluorhydric Acid in cement Factories from Romania. *International Journal of Environmental Research and Public Health*, **17**(3), 1019.

Vos, T., Abajobir, A. A., Abate, K. H., Abbafati, C., Abbas, K. M., Abd-Allah, F., & Abdulkader, R. S. (2017). Global, regional, and national incidence, prevalence, and years lived with disability for 328 diseases and injuries for 195 countries, 1990–2016: A systematic analysis for the Global Burden of Disease Study 2016. *The Lancet*, **390**(10100), 1211–1259.

Wadhwa, P., Jain, P., Rudrawar, S., & Jadhav, H. R. (2018). Quinoline, coumarin and other heterocyclic analogs based HIV-1 integrase inhibitors. *Current drug discovery Technologies*, **15**(1), 2-19.

Walsh, T., Worthington, H. V., Glenny, A. M., Appelbe, P., Marinho, V. C., & Shi, X. (2010). Fluoride toothpastes of different concentrations for preventing dental caries in children and adolescents. *Cochrane database of systematic reviews*, (1).

Wambu, E. W., Agong, S. G., Anyango, B., Akuno, W., & Akenga, T. (2014). High fluoride water in Bondo-Rarieda area of Siaya County, Kenya: A hydro-geological implication on public health in the Lake Victoria Basin. *BMC Public Health*, **14**(1), 462.

Wang, A., Zhou, K., Liu, X., Liu, F., Zhang, C., & Chen, Q. (2017). Granular tri-metal oxide adsorbent for fluoride uptake: Adsorption kinetic and equilibrium studies. *Journal of Colloid and Interface Science*, **505**, 947–955.

Wang, Changyao, Yang, S., Yi, M., Liu, C., Wang, Y., Li, J., & Li, Y. (2014). Graphene Oxide Assisted Fluorescent Chemodosimeter for High-Performance Sensing and Bioimaging of Fluoride Ions. *ACS Applied Materials & Interfaces*, **6**(12), 9768–9775.

Wang, Chao, Qiao, Q., Chi, W., Chen, J., Liu, W., Tan, D., & McKechnie, S. (2020). Quantitative Design of Bright Fluorophores and AIEgens by the Accurate

Prediction of Twisted Intramolecular Charge Transfer (TICT). *Angewandte Chemie*, **132**(25), 10246–10258.

Wang, Mengwei, Liu, L., Li, H., Li, Y., Liu, H., Hou, C., & Zeng, Q. (2020). Thyroid function, intelligence, and low-moderate fluoride exposure among Chinese school-age children. *Environment International*, **134**, 105229.

Wang, M., Liu, Y., Yao, Y., Han, L., & Liu, X. (2020). Comparative evaluation of bone chars derived from bovine parts: Physicochemical properties and copper sorption behavior. *Science of The Total Environment*, **700**, 134470.

Wang, Y., Nie, J., Fang, W., Yang, L., Hu, Q., Wang, Z., & Sun, J. Z. (2020). Sugar-Based Aggregation-Induced Emission Luminogens: Design, Structures, and Applications. *Chemical Reviews*, **120**(10), 4534–4577.

Yeung, M. C. L., Chu, B. W. K., & Yam, V. W. W. (2014). Anion binding properties of alkynylplatinum (II) complexes with amide-functionalized terpyridine: Host–guest interactions and fluoride ion-induced deprotonation. *ChemistryOpen*, **3**(5), 172.

Waugh, D. T. (2019). Fluoride Exposure Induces Inhibition of Sodium-and Potassium-Activated Adenosine Triphosphatase (Na$^+$, K$^+$-ATPase) Enzyme Activity: Molecular Mechanisms and Implications for Public Health. *International Journal of Environmental Research and Public Health*, **16**(8), 1427.

Welleman, I. M., Hoorens, M. W. H., Feringa, B. L., Boersma, H. H., & Szymański, W. (2020). Photoresponsive molecular tools for emerging applications of light in medicine. *Chemical Science*, **11**(43), 11672–11691.

Wimalasiri, A. K. D. V. K., Fernando, M. S., Dziemidowicz, K., Williams, G. R., Koswattage, K. R., Dissanayake, D. P., & de Silva, K. M. N. (2021). Structure–Activity Relationship of Lanthanide-Incorporated Nano-

Hydroxyapatite for the Adsorption of Fluoride and Lead. *ACS Omega*, **6**(21), 13527–13543.

Wimalawansa, S. J. (2020). Molecular and cellular toxicity of fluoride in mystery, tubulointerstitial chronic kidney disease: A systematic review. *Reviews in Environmental Science and Bio/Technology*, **19**(1), 117–147.

Wong, E. Y., & Stenstrom, M. K. (2018). Onsite defluoridation system for drinking water treatment using calcium carbonate. *Journal of Environmental Management*, *216*, 270–274.

Wu, D., Sedgwick, A. C., Gunnlaugsson, T., Akkaya, E. U., Yoon, J., & James, T. D. (2017). Fluorescent chemosensors: the past, present and future. *Chemical Society Reviews*, **46**(23), 7105-7123.

Wu, F., Wang, H., Xu, J., Yuan, H.-Q., Zeng, L., & Bao, G. M. (2018). A new fluorescent chemodosimeter for ultra-sensitive determination of toxic thiophenols in environmental water samples and cancer cells. *Sensors and Actuators B: Chemical*, **254**, 21–29.

Wu, J., Liu, W., Ge, J., Zhang, H., & Wang, P. (2011). New sensing mechanisms for design of fluorescent chemosensors emerging in recent years. *Chemical Society Reviews*, **40**(7), 3483-3495.

Wu, X., Wang, H., Yang, S., Tian, H., Liu, Y., & Sun, B. (2019). A novel coumarin-based fluorescent probe for sensitive detection of copper(II) in wine. *Food Chemistry*, **284**, 23–27.

Wu, Y., Ji, J., Zhou, Y., Chen, Z., Liu, S., & Zhao, J. (2020). Ratiometric and colorimetric sensors for highly sensitive detection of water in organic solvents based on hydroxyl-containing polyimide-fluoride complexes. *Analytica Chimica Acta*, **1108**, 37–45.

Xia, Y., Li, M., Xu, A., Zhang, Z., Sun, A., Ding, S., & Liu, Y. (2021). Sensing mechanism of fluorogenic urea with fluoride in solvent media: A new fluorescence quenching mechanism. *Spectrochimica Acta Part A: Molecular and Biomolecular Spectroscopy*, **246**, 118992.

Xiong, W., Gong, Y., Che, Y., & Zhao, J. (2019). Sensitive Discrimination of Nerve Agent and Sulfur Mustard Simulants Using Fluorescent Coassembled Nanofibers with Förster Resonance Energy Transfer-Enhanced Photostability and Emission. *Analytical Chemistry*, **91**(3), 1711–1714.

Yadav, K. K., Gupta, N., Kumar, V., Khan, S. A., & Kumar, A. (2018). A review of emerging adsorbents and current demand for defluoridation of water: Bright future in water sustainability. *Environment International*, **111**, 80–108.

Yadav, S. (2019). A Comparative Study of Removing Fluoride from Drinking Water using Agro-Industrial Waste & PAC. *International Journal for Research in Applied Science and Engineering Technology*, **7**(8), 217–222.

Yang, G., Jin, X., Chen, K., & Yang, D. (2020). Hydrogen bonding interactions induced excited state proton transfer and fluoride anion sensing mechanism for 2-(3, 5-dichloro-2, 6-dihydroxy-phenyl)-benzoxazole-5-carboxylicacid. *Journal of Physical Organic Chemistry*, **33**(6), 4054.

Yang, S., Liu, Y., & Feng, G. (2013). Rapid and selective detection of fluoride in aqueous solution by a new hemicyanine-based colorimetric and fluorescent chemodosimeter. *RSC Advances*, **3**(43), 20171.

Yao, R., Meng, F., Zhang, L., Ma, D., & Wang, M. (2009). Defluoridation of water using neodymium-modified chitosan. *Journal of Hazardous Materials*, **165**(1–3), 454–460.

Yazdi, S. H., & Vosoogh, A. (2019). Mini Review on Heavy Metals in Groundwater; Pollution and Removal. *J. Biochem. Tech*, **2**, 149-16.

Yeap, G. Y., Hrishikesan, E., Chan, Y. H., & Mahmood, W. A. K. (2017). A new emissive chalcone-based chemosensor armed by coumarin and naphthol with fluorescence "turn-on" properties for selective detection of F− ions. *Journal of fluorescence*, **27**(1), 105-110

Yousefi, M., Ghalehaskar, S., Asghari, F. B., Ghaderpoury, A., Dehghani, M. H., Ghaderpoori, M., & Mohammadi, A. A. (2019). Distribution of fluoride contamination in drinking water resources and health risk assessment using geographic information system, northwest Iran. *Regulatory Toxicology and Pharmacology*, **107**, 104408.

Yousuf, A., Manzoor, S. O., Youssouf, M., Malik, Z. A., & Khawaja, K. S. (2020). Fly ash: production and utilization in India-an overview. *J Mater Environ Sci*, **11**(6), 911-921.

Zero, D. T., Raubertas, R. F., Pedersen, A. M., Fu, J., Hayes, A. L., & Featherstone, J. D. B. (1992). Studies of Fluoride Retention by Oral Soft Tissues after the Application of Home-use Topical Fluorides. *Journal of Dental Research*, **71**(9), 1546–1552.

Zhan, C.-G., & Dixon, D. A. (2004). Hydration of the Fluoride Anion: Structures and Absolute Hydration Free Energy from First-Principles Electronic Structure Calculations. *The Journal of Physical Chemistry A*, **108**(11), 2020–2029.

Zhang, K., Liu, J., Zhang, Y., Fan, J., Wang, C.-K., & Lin, L. (2019). Theoretical Study of the Mechanism of Aggregation-Caused Quenching in Near-Infrared Thermally Activated Delayed Fluorescence Molecules: Hydrogen-Bond Effect. *The Journal of Physical Chemistry C*, **123**(40), 24705–24713.

Zhang, X., Zhang, L., Li, Z., Jiang, Z., Zheng, Q., Lin, B., & Pan, B. (2017). Rational Design of Antifouling Polymeric Nanocomposite for Sustainable Fluoride Removal from NOM-Rich Water. *Environmental Science & Technology*, **51**(22), 13363–13371.

Zhang, Y., Yang, X., Sun, G., Zhang, H., Liu, X., Zhu, F., & Qin, S. (2018). Colorimetric chemosensors based on diketopyrrolopyrrole for selective and reversible recognition of fluoride ions. *Spectrochimica Acta Part A: Molecular and Biomolecular Spectroscopy*, **199**, 161–169.

Zhang, Y., Zhou, B. H., Tan, P. P., Chen, Y., Miao, C. Y., & Wang, H. W. (2020). Key Role of Pro-inflammatory Cytokines in the Toxic Effect of Fluoride on Hepa1-6 Cells. *Biological trace element research*, **197**(1), 115-122.

Zhao, I. S., Gao, S. S., Hiraishi, N., Burrow, M. F., Duangthip, D., Mei, M. L., Lo, E. C.-M., et al. (2018). Mechanisms of silver diamine fluoride on arresting caries: A literature review. *International Dental Journal*, **68**(2), 67–76.

Zhao, J., Wu, W., Sun, J., & Guo, S. (2013). Triplet photosensitizers: from molecular design to applications. *Chemical Society Reviews*, **42**(12), 5323-5351.29.

Zhao, Y., Li, Y., Wang, J., Manthari, R. K., & Wang, J. (2018). Fluoride induces apoptosis and autophagy through the IL-17 signaling pathway in mice hepatocytes. *Archives of Toxicology*, **92**(11), 3277–3289.

Zhou, Z., Yan, X., Lai, Y.-H., & Zare, R. N. (2018). Fluorescence Polarization Anisotropy in Microdroplets. *The Journal of Physical Chemistry Letters*, **9**(11), 2928–2932.

Zhu, F., Guo, Z., & Hu, X. (2020). Fluoride removal efficiencies and mechanism of schwertmannite from $KMnO_4/MnO_2$–Fe(II) processes. *Journal of Hazardous Materials*, **397**, 122789.

Zhu, J.-J., & Jiang, J.-G. (2018). Pharmacological and Nutritional Effects of Natural Coumarins and Their Structure-Activity Relationships. *Molecular Nutrition & Food Research*, **62**(14), 1701073.

Zhu, L., Younes, A. H., Yuan, Z., & Clark, R. J. (2015). 5-Arylvinylene-2, 2′-bipyridyls: Bright "push–pull" dyes as components in fluorescent indicators for zinc ions. *Journal of Photochemistry and Photobiology A: Chemistry*, **311**, 1-15.

Zimmerman, J. R., Criss, C., Evans, S., Ernst, M., Nieszala, M., Stafford, A., & Szczerba, J. (2018). Fluorescent sensor for fluoride anion based on a sulfonamido-chromone scaffold. *Tetrahedron Letters*, **59**(25), 2473–2476.

APPENDICES

APPENDIX I: ^{1}H NMR spectrum of compound 1

SA_17J_MeOD_500MHz.1.fid — Proton
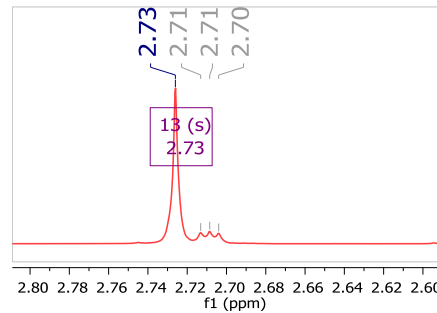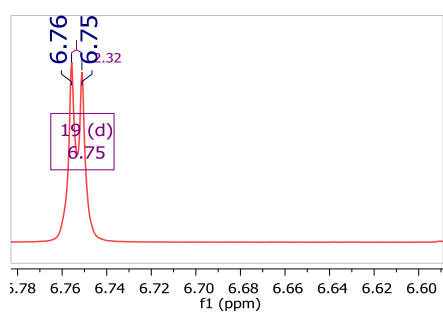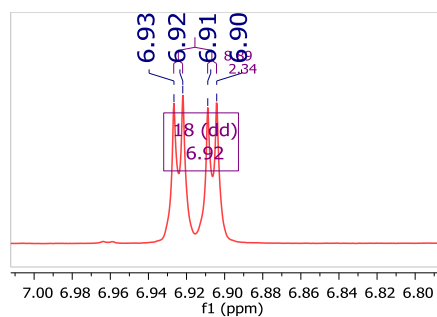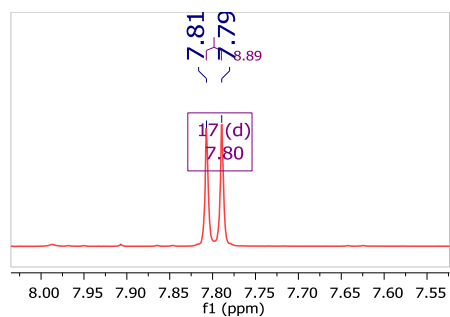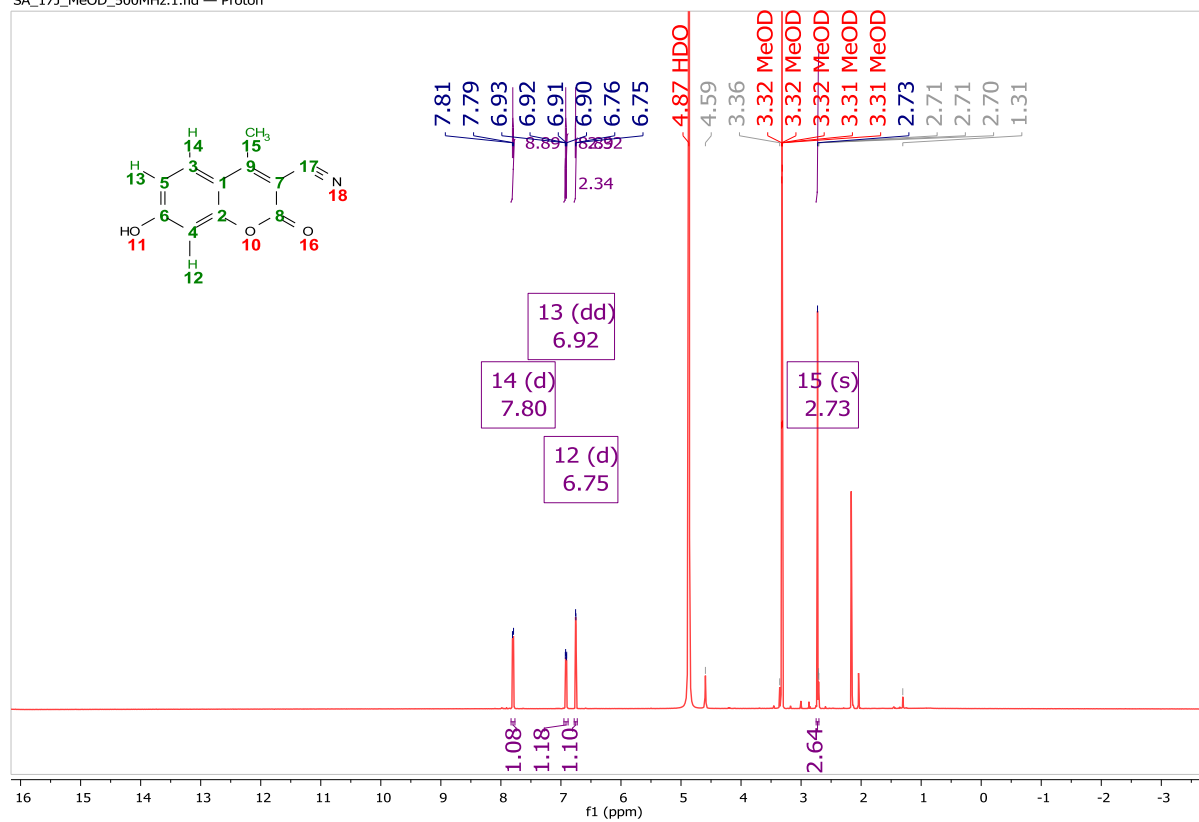
APPENDIX II: ^{13}C NMR spectrum of compound 1
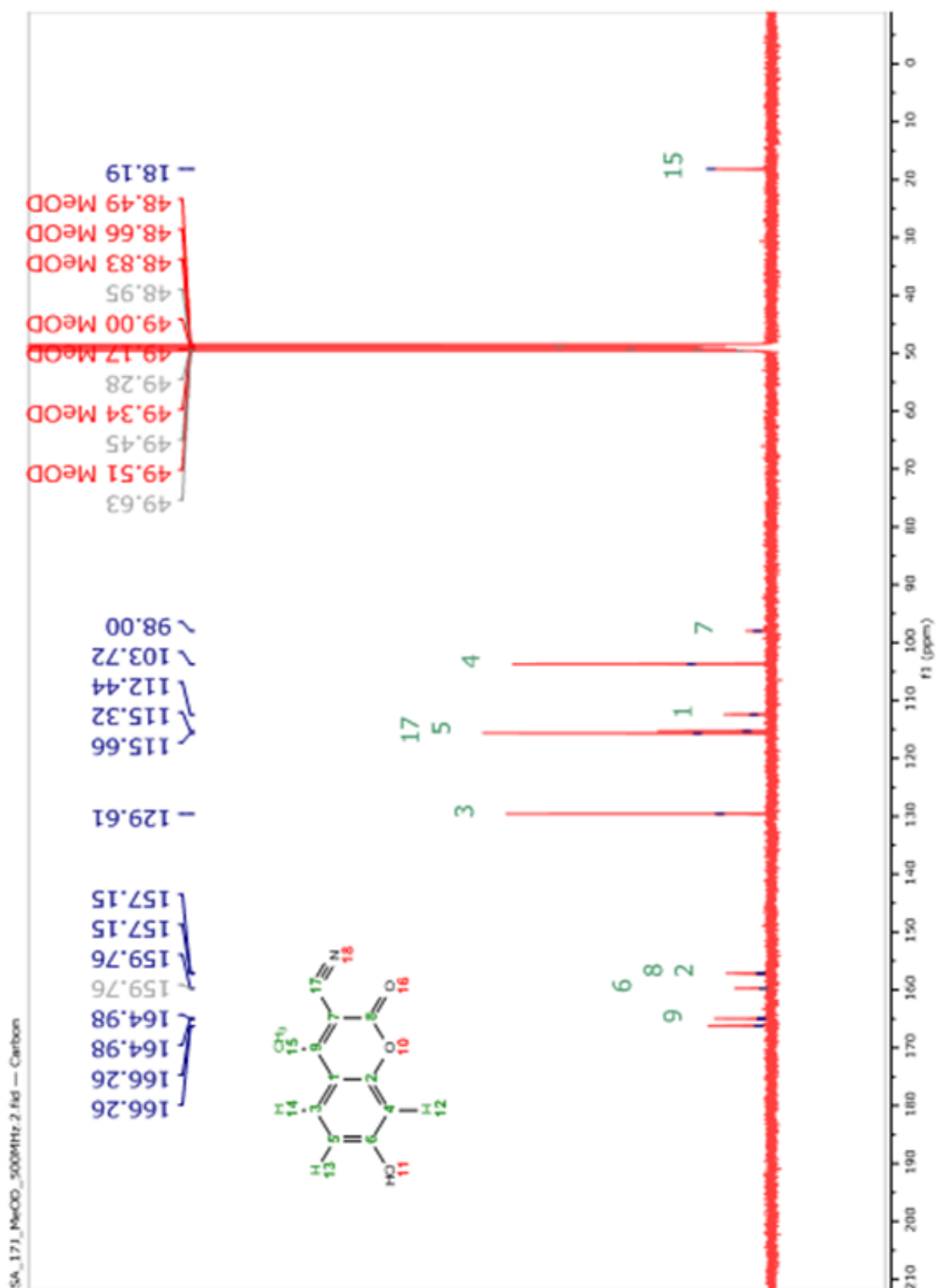
APPENDIX III: ^{1}H-^{1}H COSY spectrum of compound 1


SA_17J_MeOD_500MHz.3.ser — COSY
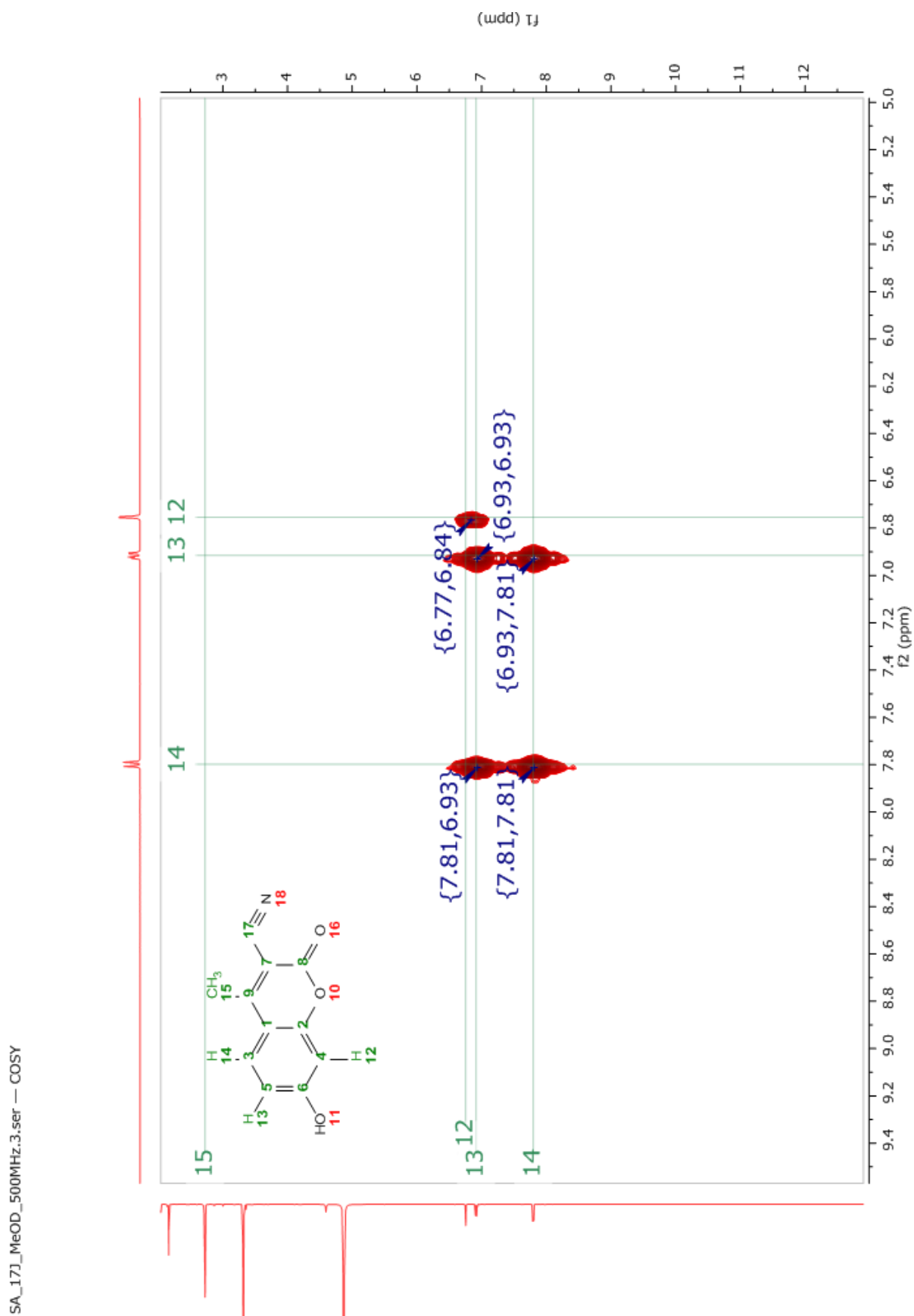
APPENDIX IV: ^{1}H-^{13}C HSQC spectrum of compound 1
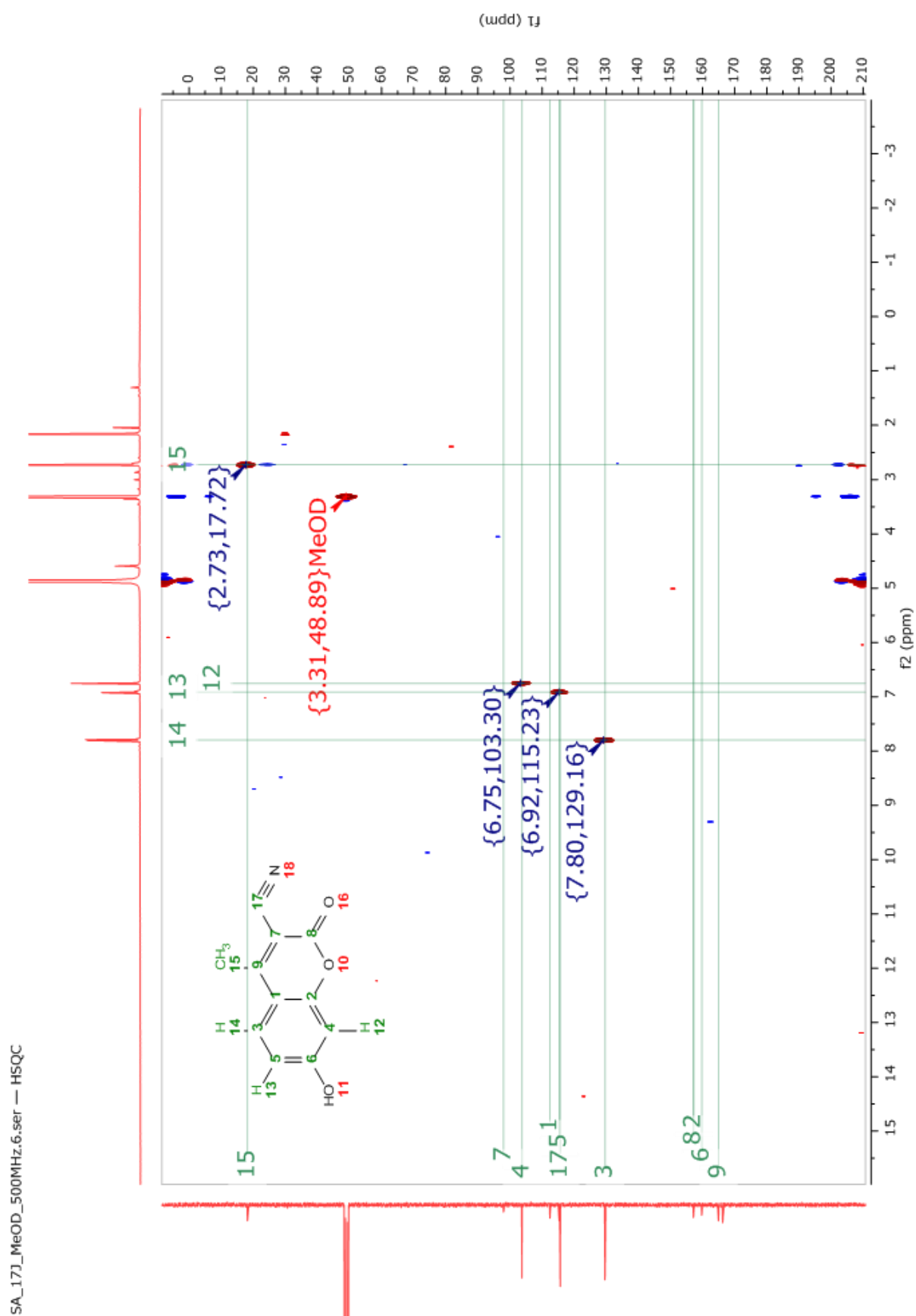
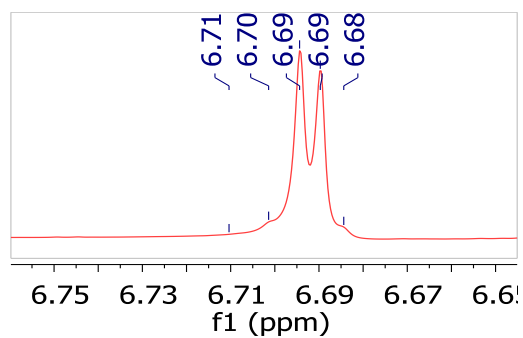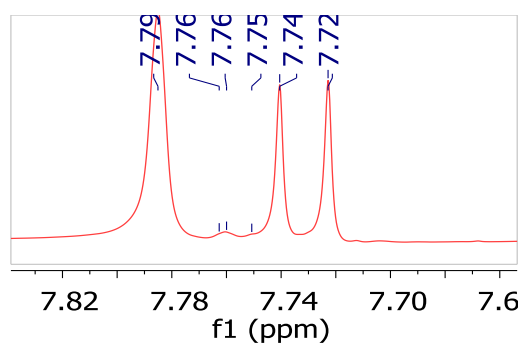# APPENDIX V: ^{1}H-^{13}C HMBC spectrum of compound 1

SA_171_MeOD_500MHz.7.ser — HMBC
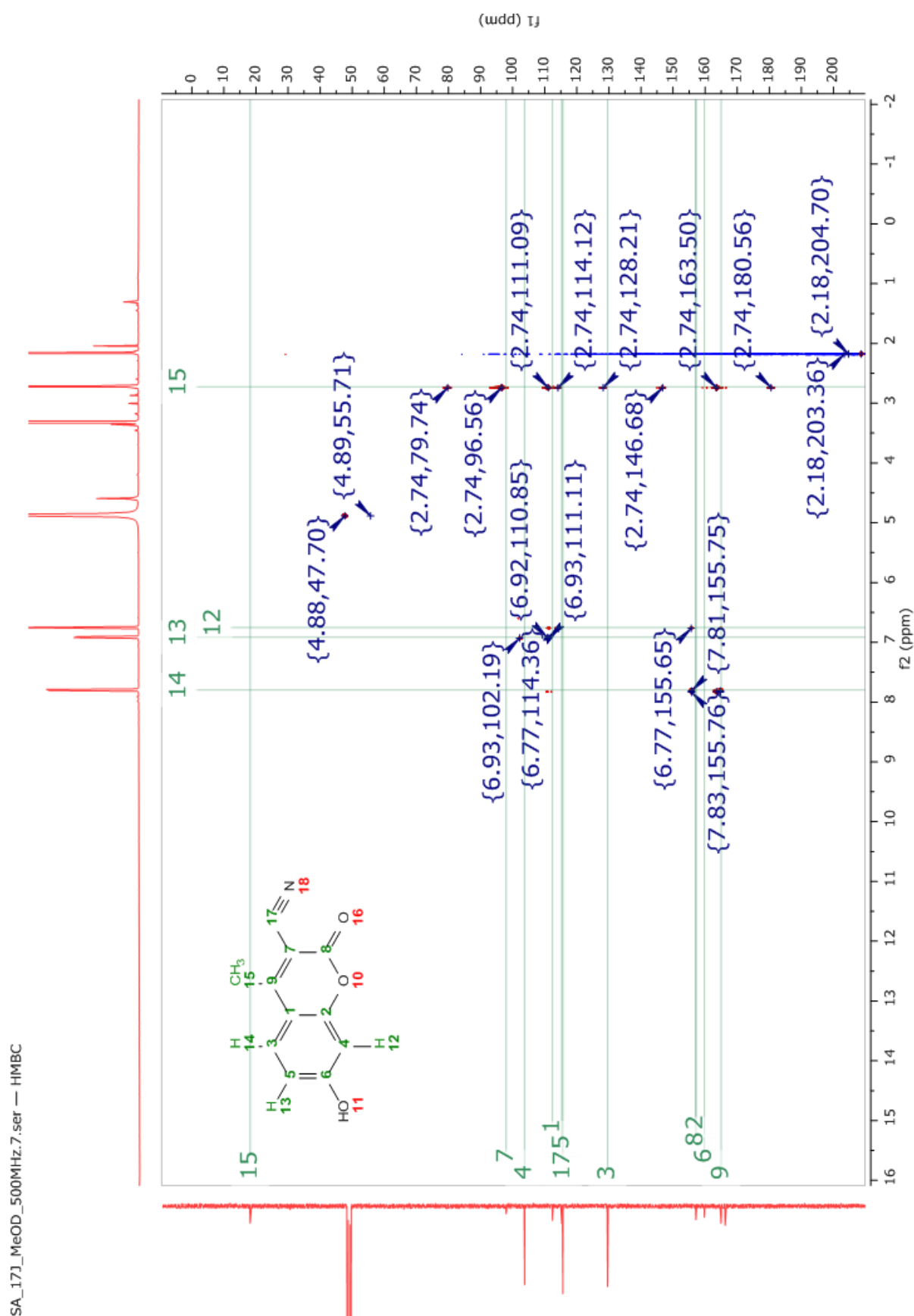
APPENDIX VI: ^{1}H-^{1}H TOCSY spectrum of compound 1
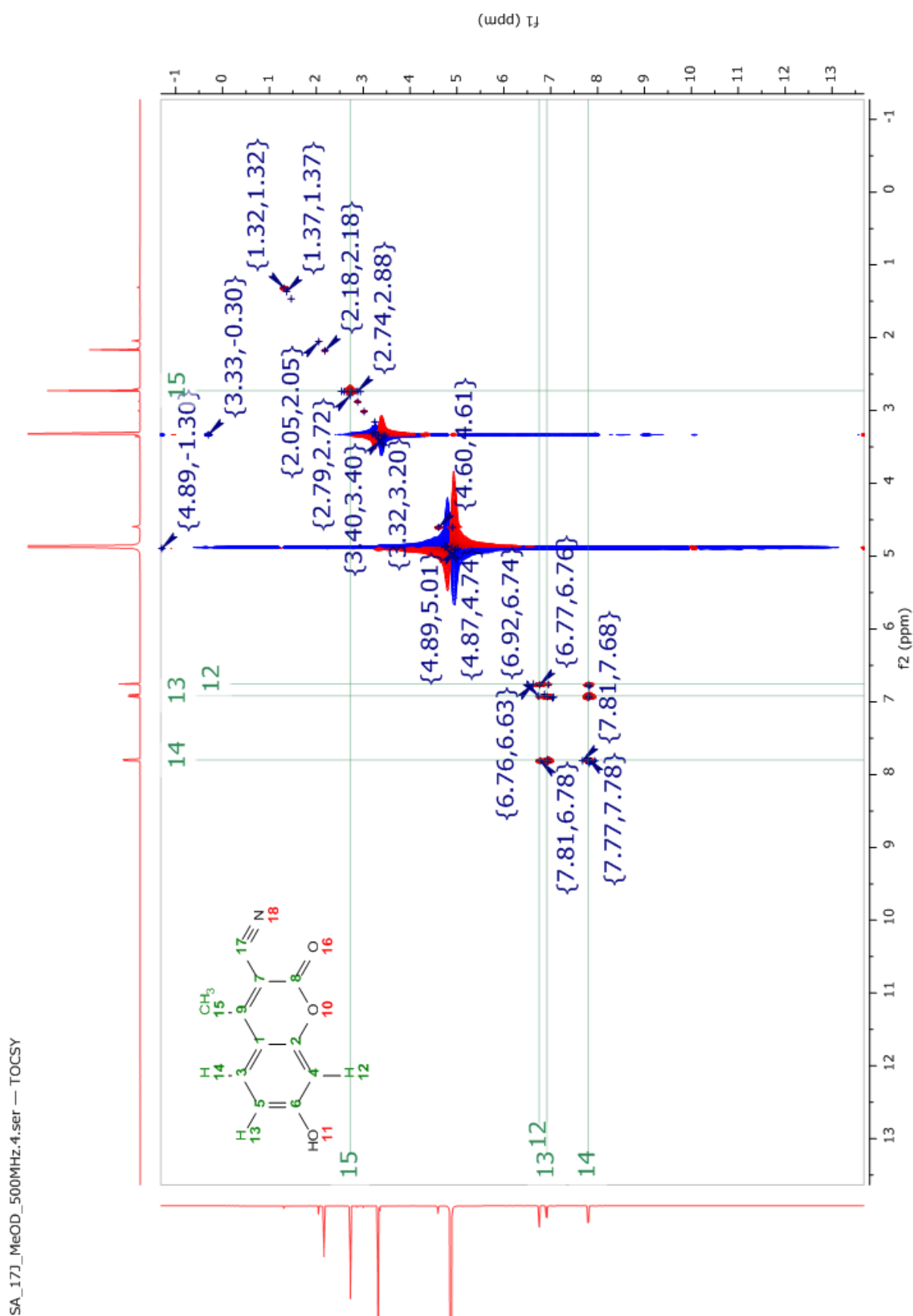
APPENDIX VII: ¹H-¹H NOESY spectrum of compound 1
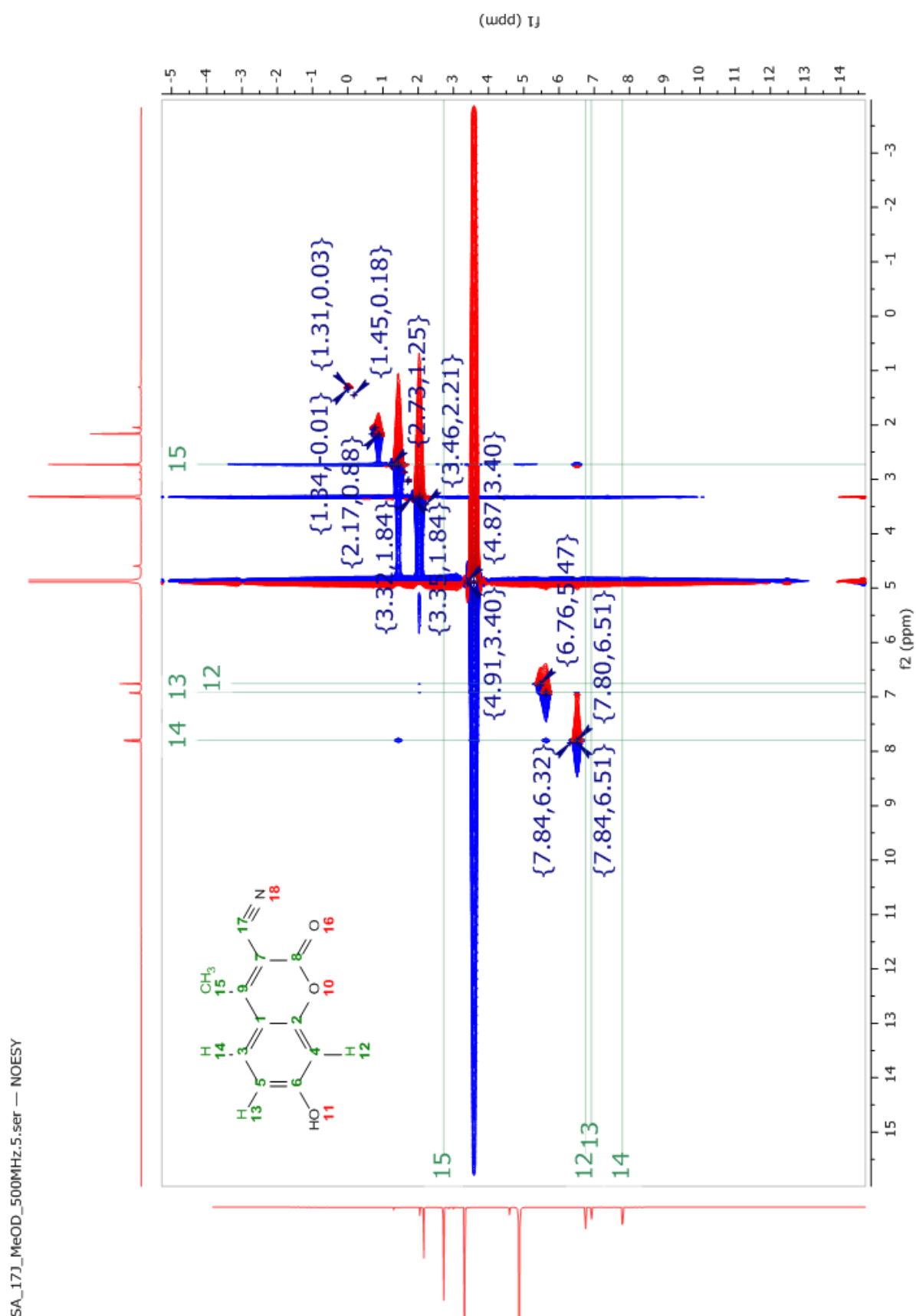
APPENDIX VIII: Diode Array chromatograph of compound 1
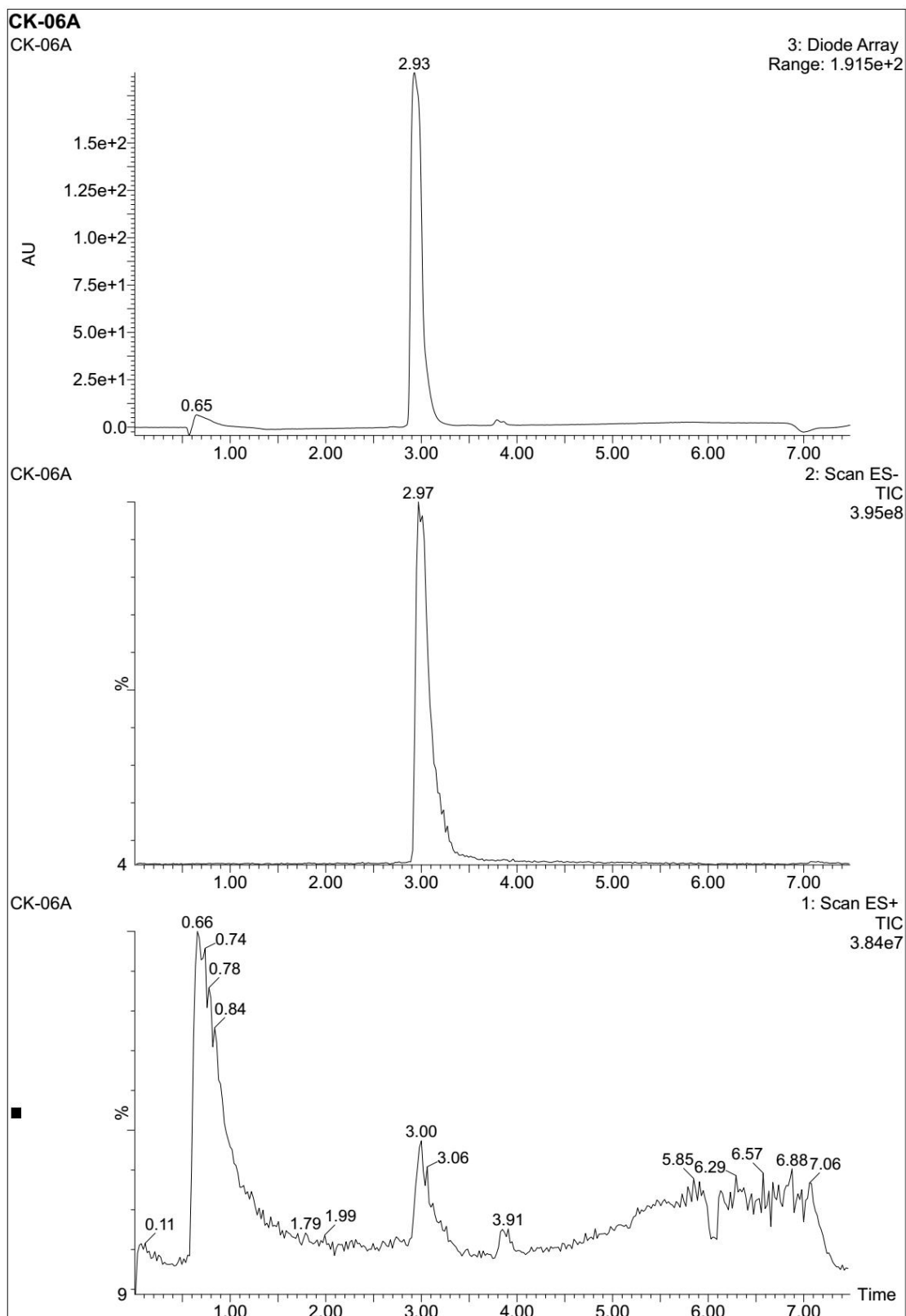
APPENDIX IX: Mass spectrum of compound 1
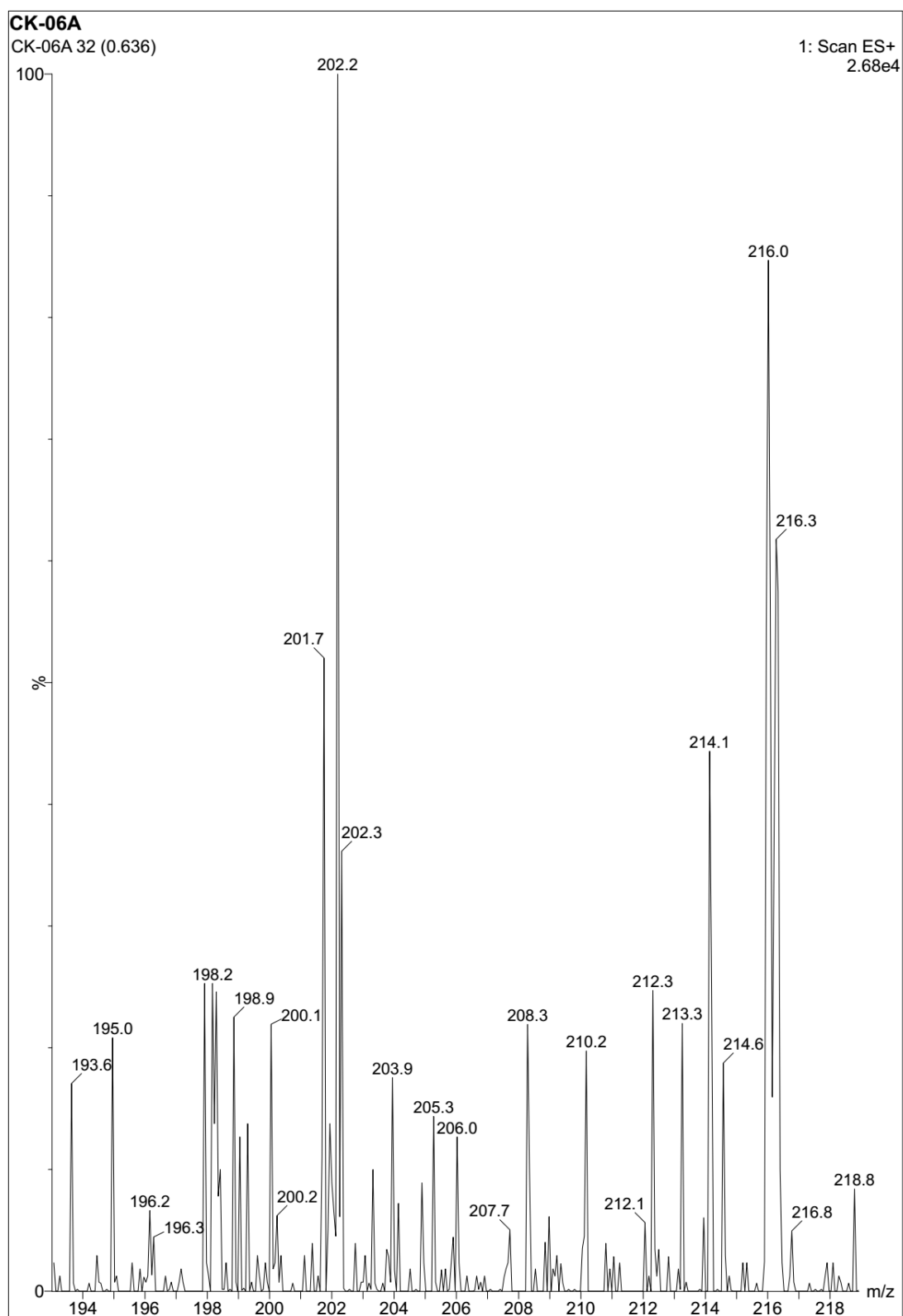
APPENDIX X: ^{1}H NMR spectrum of compound 2

SA-71L-MeOD-500MHz.1.fid —
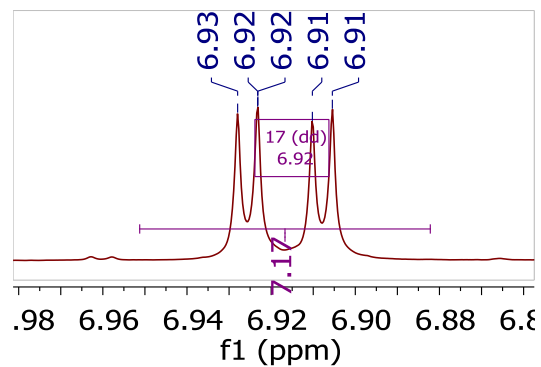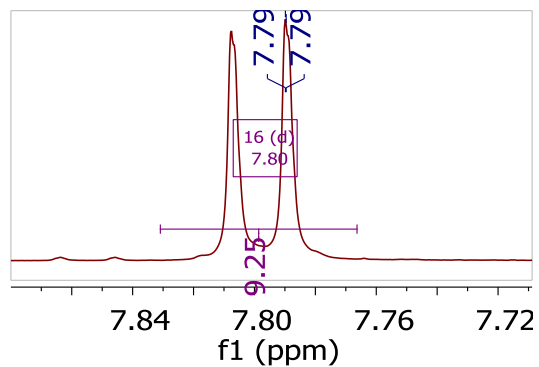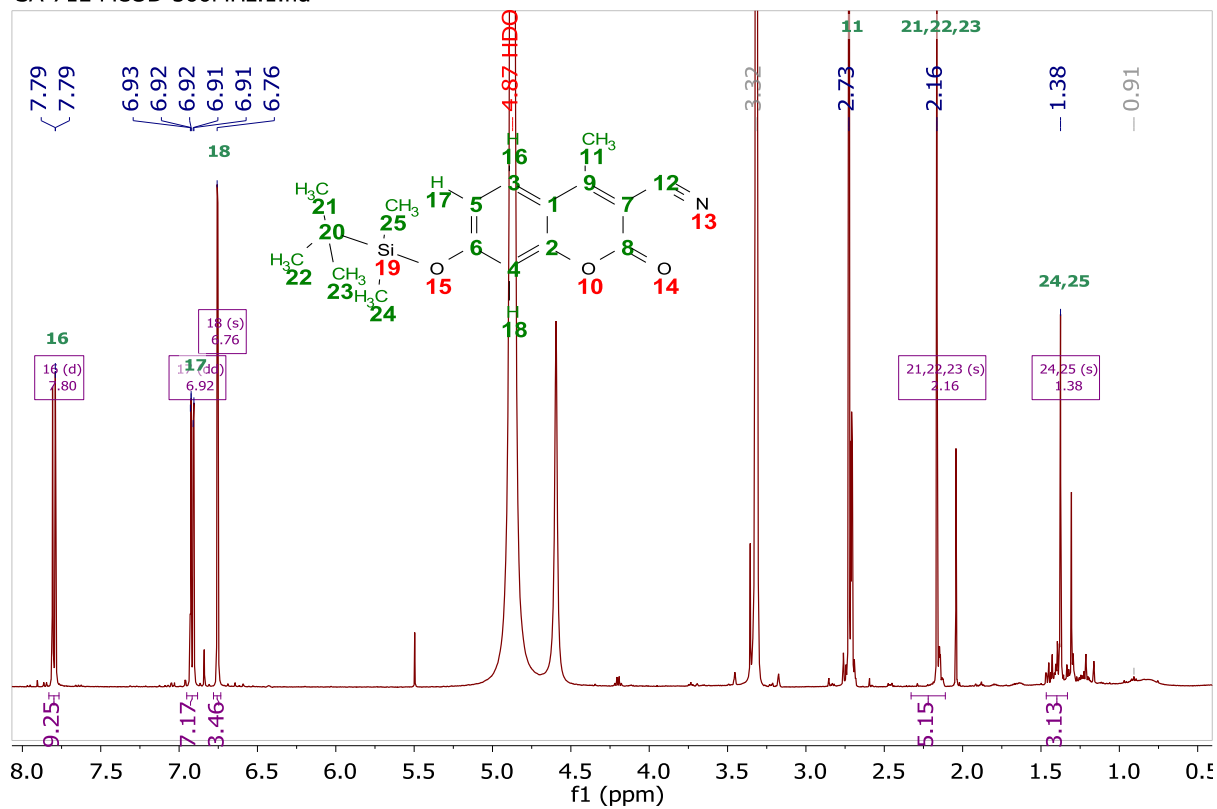
APPENDIX XI: ^{13}C-NMR spectrum of compound 2
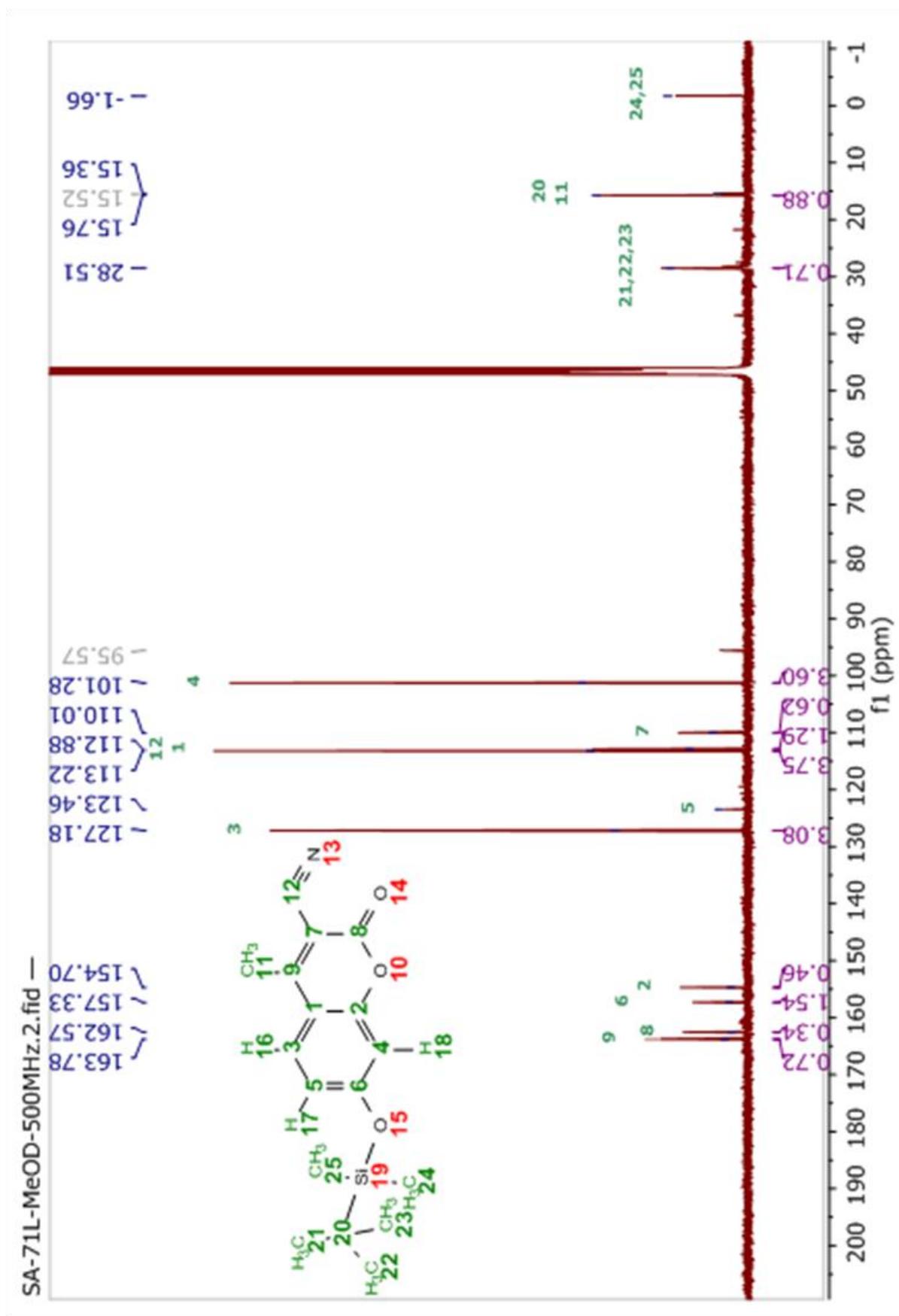
APPENDIX XII: ^{1}H-^{1}H COSY spectrum of compound 2
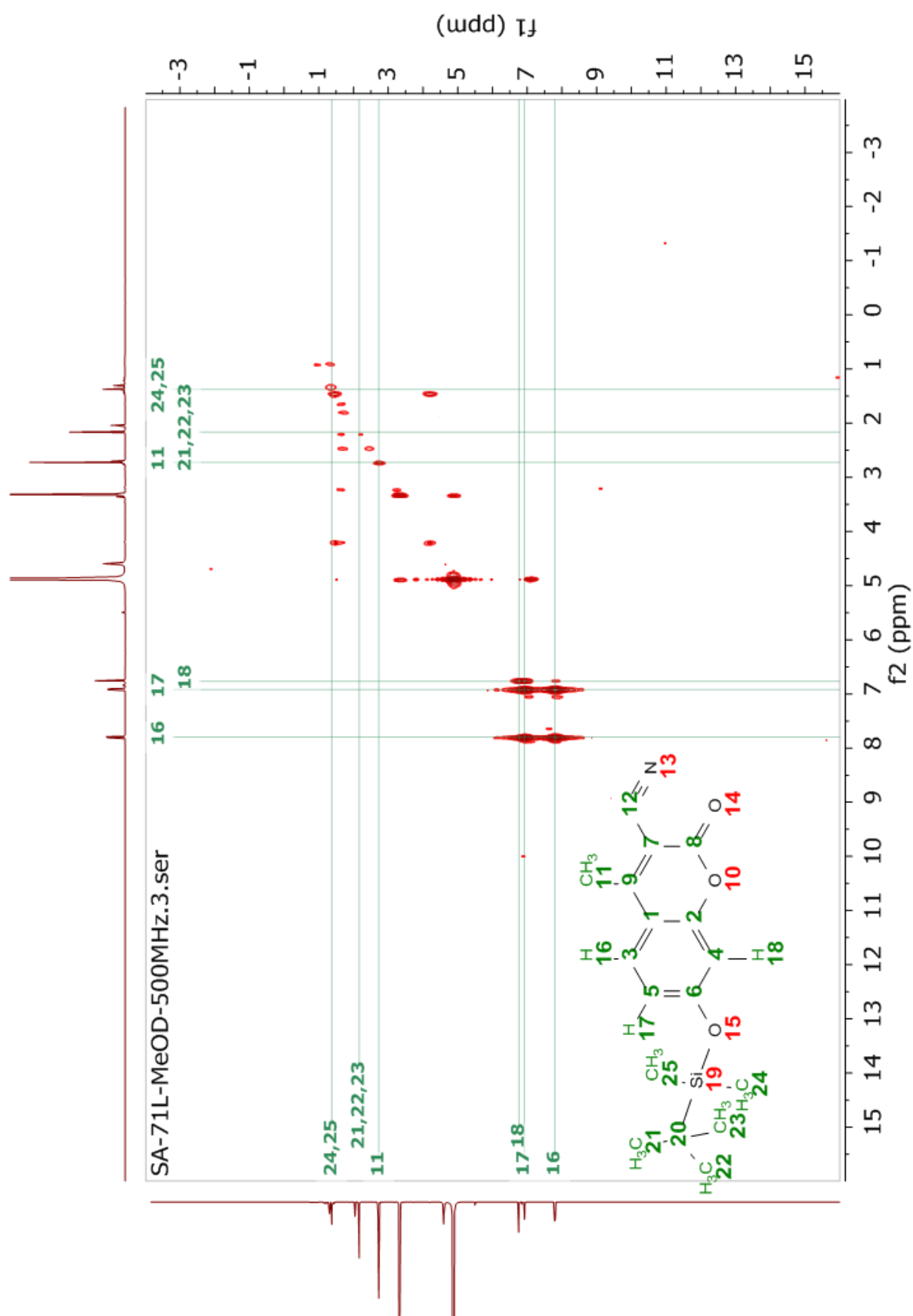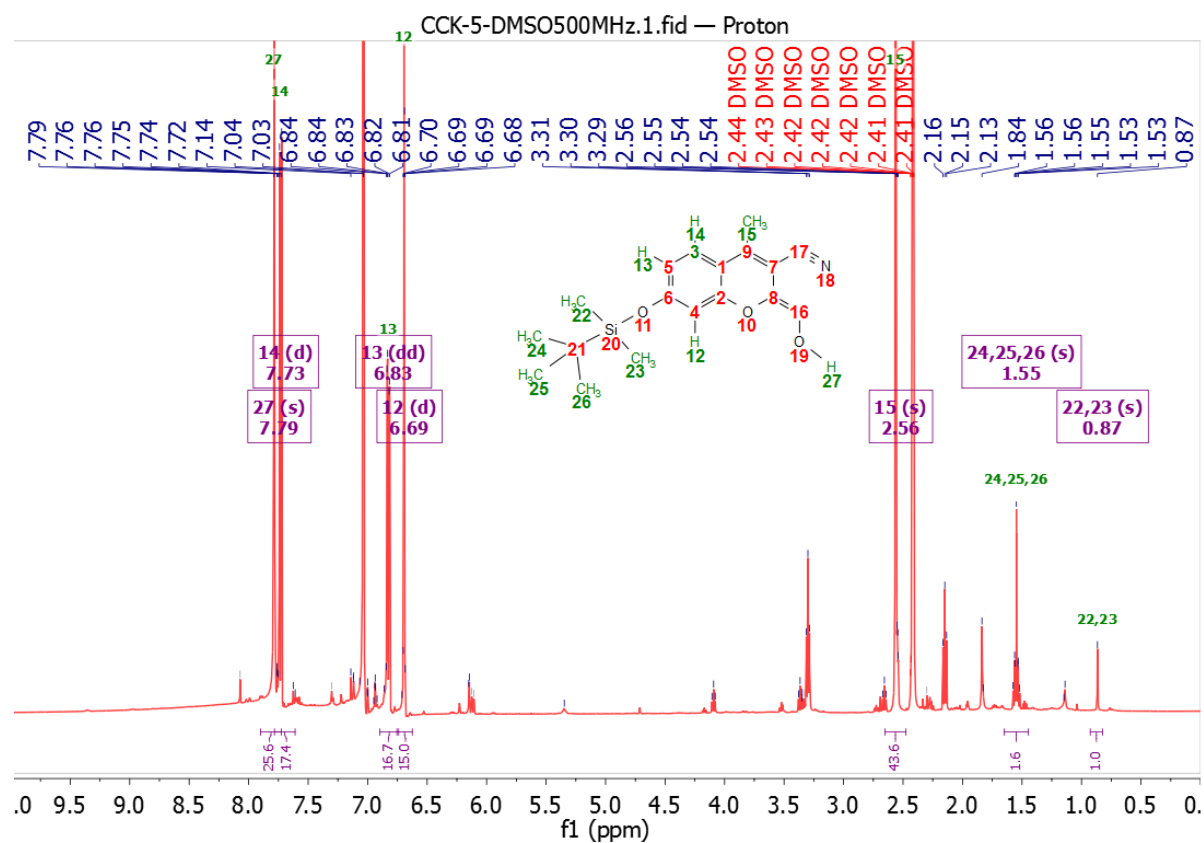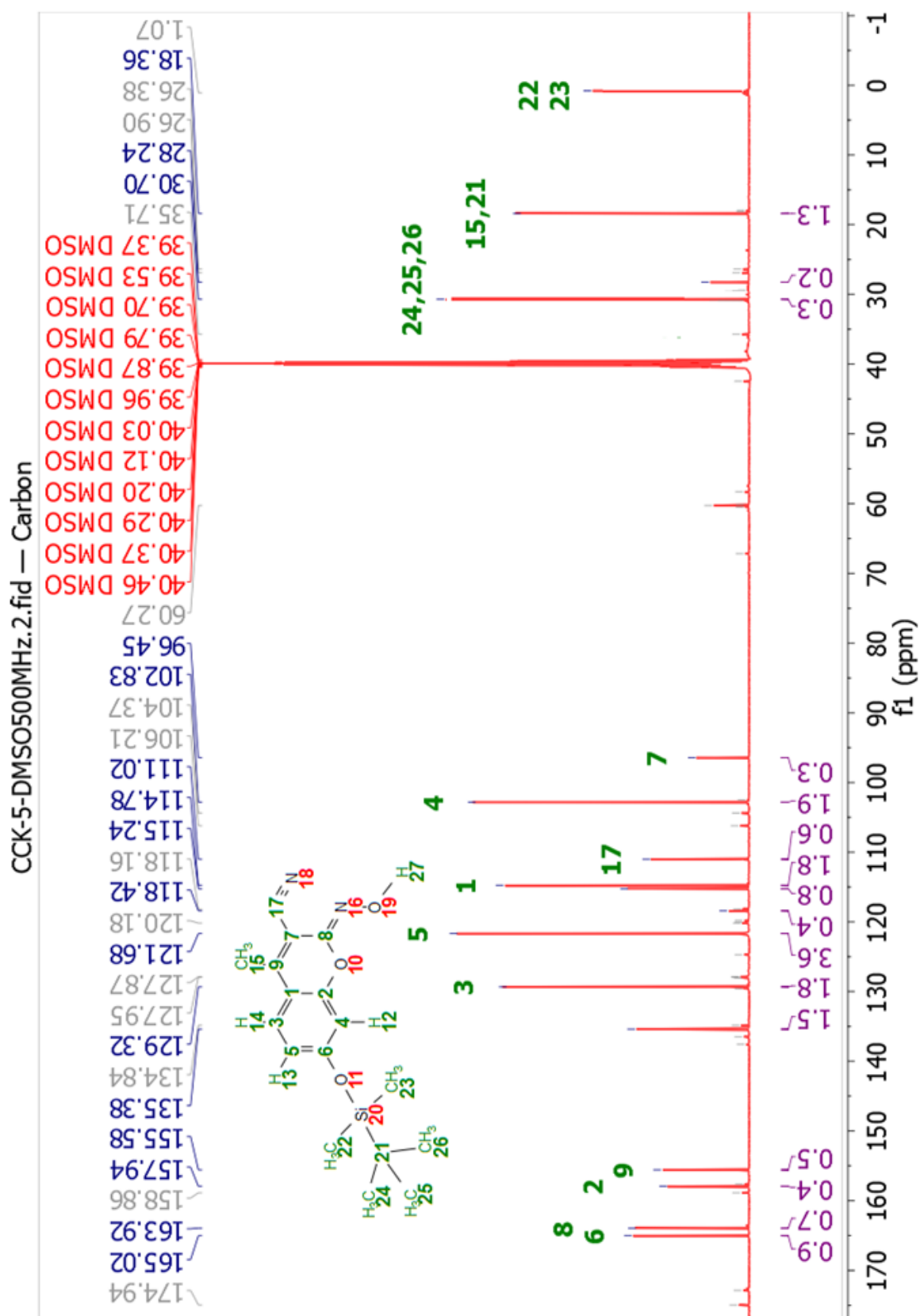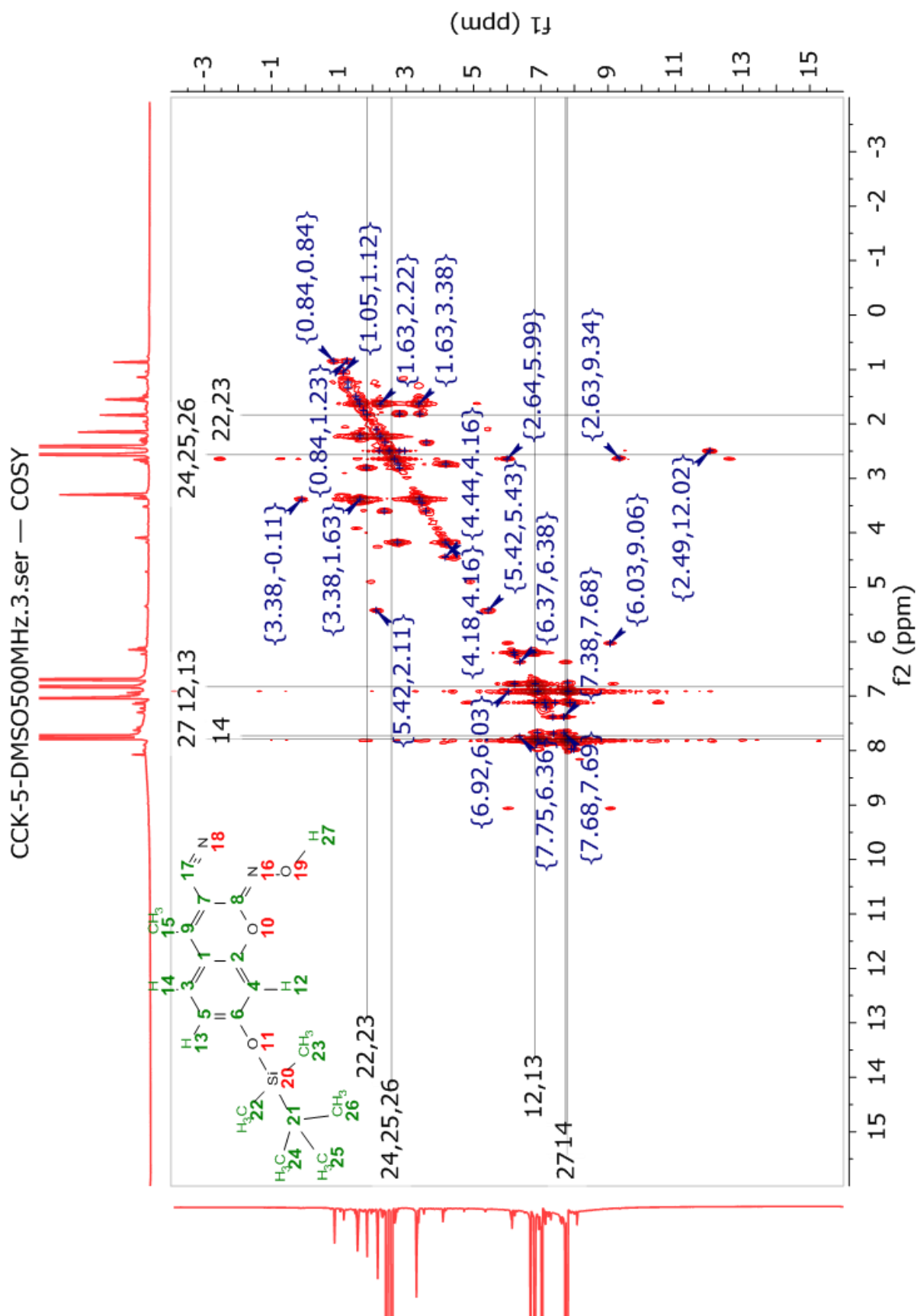
APPENDIX XIII: ^{1}H-^{13}C HSQC spectrum of compound 2
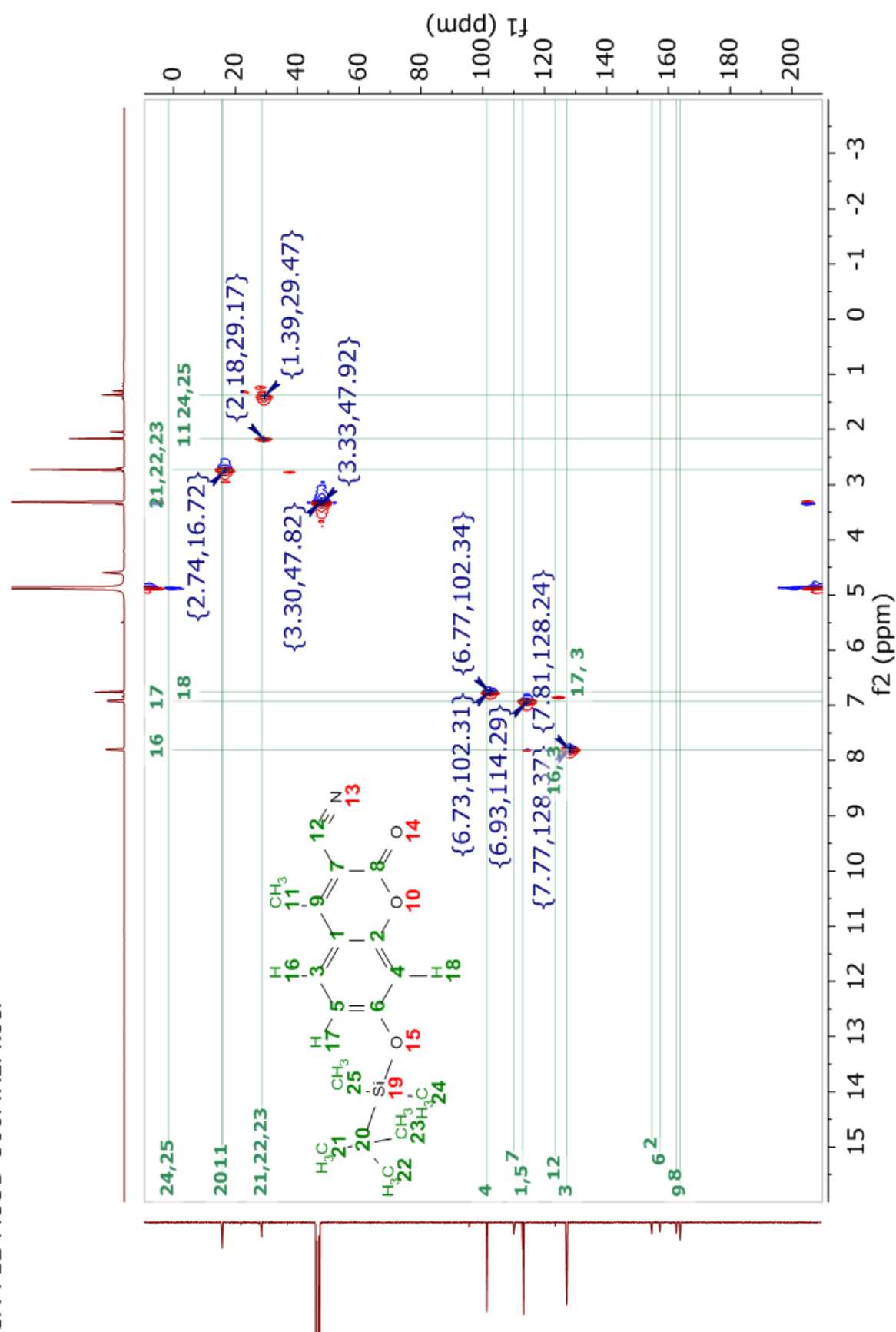
APPENDIX XIV: ^{1}H-^{13}C HMBC spectrum of compound 2
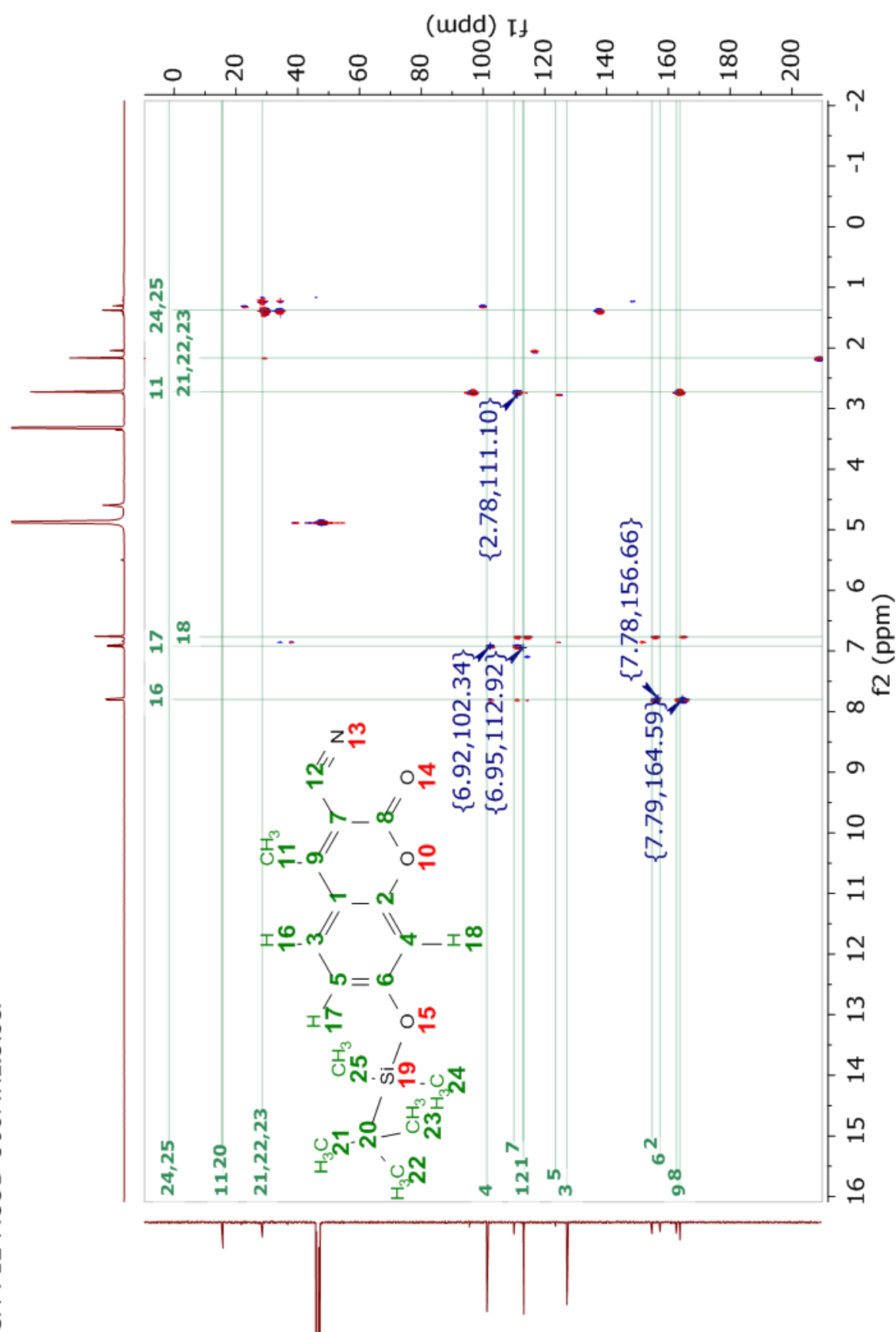
APPENDIX XV: ^{1}H-^{1}H TOCSY spectrum of compound 2
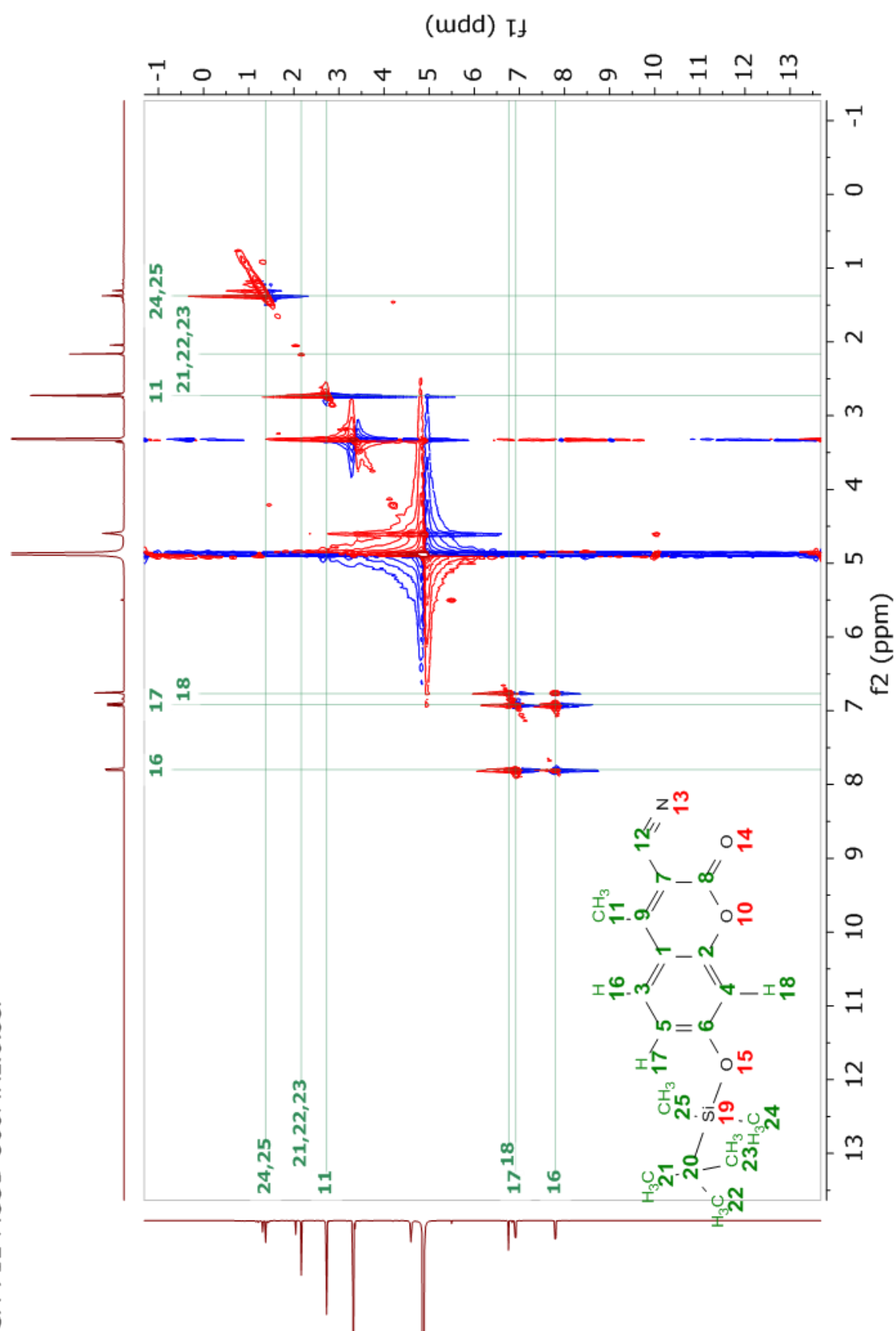
APPENDIX XVI: ^{1}H-^{1}H NOESY spectrum of compound 2
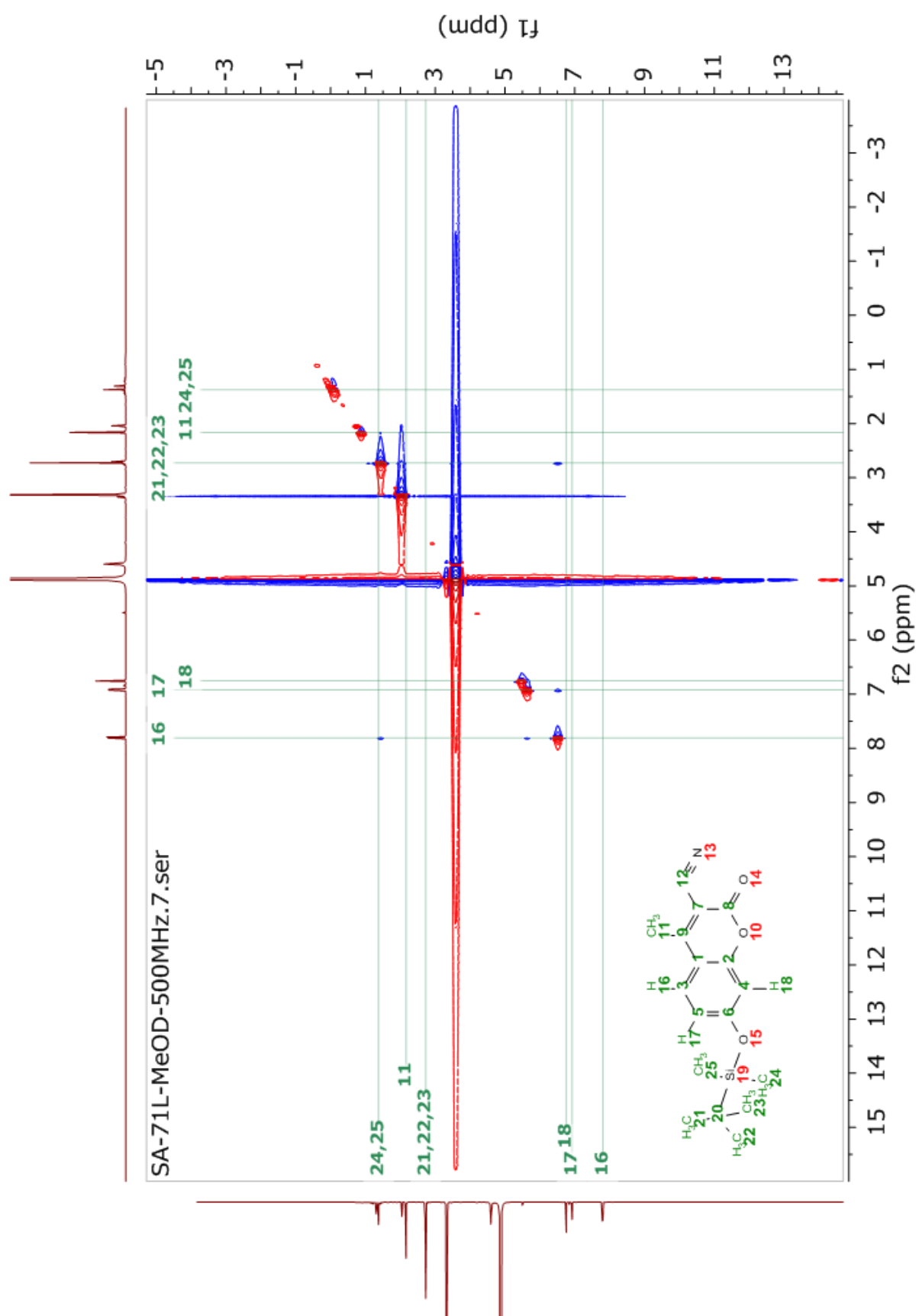
APPENDIX XVII: Diode ArrayChromatogram of compound 2
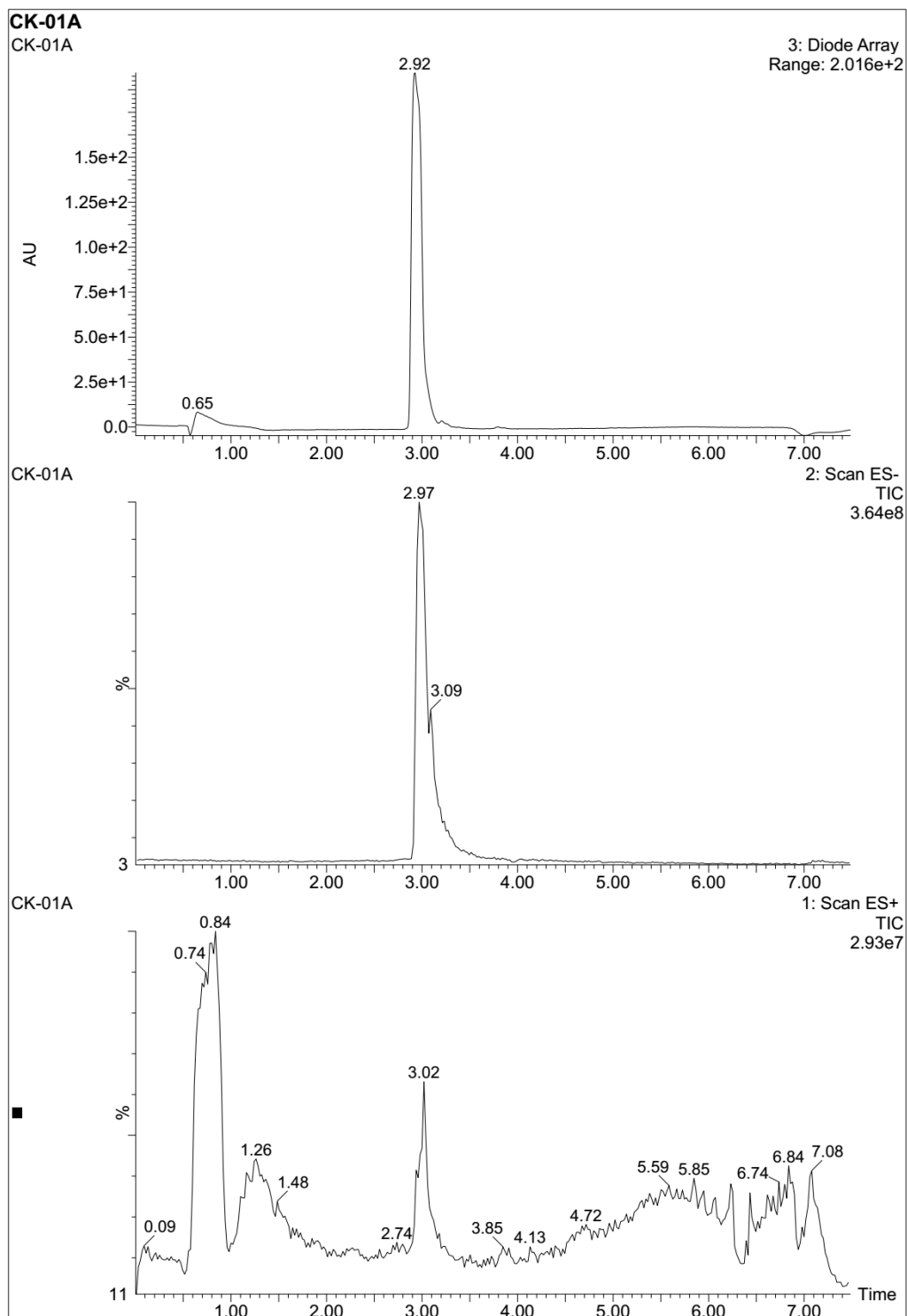
APPENDIX XVIII: Mass Spectrum of compound 2
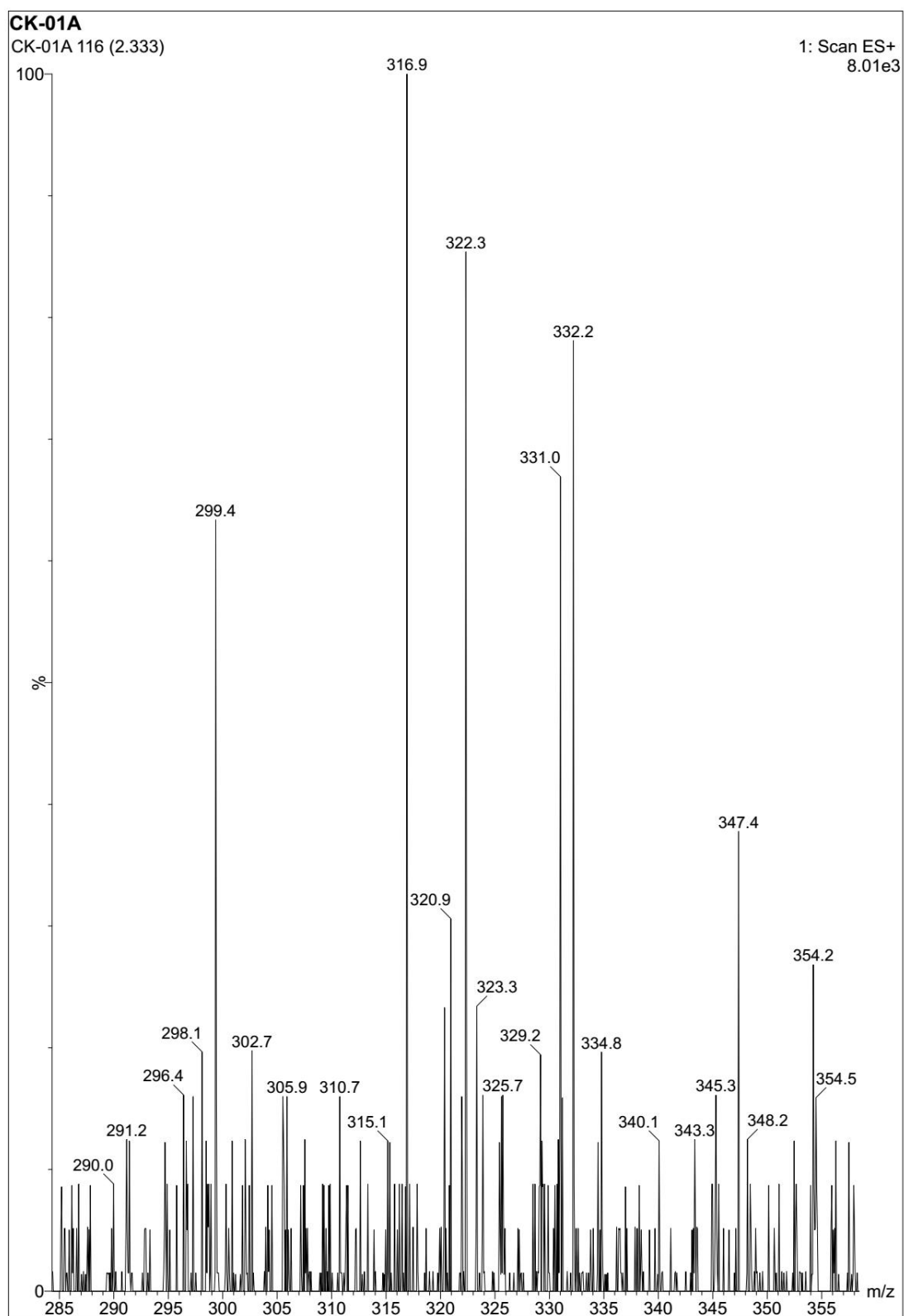
APPENDIX XIX: ^{1}H NMR of compound 3
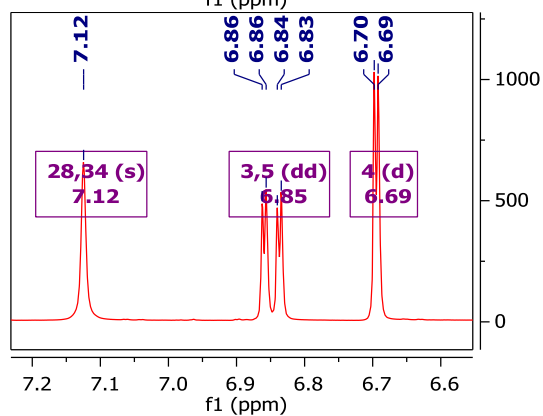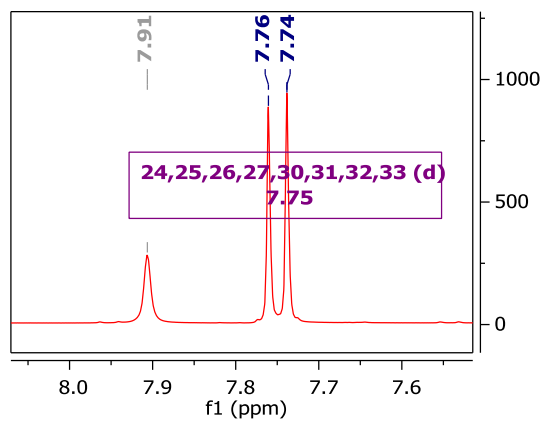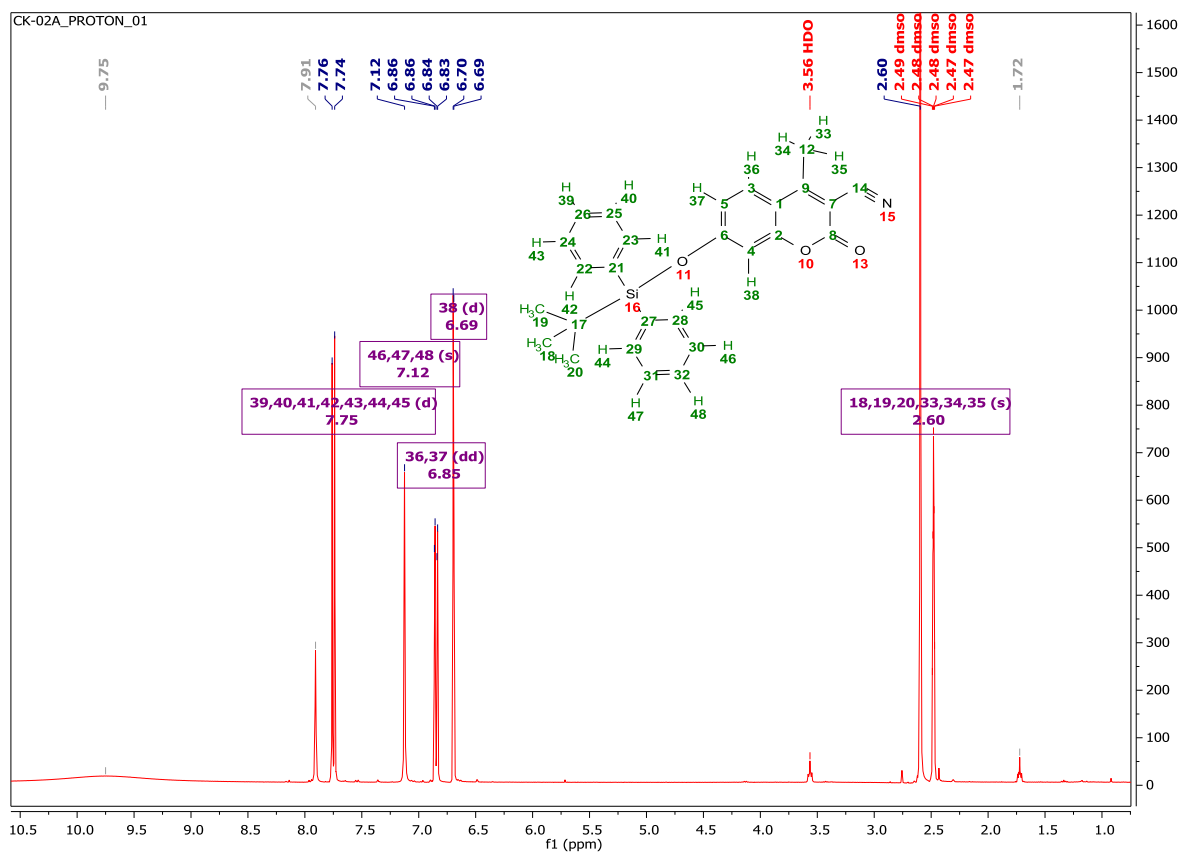
APPENDIX XX: ^{13}C NMR of compound 3
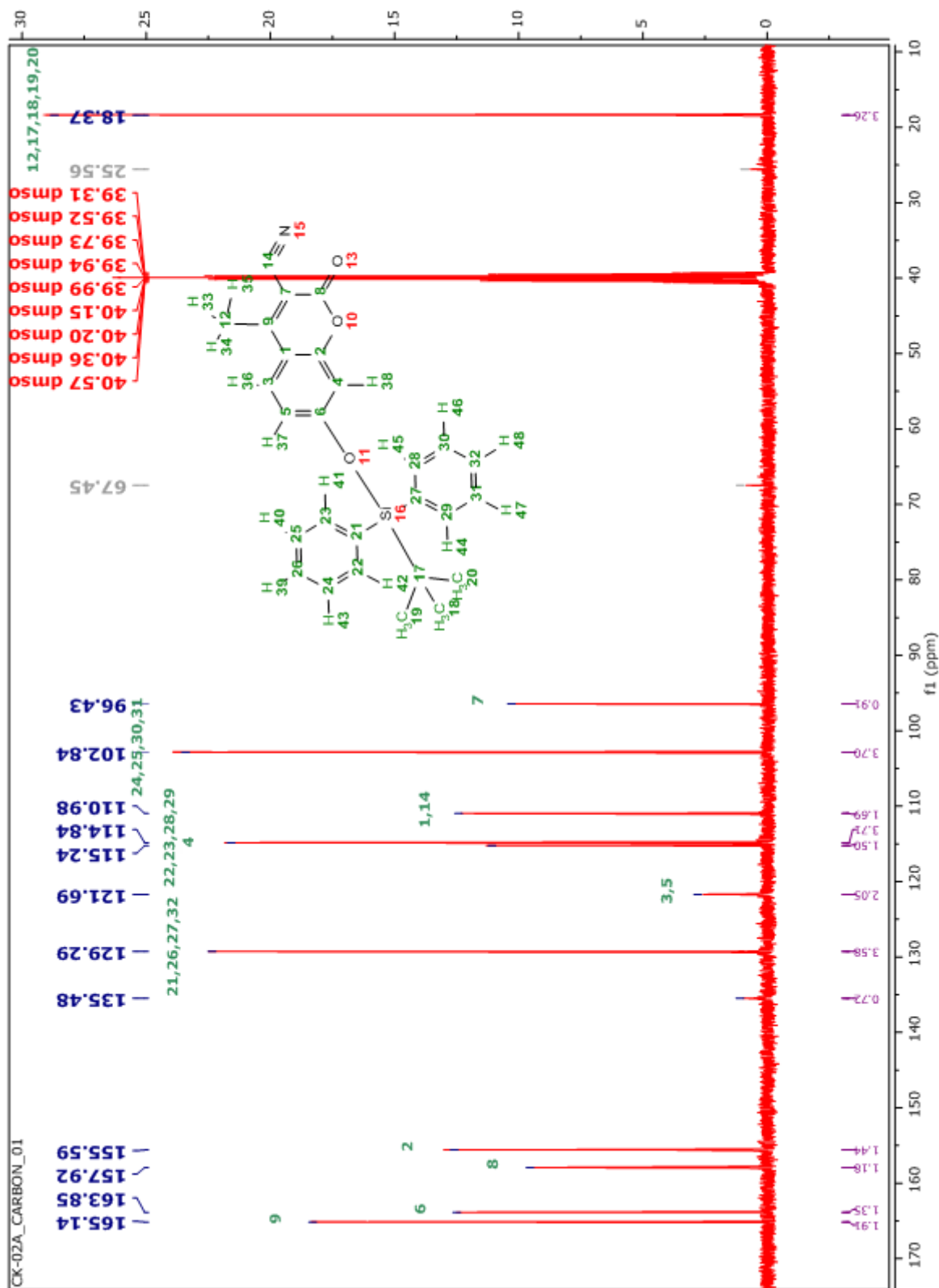
APPENDIX XXI: ^{1}H-^{13}C HSQC spectrum of compound 3
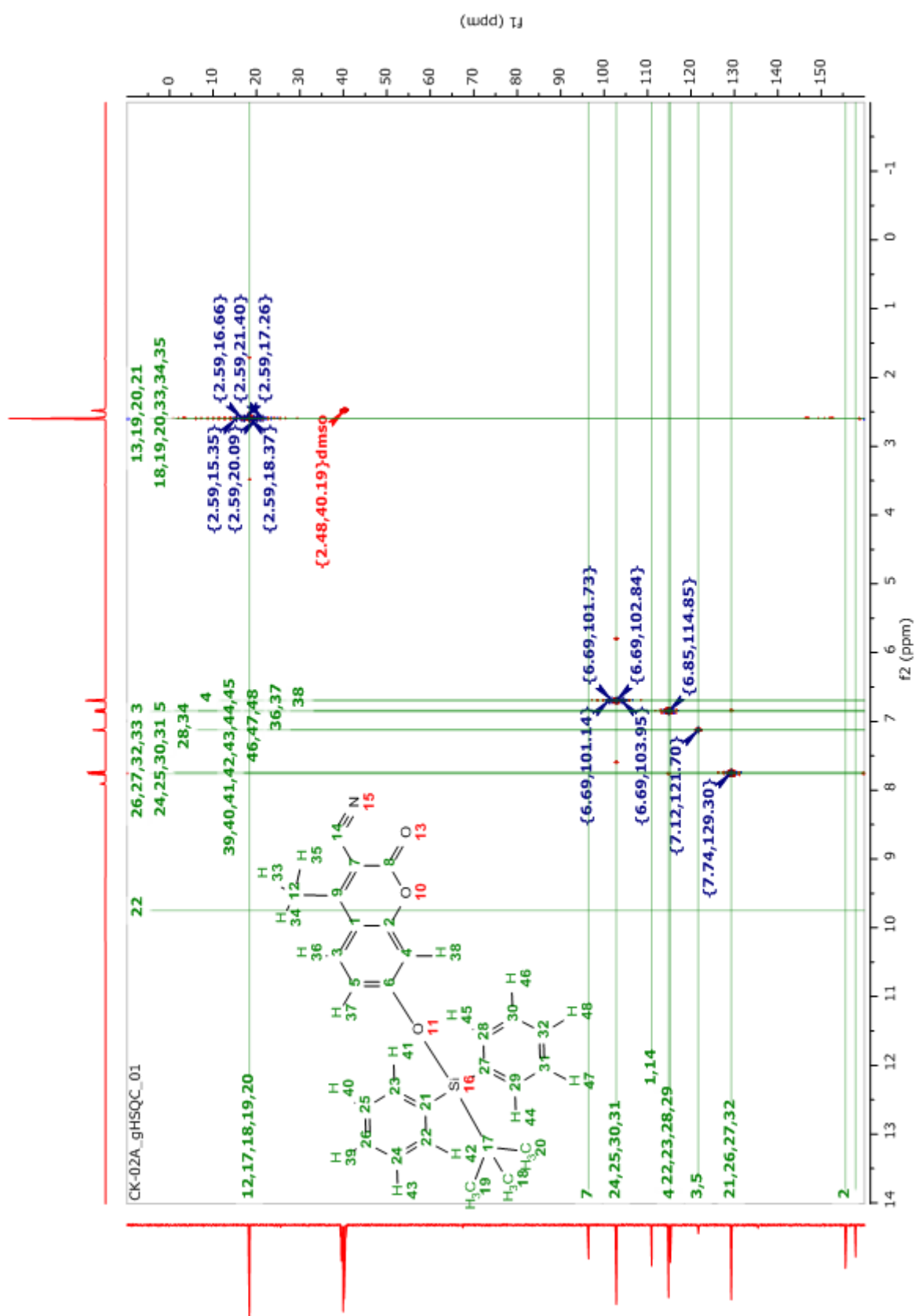
APPENDIX XXII: ^{1}H-^{13}C HMBC spectrum of compound 3
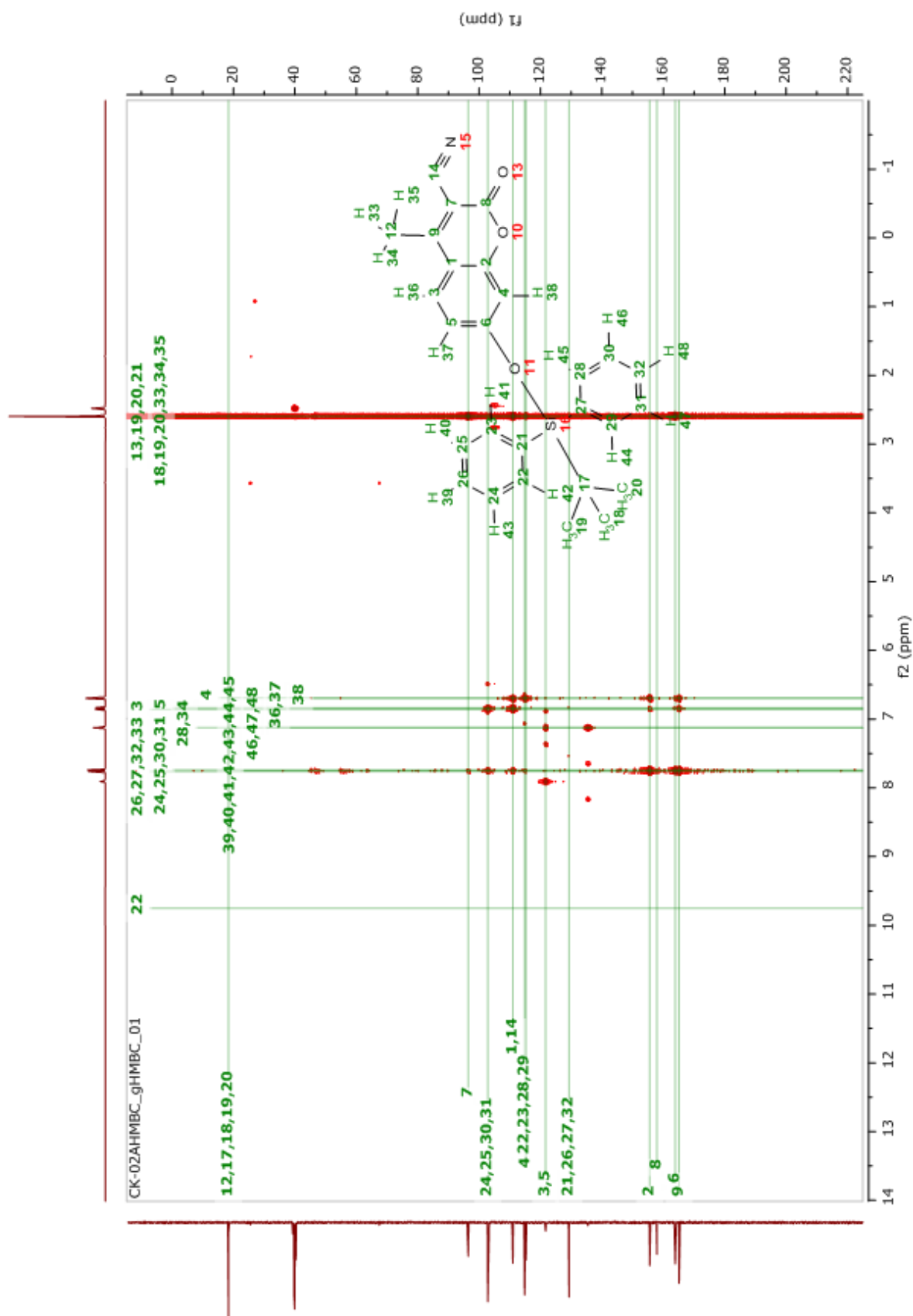
APPENDIX XXIII: Diode Array Chromatogram of compound 3
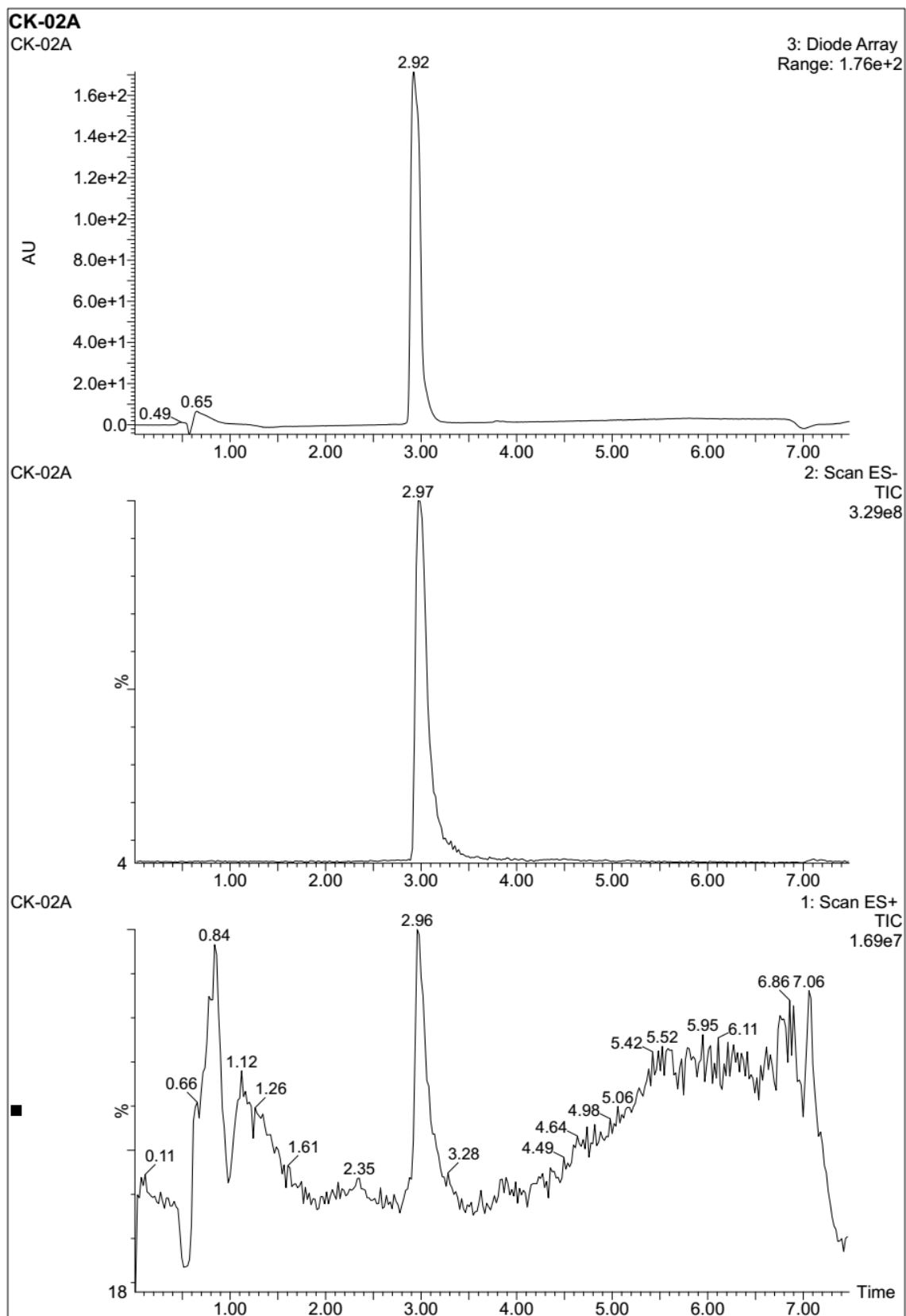
APPENDIX XXIV: Mass spectrum of compound 3
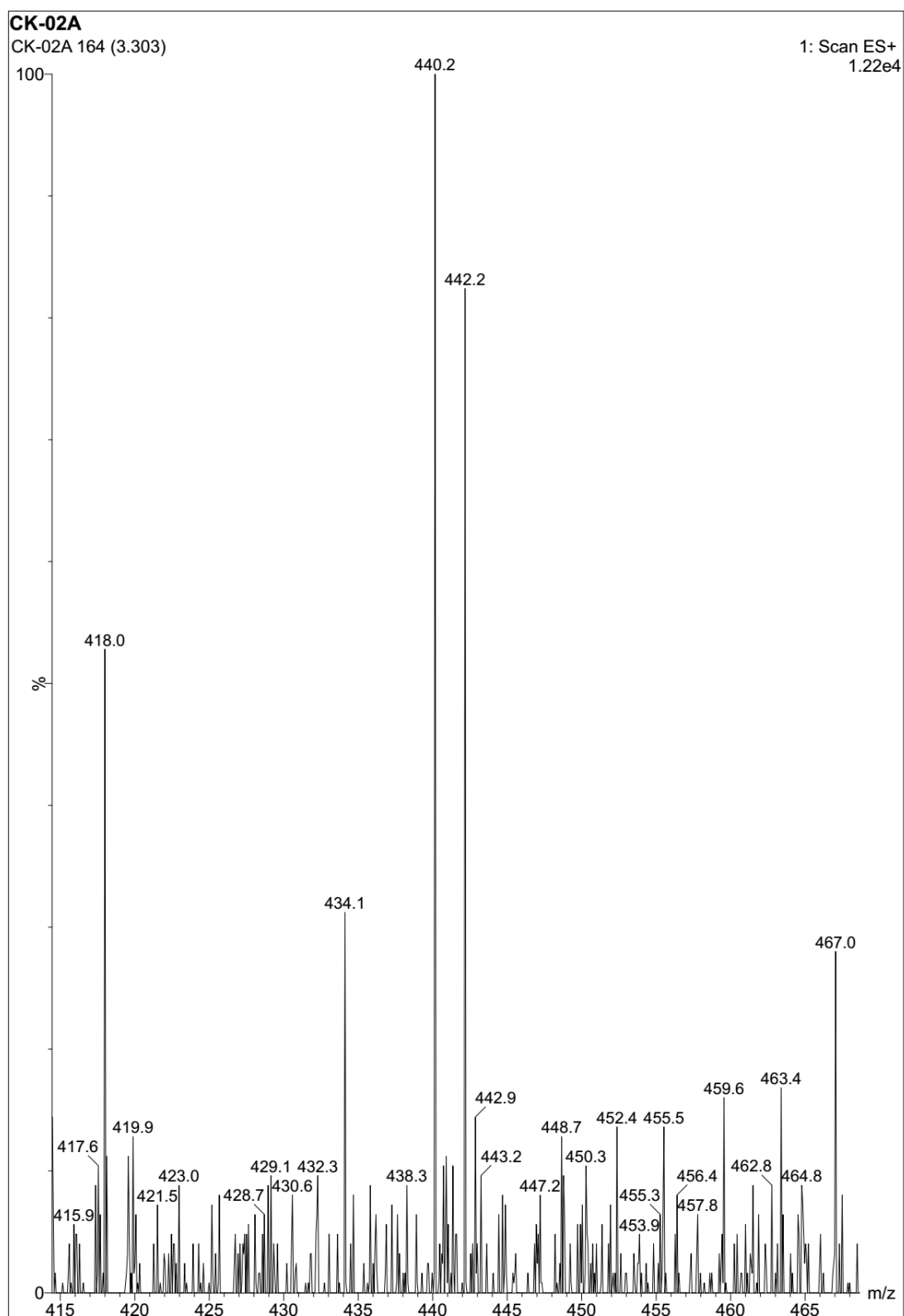
APPENDIX XXV: ¹H NMR spectrum of compound 4
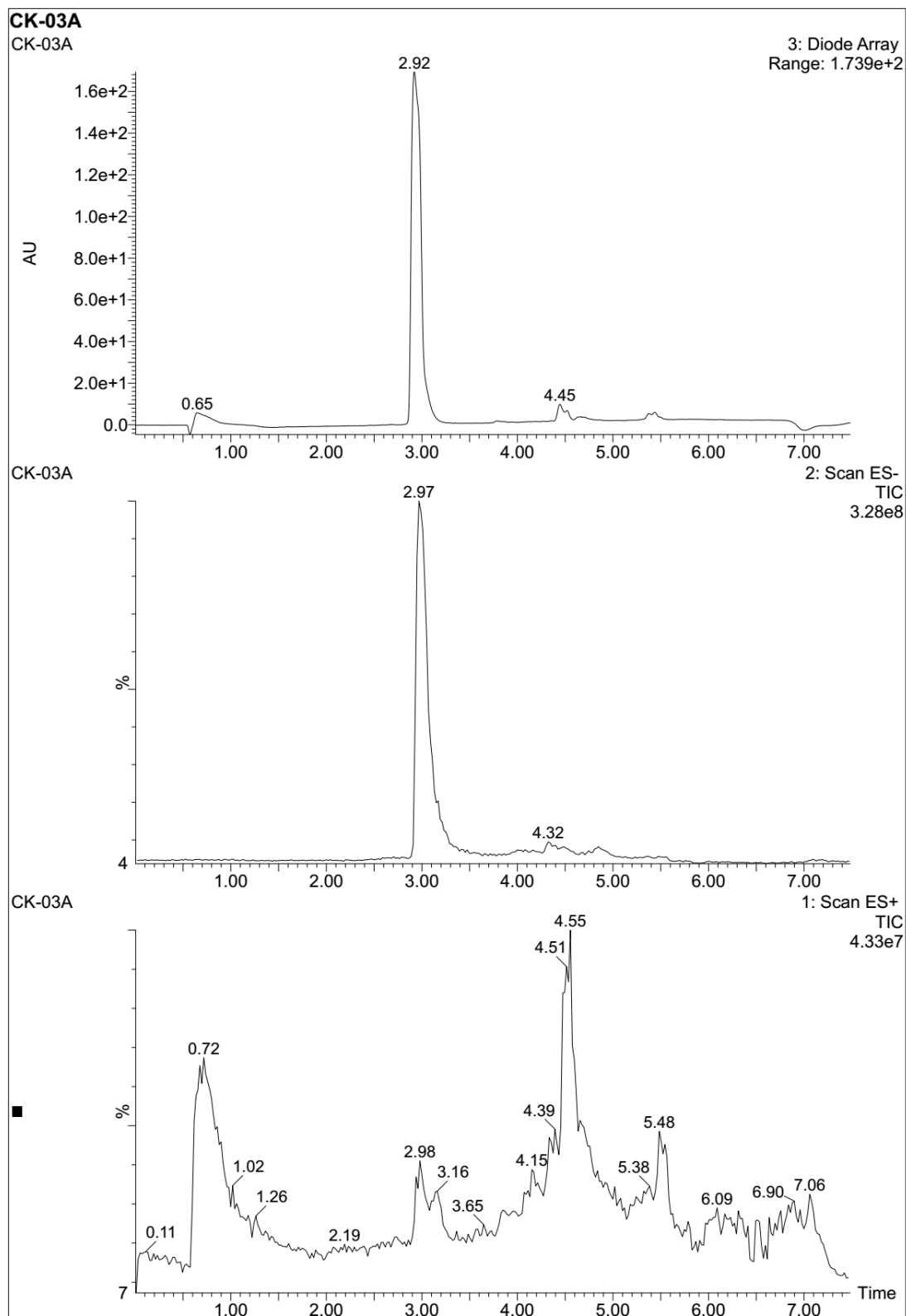

CCK-5-DMSO500MHz.1.fid — Proton
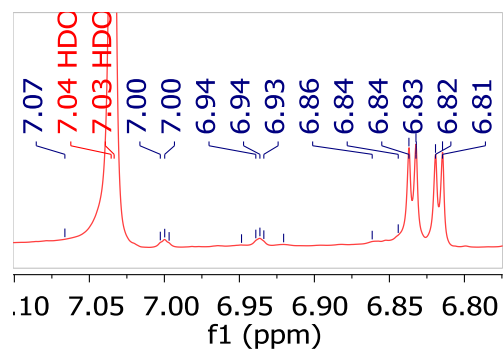
APPENDIX XXVI: ¹³C NMR spectrum of compound 4

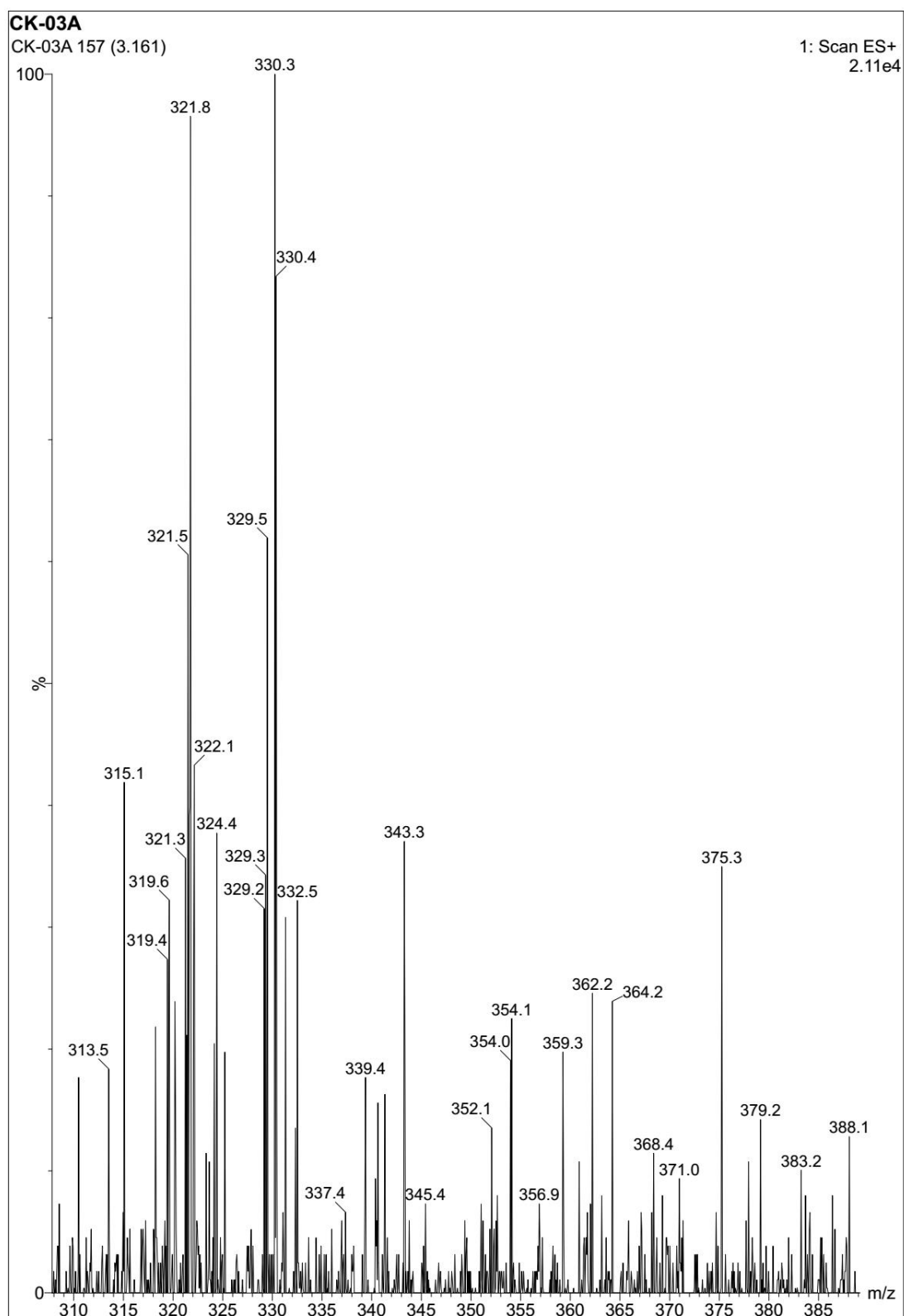**APPENDIX XXVII: ^{1}H-^{1}H COSY spectrum of compound 4**

APPENDIX XXVIII: ^{1}H-^{13}C HSQC spectrum of compound 4
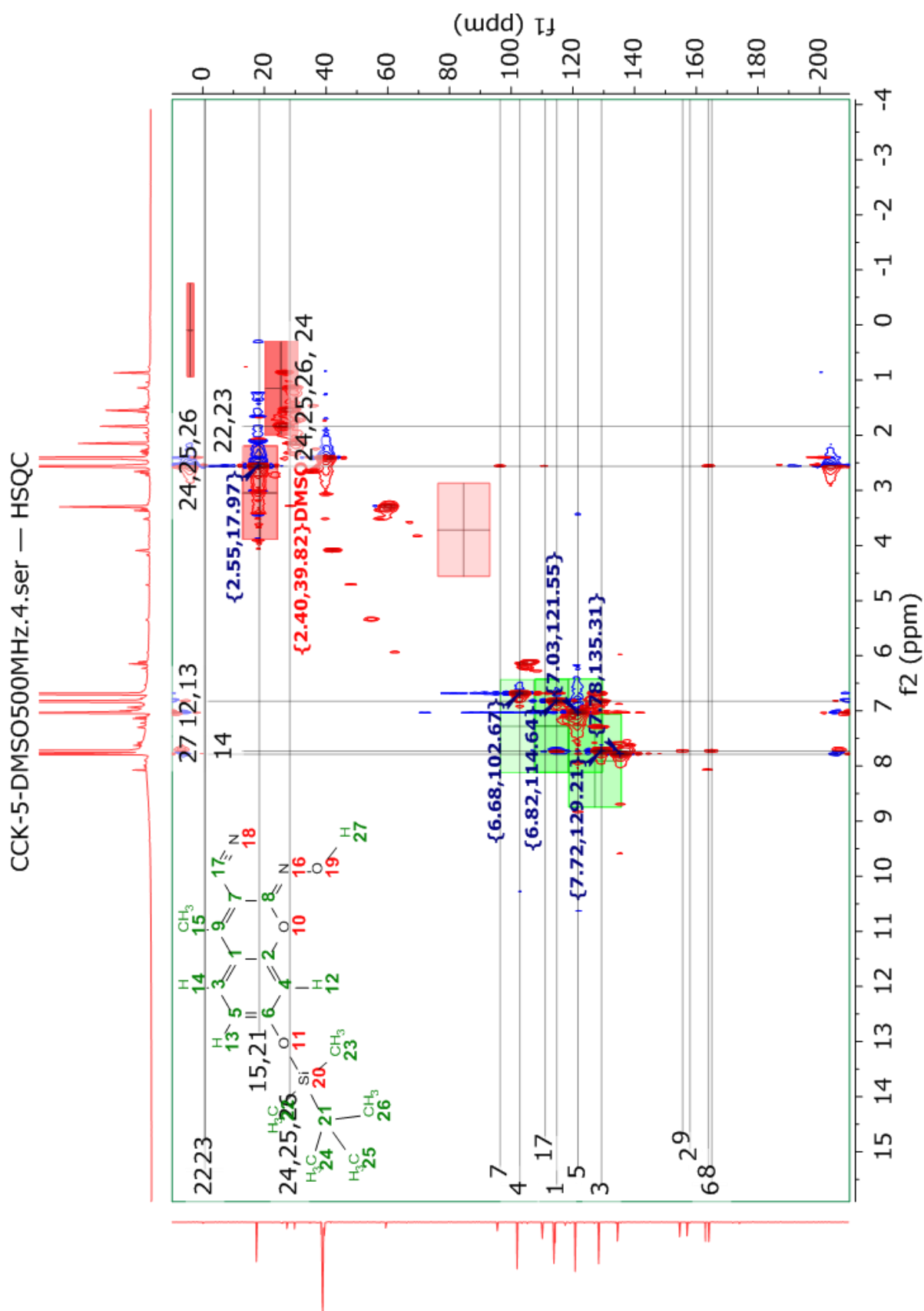
APPENDIX XXIX: ^{1}H-^{13}C HMBC spectrum of compound 4
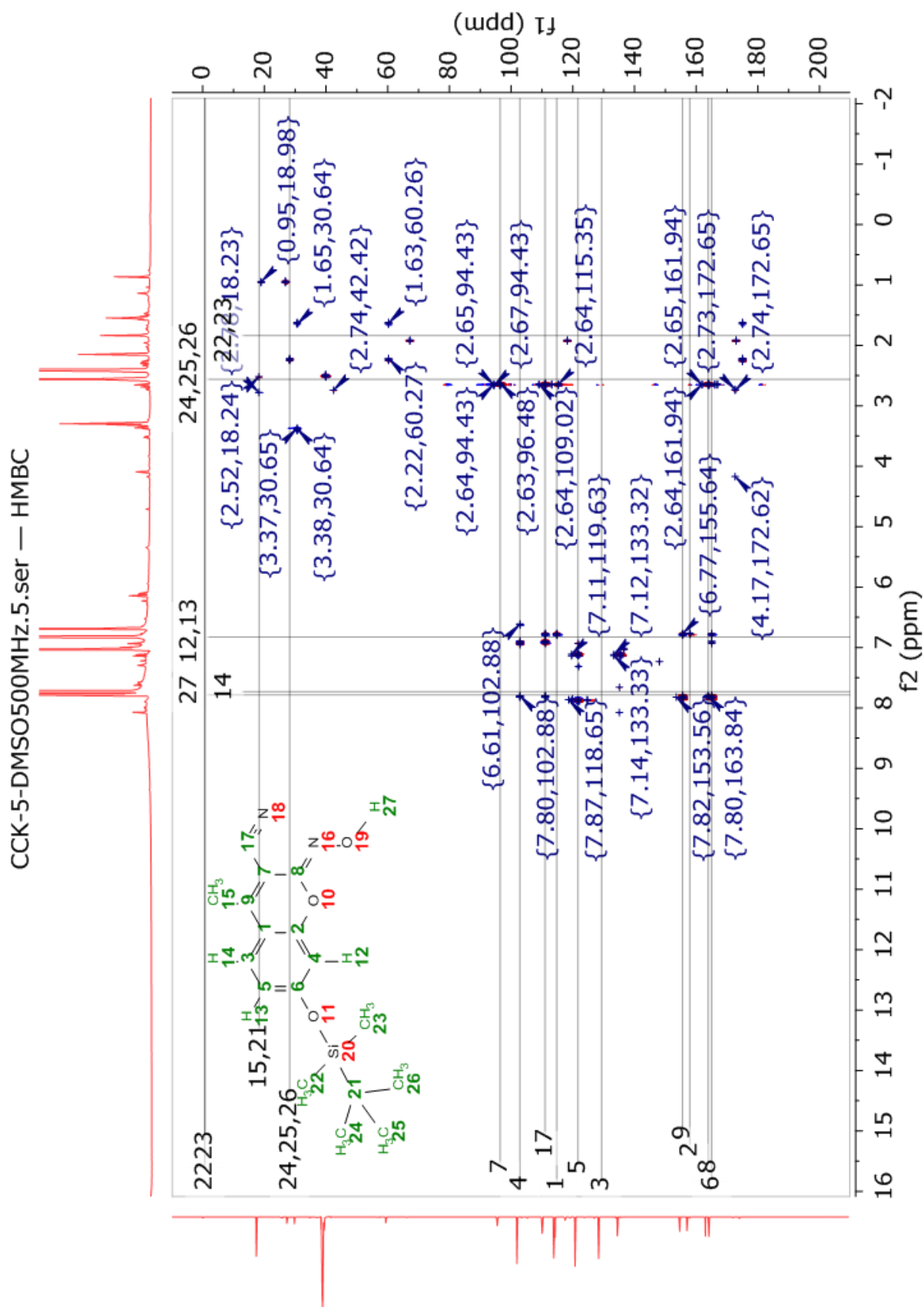
APPENDIX XXX: Diode array chromatograph of compound 4

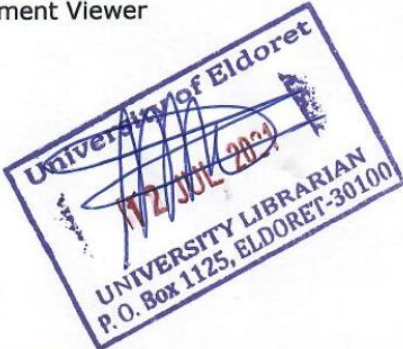**APPENDIX XXXI: Mass spectrum of compound 4**

APPENDIX XXXII: Turnitin Originality Report

Document Viewer

Turnitin Originality Report

Processed on: 12-Jul-2021 08:55 EAT
ID: 1618567533
Word Count: 50166
Submitted: 1

SC/PHD/004/15 By Akumu Otieno Edwin

Similarity Index	Similarity by Source	
	Internet Sources:	9%
17%	Publications:	11%
	Student Papers:	4%

include quoted   include bibliography   excluding matches < 5 words   mode:

quickview (classic) report ⌄   Change mode   print   refresh   download

---

1% match (Internet from 17-Jul-2020)
https://www.mdpi.com/1996-1944/7/9/6317/htm

1% match (publications)
Cametti, Massimo, and Kari Rissanen. "Recognition and sensing of fluoride anion", Chemical Communications, 2009.

1% match (publications)
Duxia Cao, Zhiqiang Liu, Peter Verwilst, Seyoung Koo, Paramesh Jangjili, Jong Seung Kim, Weiying Lin. "Coumarin-Based Small-Molecule Fluorescent Chemosensors", Chemical Reviews, 2019

1% match ()
Int J Mol Sci. 2020 Jun 29; 21(13):4618

1% match (publications)
M. Barathi, A. Santhana Krishna Kumar, N. Rajesh. "Impact of fluoride in potable water − An outlook on the existing defluoridation strategies and the road ahead", Coordination Chemistry Reviews, 2019

<1% match (Internet from 06-Jul-2020)
https://www.mdpi.com/1422-0067/21/13/4618/htm

<1% match (Internet from 08-Jul-2020)
https://www.mdpi.com/1422-0067/21/13/4618/html

<1% match (Internet from 01-Sep-2020)
https://www.mdpi.com/1420-3049/25/7/1520/htm

<1% match (Internet from 04-Jun-2019)
https://www.mdpi.com/1996-1944/7/9/6317/html